

UNIVERSITY OF NAPLES

“FEDERICO II”



PhD in Chemical Sciences

XXIX Cycle

2014-2017

*Design, Synthesis and Processing of Bio-Inspired
Soft Materials:
Toward New Optoelectronic Devices*

Dr Valeria Criscuolo

Supervisors

Dr Paola Manini

Dr Maria Grazia Maglione

Assessor

Prof. Ugo Caruso

PhD Coordinator

Prof. Luigi Paduano

~CONTENTS~

⊖ INTRODUCTION	4
• References	12
⊖ SECTION 1: Design, synthesis and characterization of new nature-inspired organic electroluminescent emitters and their application in opto-electronic devices	
○ INTRODUCTION	15
• References	36
○ CHAPTER 1: Eumelanin-inspired triazatruxenes as novel blue emitters	
• Introduction	38
• Results and Discussion	43
• Conclusions	73
• Experimental Section	74
• References	81
○ CHAPTER 2: Dopamine-inspired iridium (III) complexes as red emitters	
• Introduction	84
• Results and Discussion	92

•	Conclusions	112
•	Experimental Section	113
•	References	125
○	CHAPTER 3:	
	Synthesis and photophysical properties of iridium (III) complexes with pyridophenoxazinone ligands	
•	Introduction	127
•	Results and Discussion	129
•	Conclusions	136
•	Experimental Section	137
•	References	141
⊖	SECTION 2:	
	Design, synthesis and properties of eumelanin-based semiconductors and their applications in electronic devices	
○	INTRODUCTION	143
•	References	150
○	CHAPTER 1:	
	Novel approaches to the deposition of eumelanin thin films	
•	Introduction	152
•	Results and Discussion	154

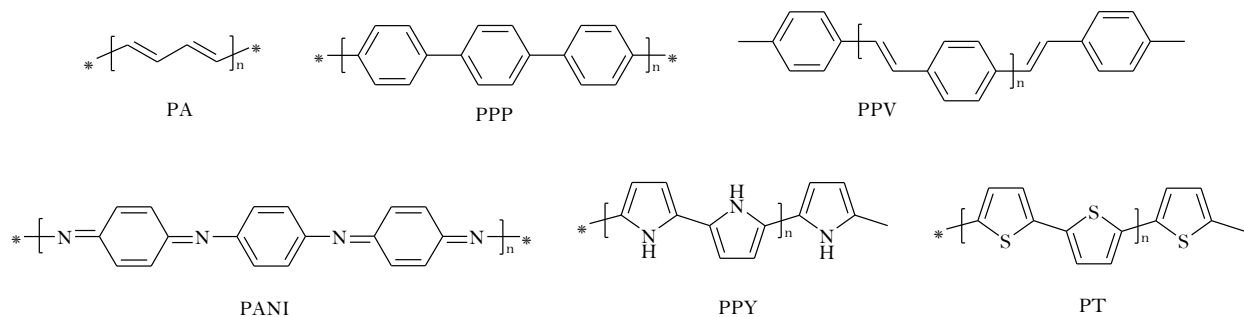
•	Conclusions	160
•	Experimental Section	161
•	References	164
○	CHAPTER 2:	
	Electrical properties of eumelanin thin films	
•	Introduction	166
•	Results and Discussion	169
•	Conclusions	181
•	Experimental Section	182
•	References	184
○	CHAPTER 3:	
	New melanin-based bio-interfaces	
•	Introduction	186
•	Results and Discussion	188
•	Conclusions	192
•	Experimental Section	193
•	References	195
⊖	LIST OF PUBLICATIONS	196
⊖	COMMUNICATIONS AT MEETINGS	197

~INTRODUCTION~

Modern mankind is surrounded by electronic devices without which it seems to be impossible to live. The birth of electronics can be traced back in the 1835 with the invention of the relay, a remote switch controlled by electricity, by Joseph Henry; from that breakthrough invention, electronic devices have become ubiquitous in modern technology, finding their way into nearly all industries including telecommunications, automotive, consumer electronics and many others.

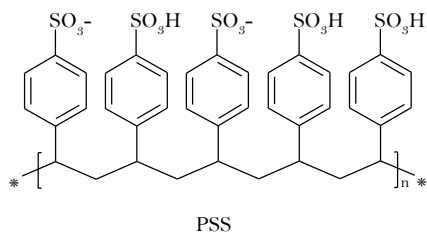
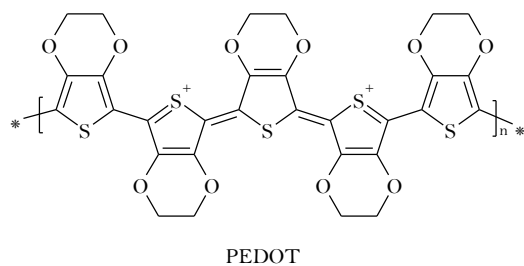
The interest on conducting organic compounds virtually started in the same period, when in 1862 Dr H. Letheby of the College of London Hospital was able to produce green and blue pigments (polyanilines) starting from aniline salts treated with sulphuric acid and electrically oxidized. Surprisingly, while the reactants were markedly electrically insulating, the obtained pigments were characterized by a partly metallic behavior, being able to conduct electricity.¹ This discovery changed the common scientific idea that polymers can only be insulators.

For almost one century there have been few studies concerning the electrical conductivity of organic polymers, probably due to the lack of appropriate experimental equipment and theories. Finally in 1977 H. Shirakawa, A. G. MacDiarmid, A. J. Heeger and their co-workers, the so-called "Pennsylvania group", published their well-known paper describing the electrical properties of polyacetylene, the prototype of all conjugated polymers.² This seminal work was awarded with the Nobel Prize in Chemistry in 2000 and opened a new era for organic compounds. Extensive theoretical and experimental studies followed this work and were initially focused on the properties of *trans*-polyacetylene (PA)³ and then shifted towards environmentally more stable conjugated polymers such as poly-*p*-phenylene (PPP),⁴ poly-*p*-phenylenevinylene (PPV),⁵ polyanilin (PANI),⁶ polypyrrole (PPy)⁷ and polythiophene (PT)⁸. These polymers overcame the limited stability of polyacetylene by stabilizing the polyene structure with heteroatoms or arene moieties.⁹



A further step forward was made in 1963 by Pope, describing for the first time the phenomenon of the electroluminescence of organic materials, and in detail of anthracene crystals by applying a direct current in vacuum.¹⁰ This opened the way to the development and fabrication organic optoelectronic devices.

During the eighties and nineties, this new field of organic chemistry flourished addressing many efforts in synthesizing novel electroactive materials for the realization of the devices. The discovery of the conductive polymer poly(3,4-ethylenedioxythiophene) polystyrene sulfonate (PEDOT:PSS) is the best example of this research and today is still the most important and utilized organic semiconductor.¹¹



PEDOT:PSS

In this period, the design and fabrication of the first organic semiconductor-based electronic devices, such as Field Effect Transistors, Light Emitting Diodes and Photovoltaic Cells, run in

parallel and the expression “organic electronics” started to be used in scientific publications to indicate the electronic based on devices whose active materials are organic compounds, especially in contrast to “traditional” silicon-based electronics.

The rapid growth of the number of research works published during that period witnessed the importance and the advantages of replacing typical inorganic semiconductors with organic ones. First of all, the unique mechanical properties of organic materials allow the fabrication of flat, light, flexible and large-area devices¹² that can be realized with any kind of geometry on different types of substrates, such as plastics, paper and even textile for wearable electronics. Basically, organic semiconductors can overcome the intrinsic rigidity of inorganic materials that limit the manufacturing of bendable and stretchable devices for different applications. Another advantage is the easy and low-cost processing of the organic-based devices. Whereas conventional silicon technology requires high-temperature and high-vacuum deposition processes and sophisticated photolithographic patterning methods, organic-based devices can be fabricated by using low temperature solution processing techniques, such as roll-to-roll or ink-jet printing.¹³

Finally, organic materials can be easily designed in order to confer specific properties that can make conductivity or electroluminescence to fit specific requirements. This can be achieved via the insertion of proper functional groups, modification of the skeleton backbone or of the degree of π -conjugation, by using the toolbox of organic chemistry.¹⁴

Initially the use of organic semiconductors in electronic devices proved very limited due to several drawbacks: 1) the reproducibility and carrier mobility in organic semiconductors were very low; 2) the fabricated devices required very high voltages (e.g. 400V) because of the high crystal thickness (in the micrometer to millimeter range) and poor contact between the organic compound and the electrodes limiting an efficient charge injection; 3) the poor control over material purity, structure ordering and stability. The first available organic materials were intractable, immobile, or even insoluble.¹⁵ Nevertheless, the rapid advancement of the materials and processing has enabled the development of soluble organic compounds. Solubility is a key prominent feature, one that opened the possibility for cheap and high-volume production of printed electronics.

The devices initially developed with the rise of organic electronics were: organic thin-film transistors (OTFTs), organic photovoltaic cells (OPVCs) and organic light-emitting diodes (OLEDs).

An OTFT is a three-terminal device, in which the voltage applied to a gate electrode controls the current flow between a source and a drain electrode under an imposed bias (Figure 1).¹⁶ It is the fundamental building block for basic analytical circuits and is essential for the fabrication of modern memory devices, integrated circuits, and microprocessors used in personal computers and laptops.

The discovery of the field effect in organic semiconductors can be dated back to 1970,¹⁷ yet the potential use of the OTFT (at that time mostly referred to as metal-insulator-semiconductor field-effect transistor MISFET) as an electronic device was only identified in 1983 when Ebisawa et al. reported on the first attempt to fabricate an OTFT using polyacetylene as an active semiconducting layer.¹⁸ From this point forward, several studies were devoted to the realization of successful TFTs based on organic semiconductors such as polythiophenes and metallophthalocyanines. However, their carrier mobilities were very low, ranging from 10^{-5} up to 10^{-4} cm^2/Vs . In 1990 Garnier et al. reported carrier mobility as high as 4.3×10^{-1} cm^2/Vs for TFTs that used evaporated hexathiophene as an active material, approaching and even reaching the performance of amorphous silicon (carrier mobilities in conventional a-Si:H TFTs are in the range of 10^{-1} to 1 cm^2/Vs).¹⁹

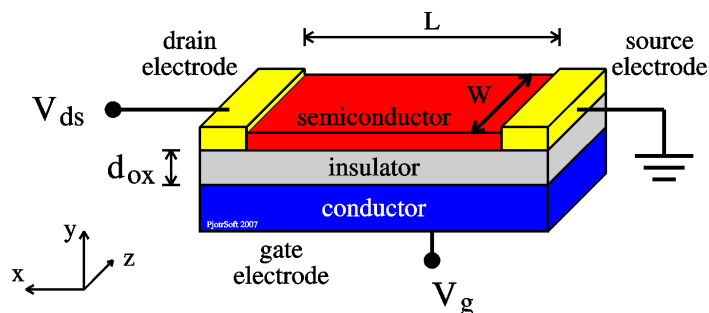


Figure 1. Scheme of an OTFT device configuration.

An OPVC is a two-terminal optoelectronic device based on organic materials that is able to convert the absorbed solar light into electricity.²⁰ It is usually realized using as cathode a reflecting metal and as anode a transparent conducting oxide in order to collect the light. The active organic compound is sandwiched between the two electrodes and upon light absorption produces an exciton; the produced charges, positive and negative, are then transported and collected by the electrodes to produce electricity (Figure 2).

The use of conjugated polymers, such as poly(sulphur nitride) and polyacetylene, for the realization of OPVCs was firstly investigated in the 1980s; their power conversion efficiencies, however, were below 0.1%.²¹ A major breakthrough came in 1986 when the American physical chemist Ching W. Tang discovered that a two-layer OPVC by bringing a donor and an acceptor in one cell could dramatically improve the efficiency up to 1%.²²

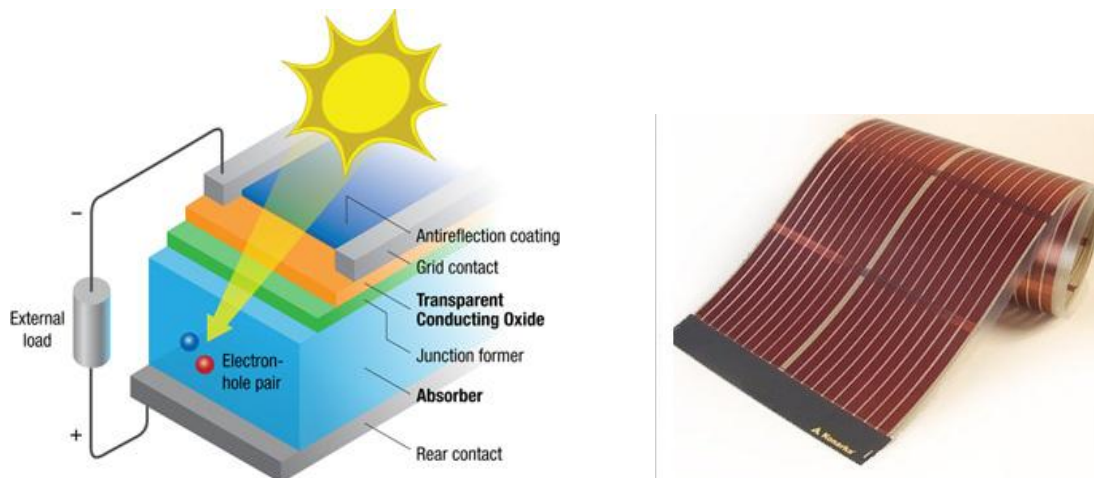


Figure 2. Scheme of an OPVC device configuration (left) and an example of printed large area OPVC (right).

An OLED is a two-terminal multilayer optoelectronic device that emits light when a bias is applied at the electrodes, whose active components are organic compounds.²³ The device architecture is similar to OPVCs whereas the mechanism of operation is opposed (Figure 3).

OLEDs were firstly presented in 1987 by Ching W. Tang and Steven Van Slyke that realized the first prototype using a double layer structure of organic thin films (8-hydroxyquinoline aluminum Alq_3 and aromatic diamine).²⁴ Later, in 1990, the research on polymer electroluminescence culminated in the first successful demonstration of green-yellow polymer-based OLED using 100nm thick film of poly(p-phenylenevinylene) as an active layer.²⁵ The working mechanism, device fabrication and materials will be discussed in details in Section 1 - Introduction.

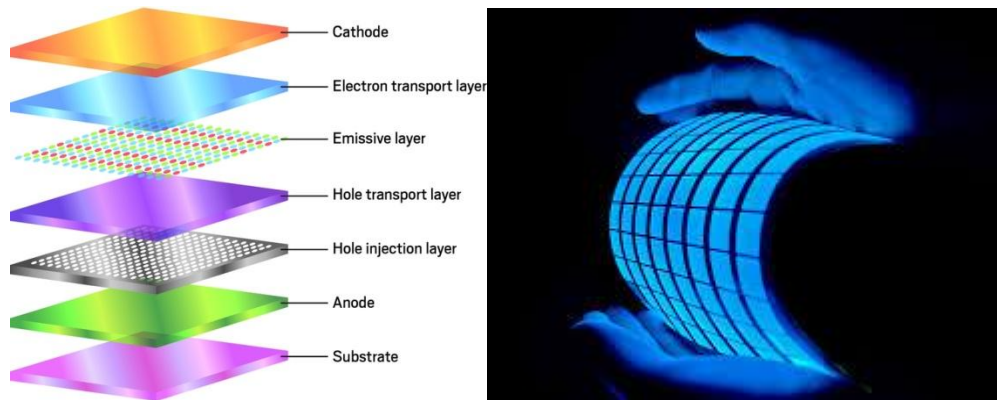


Figure 3. Scheme of an OLED device (left) and an example of a flexible OLED (right).

Nowadays organic electronics is part of everyday life, with many marketed electronic products integrated and produced with organic active materials. For example, the South-Korean company Samsung launched in August 2013 the first 55 inch full high-definition (Full HD) OLED TV with a curved panel (S9C series) while LG company already has a whole product line for OLED TVs and the German company Heliatek is commercializing ultra-light, thin and flexible OPVs with the brand HeliaFilm® (Figure 4).



Figure 4. Full HD OLED TV with a curved panel S9C series by SAMSUNG.

Even so, the research in this field is still open and very active in many different directions, from the development of more efficient electroactive materials as well as new substrates, to new fabrication technologies and techniques and novel device architectures.

Recently, the research activity on organic electronic is moving toward the realization of bio-compatible and bio-degradable devices able to achieve ambitious goals for biomedical application.¹⁴ This new trend was first described in 2007 by Magnus Berggren and Agneta Richter-Dahlfors in a seminal review in which they coined the term “Organic Bio-electronics” to describe electronic devices able to translate the electronic signals into bio-signals and vice versa.²⁶ Organic bio-electronics can be applied to biological systems to selectively sense, record, and monitor different signals and physiological states, as well as to convert relevant parameters into electronic readout for further processing and decision making. Organic electronic materials can conduct and process both electronic and ionic (bio)signals, tightly coupled via electron-ion charge compensation. Moreover, organic electroactive molecules and polymers with specific physical-chemical properties can be designed and synthesized, thus enabling the manufacture of more performing bioelectronics devices. All these properties make organic bioelectronics a truly unique communication bridge across the biology-technology gap.²⁷

Since biological signals in living organisms are transmitted through an aqueous medium, a suitable device for the detection and/or control of such signals needs to be able to work in water. For this purpose organic electrochemical transistors (OECTs) exhibit unique features for their strategic combination with biomedical interfaces, simple and low voltage operation regime and sensing ability in aqueous environment.

The OECT, first reported by White et al.,²⁸ is a three terminal device in a transistor configuration (source, gate, and drain) (Figure 5). The source and drain are connected by an organic conducting material in which an electronic current is generated (I_d) in response to a potential difference. A variable potential at the gate controls the magnitude of the drain current (I_d) by doping and dedoping the channel.²⁹

These devices have been used as converters between ionic currents in the electrolyte and electronic currents in the organic channel, and as sensors to monitor the adhesion of cancer cells and fibroblasts cultured directly on the channel. OECTs have also been employed as sensors for hydrogen peroxide, glucose and dopamine by exploiting the ability of the conducting polymer channel to detect electrochemical reactions in the electrolyte.³⁰

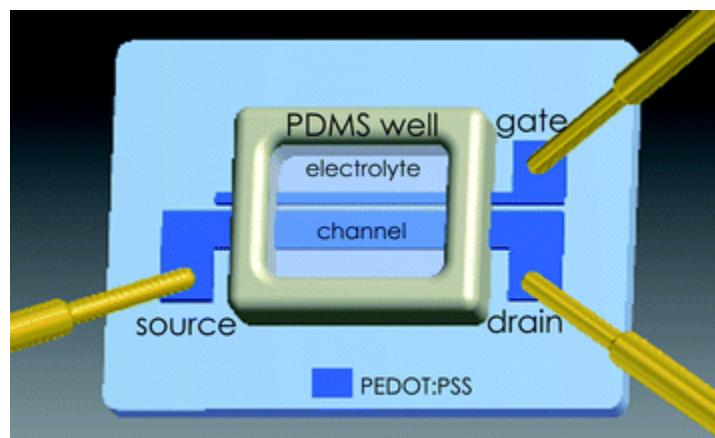


Figure 5. Scheme of an OECT.

In the last decades different kind of bio-electronic devices have been fabricated and used for tissue regeneration and/or therapeutic uses.

Along with the field of bioelectronics, “green electronics” is an emerging and stimulating interdisciplinary research area aimed at exploiting the potentiality of natural compounds and their derivatives as functional materials for electronic devices. Main goals of this brand new field are first of all the reduction of the costs of production and the fabrication of the device and the more sustainable and bio-degradable devices resulting in a lower environmental impact.

The green electronics field may prove to be the suitable host for welcoming natural and nature-inspired organic materials and a perfect trampoline for achieving the ambitious goal of “green” and sustainable electronics future.

Taking inspiration from this scenario, the research work carried out during my PhD course has been focused on the following two main topics:

- 1) The design, synthesis and characterization of new nature-inspired organic electroluminescent emitters and their application in opto-electronic devices. This work will be discussed in the SECTION 1.
- 2) The design, synthesis and properties of eumelanin-based semiconductors and their applications in electronic devices. This work will be discussed in the SECTION 2.

REFERENCES

- [1]. H. Letheby, *J. Chem. Soc.*, **1862**, *15*, 161-163
- [2]. Chiang, C. K.; Fincher, C. R.; Park, Y. W.; Shirakawa, H.; Louis, E. J.; Gau, S. C.; MacDiarmid, A. G. *Phys. Rev. Lett.* **1977**, *39*, 1098-1101
- [3]. (a) Shirakawa, H.; Louis, E. J.; MacDiarmid, A. G.; Chiang, C. K.; Heeger, A. J. *J. Chem. Soc., Chem. Commun.* **1977**, 578-580; (b) Chiang, C. K.; Park, Y. W.; Heeger, A. J.; Shirakawa, H.; Louis, E. J.; MacDiarmid, A. G. *J. Chem. Phys.* **1978**, *69*, 5098-5104.
- [4]. Ivory, D. M.; Miller, G. G.; Sowa, J. M.; Shacklette, L. W.; Chance, R. R.; Baughman, R. H. *J. Chem. Phys.* **1979**, *71*, 1506-1507.
- [5]. Wnek, G. E.; Chien, J. C. W.; Karasz, F. E.; Lillja, C. P. *Polymer* **1979**, *20*, 1441-1443.
- [6]. Diaz, A. F.; Logan, J. A. *J. Electroanal. Chem.* **1980**, *111*, 111-114.
- [7]. Diaz, A. F.; Castillo, J. I. *J. Chem. Soc., Chem. Commun.* **1980**, 397-398.
- [8]. Tourillon, G.; Garnier, F. *J. Electroanal. Chem.* **1982**, *135*, 173-178.
- [9]. *Handbook of Conducting Polymers*, 2nd ed., Eds.: Skotheim, T. A.; Elsenbaumer, R. L.; Reynolds, J. R. Marcel Dekker, New York, **1998**.
- [10]. M. Pope, H. Kallmann, P. Magnante, *J. Chem. Phys.* **1963**, *38*, 2042
- [11]. L. Groenendaal, F. Jonas, D. Freitag, H. Pielartzik and J. R. Reynolds, *Adv. Mater.* **2000**, *12*, 481-494.
- [12]. Arias, A. C.; MacKenzie, J. D.; McCulloch, I.; Rivnay, J.; Salleo, A., *Chem. Rev.* **2010**, *110*, 3-24.
- [13]. M. Berggren, D. Nilsson and N. D. Robinson, *Nature Materials* **2007**, *6*, 3-5
- [14]. J. Rivnay, R. M. Owens, and G. Malliaras, *Chem. Mater.* **2014**, *26*, 679-685
- [15]. A. Moliton, R.C. Hiorns, *Polym. Int.* **2012**, *61*, 337-341
- [16]. G. Horowitz, *Adv. Mater.* **1998**, *10*, 365-377
- [17]. D.F. Barbe, C.R. Westgate, *J. Phys. Chem. Solids* **1970**, *31*, 2679-2687
- [18]. F. Ebisawa, T. Kurokawa, S. Nara, *J. Appl. Phys.* **1983**, *54*, 3255-3259
- [19]. F. Garnier, G. Horowitz, X. Peng, D. Fichou, *Adv. Mater.* **1990**, *2*, 592-594
- [20]. D. Wöhrle and D. Meissner, *Adv. Mat.*, **1991**, *3*, 129-138.
- [21]. H. Spanggaard, F.C. Krebs, *Sol. Energy Mater. Sol. Cells*, **2004**, *83*, 125-146
- [22]. C.W. Tang, *Appl. Phys. Lett.* **1986**, *48*, 183-185
- [23]. B. Geffroy, P. le Roy and C. Prat, *Polym Int*, **2006**, *55*, 572-582
- [24]. C.W. Tang, S.A. VanSlyke, *Appl. Phys. Lett.*, **1987**, *51*, 913-915

- [25]. J.H. Burroughes, D.D.C. Bradley, A.R. Brown, R.N. Marks, K. Mackay, R.H. Friend, R.L. Burns, A.B. Holmes, *Nature*, **1990**, *347*, 539–541
- [26]. M. Berggren, A. Richter-Dahlfors, *Adv. Mater.* **2007**, *19*, 3201–3213.
- [27]. D. T. Simon, E. O. Gabrielsson, K. Tybrandt and M. Berggren, *Chem. Rev.* **2016**, *116*, 13009–13041
- [28]. H. S. White, G. P. Kittlesen, M. S. Wrighton, *J. Am. Chem. Soc.*, **1984**, *106*, 5375.
- [29]. X. Strakosas, M. Bongo, R. M. Owens, *J. APPL. POLYM. SCI.*, **2015**, *15*, 41735
- [30]. G. Tarabella, G. Nanda, M. Villani, N. Coppede, R. Mosca, G. G. Malliaras, C. Santato, S. Iannotta and F. Cicoira, *Chem. Sci.*, **2012**, *3*, 3432–3435

SECTION 1

DESIGN, SYNTHESIS AND CHARACTERIZATION OF NEW NATURE-INSPIRED ORGANIC ELECTROLUMINESCENT EMITTERS AND THEIR APPLICATION IN OPTO-ELECTRONIC DEVICES

~INTRODUCTION~

The lighting evolution is a very fascinating story that can be traced back to ancient times when men, looking for artificial lighting, generated both heat and lighting using fire, as archaeological findings can attest. The first electric lamp was the carbon-arc lamp, demonstrated in 1801 by Sir Humphrey Davy, an English chemist. Electric lights became popular only after the incandescent lamp was developed independently by Sir Joseph Swan in England and Thomas Edison in the United States. The latter patented his invention in 1880 and subsequently made it the commercial success that it is today. Since 1880, electric lighting devices became increasingly efficient: the tungsten lamp (1906), the sodium vapor lamp (1930s), the fluorescent tube (1940s) and the halogen lamp (1960s) (Figure 1.1). In the 1980s a bulb-fluorescent tube hybrid device appeared for the first time: the compact fluorescence lamp. However, the high price, long dimming times, poor white quality and the high energy consumption left unsatisfied the consumers. Nowadays, about one million barrels of oil are burned daily to provide lighting to a lot of people at a very high cost in terms of safety and health hazards. This moved for the birth of a new lighting era, that is the Solid-State Lighting era (SSL). In this emerging concept for illumination, selected semiconducting materials can produce visible light under the action of an electrical field (electroluminescence) in suitably engineered devices where the transport of charge occurs in one specific direction (diodes). Through this approach, the primary product of these lighting devices is the photon itself, unlike traditional sources where visible light is essentially a by-product of other processes, such as heating or discharging. As a result, SSL produces visible light with reduced heat generation and energy dissipation, while its solid-state nature provides greater resistance and lifetime, with limited impact on the environment.

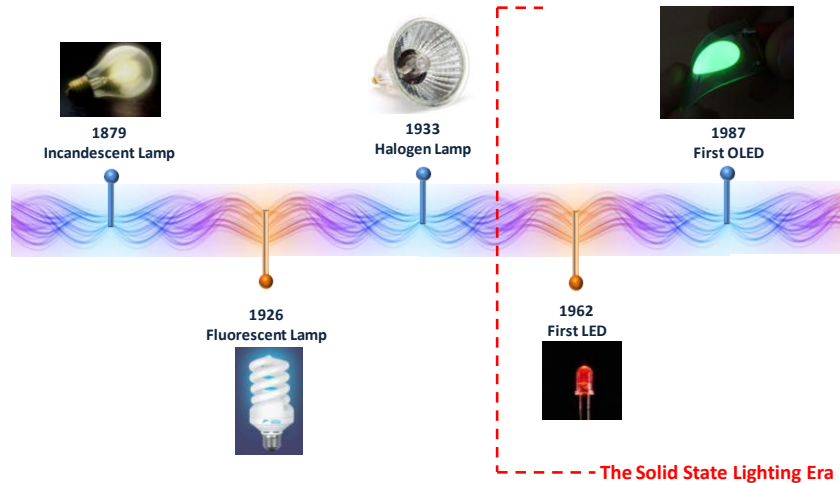


Figure 1.1. Technologic evolution of lighting sources.

First examples of SSL devices are LEDs (Light Emitting Diodes), an inorganic-based semiconductor device that emits visible light of a defined color when a voltage is applied. In 1962, the first developed red LED was commonly used as small indicator light on electronic devices. Green and yellow LEDs were introduced in the 1970s, and were used in watches, calculators, electronics, traffic lights and exit signs. By 1990, LEDs of 1 lumen output were available in red, yellow and green.

In 1993, the first high-brightness blue LED was developed by Isamu Akasaki, Hiroshi Amano and Shuji Nakamura that were awarded of the Nobel Prize in Physics in 2014. Because red, blue and green are the three primary colors of light, LEDs could now produce virtually any color, including white light. High-brightness LEDs are also considered "illuminator" type LEDs and are used in clusters as the light source for many different forms of luminaires.

LED lighting is more efficient, durable, versatile and long lasting than incandescent lighting. Another benefit is that LEDs emit light in a specific direction, whereas fluorescent lamps "diffuse", emitting light and heat in all directions.¹

Since 1987, with the first report on an efficient organic light emitting diode from C. W. Tang and S. A. Van Slyke, along with the rise of the organic electronics, a new technology has emerged as valid alternative to LED devices, which is the Organic Light Emitting Diodes (OLEDs). Based on organic electroluminescent materials, OLEDs exhibit many advantages compared to LED devices: 1) the compatibility with different substrates that allow the fabrication also of flexible devices; 2) the wide color tuning with the proper choice of the organic emitter; 3) the possible use of roll-to-roll and printing technologies for large-area

devices; 4) superior color quality and higher brightness with a wider view angle for high quality displays. For these reasons OLEDs are already used in flat-panels, e.g. computers, TV screens and mobile phones, but also in light art and fashion industry.

A step forward in the sector of SSL is represented by light emitting electrochemical cells (LEECs) (Figure 1.2). Since the first report in 1995 by Q. Pei et al that used a semiconducting polymer, an ion-conducting polymer and an inorganic salt sandwiched between two electrodes,² LEECs have aroused great interest in recent years. Compared to OLED devices using neutral emitters and a multilayer structure, LEECs contain ionic species in their solution-processed single active layer. This enables LEECs to use inert metals (such as Au, Ag or Al) as cathodes and to work under low operating voltages. With these appealing merits (single-layer, solution-process, air-stable cathodes, low driving voltages, etc.), LEECs have emerged as promising candidates for next-generation solid state lighting sources.



Figure 1.2. Flexible LEEC device produced by LunaLEC.

Further interest in organic optoelectronics has been generated by the realization of organic light emitting field effect transistors (OLEFETs or OLETs), a new class of versatile multifunctional devices that combine the current modulating function of an OFETs with the inherent light generation of OLED.³

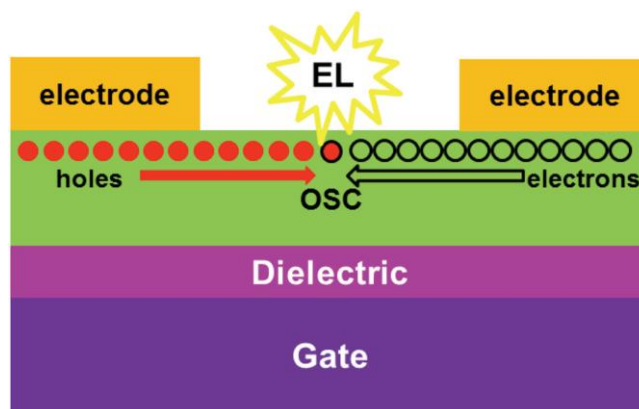


Figure 1.3. Scheme of OLET device

In contrast to OFET devices where it is not required the simultaneous injection of holes and electrons, in an OLET device source and drain need an appropriate work function enabling an efficient electron injection in the lowest unoccupied molecular orbital (LUMO) and a hole injection in the highest occupied molecular orbital (HOMO) of the organic semiconductor. If the organic semiconductor is electroluminescent, holes and electrons form excitons that recombine radiatively to generate light in the transistor channel (Figure 1.3).

From a technological perspective, the advantage of integrating an OLED with a transistor relies on the fact that in active-matrix displays, each pixel, composed by a single OLED, has to be driven by a single transistor, thus requiring a complex array of circuits. In contrast, no supplementary devices are needed when OLETs are employed for similar applications.

For the sake of simplicity in the next steps the attention will be focused mainly on the OLED and LEEC technology. This will allow a better understanding of the device fabrication, functioning and characterization process that will be discussed in the following chapters of this Section.

➤ Principles of light emission

Typically, organic molecules in their ground state have paired electrons in all the orbitals, thus a total spin equal to zero gives a singlet state (S_0). Upon the absorption of an incident radiation of a given energy, an electron from the outer orbital can be promoted to an unoccupied high energy orbital leading the molecule to an excited state (S_1). This process is governed by the Franck-Condon principle: the absorption of a photon is an instantaneous process that occurs in femtoseconds and the nuclear configuration of the molecule experiences no significant change since nuclei are much more massive than electrons and the electronic transition takes place faster than the nuclei can respond, leading to a vertical transition. This can be illustrated by a potential energy diagram (Figure 1.4). Moreover, during an absorption process an electron cannot change its spin according to selection rules, so transitions can occur only between states with the same spin ($S_0 \rightarrow S_1$). Each electronic state is composed by several vibrational states and after the absorption and according to the Franck-Condon principle an electron can be promoted in anyone of these states.

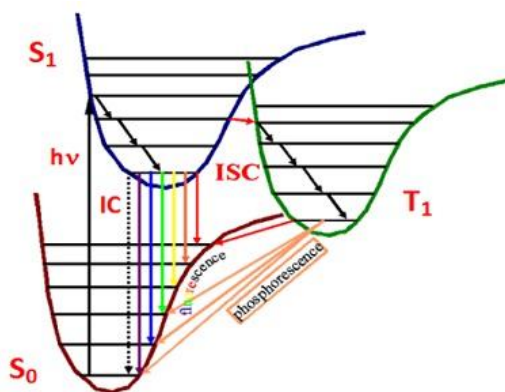


Figure 1.4. Franck-Condon absorption principle.

The relaxation path can be either radiative or non-radiative and is exemplified with the Jablonsky energy diagram (Figure 1.5). Non-radiative processes occur when an electron from an excited state decays to the ground state with the conversion of the absorbed energy into heat. A radiative relaxation on the other hand is accompanied by the emission of a photon of discrete energy; this can occur only from the lowest level of an excited state. The first event is an internal relaxation in which an electron decays from a high vibrational state to a lower one in a non-radiative way. Once a molecule reaches the lowest vibrational level of an excited state S_1 , it can return to the ground state by photon emission. This process is called fluorescence.

The lifetime of an excited S_1 is approximately 10^{-9} to 10^{-7} sec and therefore the decay time of fluorescence is of the same order of magnitude. If fluorescence is unperturbed by competing processes, the lifetime of fluorescence corresponds to the intrinsic lifetime of the excited S_1 . The energy of this transition is different from the absorption energy and this change in photon energy causes a shift of the fluorescence emission to longer wavelength, compared to the absorption spectrum, which is referred to as the Stokes shift.

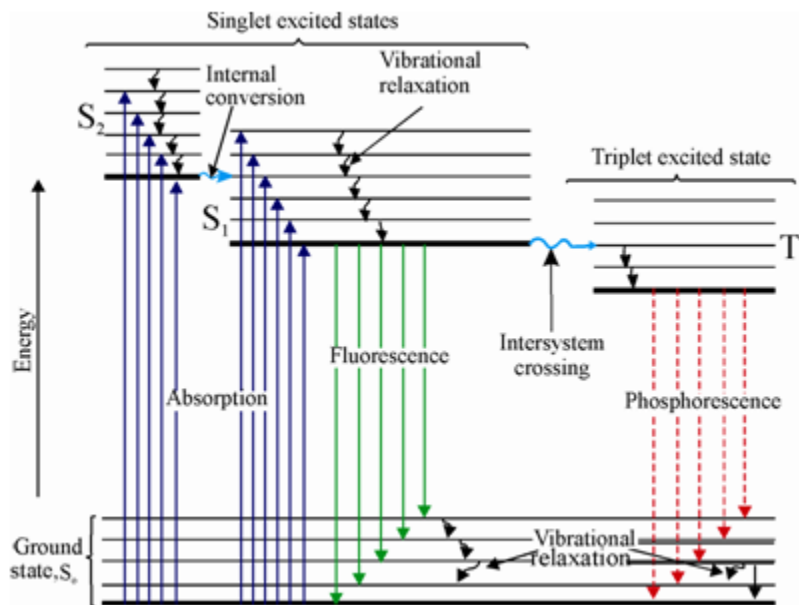


Figure 1.5. Jablonsky energy diagram.

According to selection rules, triplet states (T) cannot be populated by direct absorption of a radiation, e.g. an electron from the singlet ground state cannot be directly promoted in a T state because it should undergo to a spin change. But for many molecules a T_1 state can be populated from the lowest excited S_1 state by means of an intersystem crossing conversion (ISC), a spin-dependent internal process generally less probable than a S-S process. The mechanism for intersystem crossing involves vibrational coupling between the S_1 state and a T_1 state. Intersystem crossing can compete with fluorescence emission from the lowest vibrational level of an S_1 state, but cannot compete with vibrational deactivation from higher vibrational level of a S_1 . Once intersystem crossing has occurred the molecule undergoes the usual internal conversion process (10^{-13} to 10^{-11} sec) and falls to the lowest vibrational level of the T_1 . Since the difference in energy between this latter and the lowest vibrational level of the lowest S_1 is

large compared to thermal energy, repopulation of a S_1 from a T_1 is highly improbable. The radiative transition between the lowest T_1 and the ground state is called phosphorescence.

This transition is less probable than the $S_1 \rightarrow S_0$ one and can easily undergo deactivation processes. There are two main factors that tend to enhance a radiationless transition between the lowest T_1 and the S_0 . First the energy difference between the T_1 and the S_0 is smaller than the difference between the lowest S_1 and the S_0 . This tends to enhance vibrational coupling between these two states, and therefore to enhance internal conversion. Second, and more important, the lifetime of a T_1 is much longer than that of an S_1 (about 10^{-4} to 10 sec) and therefore a loss of excitation energy by collisional transfer is more probable. This second process is so important that in solution at room temperature it is often the dominant pathway for the loss of T_1 excitation energy. If a molecule is placed in a rigid medium, such as in a polymeric matrix, or is kept at very low temperatures, the collisional processes are minimized and a radiative transition between the lowest T_1 and the S_0 is observed. As phosphorescence originates from the lowest T_1 , it will have a decay time approximately equal to the lifetime of the T_1 (ca. 10^{-4} to 10 sec).

The phosphorescence emission is more favorable for organic transition metal complexes, in which the central metal ion induces significant spin-orbit coupling (SOC). For these complexes, the intersystem crossing to the T_1 state is usually very efficient and thus, at an energy separation between the S_1 and T_1 states of several 10^3 cm^{-1} , a singlet S_1 emission is not observed. Moreover, the radiative $T_1 \rightarrow S_0$ rate can become relatively large for compounds with central metal ions with large spin-orbit coupling constants so that efficient phosphorescence can occur even at ambient temperature.

➤ OLED devices

An organic light emitting diode (OLED) is an optoelectronic device consisting of an organic thin film sandwiched between two electrodes, typically a transparent anode, i.e. indium tin oxide (ITO), and a high work function cathode typically calcium, magnesium, or lithium fluoride-aluminum (Figure 1.6).⁴

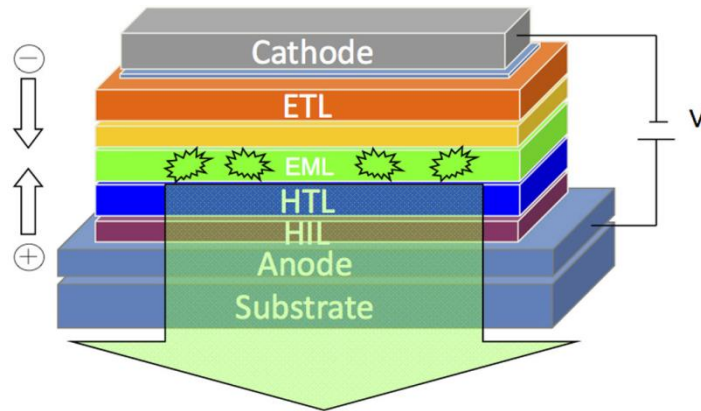


Figure 1.6. Depiction of the structure of an OLED device structure.

The mechanism of light emission is based on the electroluminescence (EL). When a voltage is applied to the electrodes, holes and electrons, respectively from the anode and the cathode, are injected into the device and, thanks to the internal electric field, reach the emissive layer creating an exciton. This latter is a bound electron-hole pair composed by an electron located in the LUMO and a hole in the HOMO of the emitting layer, which can transport energy without a net electrical charge. The recombination of the exciton, thus the relaxation of the excited state of the molecule to the ground state, produces light with a wavelength defined by the HOMO-LUMO gap. Depending on the choice of organic materials for the emissive layer, OLEDs can be designed to emit any color, including white light with various color temperatures.

In brief, the fundamental physical process of the OLEDs can be divided into four steps: charge injection, transport, recombination and radiative exciton decay.

Since holes and electrons have different mobilities and need to reach respectively the HOMO and the LUMO orbitals of the emitting layer, with energy levels very different from those of the electrodes, improved device performances are achieved when a multilayer device configuration is adopted (Figure 1.7).

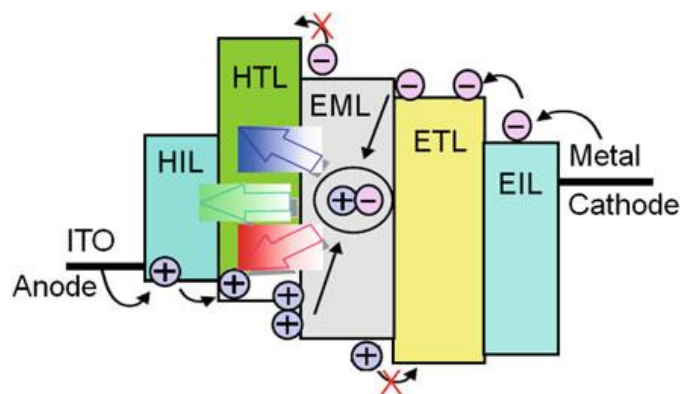
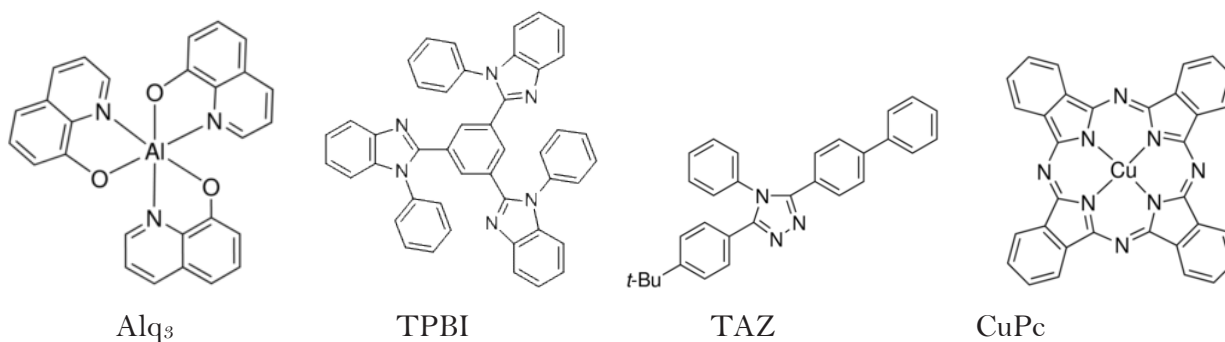


Figure 1.7. Schematic representation of energy levels in an OLED device and flow of electrons and holes.

To this aim, hole injection/transport layer (HTL) and electron injection/transport layer (ETL) are inserted to balance the charge injection and transport and control the recombination.

In details, hole injection materials are used to reduce the height of the barrier (also termed a potential barrier) against hole injection from the anode and are selected so that the HOMO level is located between the HOMO of the hole transportation material and the work-function of the anode. The material layer involved in this process is called the hole injection layer (HIL). Copper phthalocyanine (CuPc) and PEDOT:PSS are popular choices; PEDOT:PSS can smooth the surface of ITO, decrease device turn-on voltage and reduce the probability of electrical short circuits.



In a similar fashion, electron transport material is used to transport electrons injected from the cathode. This layer, called the electron transport layer (ETL), is sometimes used together with the electron injection layer (EIL), such as LiF, to increase the electron injection capability. Sometimes the ETL is used without EIL when the cathode work-function matches with the LUMO of the ETL. Just like the hole transport layer, the electron transport layer should have

a band-gap wider than that of the emission layer. To date, the most widely used electron transport materials are some metal chelates (Alq₃, Be and Zn chelates). 2,2',2''-(1,3,5-Phenylene)tris(1-phenyl-1*H*-benzimidazole) (TPBI), 3-(4-biphenyl)-4-phenyl-5-tert-butylphenyl-1,2,4-triazole (TAZ) and oxadiazole derivatives have also been widely used as electron transporting materials.

In order to confine charges in the active layer, a hole-blocking layer (HBL) and an electron-blocking layer (EBL) are added to prevent holes and electrons leakage and usually it corresponds with the ETL. All the inserted layers have to be chosen according to energetic considerations with the aim of reducing energy barriers between different layers. An ideal device configuration is depicted in Figure 1.7 in which is shown the flow of charge carriers from the electrodes to the emitting layer.

It can be seen that the introduction of HIL and EIL helps to effectively reduce the barrier for charge injection. Matched energy levels will greatly enhance the device efficiency.

The emitting layer can be constituted by small molecules (SMOLED),⁵ polymers (POLED or PLED)⁶ or transition metal complexes (TMC-OLED).⁷ In the latter case electroluminescence may also come from the accessible triplet exciton.

In recent years, PHOLEDs (Phosphorescent OLEDs) are gaining a dominant position in the field of OLED devices owing to their superior efficiency, which makes them suitable for high performance and high brightness displays and solid state lighting. The upper limit in the external quantum efficiency of 5% observed in fluorescent small molecule organic devices has been overcome by harvesting both the singlet and triplet excitons to produce a large emission of photons in PHOLEDs.

According to spin statistics, four different combinations of excited states are possible, one combination of antiparallel spin giving a singlet (accounting for the 25% of excitons), and three combinations of parallel spin giving a triplet (accounting for the 75% of excitons) (Figure 1.8).

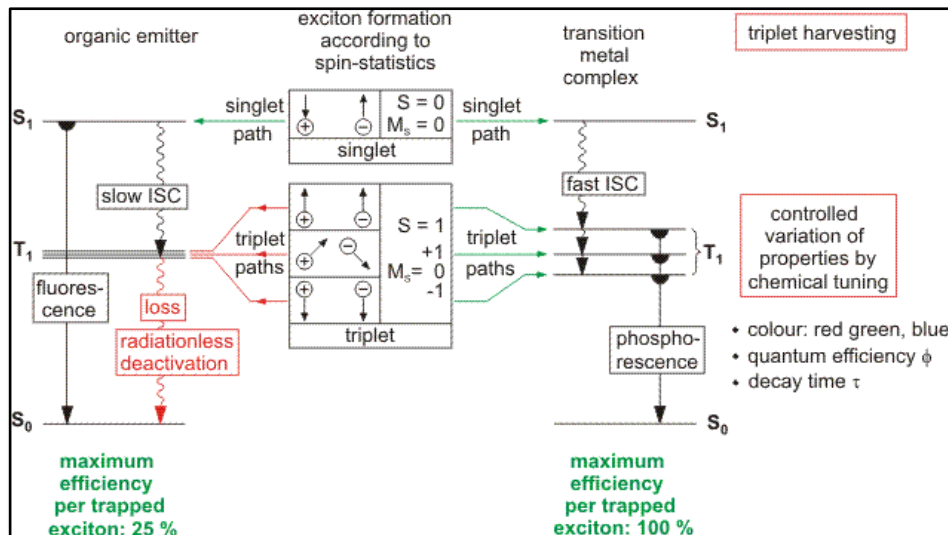


Figure 1.8. Electroluminescence excitation processes for organic and organo-transition metal emitters.

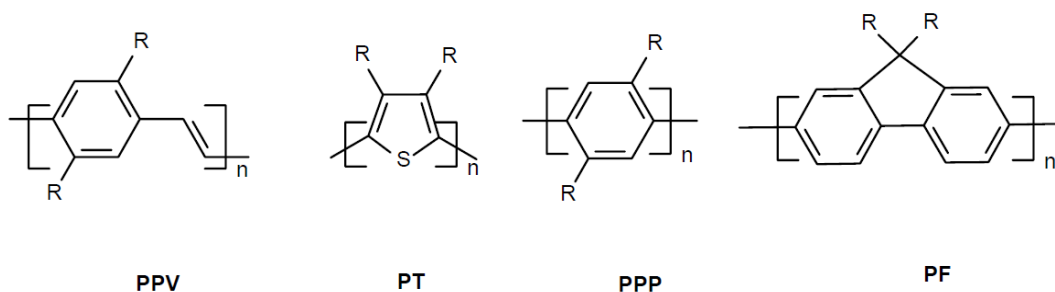
In the case of organic emitters, once excitons are formed, an efficient fast decaying singlet emission ($S_1 \rightarrow S_0$) is observed with lifetimes in the order of one ns and with a fluorescence quantum yield of almost 100%, if the $S_1 \rightarrow T_1$ intersystem crossing rate is smaller than the fluorescence rate. On the other hand, since the probability for the radiative $T_1 \rightarrow S_0$ transition is also very small, the deactivation of the T_1 state occurs normally non-radiatively at ambient temperature. Therefore, 75% of the excitons, namely the triplet excitons, are lost for the emission.

In organic transition metal complexes, the central metal ion induces significant spin-orbit coupling (SOC). For these complexes, the intersystem crossing to the T_1 state is usually very efficient and thus, at an energy separation between the S_1 and T_1 states of several 10^3 cm^{-1} , a singlet S_1 emission is not observable. Moreover, the radiative $T_1 \rightarrow S_0$ rate can become relatively large for compounds with central metal ions with large spin-orbit coupling constants so that efficient phosphorescence with a quantum yield of almost 100% can occur even at ambient temperature. Consequently, all four possible spin orientations of the excitons can be harvested and populate the lowest T_1 state. By this process, in principle, we can obtain a four times higher electro-luminescence efficiency with phosphorescent triplet emitters than with fluorescent singlet emitters, reaching a theoretical internal quantum efficiency of 100%.⁸

Among small molecules, Alq₃, coumarin, rubrene and zinc, beryllium, copper and barium chelates have been widely used as emitters in SMOLEDs. Fluorescent small molecules can be

easily synthesized and purified and up to now all the three primary colors, red, green and blue (RGB) can be produced with high brightness and efficiency. However, the poor solubility of small molecules doesn't allow solution deposition; thus, thin films are usually prepared by vacuum vapor deposition, a time consuming and very expensive technique. Furthermore, small molecules tend to crystallize readily with a consequent reduction of the lifetime of the device.

The development of fluorescent polymers for OLED applications runs almost in parallel. The semiconducting properties of conjugated polymers result from their extensively delocalized π -orbitals along the polymer chains. Initially the first green light-emitting polymer, PPV, was prepared from precursor route. However, its insoluble, intractable and infusible properties make its deposition very hard. Its derivative poly[2-methoxy-5-(2-ethylhexyloxy)-*p*-phenylenevinylene] (MEH-PPV) exhibited a better solubility by introducing a dialkoxy side chain. It was found that the introduction of this substituent not only has a favorable effect on solubility of the polymer, but also allows the modification of the electronic properties, e.g. bandgap, electron affinity and ionization potential, which resulted in a shift of the light emission to the red region. For these reasons, fluorescent polymers, like PPV and its derivatives, have soon attracted great interest and have been extensively studied so that blue, green and red emissions have been achieved. Polythiophene (PT) and its derivatives provided a new series of materials from red to blue light emission. As for red emitters, the most widely known polymers were MEH-PPV and regioregular poly(3-hexylthiophene) (P3HT), while poly(*para*-phenylene) (PPP), polyfluorene (PF) and their derivatives are the most widely used blue emitters which realized bright and high efficient light emission.



Soluble polymers enable the use of solution-based printing techniques like roll-to-roll, gravure and so on, reducing costs of production and allow the fabrication of large-area devices.

Transition heavy metal (Pt, Ru, Ir, Re, Os) complexes and rare-earth metal (Eu, Tb) complexes containing suitable ligands have realized highly efficient phosphorescence at room temperature.

The photo-physics of these cyclometalated complexes have been extensively investigated. Their luminescence originates from the lowest triplet metal to ligand charge transfer excited state ($^3\text{MLCT}$). In the process of MLCT, an electron located in a metal-based d -orbital is transferred to the ligands. In the last decade much attention has been directed to phosphorescent materials for the high external quantum efficiency (EQE) exhibited by the corresponding PHOLED devices.

In these phosphorescent materials, metals act as light transfer centers and ligands (organic part) tune light emission color, solubility of complexes, exciton lifetime and thus device efficiency. The choice of the central metal can also define the emission of the complex that can range from visible colors, in the case of iridium, platinum and some ruthenium complexes, to polychromatic or near-IR emission, as for ruthenium and osmium complexes,⁹ to IR emission with rare-earth metals as europium or terbium (Figure 1.9).¹⁰

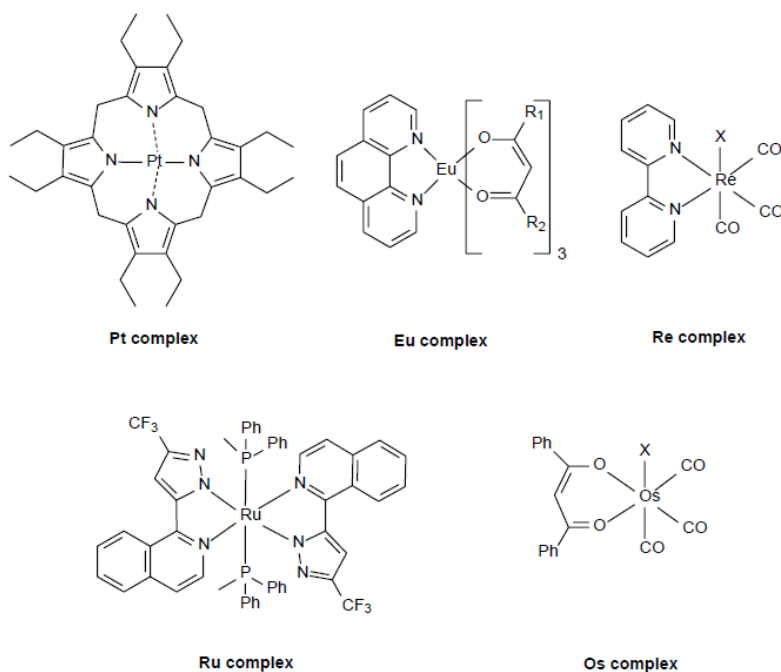


Figure 1.9. Phosphorescent cyclometalated complexes used in PHOLED devices.

In PHOLEDs usually the emitting layer is a blend of the proper TMC, called “guest” material, with a material that is able to boost the triplet exciton, called “host”. When electrons and holes are initially injected into the organic small-molecule or polymer host materials, the excitation is transferred to the organometallic emitter, producing phosphorescent excited states.

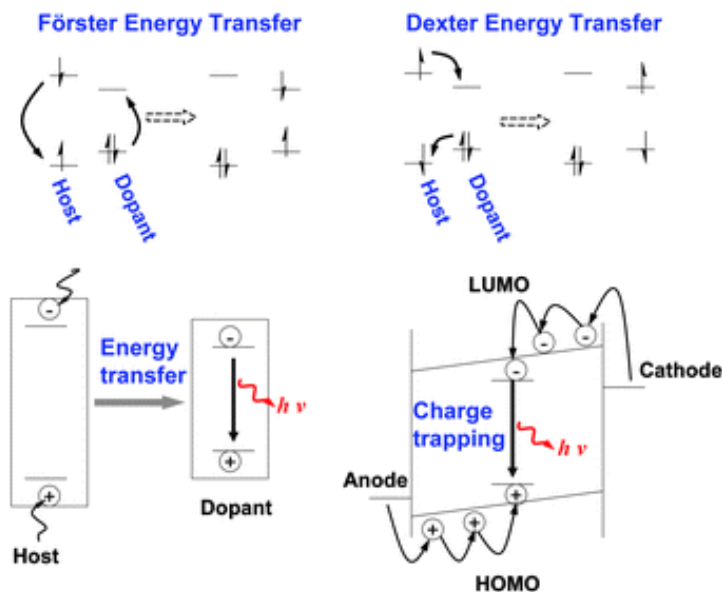


Figure 1.10. Schematic mechanisms of Förster and Dexter energy transfer

As usual, the efficient excitation transfer consists of Förster and Dexter energy-transfer from the host transport to the metal-organic center. In an efficient Förster energy-transfer, the singlet excited state energy is transferred from the host to the phosphorescent guest because of the dipole-dipole interaction, leading to lower self-absorption losses owing to the red-shift of the emission relative to the absorption in the blends. The efficiency of the Förster energy-transfer is dependent on the overlap between the host emission spectrum and the guest absorption spectrum. The Dexter energy-transfer is a process in which two molecules (intermolecular) or two parts of a molecule (intramolecular) bilaterally exchange their electrons. In host-guest systems, the direct quantum mechanical tunnelling of electrons between the host and guest is warranted during the Dexter energy-transfer of a neutral exciton from the host to a neutral exciton on the guest. In addition, a Dexter energy-transfer allows singlet-singlet and triplet-triplet energy-transfer.¹¹

➤ LEEC devices

A LEEC is a two-terminal device, composed of a single layer of a solution-processable ionic electroluminescent material sandwiched between two electrodes. As in OLEDs, emission of light occurs with the formation of an exciton in the emitting layer under bias; but unlike OLEDs, the charge separation of the ionic emitting layer warrants a more easy movement of holes and electrons through the device, so there is no need for a multi-layer configuration.

LEEC electroluminescent materials can be either conjugated light-emitting polymers or ionic transition-metal complexes. In the first case the device is termed polymer-LEEC (PLEECs) and the emitting layer is constituted by three components: an electroluminescent polymer, organic salt and a semiconducting polymer (Figure 1.11). In the second case the device is termed iTMC-LEECs (ionic transition metal complex-LEEC) and the emitting layer is constituted by a single component, which is an organic salt of a transition metal complex. ¹²

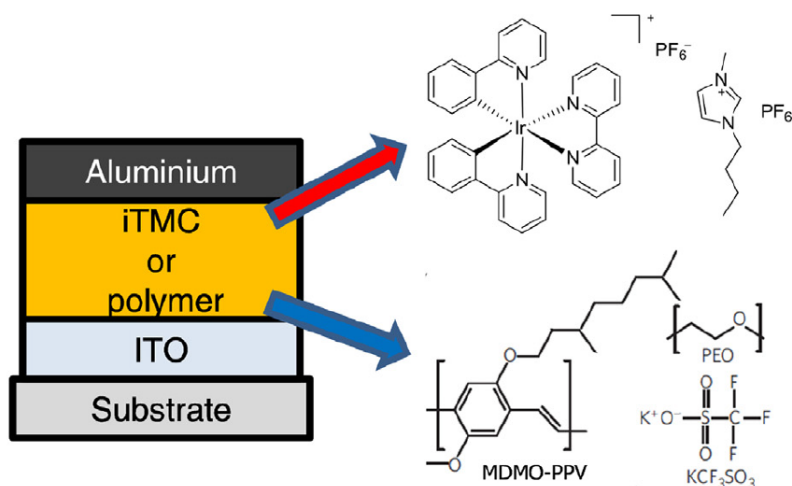


Figure 1.11. A simplified LEEC device structure and examples of light emitting materials..

Both types of devices have been studied for over 15 years, throughout which many materials, device concepts and driving schemes have been tested. This research has highlighted many advantages of LEEC versus OLED devices. The most important is the low cost and time of production of the device due to: i) the single layer configuration of LEECs; ii) the possible use of air-stable cathodes; iii) encapsulation of the device is no longer required.

But there are still many issues that have to be addressed, concerning the lifetime of the LEEC devices, the low luminance and the high turn-on time (the time required to reach a luminance of 100 cd m^{-2}). This is due to the fact that the working mechanism of LEECs has not been fully understood and clarified. To date two competing models seem to better explain the LEEC functioning: the Electrochemical Doping (ECD) model and the Electrodynamic (ED) model (Figure 1.12).¹³

Both models agree with the fact that the injection barrier for electrons and holes is reduced by the separation of the ions in the light-emitting layer upon application of a bias.

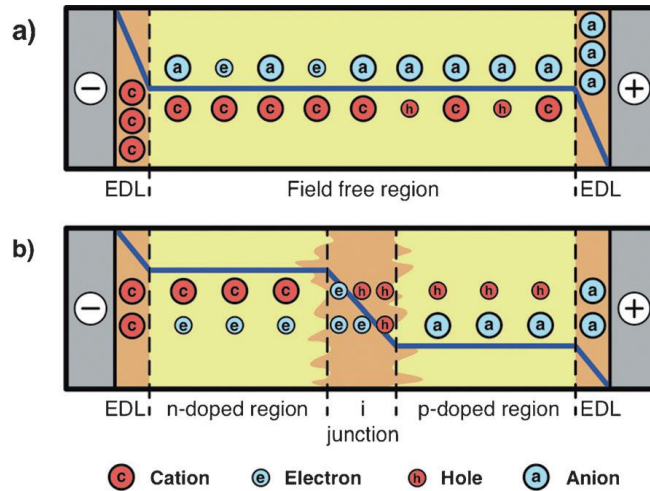


Figure 1.12. Illustration of the potential profile as well as the electronic and ionic charge distribution in a LEEC during steady-state operation. Potential profiles and charge distributions as predicted by the a) ED and the b) ECD models.¹³

The ED model assumes that the accumulation of ions leads to the formation of electric double layers (EDLs) at the electrodes which brings about a sharp drop of the electric potential near the electrode interfaces and promotes charge injection from the electrodes. In the bulk of the material the anions and cations are still joined and light emission occurs from the so-called field-free region in the bulk of the device. The ECD model, on the other hand, assumes that the accumulation of ions at the anode and cathode leads to the formation of highly conductive *p*- and *n*-doped regions, respectively. The doped regions widen over time, until a *p*-*i*-*n* junction (*i* = intrinsic, undoped) between them is formed. Across the intrinsic region formed, the applied potential drops substantially and favors charge recombination and light emission. In both cases, mobile ions in the emitting layer create an in situ electrochemical doping that makes charge injection independent from the work function of the electrodes. This mechanism enables the use of inert metals with lower work functions (such as Au, Ag or Al) and to work under low operating voltages.

➤ Device fabrication

OLED devices can be fabricated with two different architectures depending on the direction of the light output: “bottom-emitting” and “top-emitting”.

In bottom-emitting OLEDs, light is emitted through the transparent substrate of the device, typically glass or plastic. In this configuration, the anode must be transparent while the other electrode is typically a reflective metal. In top-emitting OLED the configuration is reversed and light is emitted through the cathode that needs to be transparent.

Due to technical issues, bottom-emitting configuration is the most used and its fabrication is described below.

ITO is the best choice as anode thanks to its good conduction properties (resistivity about $10^{-4} \Omega\text{cm}$), high transparency in the visible region (up to 90% of transmittance) and high work function of 4.7 eV. It is usually deposited onto the substrate via sputtering of an alloy of $\text{In}_2\text{O}_3/\text{SnO}_2$. In this process gaseous plasma is formed and the produced ions are accelerated to the source material (target); the target is eroded by the arriving ions via energy transfer and is ejected in the form of neutral particles - either individual atoms, clusters of atoms or molecules. As these neutral particles are ejected, they will travel in a straight line until they impact the surface of the substrate where are finally deposited.

Cathodes are usually composed by a reflective metal such as calcium, aluminum, gold, silver or alloys. They are deposited on the top of the multilayer structure of the OLED by thermal evaporation in ultra-high vacuum (Figure 1.13).

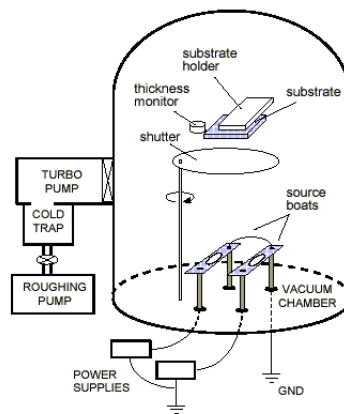


Figure 1.13. Description of the thermal evaporation in ultra-high vacuum system

Evaporation occurs when a source material is heated above its melting point in a vacuum chamber. The metal source can be melted by resistance heating, RF heating, or by a focused electron beam. The metal evaporation produced by resistive heating is usually called thermal evaporation. Materials to be deposited are loaded into a heated container called crucible (boat). It can be heated by means of an embedded resistance heater and an external power supply. As the material in the crucible becomes hot, the charge gives off its vapor. Since the pressure in the

chamber is much less than 10^{-7} mbar, the atoms of the vapor travel across the chamber in a straight line without hitting any gas molecule left in the vacuum chamber until they strike a cold surface where they condense and accumulate as a film. Evaporation systems may contain several crucibles, furthermore, if an alloy is desired, multiple crucibles can be operated simultaneously. To help start and stop the deposition abruptly, mechanical shutters are used in front of the crucibles to control the metal deposition thickness. The deposition rate is commonly measured using a quartz crystal rate monitor. This device is a resonator plate that is allowed to oscillate at the resonance frequency, which is then measured. The resonance frequency shifts due to the additional mass as material is deposited on top of the crystal.

When enough material has been added, the resonance frequency will shift by several percent and the oscillator will no longer show a sharp resonance. The sensing elements are quite inexpensive and are easily replaced. By linking the vapor pressure output of the frequency measurement system to the mechanical shutters, the thickness of the deposited layers can be well controlled over a wide range of deposition rates. Furthermore, the rate of the deposited thickness changes can be fed back to the crucible temperature to maintain a constant deposition rate, so that growth rate is controlled by tuning the temperature of the source boat. Between the metal source and the substrate, a shadow mask can be placed in order to define the area and the geometry of the deposited film.

Usually small molecules are also deposited by thermal evaporation that ensures good film quality and reproducibility. In general this technique provides high quality and ordered thin films, good control and reproducibility of film thickness, easy multilayer deposition and co-deposition of several organic and materials. On the other hand some drawbacks make this deposition process unfit for many applications such as polymer deposition, large-area and flexible device fabrication.

Solution-processable materials are preferred in order to overcome these issues and several wet-deposition techniques have been developed.

With the drop casting, a drop of a solution of the desired material is casted onto a substrate and the solvent is let to evaporate slowly. The thickness of the final film is proportional to the concentration of the solution. This method is very easy and there's a very low material waste, but the control over the uniformity and the thickness of the film is very poor. In order to improve the film features it is possible to use a combination of solvents to control the evaporation rate.

The spin coating technique is the best choice for solution-processable emitters as polymers. A typical process involves the deposition of a small puddle of a solution onto the center of a substrate that is put to spin at high speed (Figure 1.14). Centripetal acceleration will cause the solution to spread to, and eventually off, the edge of the substrate leaving a thin film on the surface.

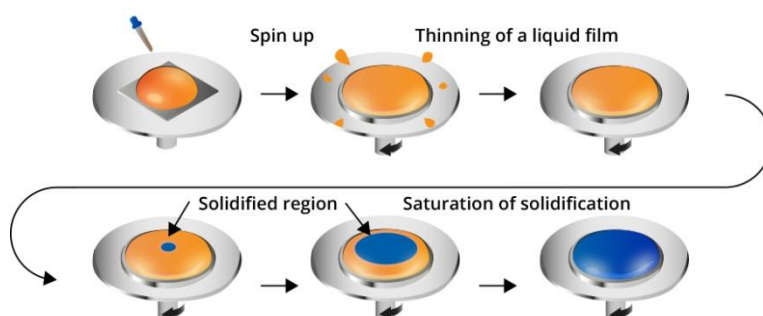


Figure 1.14. Spin coating process.

Final film thickness and other properties will depend on the nature of the material (viscosity, concentration, drying rate, percent solids, surface tension, etc.) and the parameters chosen for the spin process. Factors such as final rotational speed, acceleration, and fume exhaust contribute to how the properties of coated films are defined. One of the most important factors in spin coating is repeatability. Subtle variations in the parameters that define the spin process can result in drastic variations in the coated film. It is possible to deposit subsequently several layers using “orthogonal solvents”: once a first film is deposited, the solvent of the second film must not dissolve the previous film (e.g. a polar solvent for the first film and an apolar solvent for the second one). With this technique is possible to achieve good uniformity, reproducibility and good control on thickness down to 10 nm or less; waste of material and no large area coverage are again drawbacks of this technique.

With the dip coating, as the name suggests, the substrate is dipped into the proper solution of the active material and then withdrawn at a controlled rate. Film thickness is determined by the balance of forces at the liquid-substrate interface. This method is characterized by discrete film uniformity, very thin layers, large-area coverage and is basically an easy process; anyway the important drawbacks are a great waste of material, it's time consuming and double side coverage.

The Langmuir-Blodgett (LB) technique is one of the few methods available for manipulating the architecture of an assembly of organic molecules. This technique involves three phases: 1) the spreading of some suitable organic molecules onto a water surface; 2) the compression of the latter film to form a compact monolayer; 3) the transfer of this layer onto a suitable substrate (Figure 1.15).

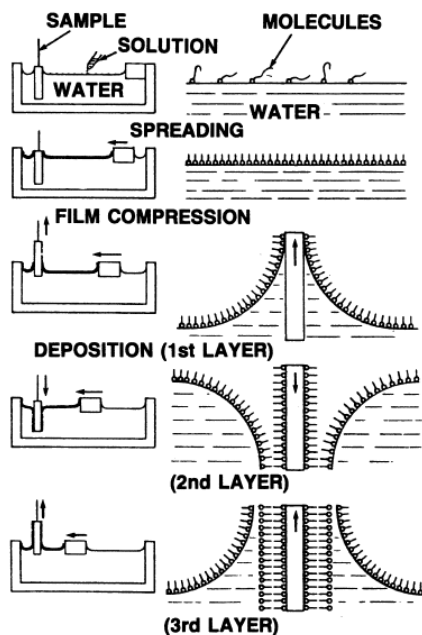


Figure 1.15. The Langmuir-Blodgett sequence.

The material is usually dissolved in an organic solvent and carefully spread on the surface of water contained in a Langmuir trough. The concentration is such that the molecules spread to a depth of one monolayer. If the surface pressure is small, the monolayer behaves as a two-dimensional gas. The surface pressure is increased by compressing the film by means of a sliding barrier. Eventually, a point is reached where all the molecules touch each other, forming a "perfect" pinhole-free monolayer. The correct degree of compression is determined by monitoring the surface tension of the water, which starts to drop when the molecules are nearly dense-packed.

At higher pressures, the monolayer will buckle and collapse. Below the collapse pressure, the monolayer can be transferred to a suitable substrate by lowering the substrate carefully through the film into the water and slowly withdrawing it. Alternatively, transfer may be affected horizontally by contacting the surface with the substrate oriented horizontally to the film surface. These procedures may be repeated successively until the required number of

monolayers is obtained. The thickness will thus be an integral multiple of the length of the amphiphilic species. In this way, ultrathin, compact, pinhole-free (at least in theory) films of constant, well-controlled thickness can be prepared.

~Aims of the research work~

On the basis of this wide scenario, the research activity that will be discussed in this section will concern the design, the synthesis and the characterization of new nature-inspired organic electroluminescent emitters and their applications in opto-electronic devices.

In details, the following points will be stressed:

- the identification of suitable nature-inspired heterocyclic platforms that can be used to develop new electroluminescent materials for opto-electronic applications;
- the design of structural modifications of natural compounds for a better match with organic electronics requirements by exploiting the theoretical approach;
- the development of new rapid and convenient synthetic strategies for a gram scale production of the organic emitters;
- the structural, photo-physical, electronic and thermal characterization of the synthesized compounds along with the investigation of the performances of the opto-electronic devices thereof.

The obtained results along with the rationale of the research will be reported in three main chapters concerning:

- 1) EUMELANIN-INSPIRED TRIAZATRUXENES AS NOVEL BLUE EMITTERS
- 2) DOPAMINE-INSPIRED IRIDIUM (III) COMPLEXES AS RED EMITTERS
- 3) SYNTHESIS AND PHOTOPHYSICAL PROPERTIES OF IRIDIUM(III) COMPLEXES WITH PYRIDOPHENOXAZINONE LIGANDS

REFERENCES

- [1]. M. Chang, D. Das, P.V. Varde, M. Pecht, *Microelectronics Reliability*, **2012**, *52*, 762–782
- [2]. Q. Pei, G. Yu, C. Zhang, Y. Yang, A. Heeger, *Science*, **1995**, *269*, 1086
- [3]. C. Zhang, P. Chen and W. Hu, *small*, **2016**, *12*, 1252–1294
- [4]. S. Kappaun, C. Slugovc and E. J. W. List, *Int. J. Mol. Sci.*, **2008**, *9*, 1527–1547
- [5]. Z. D. Popovic and H. Aziz, *JOURNAL ON SELECTED TOPICS IN QUANTUM ELECTRONICS*, **2002**, *8*
- [6]. Burroughes, J.H.; Bradley, D.D.C.; Brown, A.R.; Marks, R.N.; Mackay, K.; Friend, R.H.; Burns, P.L.; Holmes, A.B. *Nature* **1990**, *347*, 539–541.
- [7]. Evans, R.C.; Douglas, P.; Winscom, C.J., *Coord. Chem. Rev.*, **2006**, *250*, 2093–2126.
- [8]. Yersin, H., *Top. Curr. Chem.* **2004**, *241*, 1–26.
- [9]. J. L. Chen, Y. Chi and Kellen Chen, *Inorg. Chem.* **2010**, *49*, 823–832
- [10]. M. A. Katkova and M. N. Bochkarev, *Dalton Trans.*, **2010**, *39*, 6599–6612
- [11]. Yang, X.; Neher, D., Müllen, K., Scherf, U., *Wiley-VCH: Weinheim*, **2006**, 333.
- [12]. S. B. Meier, D. Tordera, A. Pertega, C. Roldan-Carmona, E. Orti and H. J. Bolink, *Materials Today*, 2014, *17*, 217–223
- [13]. R. D. Costa, E. Orti, H. J. Bolink, F. Monti, G. Accorsi and N. Armaroli, *Angew. Chem. Int. Ed.* **2012**, *51*, 8178 – 8211

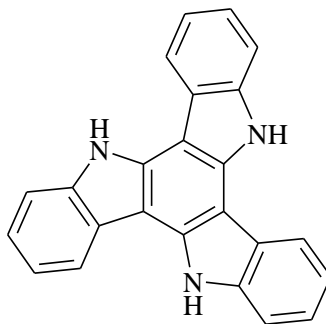
SECTION 1

CHAPTER 1

EUMELANIN-INSPIRED TRIAZATRUXENES AS NOVEL BLUE EMITTERS

~INTRODUCTION~

Among the numerous organic platforms that have attracted particular interest for their properties and applications in the field of organic electronics, triazatruxene (TAT) have recently attracted particular attention. The TAT core can be regarded as a nitrogen-doped truxene or as deriving from the fusion of three carbazole units, both of which are well studied in organic electronics.



**Triazatruxene
(TAT)**

Recent studies have shown that TATs exhibit a good charge mobility, up to $1.4 \text{ cm}^2\text{V}^{-1}\text{s}^{-1}$,¹ since they combine the good hole-transport properties of carbazoles with highly ordered columnar supramolecular arrangements, due to their disk-like extended π surface.² Moreover TATs undergo reversible redox processes,² show an intense electroluminescence³ and form stable thin amorphous films.⁴ The C_3 symmetry of the aromatic core makes TATs good candidates as building block for the build-up of star-shaped structures.⁵ In contrast to linear polymers, star-shaped polymers display a better solubility favoring the formation of thin films and enhancing luminescent properties. Moreover, the physical and optical properties of the polymer can be tuned by choosing the appropriate central core and the flexible arms conjugated with it.

The studies carried out until now have pointed out that TATs can be applied for the development of bulk heterojunction solar cells as hole selective material (Figure 1.1.1a),⁶ organic light emitting diodes (Figure 1.1.1b),⁷ and sensing devices (Figure 1.1.1c).⁸ Some TATs exhibited very large photoconductibility, and in opportunely functionalized star-shaped architectures can behave as two photon absorption chromophores (Figure 1.1.1d)⁹ or generate electroactive discotic liquid crystals with a large range of thermal stability (Figure 1.1.1e).¹⁰

Recently the potential of TATs as semiconducting materials has been tested by field-effect transistor (FET) measurements showing gate-modulated source-drain current.¹¹

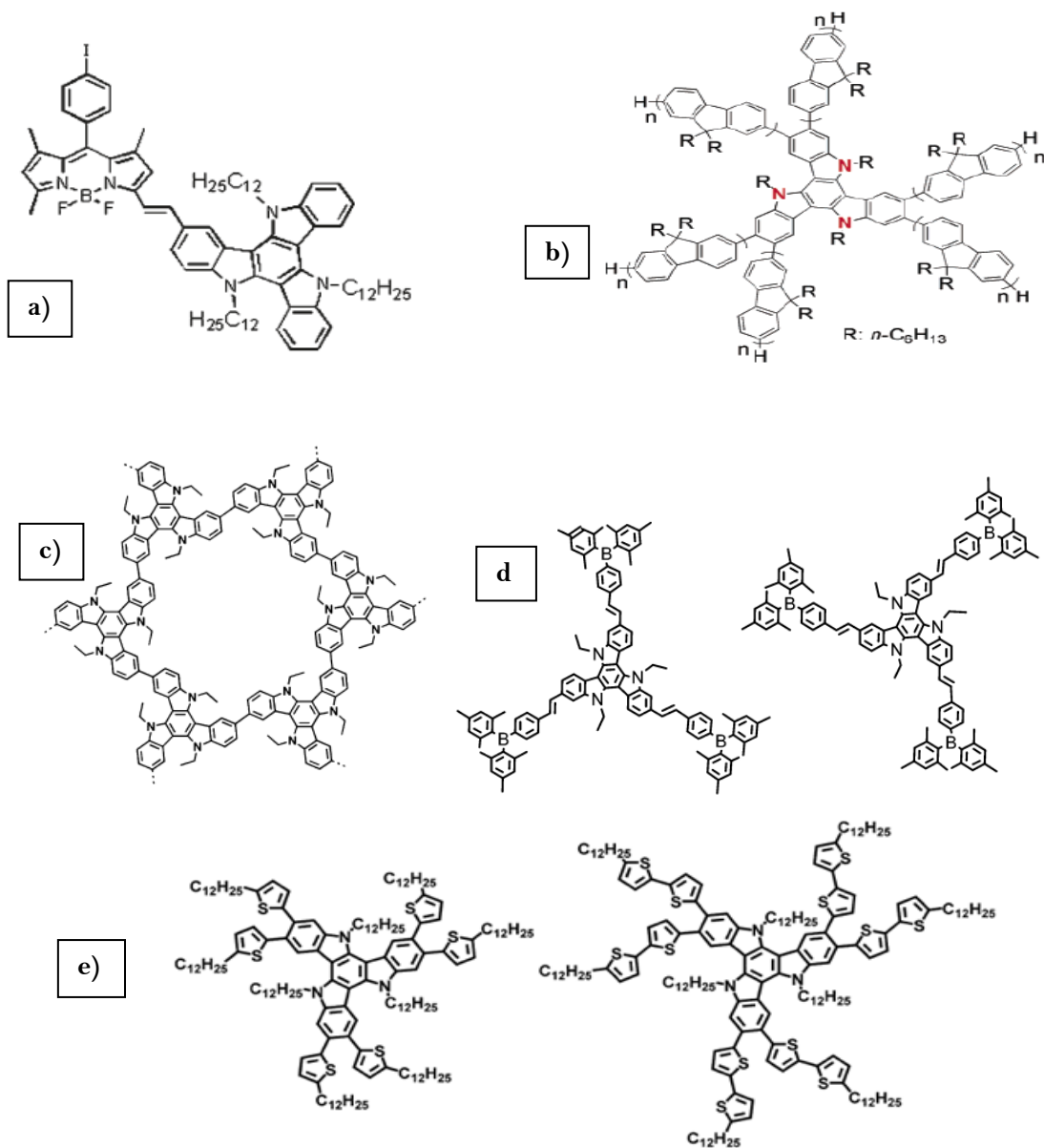
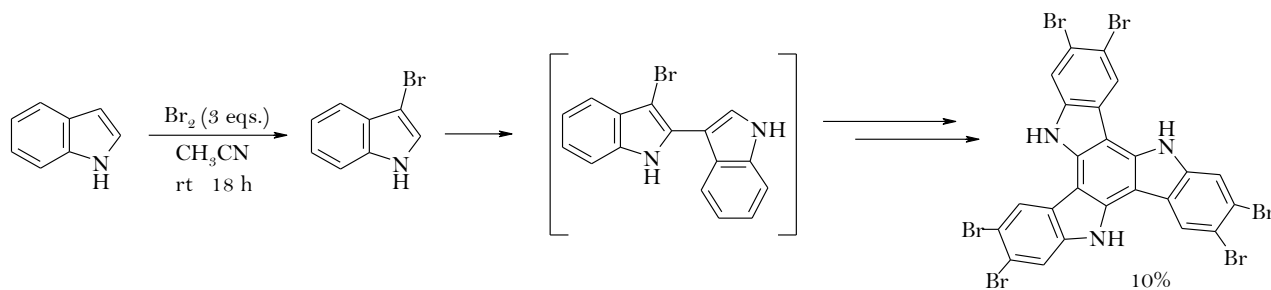


Figure 1.1.1. Examples of recent applications of TATs in organic electronics: a) bulk heterojunction solar cells as hole selective material, b) organic light emitting diodes, c) sensing devices, d) two photon absorption chromophores, e) electroactive discotic liquid crystals.

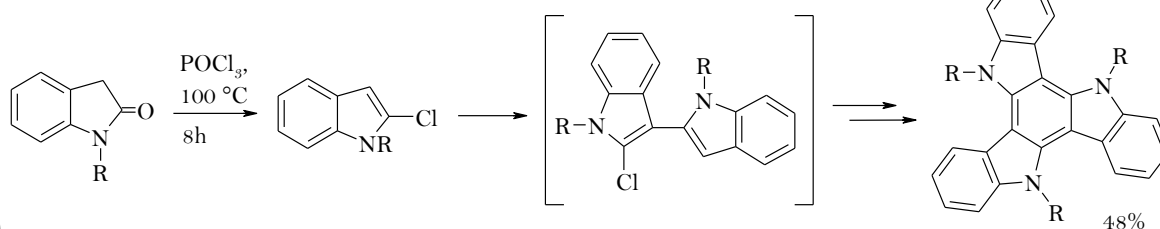
Despite the great interest toward TATs, their chemistry and versatile functionality are still under development, mainly due to the difficult construction of the core. Only three procedures

are reported in the literature for the synthesis of TAT derivatives. The first is based on the reaction of indole with bromine in acetonitrile; after 18 h reaction time it is possible to isolate after filtration and crystallization the hexabromotriazatruxene **1** in 18% overall yield (Figure 1.1.2a).¹² The second procedure leads to the formation of TATs starting from the corresponding 2-oxyindole derivative by treatment with POCl₃ at 100 °C (Figure 1.1.2b).¹³ Both the procedures envisage the formation of haloindoles as intermediates that undergo a complex sequence of couplings leading to the formation of the TAT skeleton.

a)



b)



c)

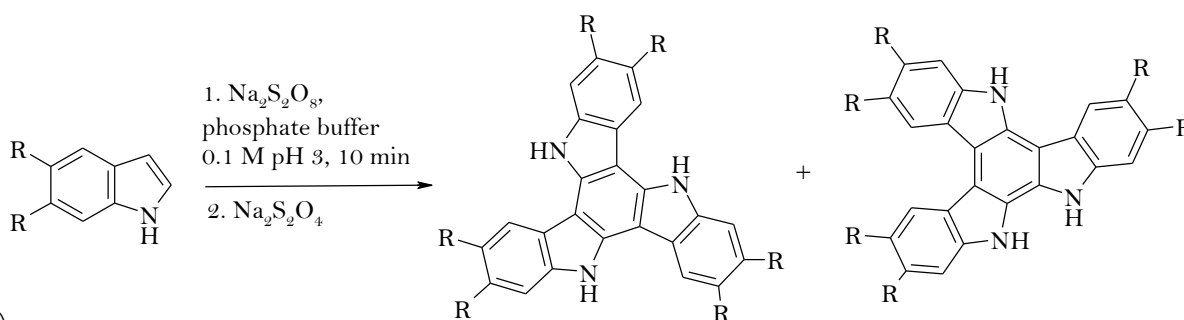
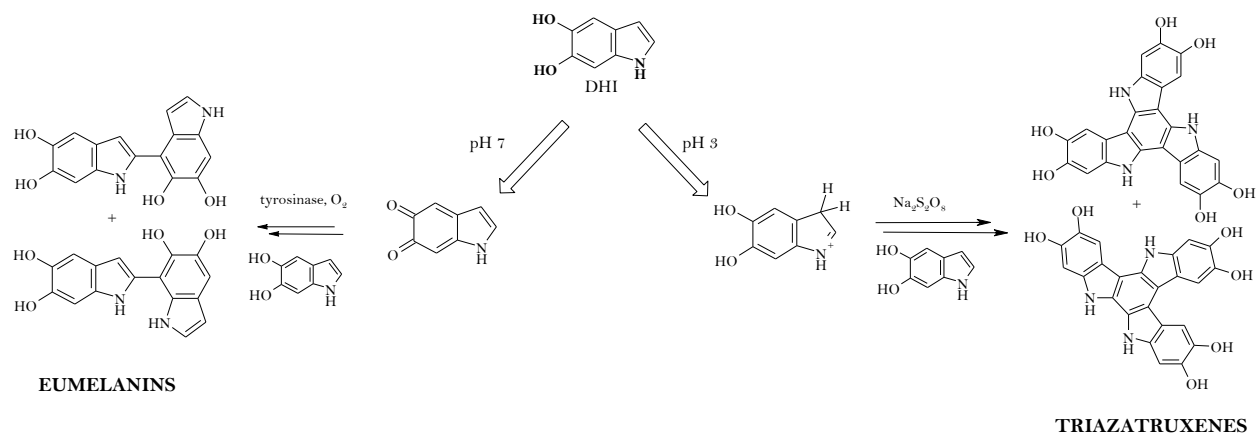


Figure 1.1.2. Synthetic procedures described in the literature affording TAT derivatives.

In 1998 a third synthetic procedure was developed by the research group of my tutor that exploits the peculiar reactivity of (di)hydroxyindoles in aqueous acidic medium (Figure 1.1.2c).¹⁴ Unexpectedly, while in neutral or alkaline medium the oxidation process of (di)hydroxyindoles leads to black insoluble eumelanin via formation of *o*-quinone intermediates,

at acidic pH the pyrrole reactivity overwhelms catechol oxidation diverting the oxidative pathway toward the formation of regioisomeric triazatruxenes (TATs) via a peculiar one-pot cyclotrimerization route (Scheme 1.1.1).



Scheme 1.1.1. pH-driven oxidative pathways of DHI.

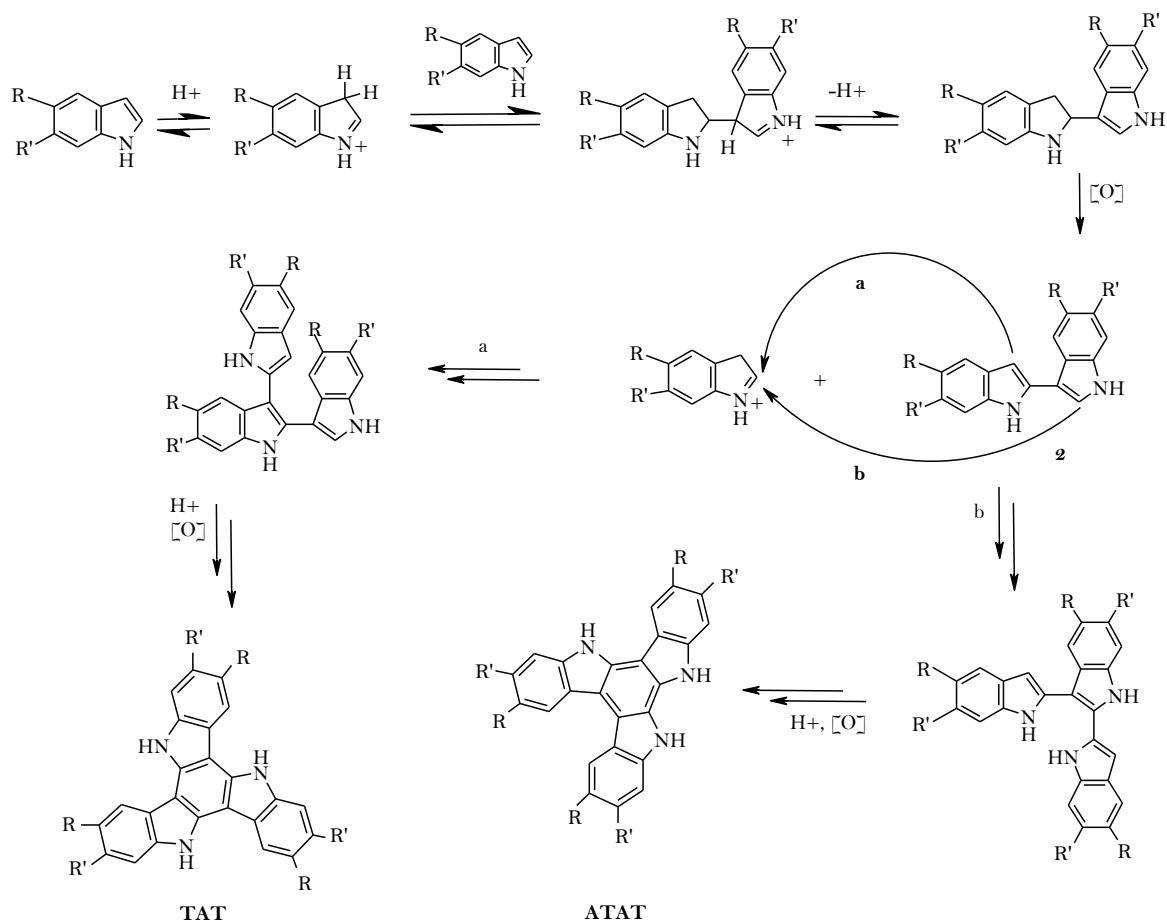


Figure 1.1.3. Mechanism proposed for the synthesis of TATs with sodium persulfate in aqueous acidic medium.

This reaction capitalizes on the typical acidic reactivity of indoles to afford, after oxidation, the intermediate 2,3'-biindole **2** (Figure 1.1.3). Thanks to the presence of electron-releasing group mainly on the 6 position of the indolic nucleus, it is possible to easily obtain, by iterating this sequence of events, two TAT derivatives, the well-known C_3 symmetrical **TAT** and the corresponding asymmetric regioisomer **ATAT**.

Compared to the former two synthetic procedures, this latter seems to work better in terms of isolated yields (about 50%), reaction time (from 5 to 30 minutes) and soft conditions (aqueous solution at room temperature); but undoubtedly the great potential of this procedure relies on the formation of asymmetrical ATATs, isolated for the first time and in good yields, whose potentiality as organic semiconductor have not been explored.

Starting from this background, in this chapter is reported the experimental activity carried out for: the synthesis, separation, and comparative characterization of eumelanin-inspired symmetric and asymmetric TATs prepared from 5,6-dimethoxyindole (*TAT_OMe* and *ATAT_OMe*), 5,6-dibenzyloxyindole (*TAT_OBnNH*, *ATAT_OBnNH*, *TAT_OBn* and *ATAT_OBn*), and 6-hydroxyindole (*TAT_Ac* and *ATAT_Ac*); the detailed characterization of their optoelectronic properties with the support of quantum chemical calculations based on TD-DFT; the preliminary investigation of self-assembly behavior in solution of these disk-like shaped platforms; the applications of these TATs as emitting materials in OLED devices.

This work has been partially carried out at the ENEA Research Center of Portici in collaboration with Dr. Maria Grazia Maglione, Ing. Paolo Tassini and Ing. Carla Minarini and in collaboration with Prof. Orlando Crescenzi, Prof. Antonio Cassinese and Dr Mario Barra (UniNA) and Prof. V. Barone (SNS Pisa)

~RESULTS AND DISCUSSION~

○ SYNTHESIS OF TATS FROM 5,6-DIMETHOXYINDOLE

The compounds 2,3,7,8,12,13-hexamethoxydiindole[3,2-*a*:3',2'-*c*]carbazole (*TAT_OMe*) and 2,3,6,7,11,12-hexamethoxydiindole[2,3-*a*:2',3'-*c*]carbazole (*ATAT_OMe*) were prepared from 5,6-dimethoxyindole according to the third synthetic procedure discussed in the introduction section and as reported in the literature.²³ In detail, 5,6-dimethoxyindole was dissolved in acetonitrile, suspended in 0.1 M phosphate buffer, pH 3, and treated with sodium persulfate (1.5 molar equivalents). After the addition of the oxidant the pale yellow mixture turned into dark blue-green and formed a precipitate. The TLC analysis of the reaction mixture showed after 10 minutes the complete consumption of the starting compound and the formation of a band constituted by two products, **A** and **B**, with very close R_f value. The reaction mixture was treated with sodium dithionite and centrifuged: the isolated precipitate was washed with water and dried under reduced pressure, whereas the supernatant was extracted with ethyl acetate. The TLC analysis indicated that the precipitate was made of **A** and **B** and that only low amount of the same compounds were present in the organic fraction of the supernatant. As reported in the literature and confirmed by NMR analysis, the products **A** and **B**, isolated as an intimate mixture due to their quite low solubility in many organic solvents, were identified as the two TATs *TAT_OMeNH* and *ATAT_OMeNH*, obtained in 92% overall yield (Figure 1.1.4).

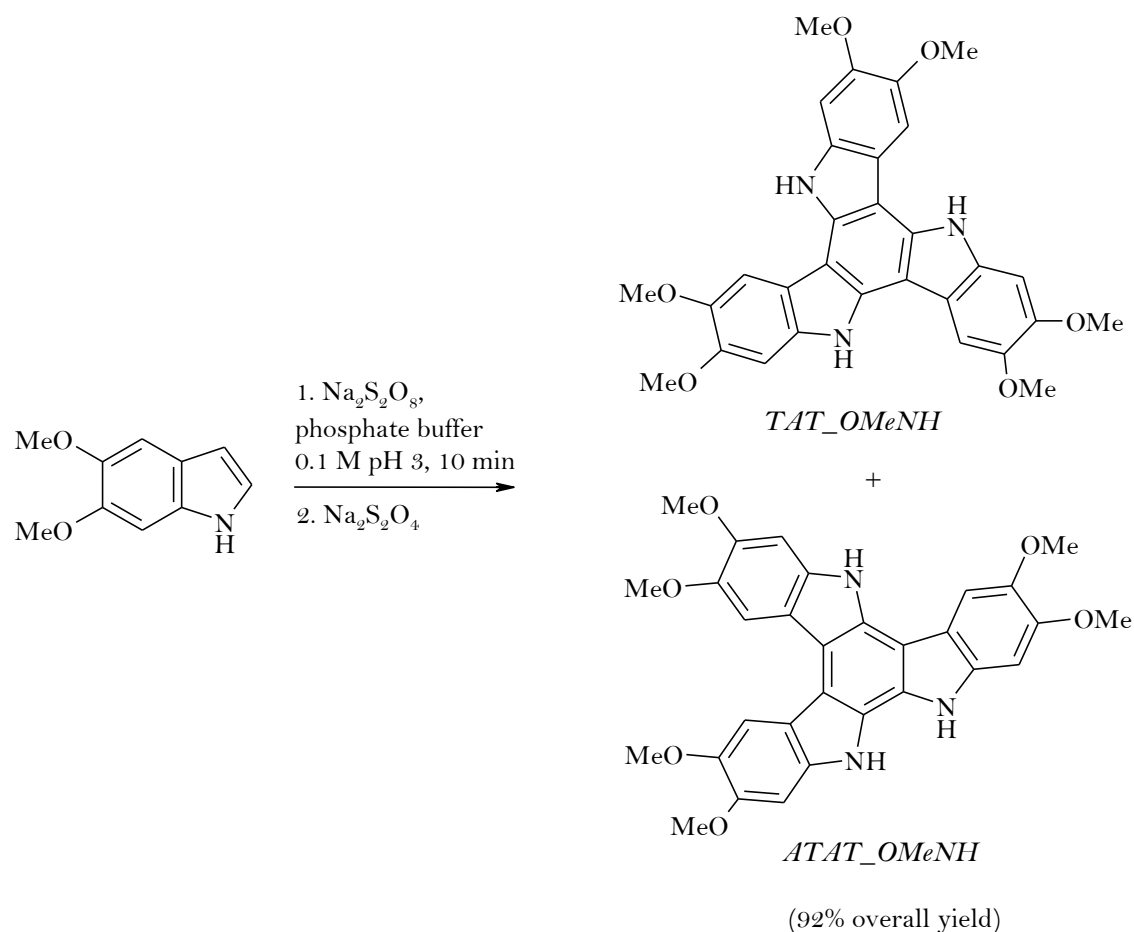


Figure 1.1.4. Synthesis of TAT_OMeNH and $ATAT_OMeNH$ from 5,6-dimethoxyindole.

In order to improve the solubility of TAT_OMeNH and $ATAT_OMeNH$ and favor the separation of the two isomers, the mixture was subjected to the alkylation of the three -NH groups with a C_{11} aliphatic chain. The TATs mixture was dissolved in dry DMSO and treated under an argon atmosphere and at 70 °C with KOH (10 molar equivalents) and 1-bromoundecane (4.5 molar equivalents). After 18 h the TLC analysis of the reaction mixture showed the total consumption of the starting compounds and the formation of two main products, **C** ($R_f = 0.63$) and **D** ($R_f = 0.59$). The reaction mixture, taken up in ethyl acetate, gave a precipitate that was isolated by centrifugation; the resulting supernatant was extracted with ethyl acetate and HCl 1.5 M. Both the fractions showed the presence of the two products **C** and **D** that were subjected to liquid chromatography on silica gel (eluant: gradient from petroleum ether to petroleum ether/ethyl acetate 8:2). This afforded **C** and **D** in pure form as pale yellow

solids and were identified by NMR and mass analysis as the two desired *N*-alkylated *TAT_OMe* and *ATAT_OMe*.

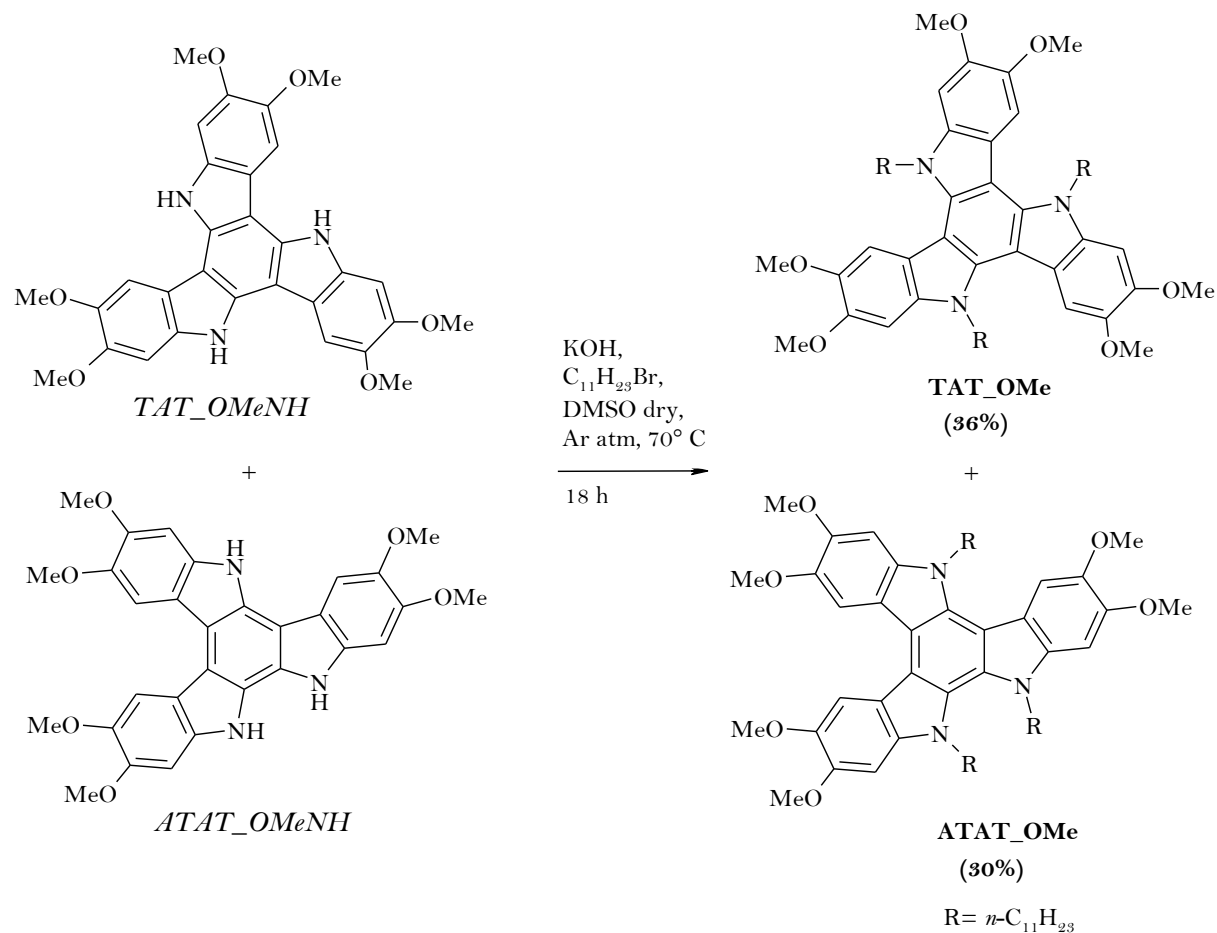


Figure 1.1.5. Synthesis of *TAT_OMe* and *ATAT_OMe*.

The 1H NMR and the ^{13}C spectra of *TAT_OMe* showed a simple pattern of signals due to the symmetry of the molecule. On the basis of 2D NMR experiments it was possible to assign all the resonances of compound *TAT_OMe* as follows (Figure 1.1.6).

Mass analysis carried out with the LDI technique showed the pseudomolecular ion peak at m/z 988, confirming the identity of the compound.

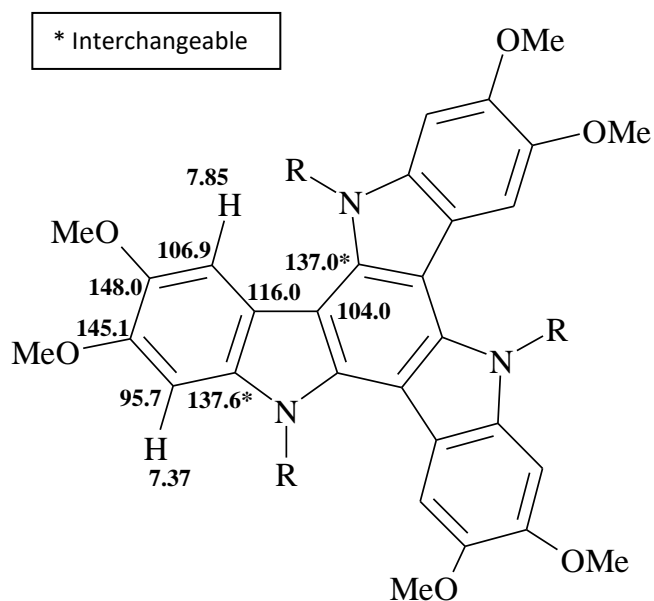


Figure 1.1.6. Assignment of ^1H and ^{13}C resonances of *TAT_OMe*.

As expected, the ^1H NMR and the ^{13}C NMR spectra appeared more complex showing the resonances of three indole units. On the basis of 2D NMR experiments it was possible to assign all the resonances of compound *ATAT_OMe* as follows (Figure 1.1.9).

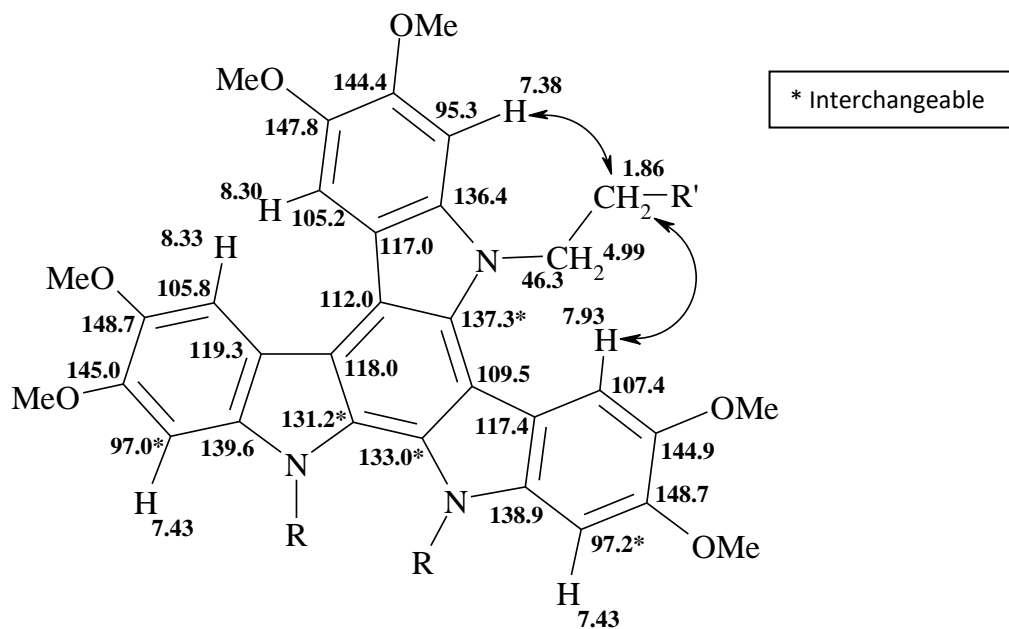


Figure 1.1.7. Assignment of ^1H and ^{13}C resonances of *ATAT_OMe*; arrows refer to ROESY contacts.

Mass analysis carried out with the LDI technique showed the pseudomolecular ion peak at m/z 988, confirming the identity of the compound.

○ SYNTHESIS OF TATS FROM 5,6-DIBENZYLOXYINDOLE

The 2,3,7,8,12,13-hexabenzoyloxydiindole[3,2- α :3',2'- ζ]carbazole (*TAT_OBnNH*) and 2,3,6,7,11,12-hexabenzoyloxydiindole[2,3- α :2',3'- ζ]carbazole (*ATAT_OBnNH*) were prepared from 5,6-dibenzoyloxyindole following the same procedure previously described. 5,6-Dibenzoyloxyindole was dissolved in acetonitrile, suspended in 0.1 M phosphate buffer, pH 3, and treated with sodium persulfate (5 molar equivalents). After the addition of the oxidant, the reaction mixture turned from pale yellow to dark blue and formed a precipitate. The TLC analysis of the reaction mixture showed after 30 minutes the complete consumption of the starting compound and the formation of two main products, *E* at $R_f = 0.48$, and *F* at $R_f = 0.37$. The reaction mixture was then treated with sodium dithionite, extracted with ethyl acetate and water and purified by liquid chromatography on silica gel. This afforded the two compounds in pure form that were identified *E* as the symmetric *TAT_OBnNH* (30% yield) and *F* as the asymmetrical *ATAT_OBnNH* (25% yield) after NMR and mass analyses.

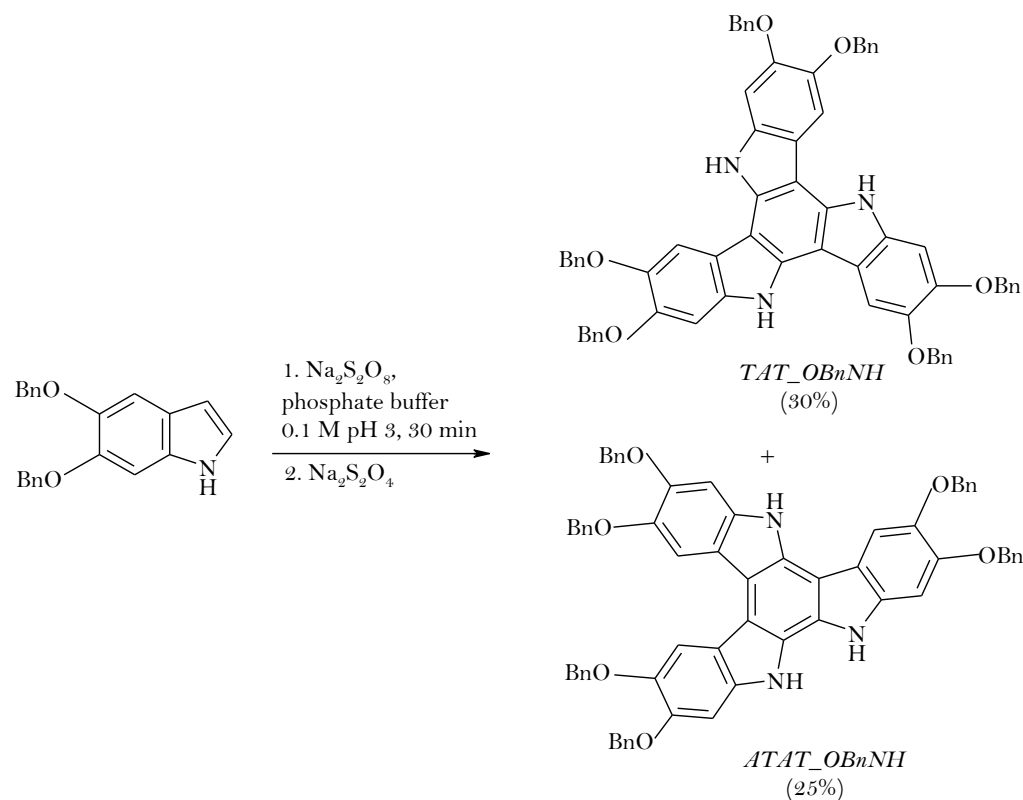


Figure 1.1.8. Synthesis of *TAT_OBnNH* and *ATAT_OBnNH* from 5,6-dibenzoyloxyindole.

On the basis of 1D and 2D NMR experiments it was possible to assign all the resonances of compound *TAT_ OBnNH* and *ATAT_ OBnNH* as follows (Figure 1.1.9).

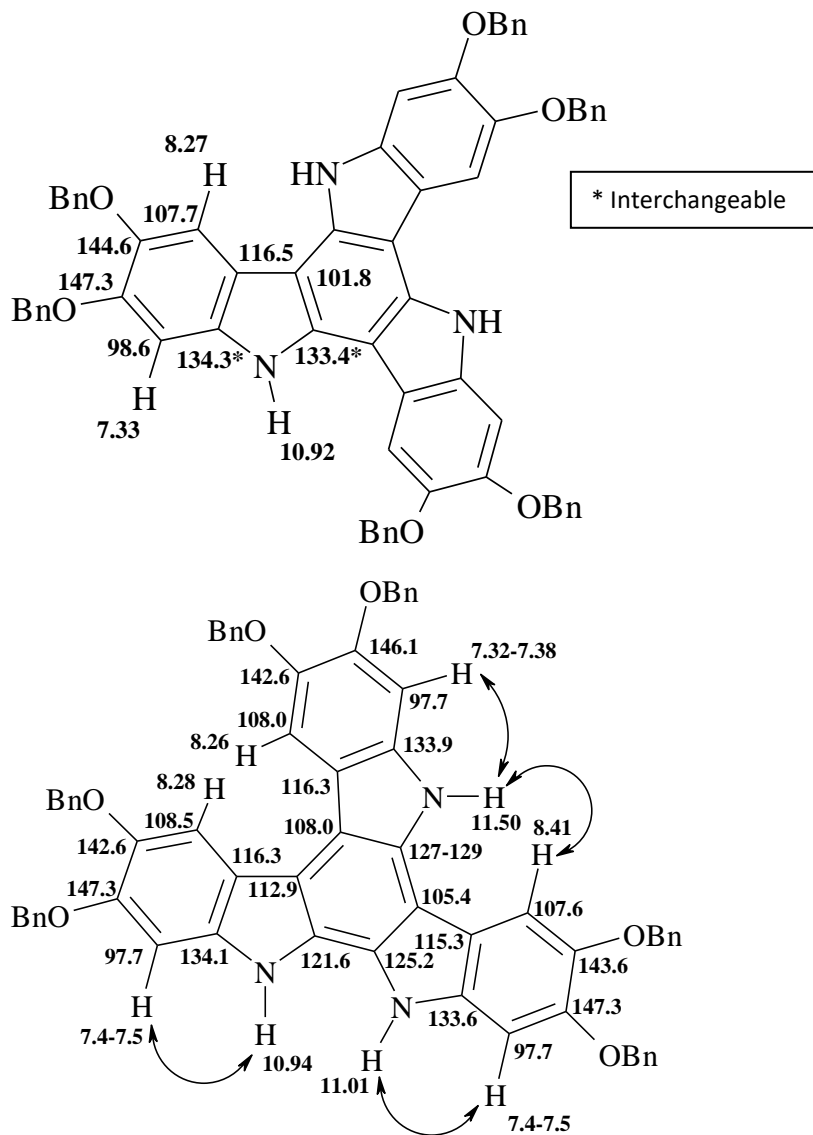


Figure 1.1.9. Assignment of ¹H and ¹³C resonances of *TAT_ OBnNH* (up) and *ATAT_ OBnNH* (below).

Mass analysis carried out with the LDI technique showed the pseudomolecular ion peak at m/z 982, confirming the identity of the compounds.

To improve the solubility of *TAT_ OBnNH* and *ATAT_ OBnNH*, the first was soluble in acetone and DMSO whereas the second was soluble only in DMSO with a very low solubility in acetone, the two isomers were subjected separately to *N*-alkylation with 1-bromoundecane

following the same procedure described for *TAT_OMeNH* and *ATAT_OMeNH* (Figure 1.1.10).

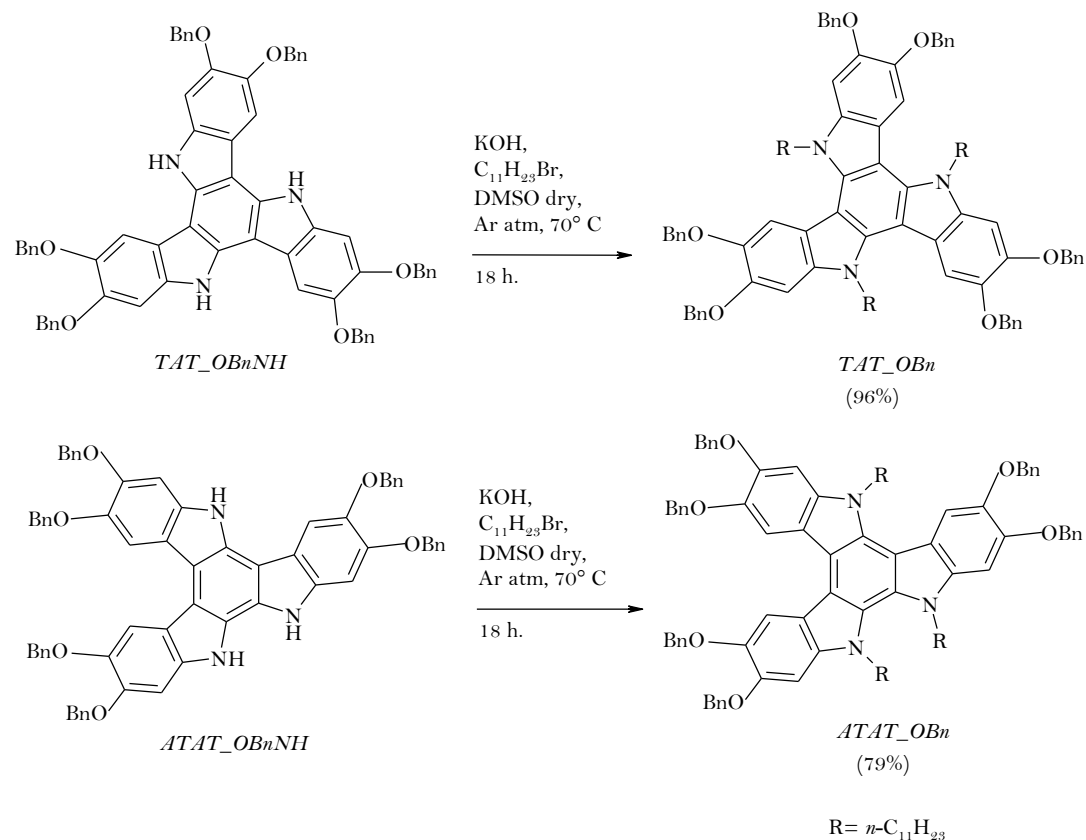


Figure 1.1.10. Synthesis of *TAT_OBn* and *ATAT_OBn*.

In both cases the TLC analysis of the reaction mixtures showed after 18 h the complete consumption of the starting compounds and the formation of a single product: **G** at $R_f = 0.82$, in the case of *TAT_OBnNH*, and **H** at $R_f = 0.79$, in the case of *ATAT_OBnNH*. The reaction mixtures, taken up in ethyl acetate, gave a precipitate that was isolated by centrifugation; the resulting supernatants were extracted with ethyl acetate and HCl 1.5 M. TLC analysis showed that the precipitates taken up in acetone were made of pure **G** or **H**, and that small amount of the same compounds were also present in the supernatants, that were so subjected to chromatographic purification. The reaction products **G** and **H** were identified as the *TAT_OBn* (96% yield) and *ATAT_OBn* (79% yield) after ^1H NMR and mass analyses.

Mass analysis carried out with the LDI technique showed the pseudomolecular ion peak at m/z 1444, confirming the identity of the compounds.

○ SYNTHESIS OF TATS FROM 6-HYDROXYINDOLE

The 2,7,12-trihydroxydiindole[3,2-a:3',2'-c]carbazole (*TAT_OH*) and 2,7,12-trihydroxydiindole[2,3-a:2',3'-c]carbazole (*ATAT_OH*) were prepared according the same procedure previously described using 6-hydroxyindole as the starting material. This latter was dissolved in acetonitrile and suspended in 0.1 M phosphate buffer, pH 3 and treated with sodium persulfate (1.5 molar equivalents). After the addition of the oxidant the reaction mixture turned from pale yellow into dark blue and formed a precipitate. The TLC analyses of the reaction mixture showed after 10 minutes the complete consumption of the reagent and the presence of a band constituted by two products, **I** and **L**, with very close R_f value. The reaction mixture was treated with sodium dithionite and centrifuged: the isolated precipitate was washed with water and dried under reduced pressure, whereas the supernatant was extracted with ethyl acetate. The TLC analysis indicated that the precipitate was made of **I** and **L** and that only low amount of the same compounds were present in the organic fraction of the supernatant. Due to the quite similar chromatographic behavior of **I** and **L**, it was not possible to isolate the pure compounds in large amounts. So, the precipitate was subjected to acetylation of the phenolic group with acetic anhydride and pyridine. After 18 h the TLC analysis of the reaction mixture showed the complete consumption of the starting compounds and the formation of two main products, **I-Ac** at $R_f = 0.70$ and **L-Ac** at $R_f = 0.46$. The reaction mixture was then dried under reduced pressure and purified by liquid chromatography on silica gel to give the compounds **I-Ac** and **L-Ac** that were identified as the TATs *TAT_Ac* (15% yield) and *ATAT_Ac* (30% yield) by NMR and mass analyses.

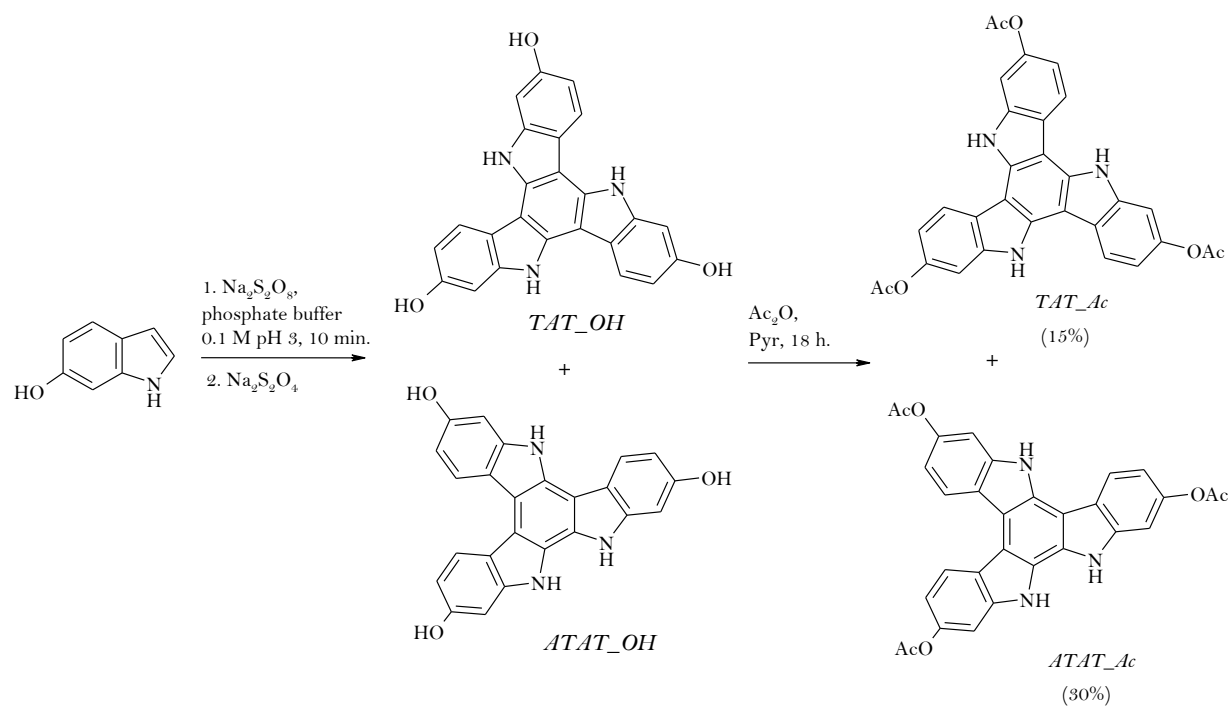


FIGURE 1.1.11. Synthesis of *TAT_Ac* and *ATAT_Ac* from 6-hydroxyindole.

On the basis of 2D NMR experiments it was possible to assign all the resonances of compounds *TAT_Ac* and *ATAT_Ac* as follows (Figure 1.1.12).

Mass analysis carried out with the LDI technique showed the pseudomolecular ion peak at m/z 520 along with the fragmentation peaks at m/z 477, 434 and 391 due to the loss of the acetyl groups, confirming the identity of the compounds.

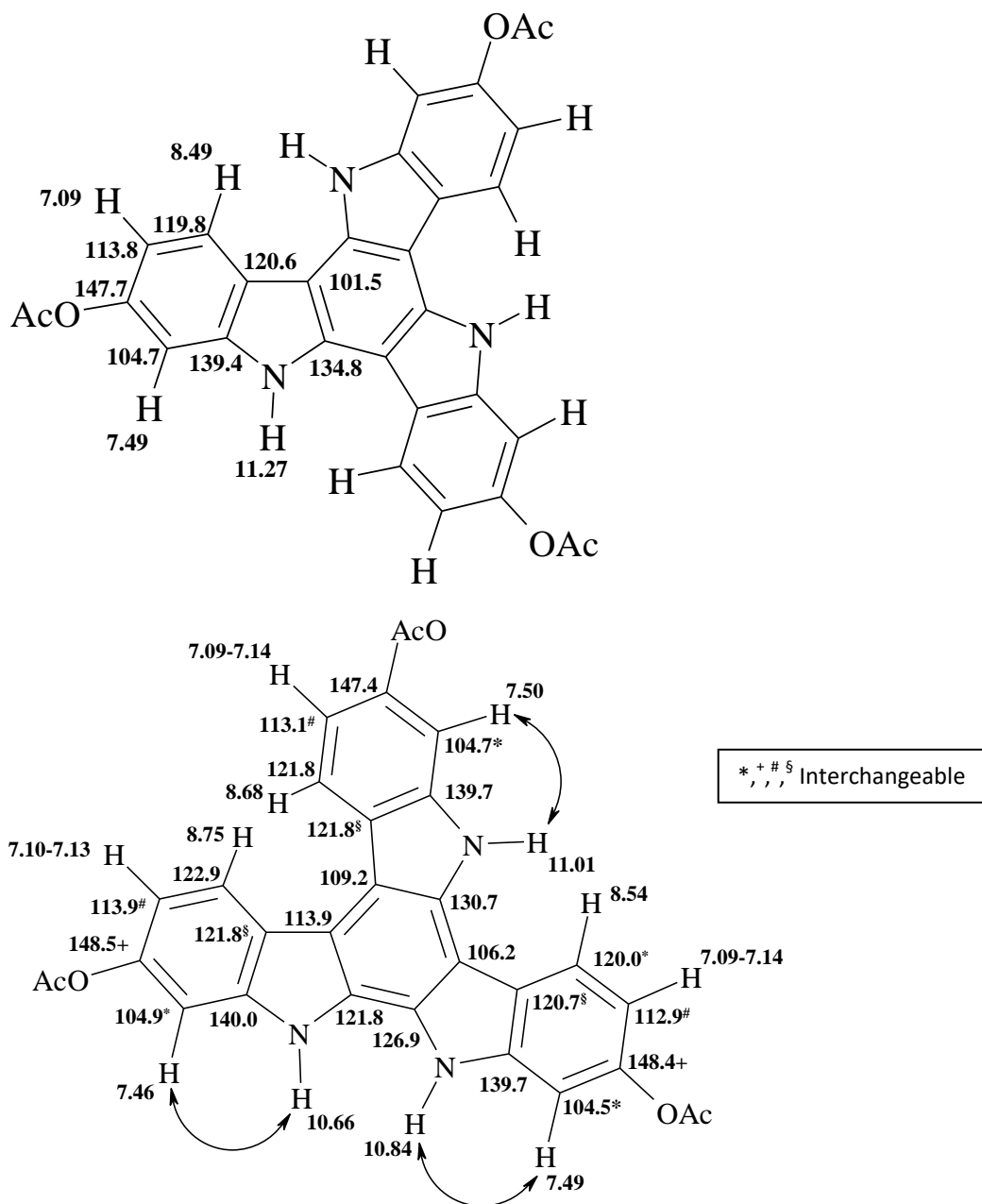


Figure 1.1.12. Assignment of ^1H and ^{13}C resonances of *TAT_Ac* (up) and *ATAT_Ac* (below); arrows refer to ROESY contacts.

Preliminary experiments were carried out to remove the acetyl groups of *TAT_Ac* and *ATAT_Ac*. In brief, the two TATs were separately dissolved in dry methanol and treated under an argon atmosphere with sodium *tert*-butoxide. After 3 h the TLC analyses of the reaction mixtures showed the complete consumption of the starting compound and the formation of a main product. The reaction mixtures were then acidified with acetic acid and extracted with

water and ethyl acetate to give the products in pure form that were identified as the TATs *TAT_OH* (83% yield) and *ATAT_OH* (83% yield), respectively, by ^1H NMR analysis.

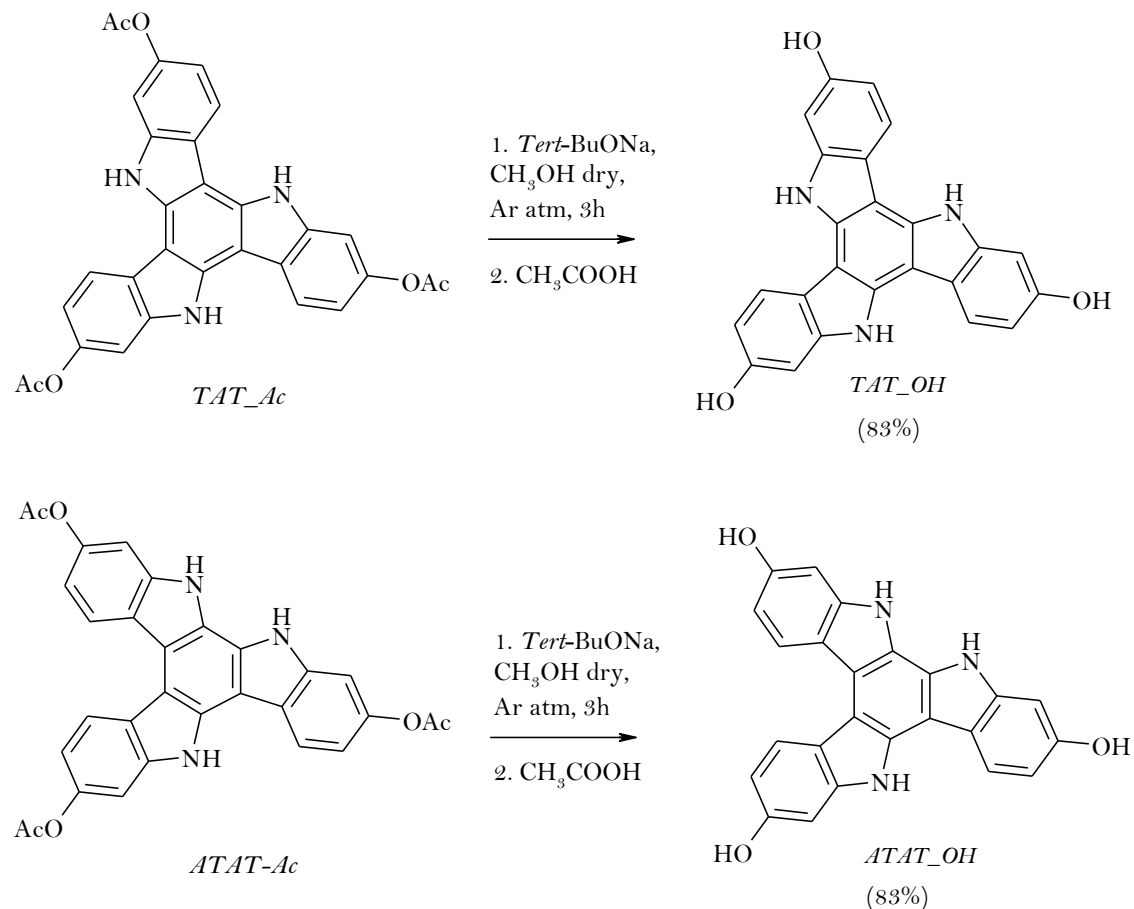


Figure 1.1.13. Synthesis of *TAT_OH* and *ATAT_OH*.

○ PHOTO-PHYSICAL PROPERTIES

The optical properties of the synthesized TATs were investigated by UV-visible and fluorescence spectroscopy in dilute solution and in thin films. The UV-visible spectra recorded in diluted solutions (1×10^{-5} M) pointed out significant differences between symmetrical and asymmetrical isomers, whereas no appreciable variations were evident by changing the substitution grade and the nature of the substituents on TAT within the same typology, that is symmetrical or asymmetrical. The photo-physical properties of the synthesized TATs and ATATs are summarized in Table 1.1.1.

Table 1.1.1. Photophysical data of TATs and ATATs.

Compound	λ_{\max} , nm (log ϵ , M ⁻¹ cm ⁻¹) ^[a]	λ_{\max} , nm (film)	λ_{em} , nm ^[a]	λ_{em} , nm (film)	Φ (%) ^[b]	E_g^{opt} , eV ^[c] soln/film
<i>TAT_OMe</i>	333 (4.94)	334, 345 (sh), 360 (sh)	405	420, 439	19 ^a /27 ^d /4 ^e	3.15/3.08
<i>ATAT_OMe</i>	336 (4.81), 366 (4.43), 379 (4.42)	335, 366 (sh), 383	425	436	28 ^a /39 ^d /30 ^e	2.97/2.93
<i>TAT_OBnNH</i>	329 (4.76), 349 (sh)	329	413, 487	393	-	3.19/2.95
<i>ATAT_OBnNH</i>	329 (4.48), 350 (sh), 373 (sh)	330, 366 (sh)	417	415	20 ^a /2 ^d /8 ^e	2.85/2.67
<i>TAT_OBn</i>	334 (4.63)	-	406	-	2 ^a	3.17/-
<i>ATAT_OBn</i>	335 (4.20), 380 (4.16)	-	429	-	41 ^a	2.93/-
<i>TAT_Ac</i>	314 (4.57), 327 (sh), 345 (4.09)	315, 346 (sh)	383, 401	410	12 ^a /21 ^d /13 ^e	3.35/3.32
<i>ATAT_Ac</i>	312 (4.60), 339 (sh), 354 (4.32), 376 (3.93), 396 (3.90)	315, 357, 397	410, 426	433	39 ^a /43 ^d /25 ^e	3.05/2.86

[a] Determined in DMSO. [b] Relative to quinine sulfate in 0.5 M H₂SO₄ ($\Phi = 0.546$). [c] Optical band gap estimated from the red edge of the longest wavelength absorption in solution. [d] Determined in THF. [e] Determined in dichloromethane.

Typically, the symmetrical series exhibited one major absorption maximum centered around 330 nm whereas the asymmetric series displayed two maxima around 330 and 350–380 nm; for all the compounds the ϵ values proved quite high. Significant differences emerged also in the photoluminescence spectra, which showed for asymmetric TATs emission bands red-shifted

with respect to those of the symmetrical isomers with higher fluorescence quantum efficiencies (Φ).

Determination of optical band gaps (E_g^{opt}) in solution indicated lower values for the asymmetric TATs relative to the symmetrical isomers.

The solvent and concentration effects on UV-visible and fluorescence spectra were analyzed. By varying the solvent from THF to the less polar DCM or to the more polar DMSO, small changes in the position of the absorption and emission maxima were observed. The shape and the position of the observed maxima did not change also with the concentration in the range of 10^{-4} to 10^{-6} M, indicating that no obvious aggregation occurred in such dilute solutions.

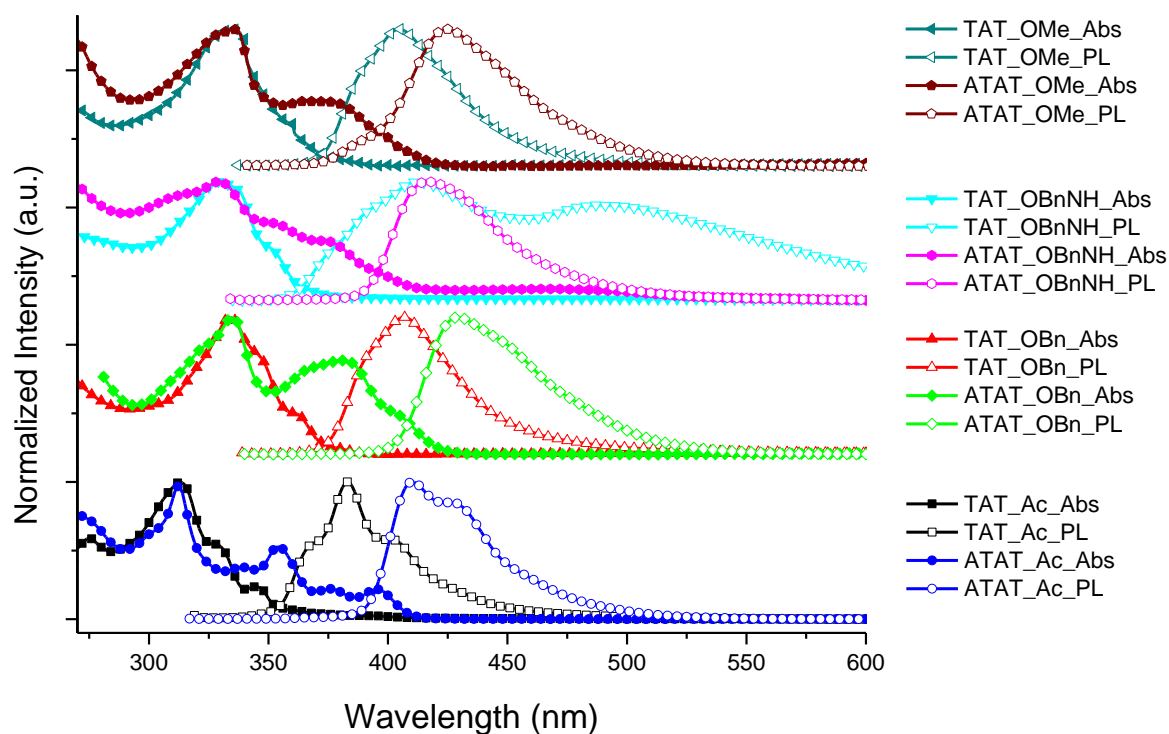


Figure 1.1.14. Normalized absorption (Abs) and photoluminescence (PL) spectra of synthesized TATs and ATATs in DMSO.

UV-visible spectra were also registered for compounds *TAT_OMe*, *ATAT_OMe*, *TAT_OBnNH*, *ATAT_OBnNH*, *TAT_Ac* and *ATAT_Ac* as thin films onto quartz plates. Film deposition was carried out by spin coating a solution of the appropriate TAT in chlorobenzene or pyridine using the following speed program: 800 rpm for 60" then 1500 rpm for 90".

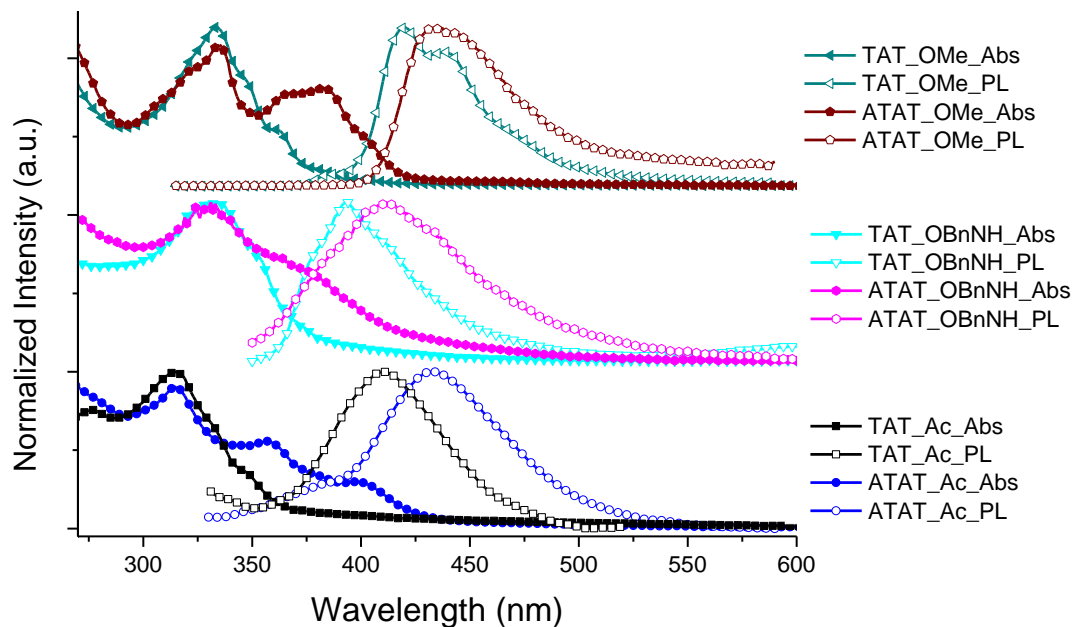


Figure 1.1.15. Normalized absorption (Abs) and photoluminescence (PL) of TATs and ATATs as thin films on quartz

For all the four tested TATs, UV-visible spectra of the films displayed a small bathochromic shift (ca. 3-5 nm) of the absorption maxima along with long tails at the lower-energy edge, suggesting that aggregation of these disk-like molecules in the solid state occurred.

○ DFT CALCULATIONS

To gain deeper insight into the structural and electronic properties of TATs, model compounds (e.g. bearing *N*-alkyl chains truncated at the methyl level) were investigated by a DFT/TD-DFT approach.

Geometry optimizations were performed with a hybrid functional (PBE0)¹⁵ and a reasonably large 6-31+G(d,p) basis set, either in vacuum or by adoption of a polarizable continuum medium (PCM)¹⁶ to account for the influence of the condensed-phase environment.

All calculations were performed with the Gaussian package of programs.¹⁷ Two conformers were predicted for symmetrical *TAT_OMe*, *TAT_OBnNH* and *TAT_OBn*, the expected C_3 -symmetric helical minimum, being slightly less stable than the distorted C_1 conformer (distortion: 5.5° in the former case and 14.9° in the latter case). Deviations from planarity are also appreciable in the C_1 conf. 1 asymmetric conformer for *ATAT_OMe*, *ATAT_OBnNH* and

ATAT_OBn (distortion: 12.7°), being again more stable than the less distorted C_1 conf. 2 conformer (distortion: 5.4°).

Table 1.1.2. Computed high-wavelength electronic transitions of the most stable conformers identified for model TATs in vacuo.

λ , nm	f	Main contributions (expansion coefficients)	λ , nm	f	Main contributions (expansion coefficients)
<i>TAT_OMe</i> , C_1			<i>ATAT_OMe</i> , C_1 conf. 1		
352.2	0.00	HOMO-1 \rightarrow LUMO (0.49); HOMO \rightarrow LUMO+1 (0.47)	373.7	0.14	HOMO-1 \rightarrow LUMO (0.67)
338.3	0.01	HOMO-1 \rightarrow LUMO+1 (-0.44); HOMO \rightarrow LUMO (0.52)	364.6	0.47	HOMO \rightarrow LUMO (0.68)
322.4	0.60	HOMO-1 \rightarrow LUMO (-0.46); HOMO \rightarrow LUMO+1 (0.49)	319.9	0.13	HOMO-1 \rightarrow LUMO+1 (-0.29); HOMO \rightarrow LUMO+1 (0.56)
321.7	0.58	HOMO-1 \rightarrow LUMO+1 (0.51); HOMO \rightarrow LUMO (0.44)	316.9	0.04	HOMO-1 \rightarrow LUMO+1 (0.59); HOMO \rightarrow LUMO+1 (0.31)
<i>TAT_Ac</i> , C_1			<i>ATAT_Ac</i> , C_1 conf. 1		
335.0	0.00	HOMO-1 \rightarrow LUMO (0.40); HOMO \rightarrow LUMO+1 (0.40)	367.9	0.15	HOMO \rightarrow LUMO (0.68)
321.5	0.00	HOMO-1 \rightarrow LUMO+1 (-0.40); HOMO \rightarrow LUMO (0.40)	339.9	0.41	HOMO-1 \rightarrow LUMO (0.67)

Calculations showed the same situation in the case of symmetric *TAT_Ac*, whereas three conformers were predicted for the asymmetric *ATAT_Ac* exhibiting comparable distortion degree from the planarity. UV-Vis spectra of the main species were computed using the time-dependent density functional theory (TD-DFT) approach,¹⁸ with the PBE0 functional and a larger 6-311++G(2d,2p) basis set. The simulated absorption spectra were in excellent agreement with experimental data. It is noteworthy that two lowest-energy transitions appear essentially dipole-forbidden in the more symmetric TATs molecule, but are allowed in

asymmetrical TATs. Moreover, irrespective of the allowed/forbidden character, both transitions are predicted at higher wavelength in asymmetrical TATs (Table 1.1.2). The combination of these two factors accounts quite well for the remarkable differences in the experimental UV-vis spectra. Solvation effects, as accounted by the PCM, cause moderate (3–4 nm) bathochromic shifts in the apparent position of the main bands, and more significant hyperchromic effects.

To get some insight into the electronic layout, the HOMO and LUMO energies and the HOMO–LUMO gaps of the most stable conformers of *TAT_Ac* and *ATAT_Ac* and of model TATS for *TAT_OMe*, *ATAT_OMe*, *TAT_OBnNH*, *ATAT_OBnNH*, *TAT_OBn* and *ATAT_OBn* for different computational levels and conditions were compared (Table 1.1.3). In this connection, it is interesting to note that in the C_3 -symmetric conformer of TAT, HOMO and HOMO-1 are degenerate, and so are LUMO and LUMO+1 (Figure 1.1.16); the distortion present in the C_1 conformer of TAT barely affects these degeneracies. By contrast, the unsymmetrical nature of the ATAT skeleton induce a significant lowering of the LUMO energy level with a consequent reduction of the HOMO–LUMO gap by about 0.4 eV for model *TAT_OMe*, *ATAT_OMe*, *TAT_OBnNH*, *ATAT_OBnNH*, *TAT_OBn* and *ATAT_OBn* and by 0.6 eV for *TAT_Ac* and *ATAT_Ac*, and an appreciable separation between HOMO+1 and HOMO, and even more between LUMO and LUMO+1. By comparison of data with those obtained from the parent triazatruxene and its *N,N,N*-trimethyl derivative), it was possible to deduce that *N*-alkylation of the TAT core induces a significant lowering of the HOMO–LUMO gap, as also does substitution of the benzenoid units with electron-releasing groups.

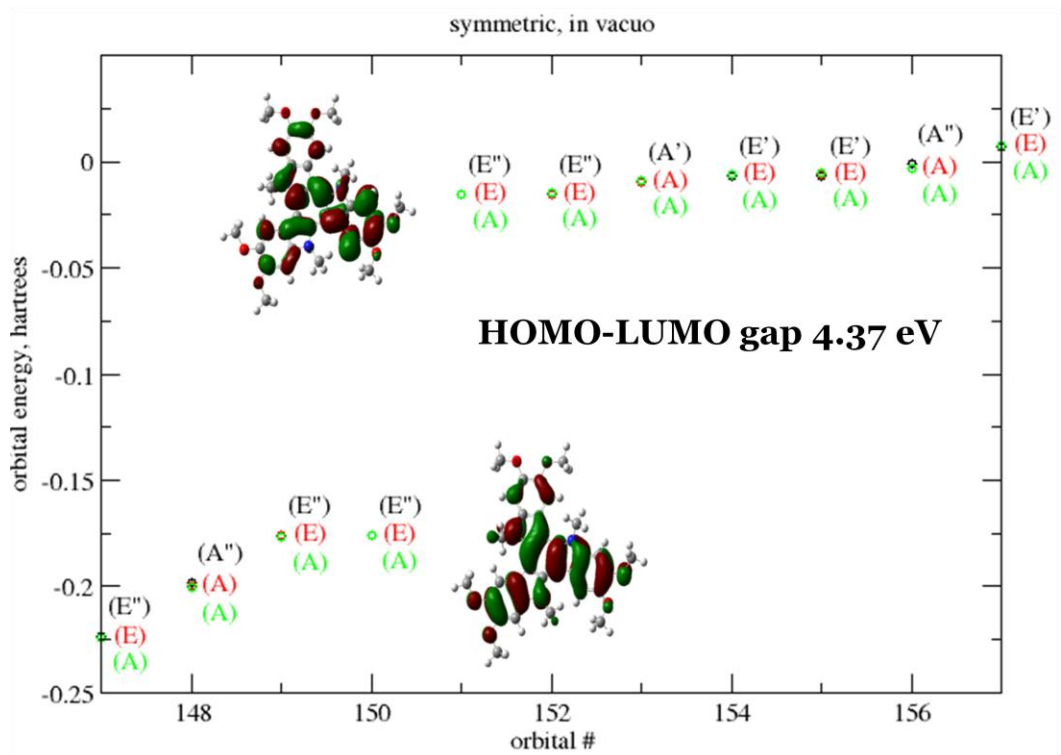
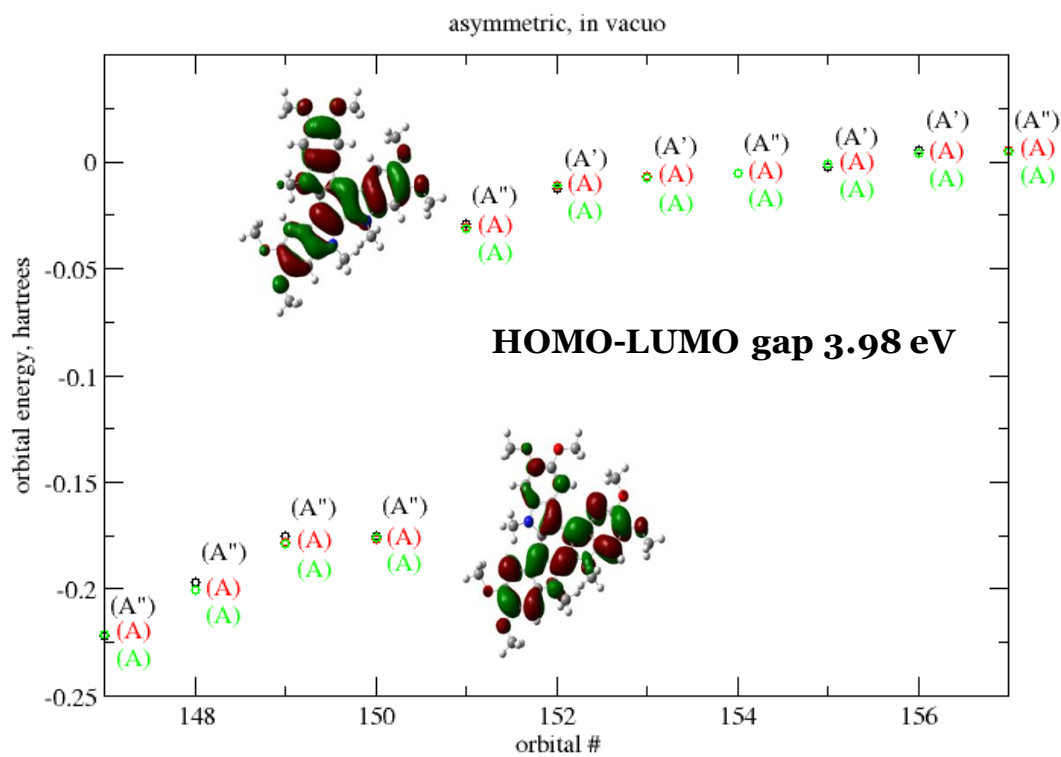


Figure 1.1.16. Orbitalic structure around the HOMO-LUMO gap in vacuo.

Table 1.1.3. Computed HOMO and LUMO energies and HOMO-LUMO gaps $\Delta_{\text{H-L}}$ (eV) of the most stable conformers identified for model *TAT_OMe* and *ATAT_OMe* and for *TAT_Ac* and *ATAT_Ac*.

	HOMO (eV) ^[a]		LUMO (eV) ^[a]		$\Delta_{\text{H-L}}$ (eV) ^[a]		
	vacuo	DMSO ^[b]	vacuo	DMSO ^[b]	vacuo	DMSO ^[b]	
<i>TAT_OMe</i> , C_1	vacuo	-4.79	-4.79	-0.37	-0.42	4.42	4.37
	DMSO ^[b]	-5.07	-5.07	-0.63	-0.67	4.44	4.39
<i>ATAT_OMe</i> , C_1 conf. 1	vacuo	-4.80	-4.82	-0.78	-0.83	4.02	3.98
	DMSO ^[b]	-5.09	-5.09	-1.05	-1.09	4.04	4.00
<i>TAT_Ac</i> , C_1	vacuo	-5.56	-5.56	-0.89	-0.94	4.67	4.62
	DMSO ^[b]	-5.69	-5.69	-0.99	-1.03	4.70	4.66
<i>ATAT_Ac</i> , C_1 conf. 1	vacuo	-5.43	-5.44	-1.32	-1.36	4.12	4.07
	DMSO ^[b]	-5.54	-5.55	-1.43	-1.48	4.12	4.07

[a] White columns: PBE0/6-31+G(d,p); grey columns: PBE0/6-311++G(2d,2p)//PBE0 / 6-31+G(d,p). [b] PCM.

○ SELF-ASSEMBLY BEHAVIOR

Intermolecular interactions involving aromatic rings are of primary importance in biochemistry, supramolecular and material chemistry.¹⁹ The recent growth of the field of organic electronics has aroused a renewed interest on the understanding of weak intermolecular interactions involving π -conjugated molecules, a prerequisite to induce their self-assembly into one-dimensional nanostructures. Face-to-face π -stacks of extended aromatics with the π -surfaces located within van der Waals distances have emerged as promising nanowires and are among the best performing organic semiconductors.²⁰ In addition, self-assembled arrays formed in solution have been successfully transferred onto solid supports,²¹ resulting in highly oriented films with important implications in the development of molecule-based electronic devices. In this context, disk-shaped molecules and related shape-persistent macrocycles have a strong tendency to exhibit aggregation in solution forming either dimeric structures or extended stacks. The aggregation behavior of this family of molecules was studied by concentration-dependent ¹H NMR spectroscopy. This is the most frequently used technique for investigation of aggregation due to stacking interaction of aromatic compounds because of its ease, precision, and the fact that the chemical shift data provide structural information for

the aggregates.²² As a matter of fact, chemical upfield shifts of the aromatic signals upon increasing the concentration in nuclear magnetic resonance spectroscopy have been well documented as a signature of aromatic interactions. When two or more aromatic units come into close vicinity of each other, the nuclei of one molecule are affected by the ring-current magnetic anisotropy of the other, resulting in resonance shifting.²²

On these basis, the self-assembly behavior in solution of the isolated TATs was investigated by analyzing the ¹H NMR spectra recorded in (CD₃)₂CO in the 1-30 mM range of concentration.

As shown in Figure 1.1.17, it was possible to notice that, in the expanded regions of the ¹H NMR spectra of compound *TAT_OMe*, the aromatic protons and the α -methylene protons of the alkyl chain exhibited an upfield shift by increasing the concentration from 2 mM to 30 mM.

The effect was more pronounced for H_B with a $\Delta\delta = 5.1\%$ with respect to H_A with a $\Delta\delta = 3.5\%$ (Figure 1.1.18); a significant upfield effect can also be observed for the α -CH₂ protons of the *N*-undecyl chains ($\Delta\delta = 7.0\%$).

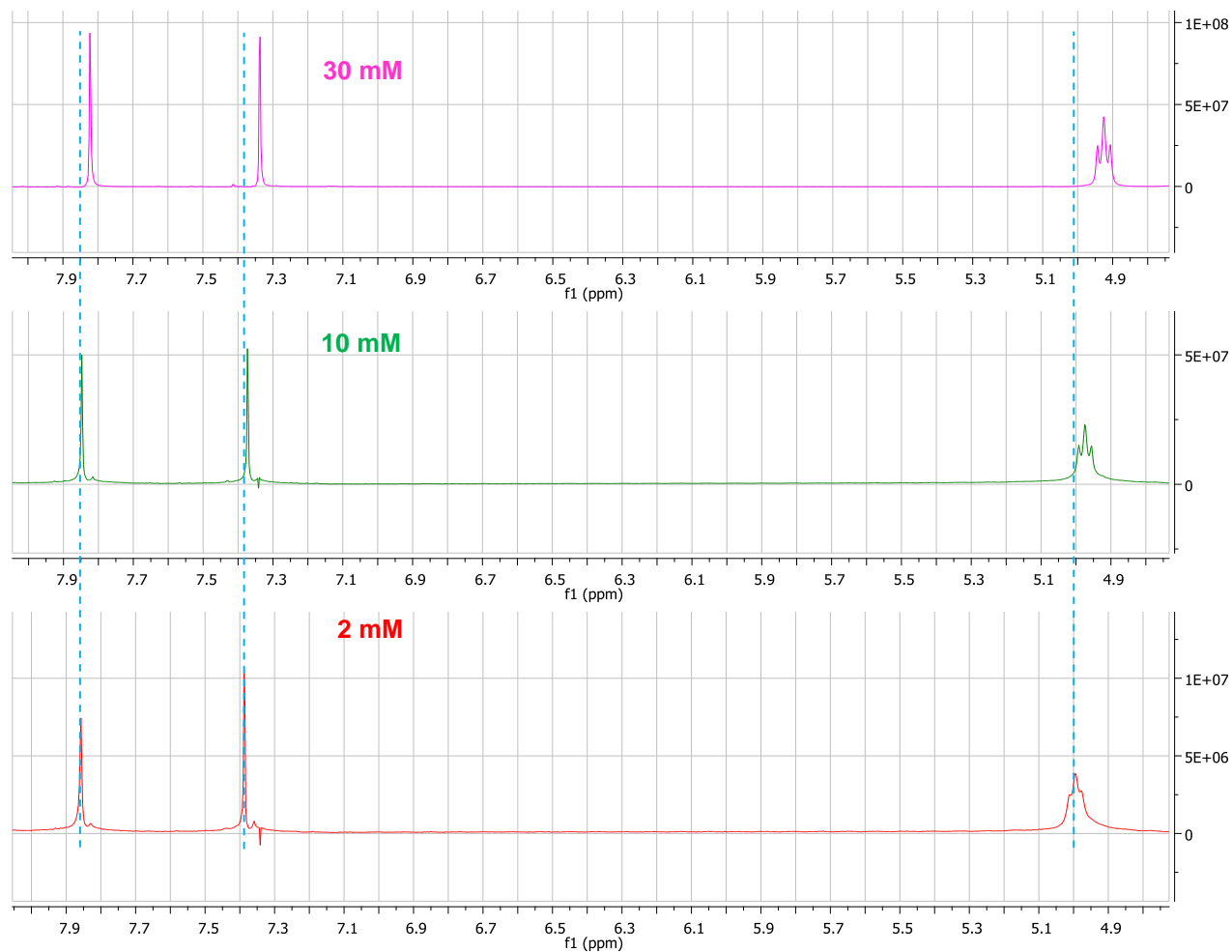


Figure 1.1.17. ¹H NMR spectra (expanded region) of *TAT_OMe* at different concentrations: 2 mM (red trace), 10 mM (green trace) and 30 mM (magenta trace).

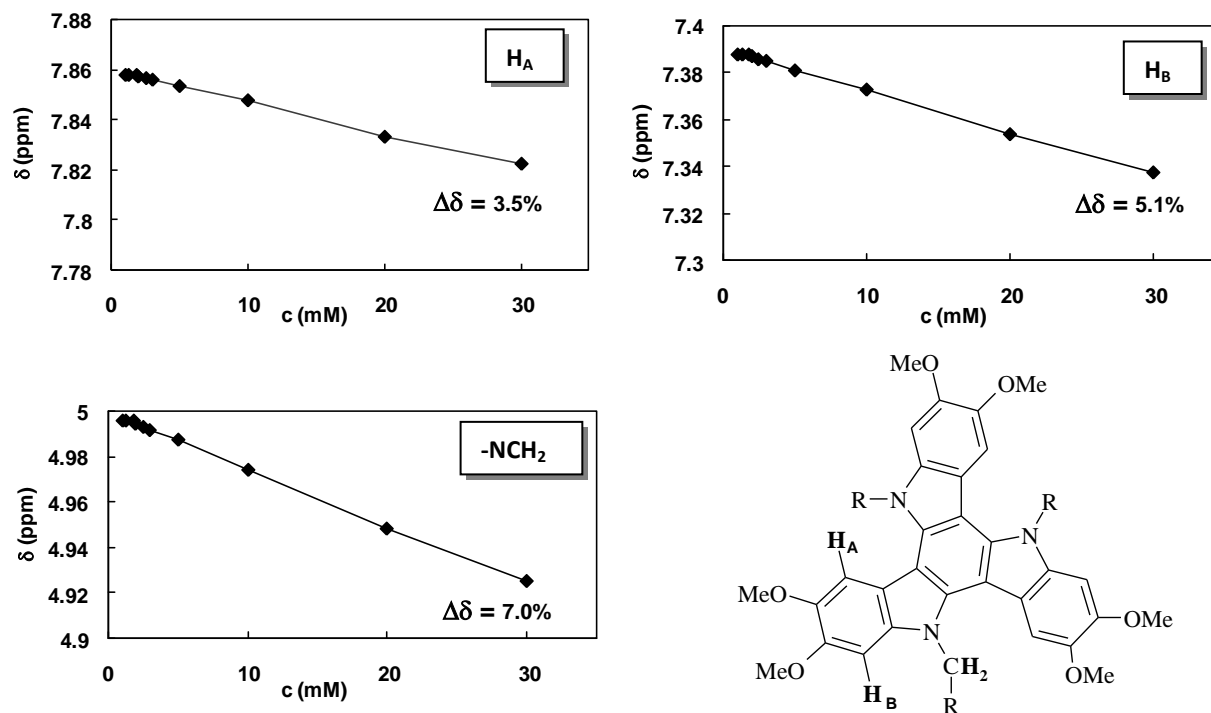


Figure 1.1.18. Shift of the aromatic and methylenic proton resonances of *TAT_OMe* with the concentration.

A completely different behavior was observed for the asymmetrical isomer *ATAT_OMe* for which a very low shift was detected only for two of the three $N-CH_2$ protons (Figure 1.1.29).

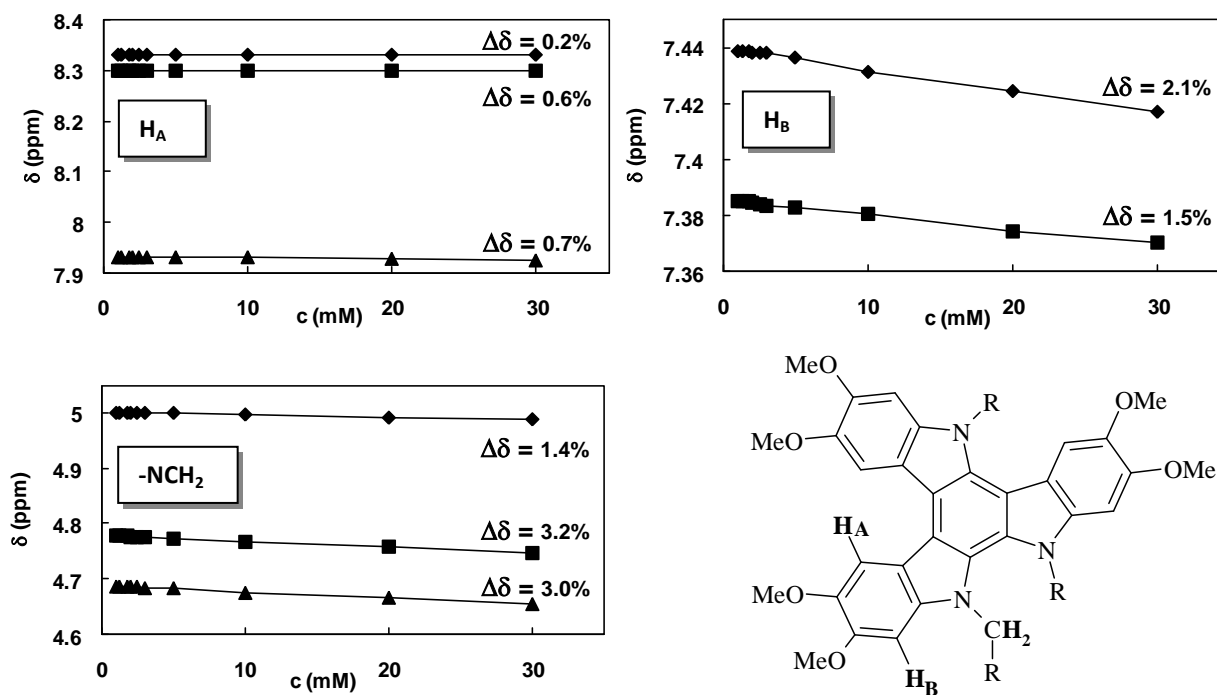


Figure 1.1.19. Shift of the aromatic and methylenic proton resonances of *ATAT_OMe* with the concentration.

Preliminary experiments have been carried out on *TAT_OBn* and *ATAT_OBn*; these have shown for both isomers a very low shift of H_A and the methylene protons –NCH₂ suggesting that no self-assembly occurred in solution (Figure 1.1.20 and 1.1.21).

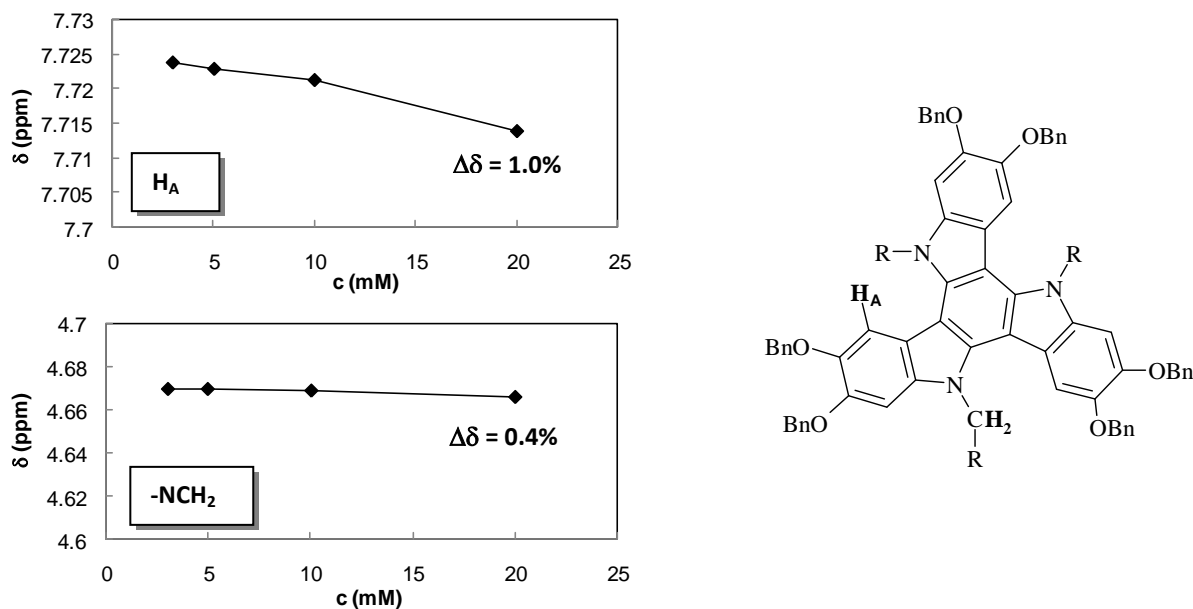


Figure 1.1.20. Shift of the aromatic and methylenic proton resonances of *TAT_OBn* with the concentration.

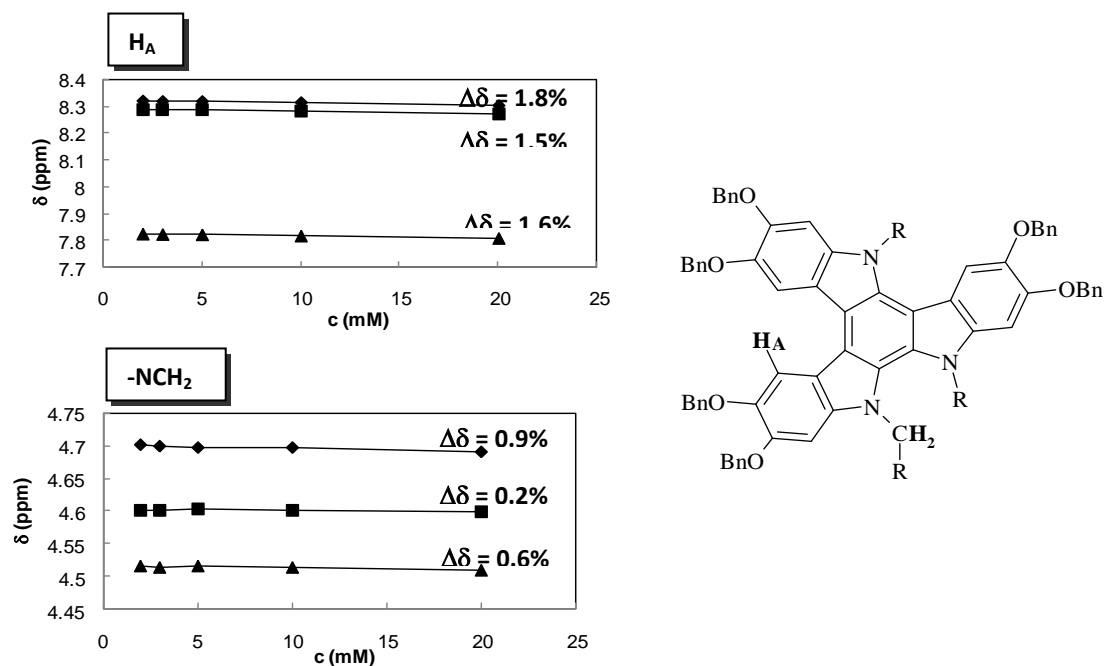


Figure 1.1.21. Shift of the aromatic and methylenic proton resonances of *ATAT_OBn* with the concentration.

The ^1H NMR spectra of *TAT-Ac* (Figure 1.1.32) showed in the low field region only a low shift of the protons of the $-\text{NH}$ groups ($\Delta\delta = 5.3\%$) with the other aromatic protons being no sensitive to concentration changes (Figure 1.1.23).

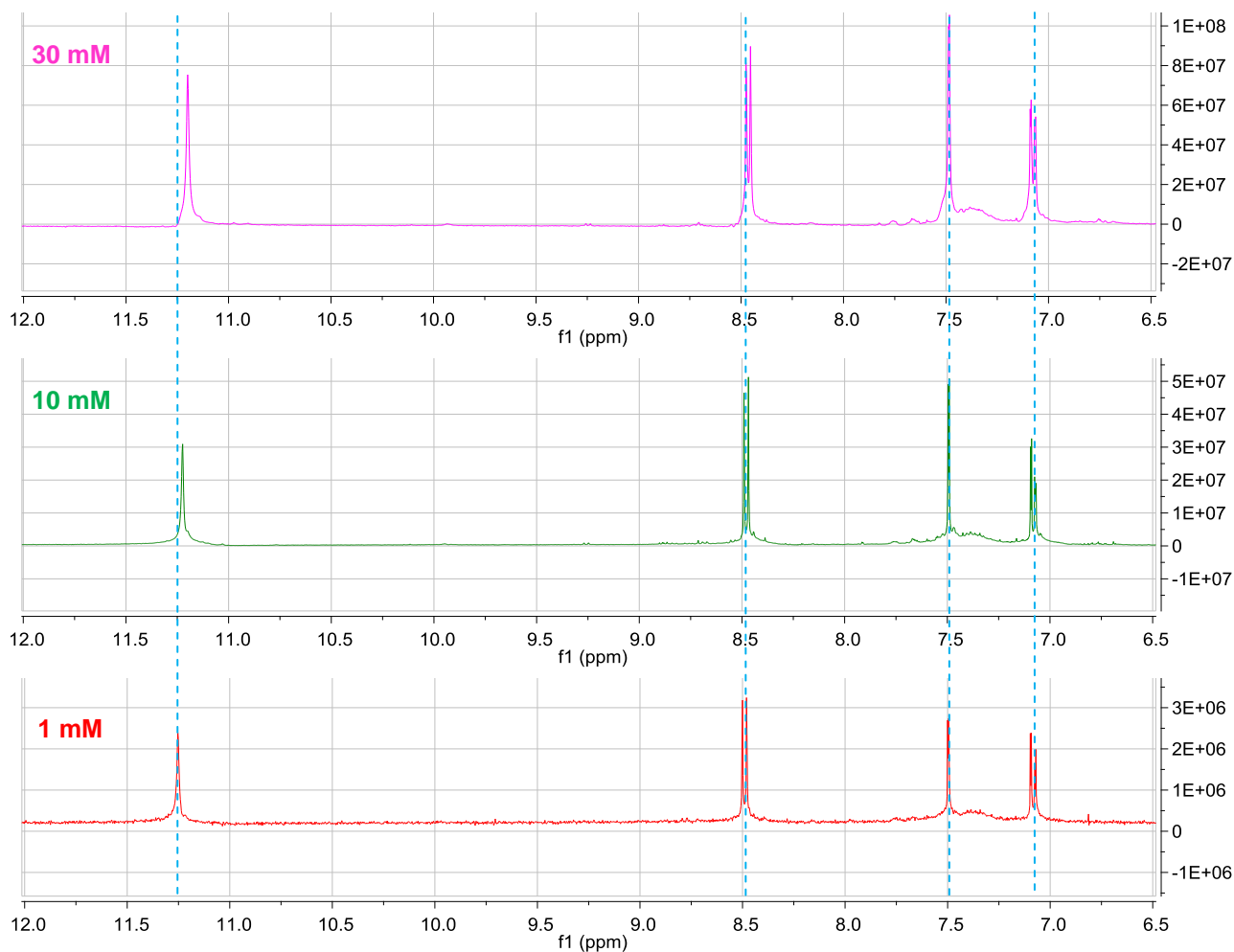


Figure 1.1.22. ^1H NMR spectra (expanded region) of *TAT-Ac* at different concentrations: 1 mM (red trace), 10 mM (green trace) and 30 mM (magenta trace).

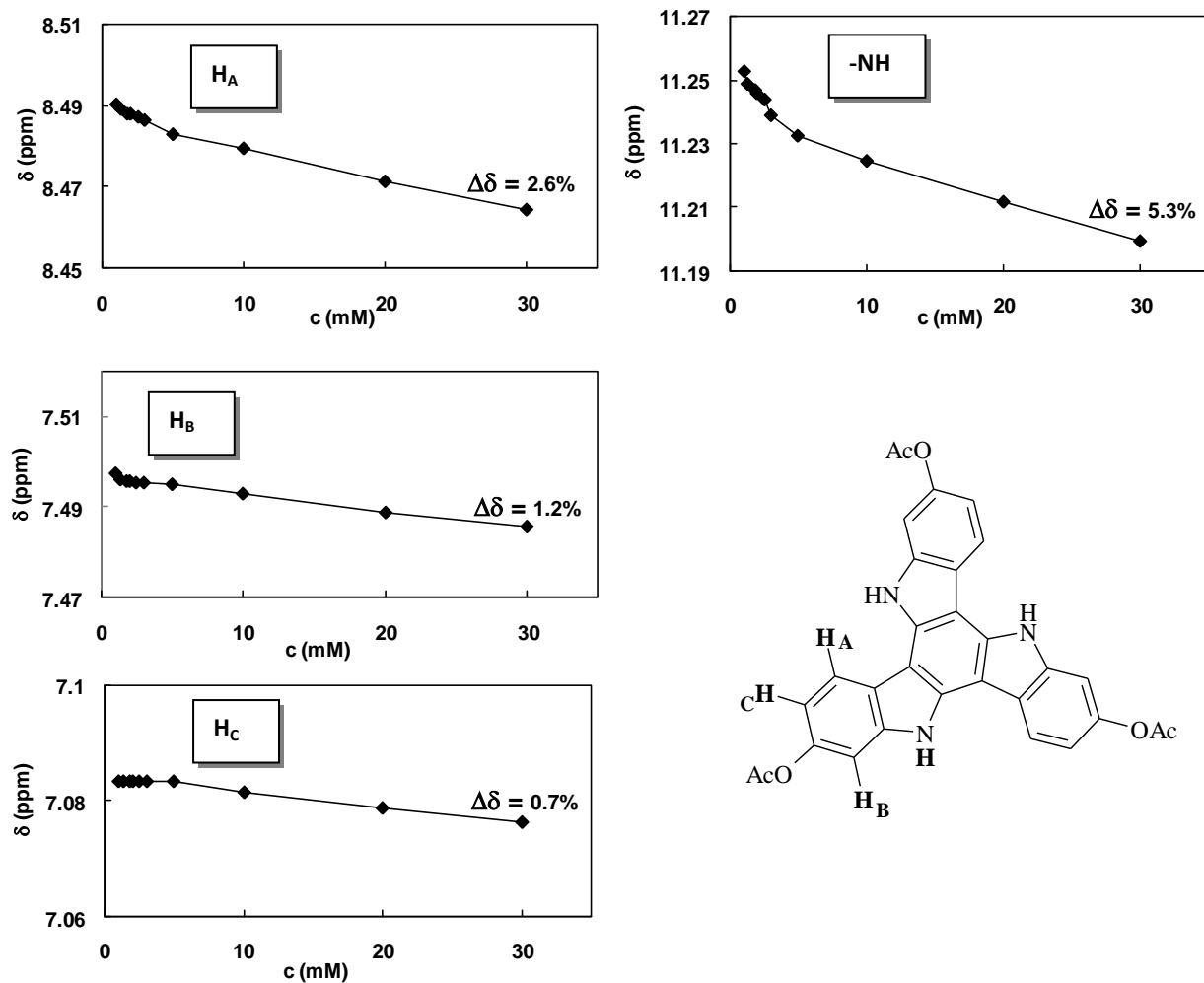


Figure 1.1.23. Shift of the aromatic and methylenic proton resonances of *TAT-Ac* with the concentration.

On the contrary, the ^1H NMR of *ATAT-Ac* (Figure 1.1.24, low field expansion) showed a significant upfield shift of the -NH protons with a $\Delta\delta$ of 14.1%, 22.0% and 28.9%, respectively, and a less pronounced shift of the aromatic H_A protons ($\Delta\delta = 11.0\%$, 10.9% and 4.0%); no appreciable shift was observed for the other aromatic protons (Figure 1.1.25).

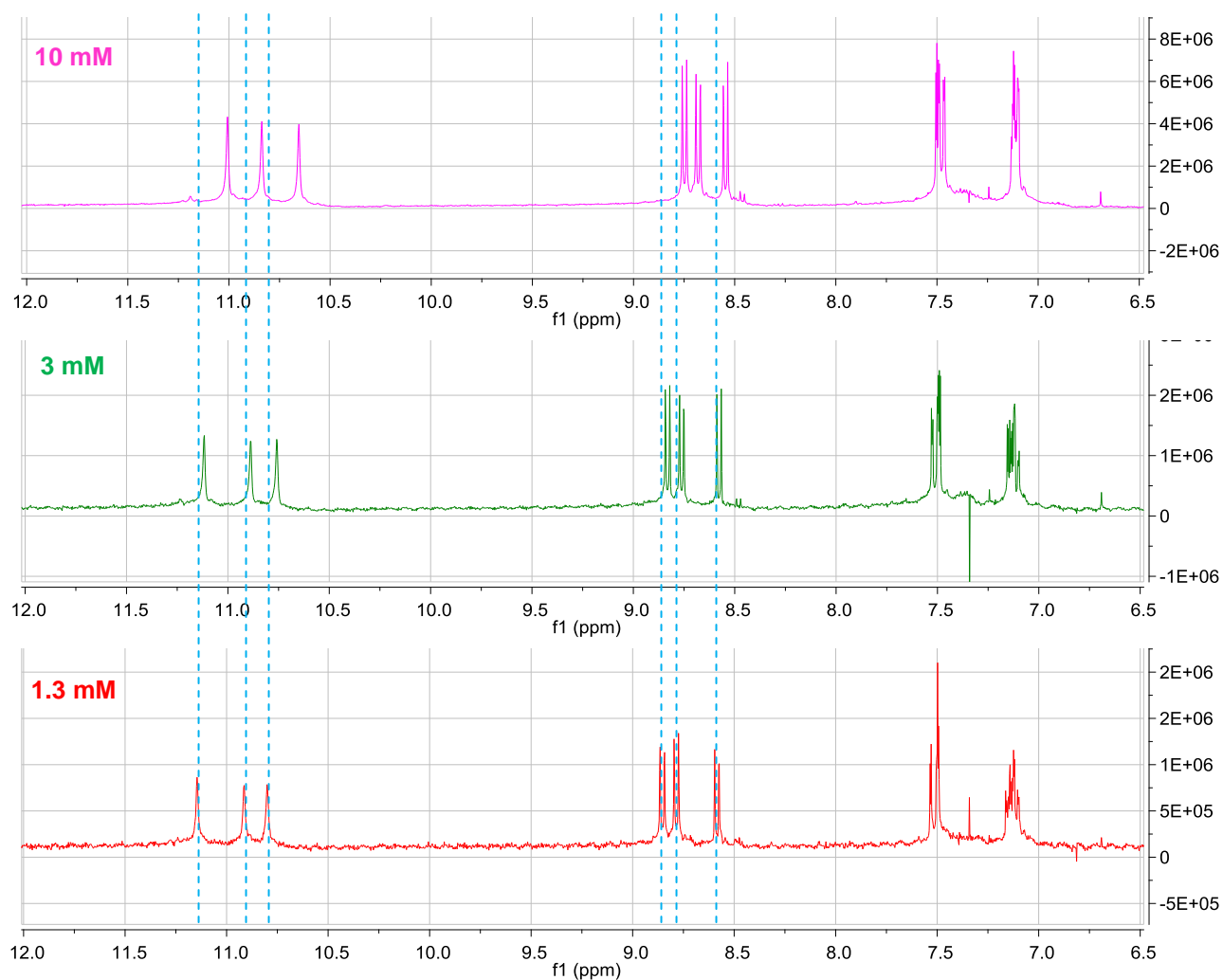


Figure 1.1.24. ¹H NMR spectra (expanded region) of *ATAT-Acat* different concentrations: 1.3 mM (red trace), 3 mM (green trace) and 10 mM (magenta trace).

The marked tendency of compound *ATAT-Ac* to form dimeric aggregate in solution was also supported by the LDI spectrum showing a peak at $m/z \approx 1039$ relative to the pseudomolecular ion of the dimer $[2M + H]^+$.

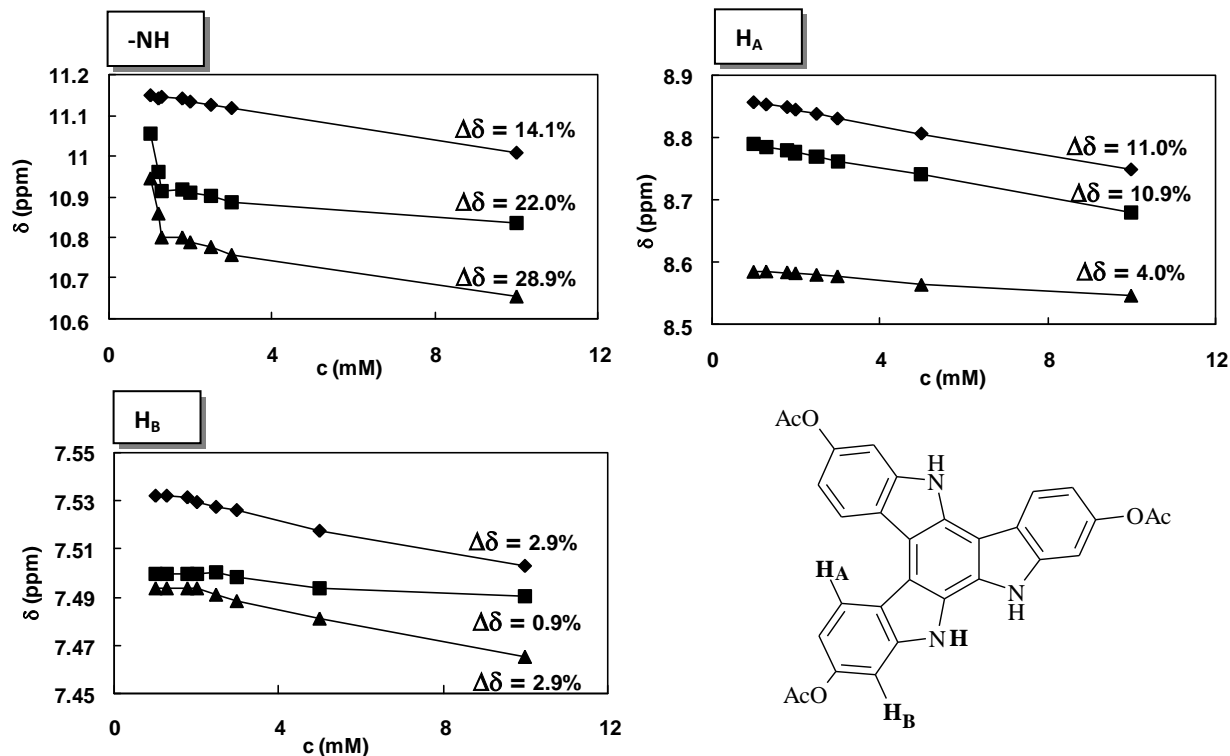


Figure 1.1.25. Shift of the aromatic and methylenic proton resonances of *ATAT-Ac* with the concentration.

○ TATs AS EMITTING LAYER IN OLED DEVICES

One of the main applications of symmetrical TATs reported in the literature is as the organic emitting layer in OLED devices,²³ whereas no applications have been reported for the asymmetric isomers. In all the reported cases, to improve the quite low photo- and electroluminescence, the symmetrical TAT core has been functionalized with polycarbazole or polyfluorene arms to generate more efficient star-shaped structures. On the basis of the optoelectronic properties described above, the potential of the asymmetric TAT core as the lightemitting layer in OLED devices was investigated. To this aim, *ATAT-OMe* and *ATAT-Ac* were selected, together with the symmetrical isomers *TAT-OMe* and *TAT-Ac* taken as references.

First experiments were addressed to the realization of good quality thin films suitable for the fabrication of OLED devices. Best results were obtained by spin coating solutions of TATs with a concentration of 10 mg/mL in chlorobenzene.

TAT film morphology was investigated by atomic force microscopy (AFM). Interestingly, TATs of the same symmetry exhibited a similar behavior: while asymmetrical TATs gave

homogeneous films decorated by peculiar ribbon-like features (Figure 1.1.26a), films from symmetrical TATs proved a lower degree of homogeneity showing the presence of large crystallites with typical height of 700-800 nm and side lengths ranging between 5 and 10 μm , with the regions separating the crystallites partially occupied by a very thin layer (few tens of nm) without any special morphological features (Figure 1.1.26).

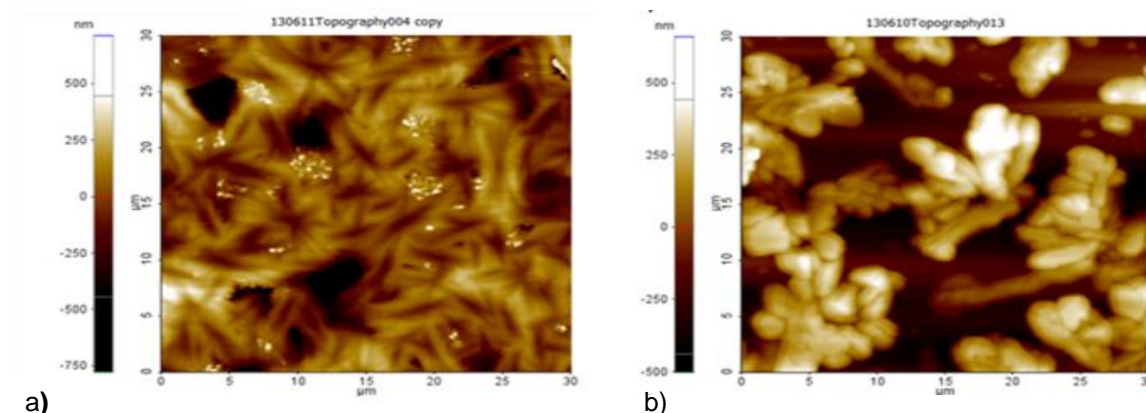


Figure 1.1.26. AFM images (size $30 \times 30 \mu\text{m}^2$) of films deposited from selected TATs: A) *ATAT_OMe*; B) *TAT_OMe*.

Preliminary electrical tests carried out to estimate the charge carrier mobility and the conductivity of the selected TATs showed that the compounds can act as modest hole transporting semiconductors.

In order to investigate the electroluminescent properties of the synthesized TATs, OLEDs with a multilayer structure were fabricated with a device configuration of ITO/PEDOT:PSS/EL/BCP/Alq₃/Ca/Al (Figure 1.1.27 left).

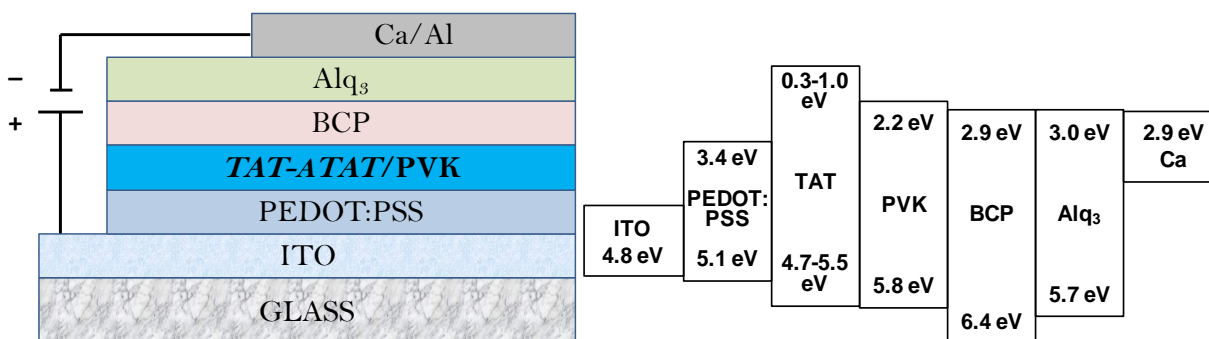


Figure 1.1.27. Tested OLED structure (left) and energy level diagram (right). Thicknesses of layers are: ITO 200 nm, PEDOT:PSS 40 nm, organic emitting layer 20 nm, BCP 9 nm, Alq₃ 10 nm, calcium 20 nm and aluminum 80 nm.

Glass substrates, coated with ITO, were cleaned by sonication in deionized water and organic solvents. An UV-O₃ treatment of ITO surface was employed, then an aqueous solution of PEDOT:PSS was spin-coated onto the substrates to a thickness of 40 nm and subsequently annealed at 130°C for 1.5 h in vacuum. The organic light emitting layer was deposited by spin-coating, whereas thin layers of 2,9-dimethyl-4,7-diphenyl-1,10-phenanthroline (BCP) and tris-(8-hydroxyquinoline)aluminum (Alq₃) were thermally deposited by vacuum evaporation as well as calcium and aluminum thin layers. The electroluminescence and electro-optical behavior of the prepared OLEDs were studied. First experiments carried out by using the TAT alone as emitting layer proved unsuccessful probably because the high energy gap between TAT and BCP LUMOs prevented a good electronic injection from the cathodes (Figure 1.1.27a). For this reason, in a second group of experiments the emitting layer was obtained by spin-coating a blend of the proper TAT and poly-9-vinylcarbazole (PVK) (5% w/w) in chlorobenzene. Key performance values for the OLED devices obtained from *ATAT_OMe*, *TAT_OMe*, *ATAT_Ac* and *TAT_Ac* and from PVK alone taken as reference are listed in Table 1.1.4. Only the device obtained from *ATAT_OMe* showed an electroluminescence at 423 nm ascribable to TAT emission, whereas the other three devices showed an electroluminescence at values closer to that exhibited by PVK alone (401 nm). Even though the performances of the *ATAT_OMe*-based device proved not so high (maximum luminance: 59.3 cdm⁻² at 12 V; power efficacy: 0.03 lmW⁻¹), this is the first case in which the asymmetric isomer shows better performances than the symmetric isomer as a light emitting material. This result opens new perspectives toward the development of new organic light emitting materials based on an asymmetric TAT central core with higher performance than those reported in the literature to date.

Table 1.1.4. Performances of the TAT-based OLED devices.^[a]

	OLED device				
	<i>TAT_OMe</i>	<i>ATAT_OMe</i>	<i>TAT_Ac</i>	<i>ATAT_Ac</i>	PVK
Electro luminescence (λ_{\max} , nm) ^[b]	406	423	396	401	401
Luminance (cd/m ²) ^[c]	14.00	11.38	14.60	34.00	47.23
Maximum efficiency (cd/A)	0.03	0.07	0.02	0.04	0.07
Maximum power efficacy (lm/W)	0.02	0.03	0.01	0.02	0.03
CIE (<i>x,y</i>) ^[d]	(0.27, 0.28)	(0.26, 0.28)	(0.28, 0.27)	(0.26, 0.27)	(0.25, 0.26)

[a] Each TAT was blended into PVK (5% w/w). [b] Taken at 5 mA. [c] Taken at 9 V. [d] The CIE coordinates are in accordance with the initial EL spectra under a current of 5 mA.

Table 1.1.5. Effects of the *ATAT_OMe*:PVK ratios on the performances of the TAT-based OLED devices.

Emitting layer: <i>ATAT_OMe</i> (% in PVK)	Electro- luminescence (λ_{\max} , nm) ^[a]	Luminance (cd/m ²) ^[b]	Maximum power efficiency (lm/W)
10	434	17.00	0.01
5	423	11.38	0.03
2	410	16.64	0.02
0	401	47.23	0.03

[a] Taken at 5 mA. [b] Taken at 9 V.

Worthy of note is also the case of the *ATAT_Ac*-based OLED device, which displayed no TAT-induced electroluminescence even though the *ATAT_Ac*-PVK LUMO gap proved lower than that in the *ATAT_OMe* device; this may be ascribed to the presence of the long alkyl chains in *ATAT_OMe* probably favoring a better interaction between TAT and PVK and then charge injection throughout the blend. Finally, to get some insight into the role of the TAT/PVK ratio on the characteristic of the device, three different OLEDs were fabricated with a 2%, 5% and 10% blend of *ATAT_OMe* in PVK. As shown in Figure 1.1.38 and Table 1.1.5, the electroluminescence of the device shifts from 401 to 434 nm upon an increase in *ATAT_OMe* content, whereas the luminance and the maximum power efficiency remains almost unaffected, confirming that *ATAT_OMe* can be used as a host material doping the PVK.

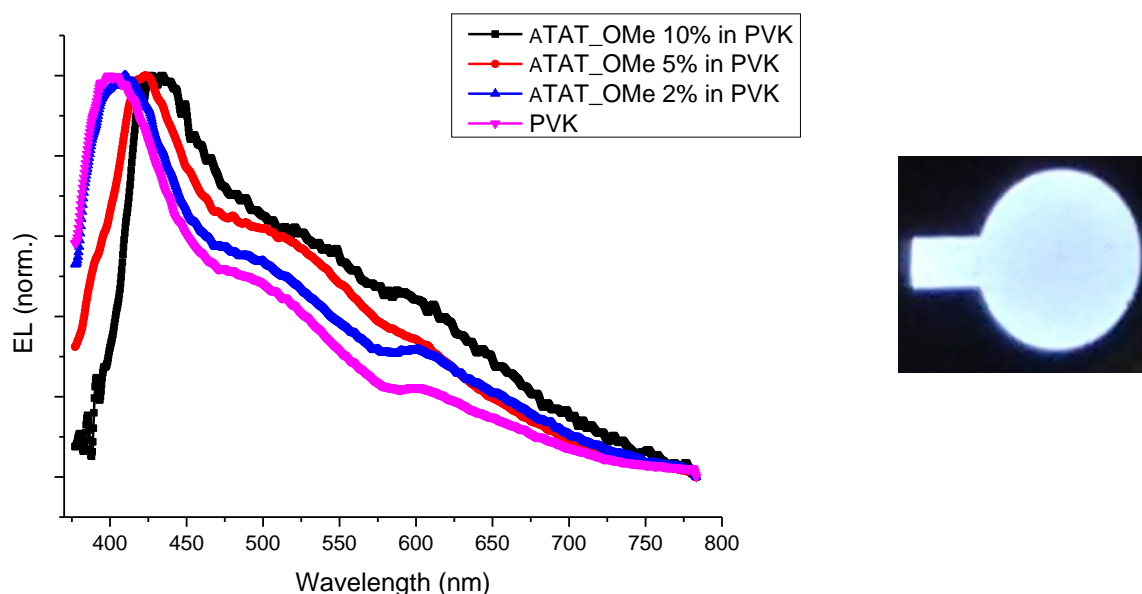


Figure 1.1.28. Normalized electroluminescence (EL) spectra taken at 5 mA of OLED devices fabricated with blends at different *ATAT_OMe*:PVK ratios as emitting layer (left), biased OLED with *ATAT_OMe* (right).

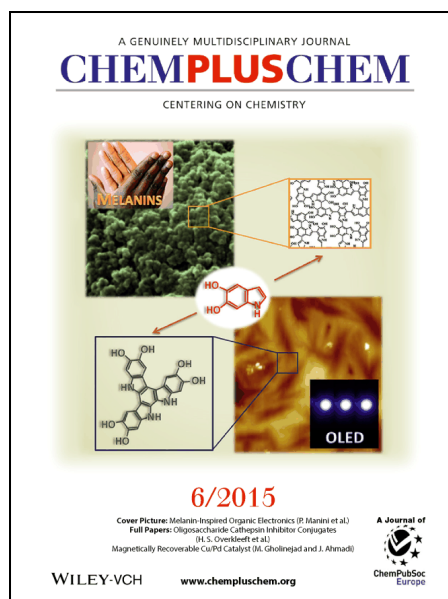
~CONCLUSIONS~

In conclusion, this chapter reports for the first time how the chemical versatility of melanin-related (di)hydroxyindoles can be used to tune the opto-electronic properties and the applications of materials thereof. While at neutral pH the formation of eumelanins is expected, a black biopolymer able to capture the light and to convert it into electrical current (e.g. in photovoltaic devices), at acidic pH the formation of triazatruxenes is observed, a peculiar cyclic triindole derivative able to emit blue light under electrical stimulation (e.g. in OLED devices). The investigation of the opto-electronic properties of the melanin-inspired TATs, supported also by theoretical calculations, denoted that the asymmetrical isomers are more suitable than the symmetrical ones for applications in organic electronics due to: a) higher fluorescence quantum efficiencies; b) lower HOMO-LUMO gaps; c) better film homogeneity. This hypothesis was confirmed by the luminance exhibited by the OLED devices fabricated with the synthesized TATs, highlighting the potentiality of the asymmetrical skeleton as new central core for light emitting materials.

Further details about results shown in this chapter can be found in the following article:

P. Manini, V. Criscuolo, L. Ricciotti, A. Pezzella, M. Barra, A. Cassinese, O. Crescenzi, M. G. Maglione, P. Tassini, C. Minarini, V. Barone, M. d'Ischia, "Melanin-Inspired Organic Electronics: Electroluminescence in Asymmetric Triazatruxenes", *ChemPlusChem*, **2015**, *80*, 919

–927



~EXPERIMENTAL SECTION~

○ MATERIALS AND METHODS

All commercially available reagents were used as received and all the solvents were analytical grade quality. Anhydrous solvents were purchased from commercial sources and withdrawn from the container by syringe, under a slight positive pressure of argon. 5,6-Dibenzoyloxyindole was prepared according to a reported procedure.^[4d] UV-vis and fluorescence spectra were recorded with a Jasco V-560 and a Jasco FP-750 instruments. The fluorescence quantum yield (Φ) was determined using quinine sulfate as the standard ($\Phi = 0.546$ in H_2SO_4).^[25] Thermogravimetric analyses (TGA) were performed by a TA Instrument SDT2960. The thermographs were obtained with a heating rate of 10 °C/min using ≈ 10 mg of the powdered sample under a nitrogen flow. Thin films were deposited with a spin coater Laurell WS-650MZ-23NPP/LITE on the appropriate substrate from hot concentrated chlorobenzene or pyridine solutions (30 mg/mL) after filtering through a 0.2 μm Whatman membrane, using the following speed program: 800 rpm for 60" and 1500 rpm for 90". NMR spectra were recorded with a Varian Gemini 200 MHz and Bruker DRX-400 MHz instruments. ^1H and ^{13}C NMR spectra were recorded in $(\text{CD}_3)_2\text{CO}$, $\text{DMSO}-d_6$ and $\text{pyridine}-d_5$; J values are given in Hz. Resonances with identical superscript may be interchanged. ^1H , ^1H COSY, ^1H , ^{13}C HSQC, ^1H , ^{13}C HMBC and ROESY experiments were run at 400.1 MHz using standard pulse programs. Atmospheric pressure laser desorption mass spectrometry (AP-LDI) analyses were performed on an Agilent 1100 Series MSD Ion Trap. Analytical and preparative TLC analyses were performed on F_{254} silica gel plates (0.25 and 0.5 mm, respectively). TLC plates were visualized using a UV lamp ($\lambda = 254$ nm) and a fluorescence lamp ($\lambda = 366$ nm). Liquid chromatography was performed on silica gel (60-230 mesh). The film morphological characterization was performed in air by using a XE100 Atomic Force Microscope by the PARK SYSTEMS company, working in true non-contact mode with amplitude regulation. For the image acquisition, Silicon doped cantilevers (resonance frequency of about 310 KHz) provided by NanosensorTM were employed.

○ SYNTHESIS OF TATs

- Synthesis of TAT_OMe and ATAT_OMe

A solution of 5,6-dimethoxyindole (500 mg, 2.8 mmol) in acetonitrile is suspended in 0.1 M phosphate buffer, pH 3 (140 mL), and treated with sodium persulfate (980 mg, 4.2 mmol) under stirring. After 5 minutes the reaction mixture is treated with sodium dithionite and centrifuged (7000 min⁻¹ for 10 min) to give a precipitate that is washed with water and dried under reduced pressure. This latter is identified as the intimate mixture of 2,3,7,8,12,13-hexamethoxydiindole[3,2-a:3',2'-c]carbazole and 2,3,6,7,11,12-hexamethoxydiindole[2,3-a:2',3'-c]carbazole by chromatographic analysis (CHCl₃/MeOH 95:5) with authentic standards and by comparison of NMR data with those reported in the literature (450 mg, 92% total yield).^[5] The mixture of hexamethoxy-TATs (440 mg, 0.84 mmol) is dissolved in dry DMSO (3.5 mL) under an argon atmosphere and treated under vigorous stirring with KOH (560 mg, 8.4 mmol) at 70 °C; after 1 h 1-bromoundecane (1 mL, 3.78 mmol) is added. After 18 h the reaction mixture, taken up in ethyl acetate, gives a precipitate that is isolated by centrifugation at 7000 min⁻¹ for 10 min. The precipitate is washed with ethyl acetate and dried under reduced pressure, whereas the supernatant is extracted with ethyl acetate and 1.5 M HCl. The organic layer is dried over anhydrous sodium sulfate and evaporated under reduced pressure. Both the precipitate and the residue are fractionated on silica gel (eluent: gradient from pure petroleum ether to petroleum ether/ethyl acetate 8:2) to give *TAT_OMe* (298 mg, 36% overall yield, R_f = 0.63 eluent petroleum ether/ethyl acetate 7:3) and *ATAT_OMe* (249 mg, 30 % overall yield, R_f = 0.59 eluant petroleum ether/ethyl acetate 7:3).

TAT_OMe: ¹H NMR (400 MHz, (CD₃)₂CO) δ ppm: 7.85 (1H × 3, s, H4, H9, H14), 7.37 (1H × 3, s, H1, H6, H11), 4.97 (2H × 3, t, J = 7.2 Hz, -NCH₂), 4.01 (3H × 3, s, -OCH₃), 4.00 (3H × 3, s, -OCH₃), 1.83 (2H × 3, m, -NCH₂CH₂), 1.0-1.3 (2H × 9, m, CH₂), 0.84 (3H × 3, t, J = 7.2 Hz, CH₃); ¹³C NMR (50 MHz (CD₃)₂CO) δ ppm: 148.0 (C3, C8, C13), 145.1 (C2, C7, C12), 137.6a (C1a, C6a, C11a), 137.0a (C15a, C5a, C10a), 116.0 (C4a, C9a, C14a), 106.9 (C4, C9, C14), 104.0 (C4b, C9b, C14b), 95.7 (C1, C6, C11), 57.5 (OCH₃ × 3), 56.4 (OCH₃ × 3), 46.8 (-NCH₂ × 3), 31.8 (CH₂ × 3), 30-28 (CH₂ × 18), 26.0 (CH₂ × 3), 21.9 (CH₂ × 3), 14.3 (CH₃ × 3); AP-LDI MS m/z 988 [M+H]⁺.

ATAT_OMe: ¹H NMR (400 MHz, (CD₃)₂CO) δ ppm: 8.33 (1H, s, H4), 8.30 (1H, s, H5), 7.93 (1H, s, H10), 7.43 (2H, s, H1, H13), 7.38 (1H, s, H8), 4.99 (2H, t, J = 7.2 Hz, -NCH₂), 4.77 (2H, t, J = 7.2 Hz, -NCH₂), 4.67 (2H, t, J = 7.2 Hz, -NCH₂), 4.12 (3H, s, -OCH₃), 4.11 (3H, s, -OCH₃), 4.03 (3H, s, -OCH₃), 4.02 (3H × 2, s, -OCH₃), 4.01 (3H, s, -OCH₃), 1.89 (2H, m, -NCH₂CH₂), 1.4–0.6 (61H, m, CH₂, CH₃); ¹³C NMR (100 MHz, (CD₃)₂CO) δ ppm: 148.7 (C3, C12), 147.8 (C6), 145.0 (C2), 144.9 (C11), 144.4 (C7), 139.6 (C1a), 138.9 (C13a), 137.3a (C9a), 136.4 (C8a), 133.0a (C14a), 131.2a (C15a), 119.3 (C4a), 118.0 (C4b), 117.4 (C10a), 117.0 (C5a), 112.0 (C5b), 109.5 (C9b), 107.4 (C10), 105.8 (C4), 105.2 (C5), 97.2b (C1), 97.0b (C13), 95.3 (C8), 56.6 (-OCH₃), 56.0 (-OCH₃), 55.8 (-OCH₃), 55.7 (-OCH₃), 55.6 (-OCH₃ × 2), 47.7 (-NCH₂), 47.3 (-NCH₂), 46.5 (-NCH₂), 31.7 (CH₂ × 3), 29.8 (CH₂ × 3), 30–28 (CH₂ × 13), 27.1 (CH₂), 26.7 (CH₂), 26.3 (CH₂), 26.0 (CH₂), 25.8 (CH₂), 22.3 (CH₂ × 3), 13.4 (CH₃ × 3); AP-LDI MS m/z 988 [M+H]⁺.

- Synthesis of TAT_OBnNH and ATAT_OBnNH

A solution of 5,6-dibenzyloxyindole (300 mg, 0.91 mmol) in acetonitrile is suspended in 0.1 M phosphate buffer, pH 3 (91.2 mL), and treated with sodium persulfate (1.1 g, 4.56 mmol) under stirring. After 30 minutes the reaction mixture is treated with sodium dithionite, extracted with ethyl acetate and water and the organic layers are fractionated on silica gel (eluent: gradient from pure petroleum ether to petroleum ether/acetone 8:2) to give 2,3,7,8,12,13-hexabenzoyloxydiindole[3,2-a:3',2'-c]carbazole (TAT_1b) (90 mg, 30%, R_f = 0.48 eluent petroleum ether/acetone 6:4) and 2,3,6,7,11,12-hexabenzoyloxydiindole[2,3-a:2',3'-c]carbazole (ATAT_2b) (74 mg, 25%, R_f = 0.37 eluent petroleum ether/acetone 6:4).

TAT_1b: ¹H NMR (400 MHz, (CD₃)₂CO) δ ppm: 10.92 (3H, s, H5, H10, H15), 8.27 (3H, s, H4, H9, H14), 7.63 (2H × 3, dd, J = 8.0, 1.8 Hz, Ph), 7.57 (2H × 3, dd, J = 8.0, 1.8 Hz, Ph), 7.38–7.44 (12H, m, Ph), 7.34–7.37 (6H, m, Ph), 7.33 (3H, s, H1, H6, H11), 5.29 (2H × 6, s, -OCH₂); ¹³C NMR (50 MHz, (CD₃)₂CO) δ ppm: 147.3 (C2, C7, C12), 144.6 (C3, C8, C13), 138.5 (3C, Ph), 138.2 (3C, Ph), 134.3a (C1a, C6a, 10a), 133.4a (3C, C5a, C10a, C15a), 128.4 (6C, Ph), 128.3 (6C, Ph), 127.9 (6C, Ph), 127.6 (6C, Ph), 127.5 (6C, Ph), 116.5 (C4a, C9a, C14a), 107.7 (C4, C9, C14), 101.8 (C4b, C9b, C14b), 98.6 (C1, C6, C11), 72.9 (-OCH₂ × 3), 71.5 (-OCH₂ × 3); AP-LDI MS m/z 982 [M+H]⁺.

ATAT_2b: ^1H NMR (400 MHz, DMSO- d_6) δ ppm: 11.50 (1H, s, H9), 11.01 (1H, s, H14), 10.94 (1H, s, H15), 8.41 (1H, s, H10), 8.28 (1H, s, H4), 8.26 (1H, s, H5), 7.65-7.51 (12H, m, Ph), 7.50-7.40 (14H, m, Ph, H1, H13), 7.38-7.32 (7H, m, Ph, H8), 5.40 (2H, s, $-\text{OCH}_2$), 5.39 (2H, s, $-\text{OCH}_2$), 5.35 (2H, s, $-\text{OCH}_2$), 5.34 (2H, s, $-\text{OCH}_2$), 5.32 (2H, s, $-\text{OCH}_2$), 5.29 (2H, s, $-\text{OCH}_2$); ^{13}C NMR (50MHz, DMSO- d_6) δ ppm: 147.3 (C2, C12), 146.1 (C7), 143.6 (C11), 142.6 (C3, C6), 137.7 (3C, Ph), 137.6 (3C, Ph), 134.1 (C1a), 133.9 (C8a), 133.6 (C13a), 127-129 (30C, Ph, C9a), 125.2 (C14a), 121.6 (C15a), 116.3 (C4a, C5a), 115.3 (C10a), 112.9 (C4b), 108.5 (C4), 108.0 (2C, C5, C5b), 107.6 (C10), 105.4 (C9b), 97.7 (3C, C1, C8, C13), 72.1 ($-\text{OCH}_2$), 71.7 (2C, $-\text{OCH}_2$), 70.5 (3C, $-\text{OCH}_2$); AP-LDI MS m/z 982 $[\text{M}+\text{H}]^+$.

- Synthesis of *TAT_OBn* and *ATAT_OBn*

The appropriate hexabenzoyloxy TAT (90 mg, 0.092 mmol) is dissolved in dry DMSO (370 μL) under an argon atmosphere and treated under vigorous stirring with KOH (52 mg, 0.92 mmol) at 70 $^\circ\text{C}$; after 1 h 1-bromoundecane (92 μL , 0.41 mmol) is added. After 18 h the reaction mixture, taken up in ethyl acetate, gives a precipitate that is isolated by centrifugation at 7000 min^{-1} for 10 min. The precipitate is washed with ethyl acetate and dried under reduced pressure to give pure 1c or 2c; the supernatant is extracted with ethyl acetate and 1.5 M HCl and the organic layer is dried over anhydrous sodium sulfate, evaporated under reduced pressure and fractionated on PLC (eluent: cyclohexane/acetone 7:3). This procedure afforded pure *TAT_OBn* (128 mg, 96% overall yield, $R_f = 0.82$ eluent cyclohexane/acetone 7:3) or *ATAT_OBn* (103 mg, 79% overall yield, $R_f = 0.79$ eluent: cyclohexane/acetone 7:3).

TAT_OBn: ^1H NMR (400 MHz, Pyridine- d_5) δ ppm: 8.30 (1H \times 3, s, H-4, H-9, H-14), 7.81 (2H \times 3, dd, $J = 8.0, 2.1$ Hz, Ph), 7.76 (2H \times 3, dd, $J = 8.0, 2.1$ Hz, Ph), 7.73 (1H \times 3, s, H-1, H-6, H11), 7.4-7.5 (18 H, m, Ph), 5.58 (2H \times 3, s, $-\text{OCH}_2$), 5.57 (2H \times 3, s, $-\text{OCH}_2$), 4.98 (2H \times 3, m, $-\text{NCH}_2$), 1.94 (2H \times 3, m, $-\text{CH}_2$), 1.0-1.4 (48H, m, $-\text{CH}_2$) 0.86 (3H \times 3, t, $J = 7.2$ Hz, $-\text{CH}_3$); ^{13}C NMR (100 MHz, Pyridine- d_5) δ ppm: 147.9 (C2, C7, C12), 144.3 (C3, C8, C13), 138.5 (3C, Ph), 138.0 (3C, Ph), 137.9a (C1a, C6a, 10a), 137.5a (3C, C5a, C10a, C15a), 128.7 (6C, Ph), 128.6 (6C, Ph), 128.0 (6C, Ph), 127.9 (6C, Ph), 127.8 (6C, Ph), 117.2 (C4a, C9a, C14a), 111.3 (C4, C9, C14), 104.3 (C4b, C9b, C14b), 98.8 (C1, C6, C11), 73.6 ($-\text{OCH}_2 \times 3$), 71.8 ($-\text{OCH}_2 \times 3$), 47.11 ($-\text{NCH}_2$), 31.8 ($\text{CH}_2 \times 3$), 30.2 ($\text{CH}_2 \times 3$), 29.7 ($\text{CH}_2 \times 3$), 29.5 ($\text{CH}_2 \times 3$), 29.4 ($\text{CH}_2 \times 3$), 29.3

(CH₂ × 3), 29.2 (CH₂ × 3), 26.7 (CH₂ × 3), 22.6 (CH₂ × 3), 14.0 (CH₃ × 3); AP-LDI MS m/z 1444 [M+H]⁺.

ATAT_OBn: ¹H NMR (400 MHz, Pyridine-d₅) δ ppm: 8.99 (1H, s, H-10), 8.97 (1H, s, H-5), 8.37, (1H, s, H-4), 7.86 (1H, s, H-13), 7.85 (1H, s, H-1), 7.7-7.8 (13H, m, Ph, H-8), 7.3-7.5 (18H, m, Ph), 5.66 (2H, s, -OCH₂), 5.65 (2H, s, -OCH₂), 5.57 (2H × 2, s, -OCH₂), 5.56 (2H, s, -OCH₂), 5.00 (2H, t, J = 6.8 Hz, -NCH₂), 4.93 (2H, t, J = 6.8 Hz, -NCH₂), 4.83 (2H, t, J = 6.8 Hz, -NCH₂), 1.48 (2H, m, -CH₂), 0.8-1.4 (61H, m); ¹³C NMR (100 MHz, Pyridine-d₅) δ ppm: 148.7 (2C, C3, C12), 147.8 (C7), 144.6 (2C, C2, C11), 143.9 (C6), 140.9 (C13a), 139.7 (C1a), 137.4 (C8a), 129.1 (C9a), 126.3 (C14a), 121.8 (C15a), 120.1 (C10a), 118.1 (C9b), 117.8 (2C, C5a, C4a), 112.1 (C5b), 112.0 (C4), 110.2 (C10), 110.1 (C5), 109.8 (C4b), 101.3 (C13), 101.2 (C1), 99.0 (C8), 74.8 (-OCH₂ × 2), 73.3 (-OCH₂ × 2), 72.5 (-OCH₂ × 2), 49.3 (-NCH₂), 48.2 (-NCH₂), 47.5 (-NCH₂), 31.8 (CH₂ × 3), 30.2 (CH₂ × 3), 29.7 (CH₂ × 3), 29.5 (CH₂ × 3), 29.4 (CH₂ × 3), 29.3 (CH₂ × 3), 29.2 (CH₂ × 3), 26.7 (CH₂ × 3), 22.6 (CH₂ × 3), 14.0 (CH₃ × 3); AP-LDI MS m/z 1444 [M+H]⁺.

- Synthesis of *TAT_Ac* and *ATAT_Ac*

A solution of 6-hydroxyindole (600 mg, 4.5 mmol) in acetonitrile is suspended in 0.1 M phosphate buffer, pH 3 (240 mL), and treated with sodium persulfate (1.6 g, 6.6 mmol) under stirring. The mixture after 5 minutes is treated with sodium dithionite and centrifuged (7000 min⁻¹ for 10 min) to give a precipitate that is washed with water, dried under reduced pressure and acetylated with acetic anhydride (1 mL) and pyridine (50 μL). After 18 h the mixture is evaporated under reduced pressure and fractionated on silica gel (eluant: gradient from hexane/ethyl acetate 1:1 to hexane/ethyl acetate 4:6) to give 1d (120 mg, 15%, R_f = 0.70 eluant hexane/ethyl acetate 3:7) and 2d (240 mg, 30%, R_f = 0.46 eluant hexane/ethyl acetate 3:7).

TAT_Ac: ¹H NMR (400 MHz, (CD₃)₂CO) δ ppm: 11.27 (3H, s, H5, H10, H15), 8.49 (3H, d, J = 8.4 Hz, H4, H9, H14), 7.49 (3H, d, J = 2.0 Hz, H1, H6, H11), 7.09 (3H, dd, J = 8.4, 2.0 Hz, H3, H8, H13), 2.34 (3H × 3, s, -COCH₃); ¹³C NMR (50 MHz, (CD₃)₂CO) δ ppm: 169.4 (3C, CO), 147.7 (3C, C2, C7, C12), 139.4 (3C, C1a, C6a, C11a), 134.8 (3C, C5a, C10a, C15a), 120.6 (3C, C4a, C9a, C14a), 119.8 (3C, C4, C9, C14), 113.8 (3C, C3, C8, C13), 104.7 (3C, C1, C6, C11), 101.5 (3C, C4b, C9b, C14b), 20.4 (3C, COCH₃); AP-LDI MS m/z 520 [M+H]⁺, m/z 477 [M-CH₃CO]⁺, m/z 434 [M-2CH₃CO]⁺, m/z 391 [M-3CH₃CO]⁺.

ATAT_Ac: ^1H NMR (400 MHz, $(\text{CD}_3)_2\text{CO}$) δ ppm: 11.01 (1H, s, H9), 10.84 (1H, s, H14), 10.66 (1H, s, H15), 8.75 (1H, d, $J = 8.4$ Hz, H4), 8.68 (1H, d, $J = 8.4$ Hz, H5), 8.54 (1H, d, $J = 8.4$ Hz, H10), 7.50 (1H, d, $J = 2.0$ Hz, H8), 7.49 (1H, d, $J = 2.0$ Hz, H13), 7.46 (1H, d, $J = 2.0$ Hz, H1), 7.09-7.14 (3H, m, H3, H6, H11), 2.36 (3H \times 2, s, $-\text{COCH}_3$), 2.34 (3H, s, $-\text{COCH}_3$); ^{13}C NMR (50 MHz, $(\text{CD}_3)_2\text{CO}$) δ ppm: 169.8 (2C, CO), 169.4 (CO), 148.5a (C2), 148.4a (C12), 147.4 (C7), 140.0 (C1a), 139.7 (2C, C13a, C8a), 130.7 (C9a), 126.9 (C14a), 123.0 (C15a), 122.9 (C4), 121.8b (3C, C4a, C10a, C5), 120.9 (C10), 120.7b (C5a), 114.6 (C4b), 113.9c (C11), 113.1c (C3), 112.9c (C6), 109.2 (C5b), 106.2 (C9b), 104.9d (C1), 104.7d (C8), 104.5d (C13), 20.5 (3C, $-\text{COCH}_3$); AP-LDI MS m/z 520 $[\text{M}+\text{H}]^+$, m/z 477 $[\text{M}-\text{COCH}_3]^+$, m/z 434 $[\text{M}-2\text{COCH}_3]^+$, m/z 391 $[\text{M}-3\text{COCH}_3]^+$.

o COMPUTATIONAL INVESTIGATION

All calculations were performed with the Gaussian package of programs. All structures were geometry optimized at the DFT level, with a hybrid functional (PBE0) and a reasonably large basis set $[\text{6-31+G(d,p)}]$. For each species, different conformations were explored. Computations were performed either in vacuo, or by adoption of a polarizable continuum medium (PCM)[26] to account for the influence of the condensed-phase environment. In view of the faster convergence, a scaled van der Waals cavity based on universal force field (UFF) radii[27] was used, and polarization charges were modeled by spherical Gaussian functions.[28] Vibrational-rotational contributions to the free energy were also computed (at 298.15 K, in the rigid rotor/harmonic oscillator approximation). UV/Vis spectra of the main species were computed in vacuo or in solution using the time-dependent density functional theory (TD-DFT) approach, with the PBE0 functional and the 6-311++G(2d,2p) basis set. To produce graphs, transitions below 5.6 eV were selected, and an arbitrary Gaussian linewidth of 0.20 eV was imposed; the spectra were finally converted to a wavelength scale.

o DEVICE FABRICATION

OLED devices were fabricated on glass slides coated with 200 nm of sputtered ITO (Indium Tin Oxide) with sheet resistance of 5-15 Ωcm^{-1} . The substrates were cleaned with deionized water and detergent in an ultrasonic bath, and then washed with acetone and 2-propanol. PEDOT:PSS (Clevios P.VP.AL4083) was spin coated onto the substrates to a thickness of 40 nm, after an UV- O_3 treatment, and annealed at 130 $^\circ\text{C}$ for 1.5 hours in vacuum. The emissive

layers were then spin coated from a chlorobenzene solution of PVK:TAT mixture of different ratios. Thin layers of BCP (2,9-Dimethyl-4,7-diphenyl-1,10-phenanthroline) (9 nm) and Alq₃ (Tris-(8-hydroxyquinoline) aluminum) (10 nm) were thermally deposited by vacuum evaporation through a mask at base pressures lower than 5×10^{-7} mbar. A thin layer of calcium (20 nm) as an electron injection cathode and an aluminum layer (80 nm) were also thermally evaporated under ultra-high vacuum. The cathode area defined the active area of 0.07 cm². Devices performances tests were carried out within a glovebox under a nitrogen atmosphere. I-V characteristics were recorded with a Keithley 2400 source meter. EL spectra were recorded by Gooch&Housego OL770 spectroradiometer coupled with an integrating sphere and a camera telescope. The CIE coordinates were calculated using 1931 observer parameters.

REFERENCES

- [1]. Garcia-Frutos, E. M.; Pandey, U. K.; Termine, R.; Omenat, A.; Barberà, J.; Serrano, J. L.; Golemme, A.; Gomez-Lor, B. *Angew. Chem.* **2011**, *50*, 7399-7402.
- [2]. García-Frutos, E. M.; Omenat, A.; Barberà, J.; Serrano, J. L.; Gómez-Lor, B. *J. Mater. Chem.*, **2011**, *21*, 6831-6836.
- [3]. Akira, B.; Ken, O.; Wolfgang, K.; Rigoberto, C. A. *J. Phys. Chem. B* **2004**, *108*, 18949-18955; Parimal, K.; Justin Thomas, K. R.; Jiann, T. L.; Tao, Y. T.; Chien, C. H. *Adv. Funct. Mater.* **2003**, *13*, 445-452.
- [4]. Gallego-Gómez, F.; García-Frutos, E. M.; Villalvilla, J. M.; Quintana, J. A.; Gutierrez-Puebla, E.; Monge, A.; Díaz-García, M. A.; Gómez-Lor, B. *Adv. Funct. Mater.* **2011**, *21*, 738-745
- [5]. Feng, G.-L. et al. *Tetrahedron Lett.* **2006**, *47*, 7089-7092
- [6]. Bura, T.; Leclerc, N.; Fall, S.; L., P.; Heiser, T.; Ziessel, R. *Org. Lett.*, **2011**, *13*, 6030-6033
- [7]. Lai, W. Y. et al. *Macromolecules* **2006**, *39*, 3707-3709
- [8]. Liu, X.; Xu, Y.; Jiang, D. *J. Am. Chem. Soc.* **2012**, *134*, 8738-8741
- [9]. Lei Ji, Qi Fang, Mao-sen Yuan, Zhi-qiang Liu, Yu-xiang Shen, and Hong-feng Chen, *Org. Lett.*, **2010**, *12*, 5192-5195.
- [10]. Jing Luo; Baomin Zhao; Jinjun Shao; Kheng Aik Lim; Hardy Sze On Chan; Chunyan Chi *J. Mater. Chem.* **2009**, *19*, 8327-8334
- [11]. Valentine, R. A.; Whyte, A.; Awaga, K.; Robertson, N. *Tetrahedron Lett.* **2012**, *53*, 657-660
- [12]. Garcia-Frutos, E. M.; Gomez-Lor, B.; Monge, A.; Gutierrez-Puebla, E.; Alkorta, I.; Elguero, J. *Chem. Eur. J.* **2008**, *14*, 8555-8561.
- [13]. (a) Franceschin, M.; Ginnari-Satriani, L.; Alvino, A.; Ortaggi, G.; Bianco, A. *Eur. J. Org. Chem.* **2010**, 134-141; (b) Hiyoshi, H.; Kumagai, H.; Ooi, H. *Pat. Appl. Publ.* WO2005077956, **2005**.
- [14]. Manini, P.; d'Ischia, M.; Milosa, M.; Prota, G. *J. Org. Chem.* **1998**, *63*, 7002-7008.
- [15]. C. Adamo, V. Barone, *J. Chem. Phys.* **1999**, *110*, 6158-6169.
- [16]. J. Tomasi, B. Mennucci, R. Cammi, *Chem. Rev.* **2005**, *105*, 2999-3093.
- [17]. M. J. Frisch et. al. Gaussian 09, Revision A.02, Gaussian, Inc., Wallingford CT, **2009**.
- [18]. a) R. E. Stratmann, G. E. Scuseria, M. J. Frisch, *J. Chem. Phys.* **1998**, *109*, 8218-8224; b) R. Bauernschmitt, R. Ahlrichs, *Chem. Phys. Lett.* **1996**, *256*, 454-464.
- [19]. Meyer, E. A.; Castellano, R. K.; Diederich, F. *Angew. Chem.*, **2003**, *42*, 1210-1250.

- [20]. Warman, J. M.; de Haas, P. M.; Dicker, G.; Grozema, F. C.; Piris, J.; Debije, M. G. *Chem. Mater.* **2004**, *16*, 4600-4609
- [21]. Jonkheijm, P.; Hoeben, F. J. M.; Kleppinger, R.; van Herrikhuyzen, J.; Schenning, A. P. H. J.; Meijer, E. W. *J. Am. Chem. Soc.* **2003**, *125*, 15941-19949
- [22]. García-Frutos, E. M.; Hennrich, G.; Gutierrez, E.; Monge, A. and Gómez-Lor, B. *J. Org. Chem.* **2010**, *75*, 1070-1076
- [23]. a) W. Y. Lai, Q.-Y. He, R. Zhu, Q.-Q. Chen, W. Huang, *Adv. Funct. Mater.* **2008**, *18*, 265-276; b) P. A. Levermore, R. Xia, W. Lai, X. H. Wang, W. Huang, D. D. C. Bradley, *J. Phys. D* **2007**, *40*, 1896-1901; c) R. Zhu, W.-Y. Lai, H.-Y. Wang, N. Yu, W. Wei, B. Peng, W. Huang, L.-T. Hou, J.-B. Peng, Y. Cao, *Appl. Phys. Lett.* **2007**, *90*, 141909.

SECTION 1

CHAPTER 2

DOPAMINE-INSPIRED IRIDIUM(III) COMPLEXES AS RED EMITTERS

~INTRODUCTION~

In the past decades transition metal complexes have been the focus of several research works due to their wide range of applications. Traditionally used as catalysts in different kind of organic reactions (i.e. the first and second generations of Grubbs's catalysts for metathesis reactions), transition metal complexes have found applications also as drugs for the treatment of cancer (i.e. cisplatin), as photosensitizer for the photodynamic therapy, and more recently as bio-sensors, as contrast agents in bio-imaging and as reactive site in polymeric carriers for drug release (Figure 1.2.1).¹

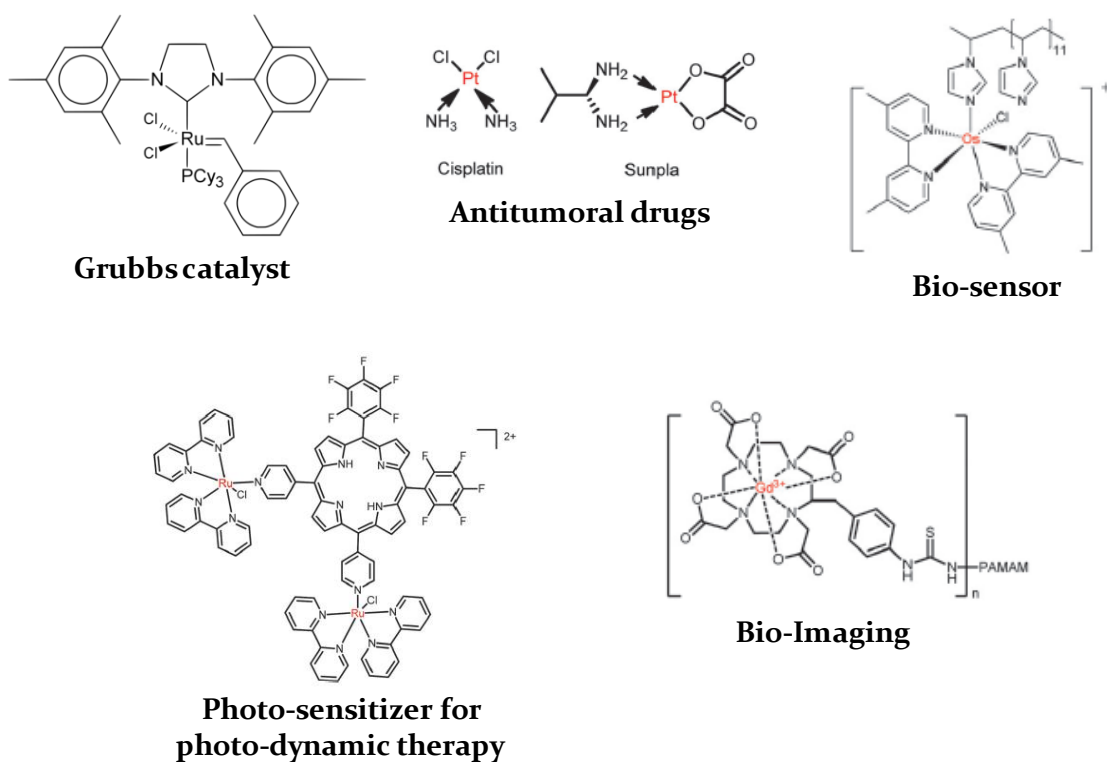


Figure 1.2.1. Examples of transition metal complexes and their applications.

Recently, with the rise of organic electronics, transition metal complexes have been object of new interest in particular for the many applications in the opto-electronic field. This research can be dated back to the '80s with the development of the first complex-based solar cell (copper phthalocyanine, 1986)² and OLED device (tris(8-hydroxyquinolinolato)aluminum(III), Alq₃, 1987)³ (Figure 1.2.2). Nowadays, transition metal complexes are commonly used as emitters in

highly efficient OLED and LEEC devices and as light absorbers in dye-sensitized solar cells for OPV devices.⁴

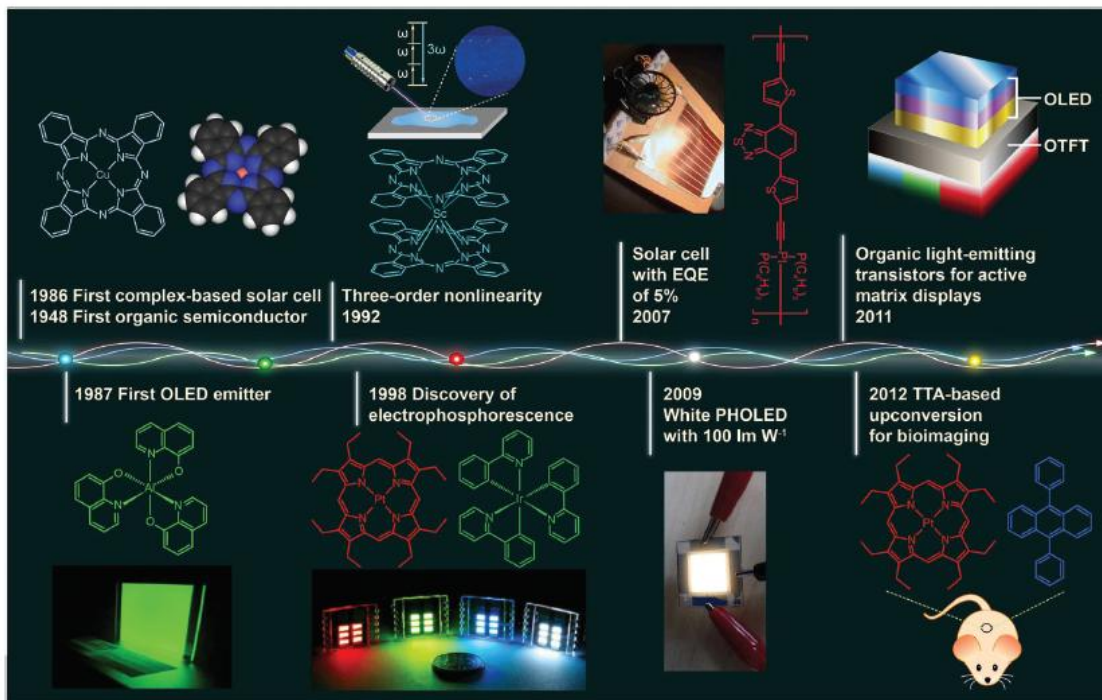


Figure 1.2.2. Milestones in the development of metal complexes in optoelectronics.

The increasing interest paid to the application of the transition metal complexes in emitting devices is due to their ability to fit well many requisites for the fabrication of OLEDs, and first of all the high efficiency obtained in particular by using octahedral $4d^6$ and $5d^6$ metal complexes (i.e. Ru(II), Os(II) and Ir(III)) (Figure 1.2.3).⁵ This is due to the peculiar electronic asset of these metal complexes allowing emission by phosphorescence.

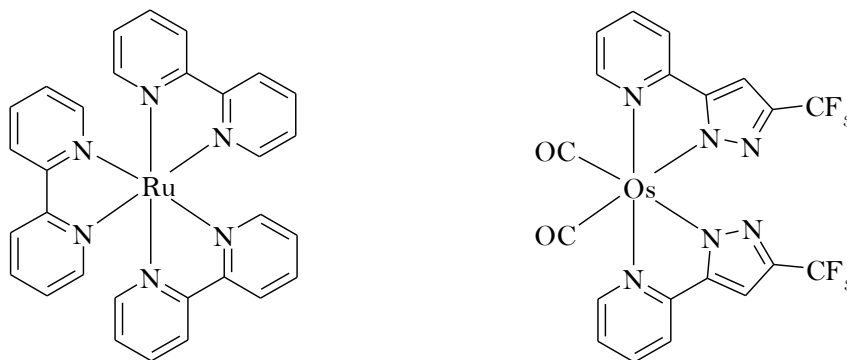


Figure 1.2.3. Examples of $4d^6$ and $5d^6$ octahedral complexes.

In metal complexes there are three types of electronic transitions, which can be understood with the aid of the energy level diagram shown in Figure 1.2.4:

- Metal-Centered (MC) electronic transitions, from the promotion of an electron from t_{2g} to e_g orbitals; according to spin selection rule, $d-d$ transitions are Laporte forbidden but due to the high spin-orbit coupling in heavy metals, a singlet state mixes to some extent with a triplet state and thus, these spin-forbidden transitions become allowed, although they are still very weak.
- Ligand-Centered (LC) transitions between $\pi-\pi^*$ orbitals located on the organic ligands.
- Metal-to-Ligand Charge Transfer (MLCT) transitions between $d-\pi^*$ orbitals.

Singlet–singlet absorption is an electronic transition from metal t_{2g} orbitals to empty ligand orbitals or centered on the ligand, that is from π orbitals to empty π^* orbitals, without spin change and characterized by large extinction coefficients. On the contrary, singlet–triplet absorption is a transition with spin change, typically forbidden by the selection rules, therefore associated with small extinction coefficients. However, a singlet excited state may be involved in spin flip, which is called intersystem crossing (ISC), resulting in an excited triplet state (See Section 1 – Introduction).

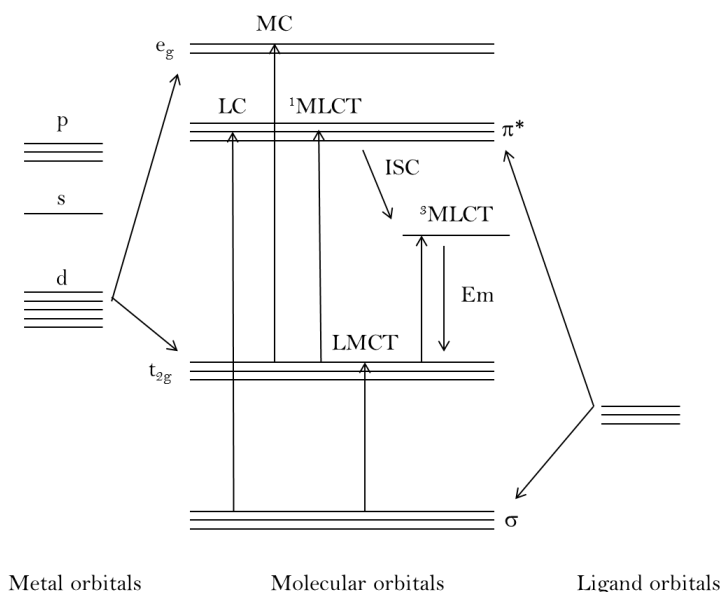
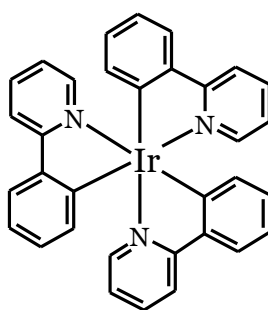


Figure 1.2.4. Schematic and simplified molecular orbital diagram for an octahedral d^6 metal complex involving 2-phenylpyridine (C_s symmetry)-type ligands in which various possible transitions are indicated.

Among organic transition metal complexes employed as phosphorescent emitters in OLEDs, iridium(III) complexes have attracted much more attention for a series of properties making them suitable for applications in highly efficient devices. These are: 1) the quasi-octahedral geometry that allows the introduction of specific ligands in a controlled manner; 2) the photo-physical and the electrochemical properties, tunable in a predictable way; 3) the stable and easily accessible oxidation and reduction states; 4) the highest triplet quantum yields; 5) the strong spin-orbit coupling. The high efficiency of iridium complexes comes from their shorter exciton lifetimes, which are within the range of 1 to 14 μs , and effectively alleviated triplet-triplet annihilation at high currents.



Ir(ppy)_3

Since 1984 when Watts isolated the tris(2-phenylpyridine) iridium(III) complex, Ir(ppy)_3 ,⁶ as a side product and reported a general protocol for the synthesis of tris(2-phenylpyridine) iridium(III) complexes in higher yields, a number of scientific researchers have dedicated their work to the synthesis of variously substituted cyclometalated iridium(III) complexes.

Key ligands for the synthesis of iridium complexes are generally derivatives of 2-phenylpyridine, 2,2'-bipyridine, picolinate or acetylacetonate that are referred to as C[^]N, N[^]N, N[^]O or O[^]O, respectively, chelating the metal center via formation of an Ir-C, Ir-N or an Ir-O bond.

C[^]N type ligands can give rise to homoleptic $[\text{Ir(C}^{\wedge}\text{N)}_3]$ or heteroleptic $[\text{Ir(C}^{\wedge}\text{N)}_2(\text{C}^{\wedge}\text{N}')]]$ neutral tris-cyclometalated complexes, depending if all the ligands are equal or different from each other. All iridium(III) complexes exhibit a quasi-octahedral geometry and are always chiral, yielding to two enantiomers (Figure 1.2.5); to distinguish the two forms, the octahedron is viewed down a 3-fold axis: the enantiomer with left-handedness is labeled Λ , and that with right-handedness is Δ .

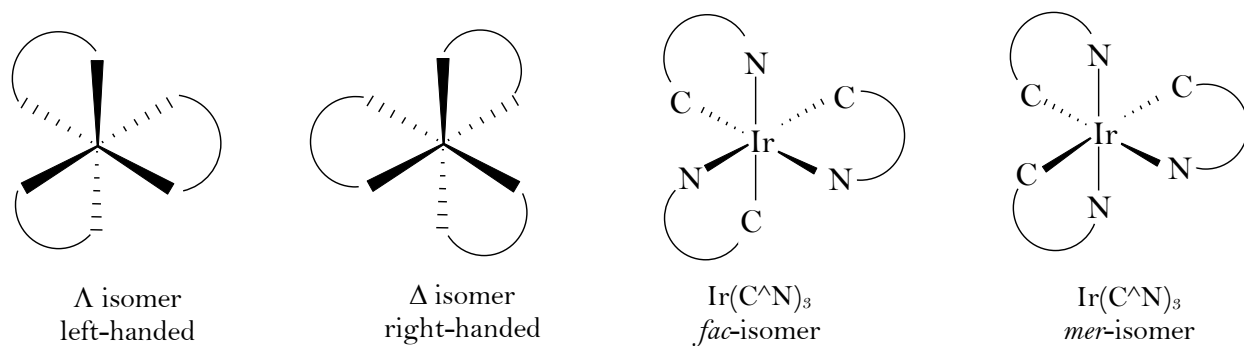


Figure 1.2.5. Λ -/ Δ -handedness enantiomers (left side) and facial/meridional isomers (right side) of cyclometalated iridium complexes.

Moreover, the tris-cyclometalated iridium(III) complexes are available in two configurationally different isomers, namely facial (*fac*) and meridional (*mer*) ones (Figure 1.2.5). The *facial* isomers usually exhibit longer lifetimes and higher quantum efficiencies compared to the *meridional* isomers, whereas, in general, *meridional* isomers display a red-shifted emission compared to the *facial* ones. The formation of *facial* isomers is favored under high reaction temperatures due to their thermodynamic stability, whereas the kinetically favored *meridional* isomers can be isolated by performing the reactions at lower temperatures; it is possible to convert the *mer*-isomer to the corresponding *fac*-isomer by thermal or photochemical processes.

A $\text{N}^{\wedge}\text{N}$ type ligand is usually referred as ancillary and leads to heteroleptic cationic complexes of general formula $[\text{Ir}(\text{C}^{\wedge}\text{N})_2(\text{N}^{\wedge}\text{N})]^+$. In this case the ligands can arrange leading to *cis* and *trans* isomers (Figure 1.2.6).

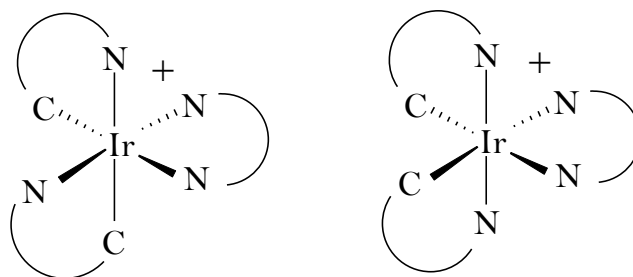


Figure 1.2.6. *cis* and *trans* isomers of cationic iridium(III) complexes.

Light emission of iridium complexes depends on the structures of both cyclometalating and ancillary ligands. Thus it is possible to endow a complex with specific photo-physical and electrochemical features by a rational choice of the ligands achieving tunable light emission over the whole visible range. In a practical approximation, the emission maximum of

luminescent iridium complexes is determined principally by the HOMO–LUMO gap. An effective strategy to tune the emission color in iridium(III) complexes relies on the selective stabilization or destabilization of the HOMO and/or LUMO of the complex. This can be achieved by the insertion of electron-withdrawing or electron-releasing substituents.

Since the analysis of the spectral properties of the archetypal Ir(ppy)₃ complex carried out by Hay using DFT,⁷ it is known that the HOMO in this complex is mainly composed of π -orbitals of the phenyl ring and the *d*-orbitals of the metal. The pyridine is formally neutral and is the major contributor to the LUMO of the complex. Therefore, electron-withdrawing substituents on the phenyl ring of the C[^]N ligand will decrease the donation to the metal and contribute to stabilize the metal-based HOMO, whereas electron-releasing substituents will lead, on the other hand, to a destabilization of the HOMO. When substituents are on the pyridine rings, the effect will mostly be a stabilization of the LUMO for electron-acceptor groups and destabilization for electron-donor groups. The position of the substituent on the phenyl or pyridine rings can also affect the HOMO or LUMO energy.

Another tool for adjusting the HOMO–LUMO levels is to select the proper heterocyclic backbone of the ligand. For example, in Figure 1.2.7 it is shown how it is possible to tune the color emission of iridium complexes (in this case from green to red) by passing from 2-phenylpyridine to 1-phenylisoquinoline ligands. This approach relies on the effect of the extended aromatic delocalization on the HOMO–LUMO gap.⁸

For what concerns the cationic iridium complexes with the general formula Ir[C[^]N]₂[N[^]N]⁺, experimental and theoretical investigations have revealed that the LUMO is located on the ancillary ligand, while the HOMOs is located on the *d*-orbitals of the metal and on the phenyl groups of cyclometalating ligands. Thus in order to tune the emission it's possible to functionalize either the ancillary or the cyclometalating ligands with electron-withdrawing or electro-donating groups as well as changing the nature of the ligands.

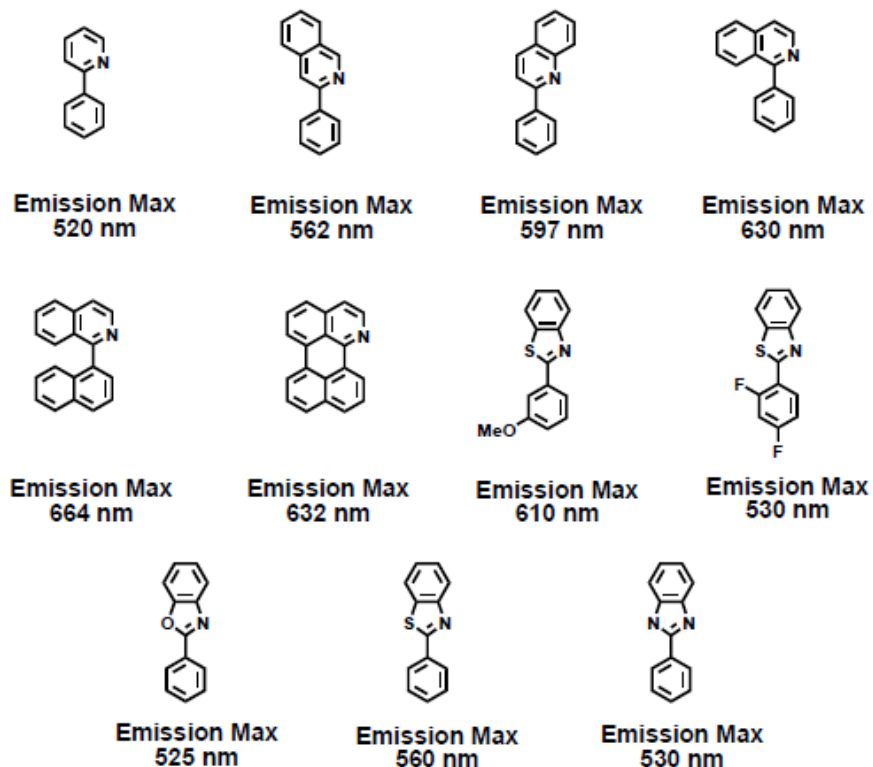


Figure 1.2.7. Tuning of color emission of iridium (III) complexes with different cyclometalating ligand.

Starting from this background, we decided to undertake the synthesis of a novel set of iridium(III) complexes obtained with dopamine-inspired ligands. Dopamine (DA) is the well-known catecholic neurotransmitter precursor of neuromelanin and monomer precursor of polydopamine (PDA), a functional melanin-like polymer that has been widely explored for its properties, such as strong adhesion and biocompatibility, in the field of material science.

In this chapter the synthesis of a series of dopamine-inspired ligands bearing the 6,7-dimethoxy-3,4-dihydroisoquinoline skeleton is reported (Figure 1.2.8). The synthesis of the corresponding iridium(III) complexes is also reported together with a comparative analysis of their photo-physical properties and performance of the corresponding OLED/LEEC devices.

This work has been partially carried out at the ENEA Research Center of Portici in collaboration with Dr. Maria Grazia Maglione.

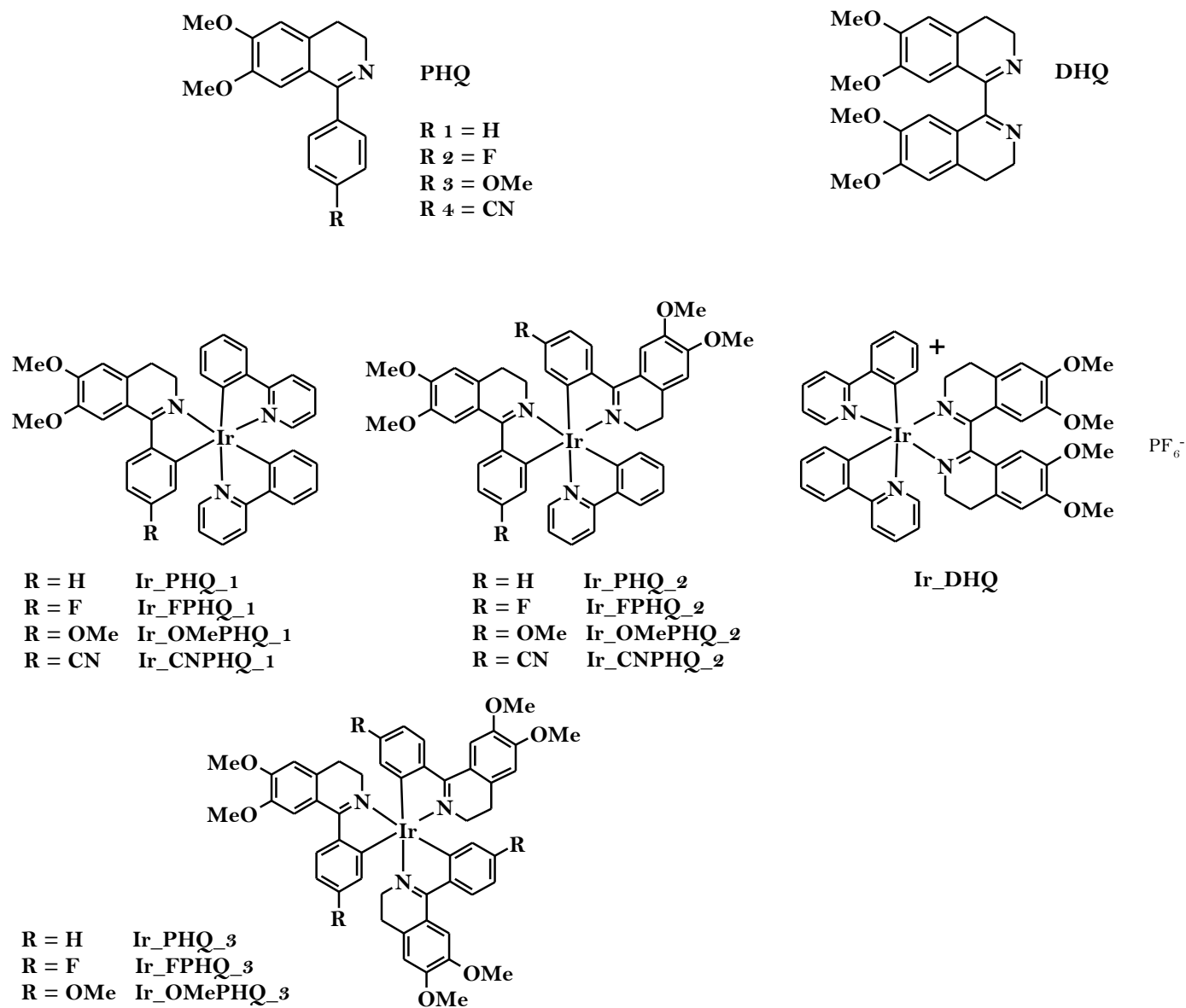


Figure 1.2.8. Synthesized ligands and iridium(III) complexes.

~RESULTS AND DISCUSSION~

○ SYNTHESIS AND CHARACTERIZATION OF DOPAMINE-INSPIRED LIGANDS

For the synthesis of the dopamine-inspired C^N cyclometalating ligands we exploited the Bischler-Napieralski reaction in order to get a set of 6,7-dimethoxy-3,4-dihydroisoquinolines substituted on the 1 position with phenyl residues, functionalized on the para-position with different groups (PHQs), or with another 6,7-dimethoxy-3,4-dihydroisoquinoline unit (DHQ).

In detail, for the synthesis of PHQ, the selected benzoic acid derivative (benzoic acid, 4-fluorobenzoic acid, 4-methoxybenzoic acid or 4-cyanobenzoic acid) was treated first with ethylchloroformate and triethylamine (TEA) in anhydrous dimethylformamide (DMF) at 0 °C, and then with *O,O*-dimethyldopamine at 60 °C. This afforded the amides *Am*₁₋₄ with yields ranging from 91 to 98% (Figure 1.2.7a). In the second step, the amides *Am*₁₋₄ were treated with POCl₃ in a mixture of ethanol/dichloromethane (EtOH/DCM) under reflux conditions to give the corresponding 1-phenyl-6,7-dimethoxy-3,4-dihydroisoquinoline derivative, obtained in pure form and in high yields after silica gel chromatography (Figure 1.2.7b).

The identity of both the amides and the 3,4-dihydroisoquinoline derivatives was confirmed by ¹H, ¹³C NMR and ESI⁺ MS spectra.

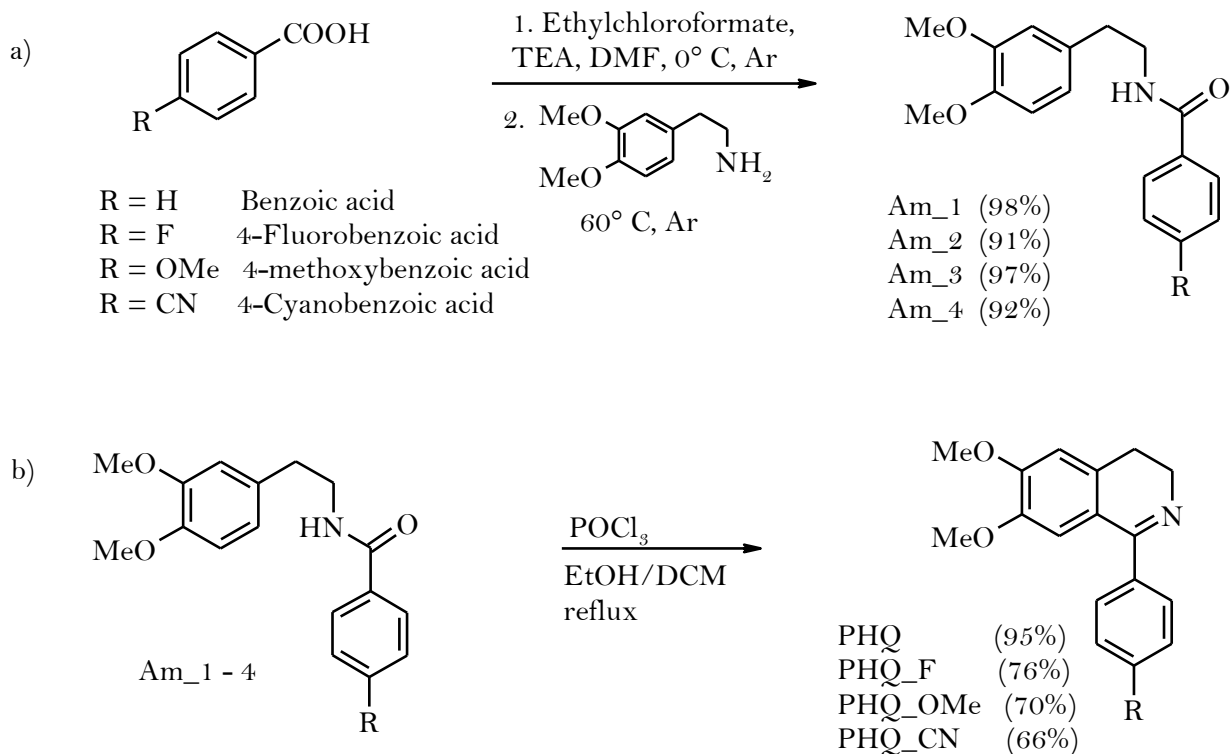


Figure 1.2.9. Synthesis of amides *Am*₁₋₄ (a) and of *PHQ*, *PHQ_F*, *PHQ_{OMe}* and *PHQ_{CN}* (b).

For the synthesis of the N^N type ancillary ligand DHQ, a procedure described in the literature was followed.⁹ In brief, the *O,O*-dimethyldopamine was treated in the first step with diethyloxalate in toluene under reflux conditions to give a bis-amide derivative (Figure 1.2.8a). This latter, in the second step, was treated with POCl₃, under the condition previously described, to give the bis(6,7-dimethoxy-3,4-dihydroisoquinoline) DHQ in high yields (Figure 1.2.8b). The identities of the compounds were confirmed by ¹H, ¹³C NMR and ESI⁺ MS spectra.

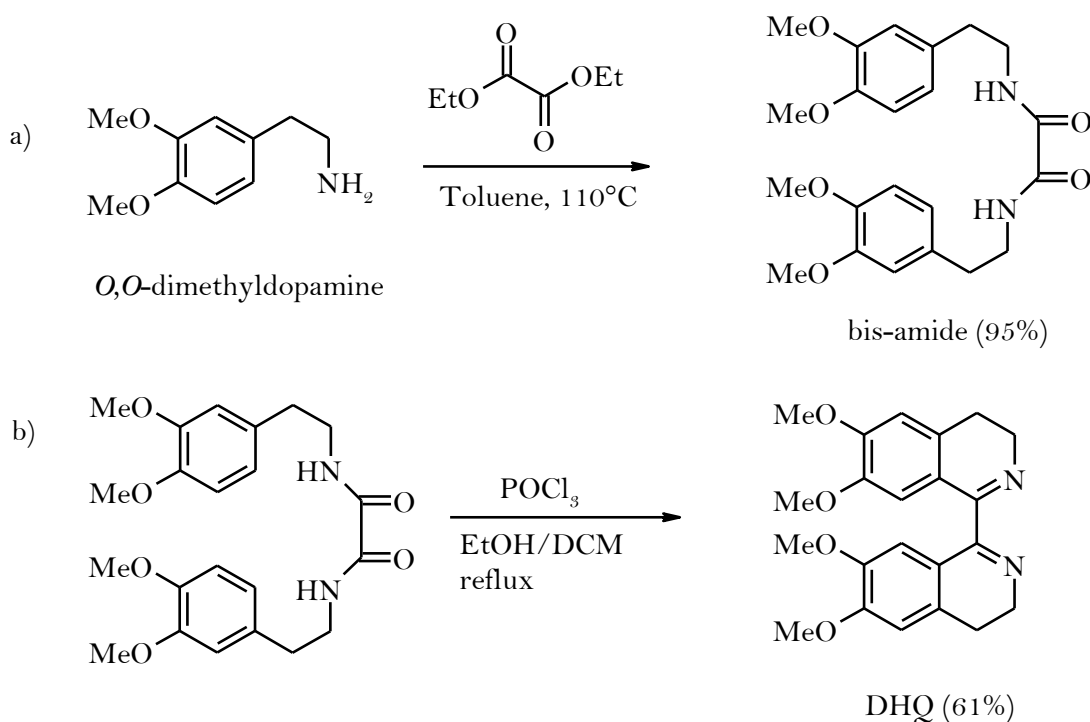


Figure 1.2.10. Synthesis of the bis-amide (a) and of the corresponding DHQ (b).

o SYNTHESIS AND CHARACTERIZATION OF IRIDIUM(III) COMPLEXES

There are two main synthetic strategies to obtain cyclometalated iridium(III) complexes (Figure 1.2.11). The first one leads to the formation of homoleptic tris-cyclometalated iridium(III) complexes by reacting IrCl₃·*n*H₂O with an excess of the selected C^N ligand at significantly higher temperatures or in presence of a chloride scavenger.¹⁰ The second one described by Nonoyama involves the intermediate formation of a dinuclear chloro-bridged

complex by reacting $\text{IrCl}_3 \cdot n\text{H}_2\text{O}$ with stoichiometric amounts of the selected cyclometalating ligand under very mild conditions. This intermediate can evolve toward the formation of the corresponding homoleptic iridium complex $\text{Ir}(\text{C}^{\wedge}\text{N})_3$ by reacting with another $\text{C}^{\wedge}\text{N}$ ligand or can lead to the formation of the heteroleptic iridium complex $\text{Ir}(\text{C}^{\wedge}\text{N})(\text{C}'^{\wedge}\text{N}')$ by reacting with a different $\text{C}'^{\wedge}\text{N}'$ ligand.

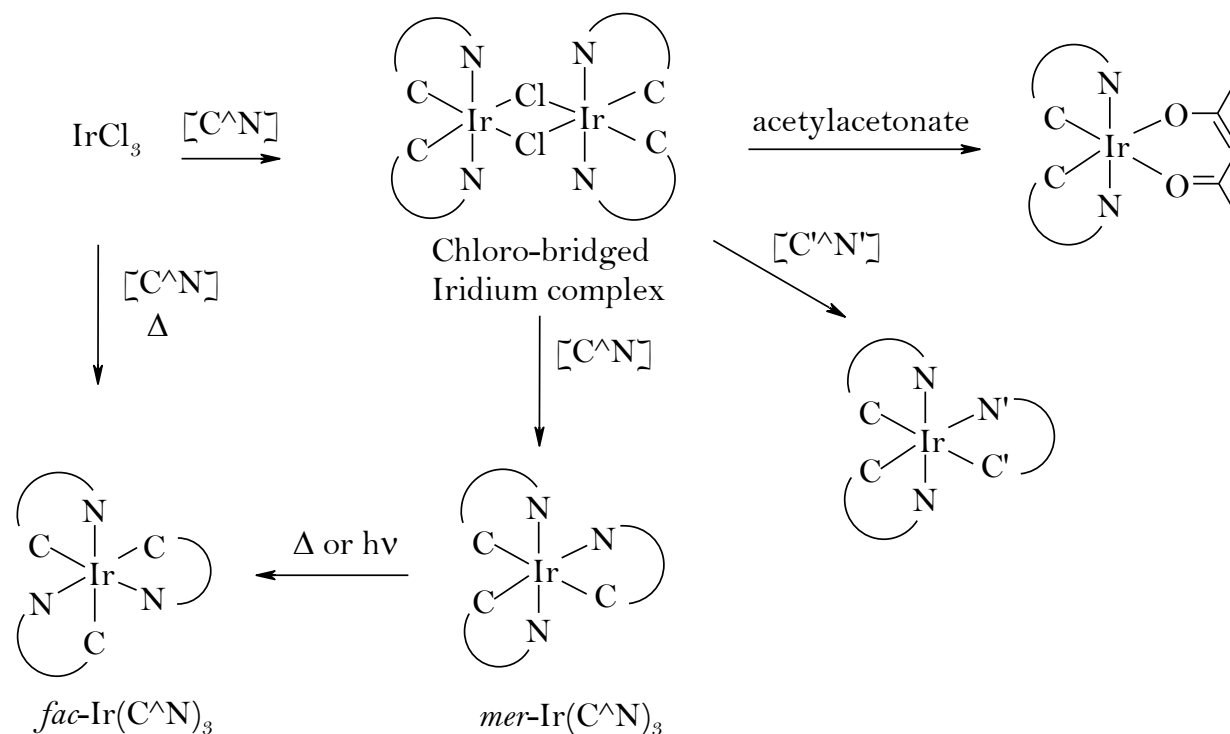


Figure 1.2.11. Synthetic pathways usually used for the synthesis of homoleptic or heteroleptic iridium(III) complexes.

For our purposes the second synthetic strategy has been pursued to prepare all the dopamine-inspired iridium(III) complexes. The first step of the procedure consisted in the synthesis of the chloro-bridged dinuclear complex ($\mu\text{-Ir}$) with the initial insertion of the 2-phenylpyridine (ppy) ligand.¹¹ In details, the reaction was carried out by treating the iridium trichloride with 2.5 molar equivalents of 2-phenylpyridine in an ethoxyethanol/water mixture under an argon atmosphere and reflux conditions (Figure 1.2.12).

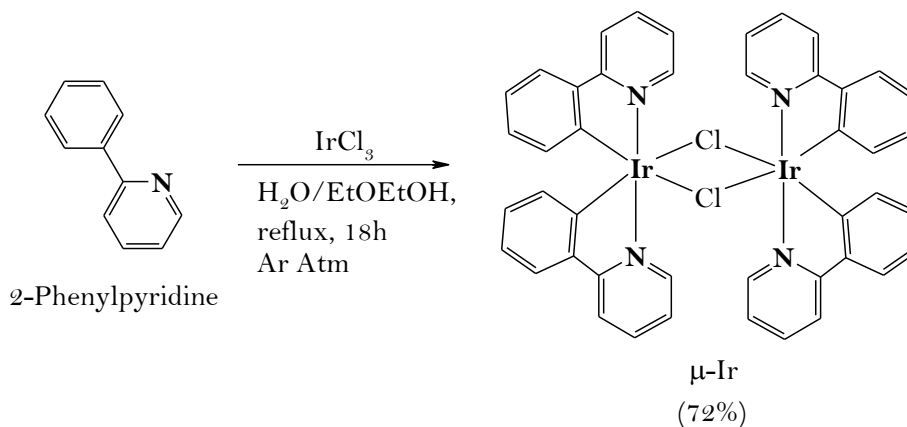


Figure 1.2.12. Synthesis of the dichloro-bridged dinuclear complex ($\mu\text{-Ir}$).

The complex $\mu\text{-Ir}$ was isolated as a yellow solid by filtration after the addition of water to the reaction mixture. Its identity and purity was checked by ^1H NMR showing a single pattern of resonances accounting for the four ppy units, suggesting a *trans* arrangement of the ligands.

Once obtained, the iridium complex $\mu\text{-Ir}$ was treated with the dopamine-based C^N ligands previously synthesized.

When using the PHQ series of ligands, the complex $\mu\text{-Ir}$ was dissolved in dry DMF and treated with an excess of the proper ligand in presence of TEA and acetylacetonone under reflux conditions and in an argon atmosphere (Figure 1.2.13). After 48 h the reaction mixture was cooled to room temperature and the solvent was evaporated under reduced pressure to afford a solid constituted by a mixture of three complexes differing for the ratio between the PHQ and the ppy ligands. All the complexes were isolated in pure form by silica gel chromatography and subjected to mono- and bi-dimensional NMR spectroscopy and ESI⁺ MS analysis in order to confirm the structure of the compounds. In the case of the ligand CN-PHQ only two complexes were isolated with a mono and bis substitution of the PHQ ligand.

To the best of our knowledge, this is the first time in which, starting from the dinuclear complex, it is possible to obtain one-pot a set of three different neutral iridium(III) complexes differing from each other for the ratio between the two cyclometalating ligands.

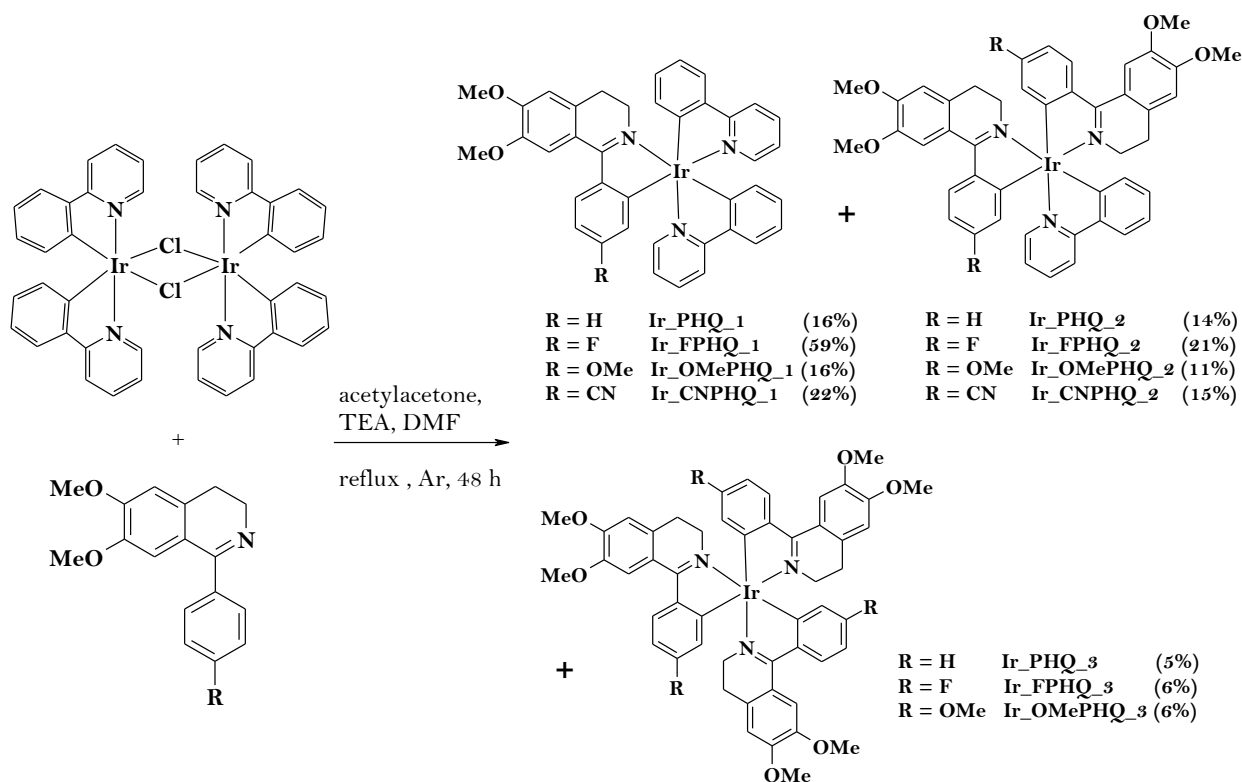


Figure 1.2.13. Synthesis of the neutral iridium(III) complexes.

All the synthesized complexes were fully characterized by ^1H and ^{13}C NMR analysis confirming the structures. ^{19}F NMR spectroscopy was also used to confirm that the *fac*-isomer of the homoleptic iridium complexes trisubstituted with PHQ_F-type ligands were formed.

For the synthesis of the cationic complex with the N^N ancillary ligand DHQ a procedure described by Neve et. al.¹² was followed that requires milder reaction conditions compared to common synthesis for iridium complexes that involve high-boiling solvents, high temperatures and long reaction time. The complex $\mu\text{-Ir}$ was dissolved in a mixture of DCM/methanol and treated with two molar equivalents of the ligand DHQ under reflux conditions. After 45 minutes, the reaction mixture was cooled to room temperature and a suspension of NH_4PF_6 in methanol was added under stirring to allow the formation of the salt (Figure 1.2.14). After 30 minutes, the mixture was evaporated under reduced pressure, taken up in DCM and filtered to remove the white inorganic solid. The supernatant composed by a complex mixture of products was subjected to silica gel chromatography. This afforded in pure form two iridium complexes; the main one was identified as the *cis* Ir_DHQ by NMR analysis, revealing in the ^1H spectrum a double pattern of resonances for the ppy unit. The second one, isolated in very low yields, was

identified by NMR analysis as the oxidative product of the previous complex (*cis* Ir_DHQ_ox), due to its low stability. Evidence of the formation of the more stable *trans* Ir_DHQ complex (TD-DFT evidences) were provided by careful inspection of the ^1H NMR spectrum of the total reaction mixture. Any attempt to isolate it by common chromatographic techniques proved unfruitful due to the complex reaction mixture and the high reactivity exhibited by this kind of complexes.

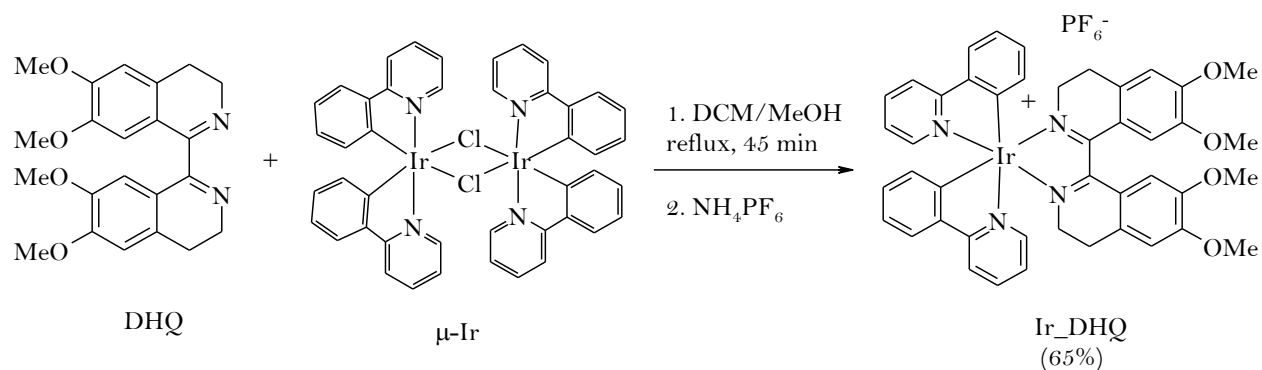


Figure 1.2.14. Synthesis of *Ir_DHQ*.

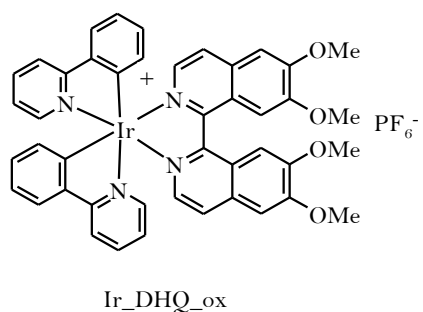


Figure 1.2.15. Compound obtained as by-product.

Complex *Ir_DHQ* was also subjected to the ESI – MS analysis revealing, in the spectrum registered in the positive ion mode, the presence of a peak at m/z 880 relative to the cationic portion of the complex, and in the spectrum registered in the negative ion mode, a peak at m/z 145 relative to the anionic species PF_6^- . The incorporation of the PF_6^- was supported also by ^{19}F NMR.

○ PHOTO-PHYSICAL PROPERTIES OF DOPAMINE-INSPIRED COMPLEXES

A comparative analysis of the photo-physical properties of the isolated complexes was carried out by UV-vis and emission spectroscopy to assess: 1) the absorption and emission profiles of

the complexes; 2) the influence of the different ratio between the ppy and the 6,7-dimethoxy-3,4-dihydroisoquinoline units within the same series of complexes; 3) the effects of the nature of the functional groups on the phenyl ring of the phenyl-3,4-dihydroisoquinoline ligands; 4) the influence of the nature of the heterocyclic platform selected as ligand; 5) the eventual role played by oxygen in quenching the emission radiation.

To this aim, dilute solutions in dichloromethane (1×10^{-5} M) of each complex were prepared and UV-vis and emission spectra were recorded. For analysis carried out in oxygen depleted conditions, each solution was purged extensively with argon prior registering the emission spectra. The overall photo-physical data are listed in table 1.2.2.

The absorption profiles of the neutral iridium(III) complexes were quite similar within each series (Figure 1.2.16). The intense maxima below 300 nm can be assigned to the spin-allowed $^1\pi-\pi^*$ transition of the cyclometalating ligand with high molar extinction coefficient ($\epsilon > 10000$ M $^{-1}$ cm $^{-1}$); for the homoleptic complexes, these bands account for the transitions within the PHQ ligands, while in the heteroleptic complexes these bands are composed by a mixture of π and π^* orbitals of both PHQ and ppy ligands.

Bands below 450 nm can be assigned to the spin-allowed metal-ligand charge transfer (1 MLCT) characterized by values of $\epsilon > 5000$ M $^{-1}$ cm $^{-1}$. The small bands ranging between 450 nm and 550 nm can be assigned to the spin-forbidden 3 MLCT band; the relatively high intensity of these bands indicates an efficient spin-orbit coupling that is a prerequisite for good phosphorescent emission.

Within each series, the absorption maxima of the complexes did not suffer any significant shift except for bands at around 300 nm confirming the nature of these states; fixing the ratio between the ppy and the PHQ units, the insertion of the fluorine and the methoxy group on the phenyl ring induced a small hypsochromic effect on the absorption maxima while the cyano group produced a bathochromic shift. Changing the nature of the dopamine-based ligand, that is with the insertion of the DHQ N N type ligand, the absorption profile displayed similar features with respect to the C N type ligand with the maxima shifted at lower wavelengths (Figure 1.2.18a).

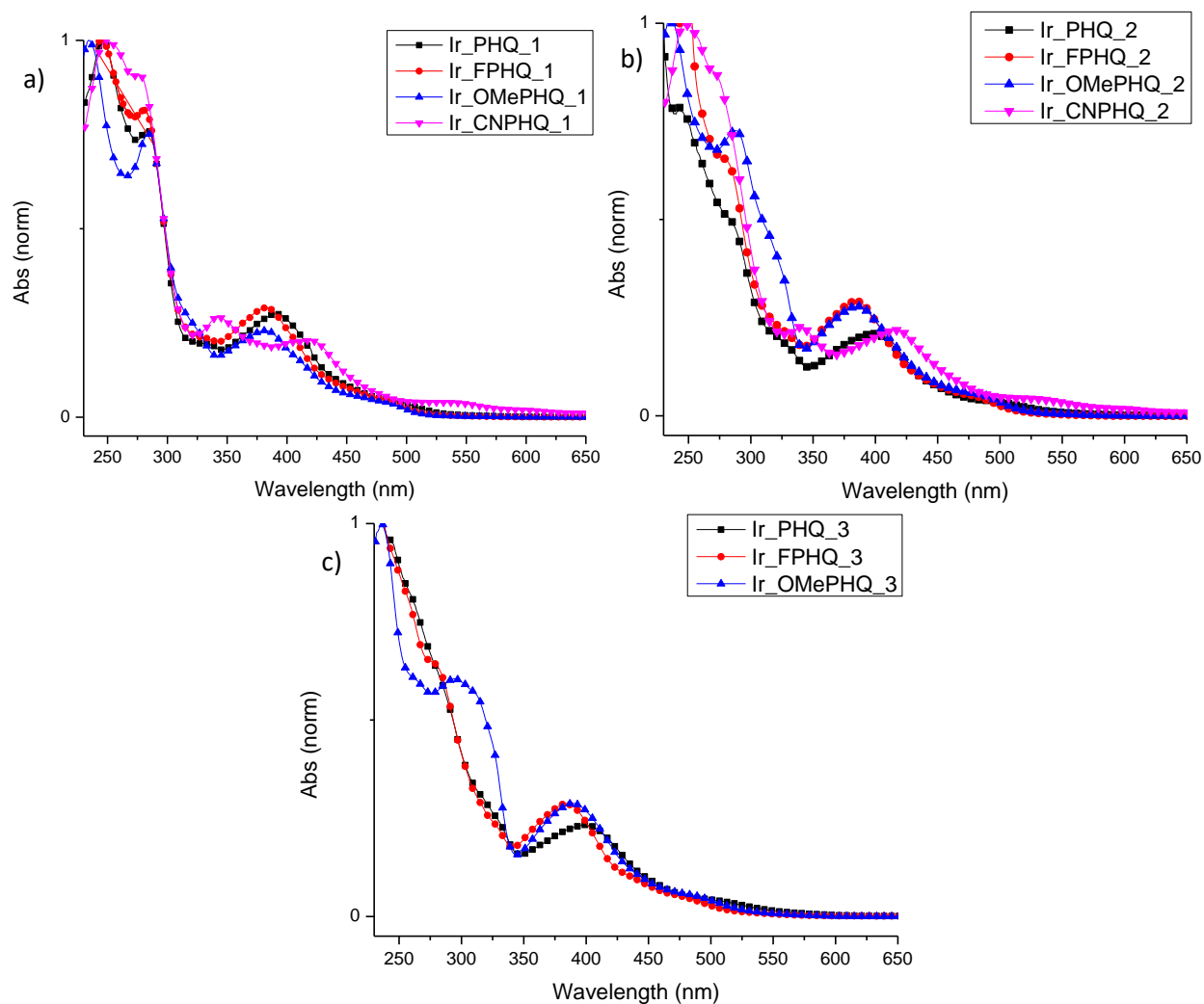


Figure 1.2.16. Normalized absorption spectra of complexes Ir_PHQ_{1-3} , Ir_FPHQ_{1-3} , Ir_OMePHQ_{1-3} and $IrCNPHQ_{1-2}$ in DCM.

The emission spectra registered in dilute solutions of DCM showed for all the complexes a red emission, with maxima ranging from 600 nm for Ir_DHQ to ~ 650 nm for Ir_CNPHQ_{1-2} . Also in this case, similar emission maxima within each series of neutral complexes were observed (Figure 1.2.17). Worthy of note is the effect of the substituents on the phenyl ring in neutral complexes on the emission wavelength (Table 1.2.2). TD-DFT calculations are in due course to rationalize these effects. Phosphorescence quantum yields proved quite high and consistent with those reported in the literature for similar iridium(III) complexes.

Emission spectra were also recorded in an oxygen depleted DCM solution in order to avoid oxygen-induced quenching of the emission from the triplet state. For most of the complexes it

was observed higher quantum yields and a significant quenching effect exerted by oxygen, with quantum yields that in some cases tripled when the emission spectrum was registered on oxygen free solutions of the complexes.

UV-vis and emission spectra for *Ir_DHQ* were recorded also as thin film on quartz. This revealed a modest red-shift of the absorption profile and the emission spectrum of the complex registered as thin films on silicon at low temperature (9 K) revealed that the red emission was composed by the overlapping of three bands centered at 600, 650 and 730 nm (Figure 1.2.18).

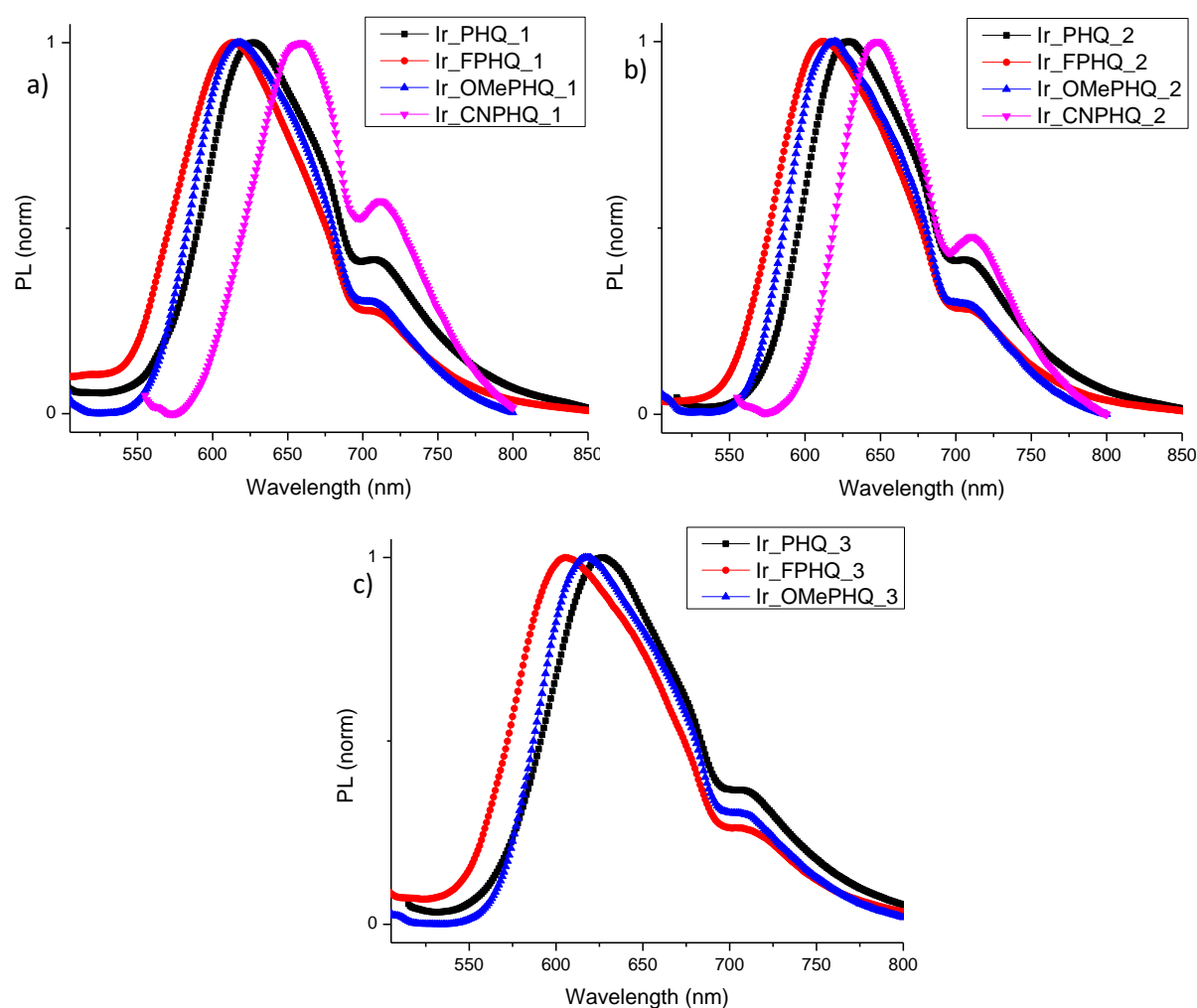


Figure 1.2.17. Normalized emission spectra of complexes *Ir_PHQ_1-3*, *Ir_FPHQ_1-3*, *Ir_OMePHQ_1-3* and *IrCNPHQ_1-2* in DCM.

Table 1.2.1. Photo-physical data of compounds *Ir_PHQ_1-3*, *Ir_FPHQ_1-3*, *Ir_OMePHQ_1-3*, *IrCNPHQ_1-2* and *Ir_DHQ*.

Compound	UV-vis	PL	Φ (λ_{em} , nm) ^b	Φ (λ_{em} , nm) ^c	E_g^{opt} , eV
	λ_{max} , nm (log ϵ , M ⁻¹ cm ⁻¹) ^a	λ_{em} , nm (λ_{ecc} , nm) ^a			
<i>Ir_PHQ_1</i>	283 (4.15), 332 (sh), 391 (3.73), 480 (2.99)	626 (480)	0.41% (626)	0.30% (620)	1.97
<i>Ir_PHQ_2</i>	283 (4.58), 320 (sh), 400 (4.17), 500 (3.39)	630 (500)	0.14% (630)	0.26% (628)	1.97
<i>Ir_PHQ_3</i>	280 (4.56), 330 (sh), 400 (4.10), 500 (3.36)	627 (500)	0.18% (627)	0.23% (625)	1.97
<i>Ir_FPHQ_1</i>	280 (4.40), 330 (sh), 382 (3.96), 480 (3.19)	613 (480)	0.24% (613)	0.70% (604)	2.02
<i>Ir_FPHQ_2</i>	280 (4.35), 325 (3.91), 385 (4.04), 480 (3.28)	613 (480)	0.15% (613)	0.40% (595)	2.02
<i>Ir_FPHQ_3</i>	275 (4.11), 325 (sh), 383 (3.73), 480 (2.95)	605 (480)	0.19% (605)	0.22% (603)	2.05
<i>Ir_OMePHQ_1</i>	284 (6.62), 382 (4.11), 490 (3.27)	617 (490)	0.21% (617)	0.61% (603)	2.40
<i>Ir_OMePHQ_2</i>	288 (4.31), 386 (3.92), 490 (3.17)	617 (490)	0.15% (617)	0.23% (615)	2.36
<i>Ir_OMePHQ_3</i>	295 (4.73), 390 (4.42), 490 (3.67)	617 (490)	0.13% (617)	0.19% (616)	2.30
<i>Ir_CNPHQ_1</i>	340 (4.13), 405 (4.00), 420 (4.02), 540 (3.18)	656, 712 (540)	0.11% (656)	0.14% (653)	2.07
<i>Ir_CNPHQ_2</i>	340 (4.10), 416 (4.04), 540 (3.17)	648, 710 (540)	0.14% (648)	0.15% (649)	2.07
<i>Ir_DHQ</i>	260 (5.08), 354 (4.08), 450 (3.48)	600 (450) (600, 650, 730) ^d	0.40% (600)	0.38% (600)	2.07

[a] Determined in diluted solutions in dichloromethane (1×10^{-5} M); [b] determined relatively to fluorescein $\Phi = 0.9$ in a 0.1 M solution of NaOH); [c] determined in oxygen free solutions of DCM; [d] determined as thin film on silicon at 9K.

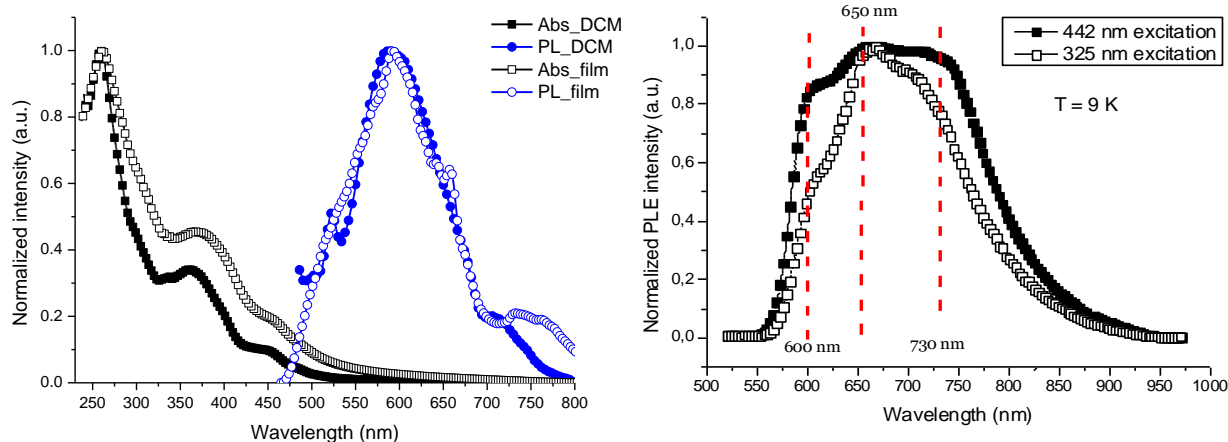


Figure 1.2.18. Normalized absorption and photoluminescence spectra of compound IrDHQ in DCM and as thin film on quartz (left); normalized photoluminescence spectra as thin film on silicon at 9 K (right).

o LEEC DEVICES with the cationic complex *Ir_DHQ*

All the isolated complexes were used as emitting materials in light emitting devices. In particular, the cationic complex *Ir_DHQ* was tested as active layer in LEEC devices. For device fabrication see experimental details. First studies were addressed to the identification of the proper cathode. In all cases the anode is a 200 nm thick layer of ITO coated with a 60 nm layer of PEDOT:PSS to smooth the roughness of ITO and facilitate charge injection. The emitting layer with a ~100 nm thickness was deposited by spin coating. We first compared silver, which has a work function close to the ITO (respectively 4.2 – 4.7 and 4.7-5.2 eV), and a double layer of calcium/aluminum, with a lower work function (2.9 and 4.0 – 4.3 eV). Ag cathode showed better performances reaching a maximum luminance of 138 cd/m², at 23 V, with respect to the Ca/Al cathode with luminance of 2.3 cd/m² at 13 V. Despite the good luminance of the device with Ag as cathode, the turn-on voltage was too high for a good device operation as well as the efficiency (0.07 cd/A) and power efficiency (0.0092 lm/W) compared to up-to-date LEEC devices that are able to work at lower voltages.¹⁴

In order to improve the device characteristics, in particular to lower the turn-on voltage, once selected the silver cathode, we tested the performance of a blend of the ionic iridium complex with the ionic liquid dimethylimidazolium dimethylphosphate (IL).¹⁵ We tested three different Ir:IL ratios, 1:2 mol/mol, 4:1 mol/mol, 2:1 mol/mol. Key performances of all the devices have

been reported in table 1.2.3. Best performances were achieved with a molar ratio of Ir:LI = 2:1 reaching a luminance of 162 cd/m² at 12 V, halving the turn-on voltage.

The recorded electroluminescence of all devices showed a broad red emission ranging between 633 and 680 nm; a progressive red shift was evident with the reduction of the IL content in the blend, suggesting that IL hinder a better aggregation of the cationic iridium complex. (Figure 1.2.19).

These results demonstrated the potentiality of this new bio-inspired Ir(III) complex ad emitting layer in LEEC devices.

Table 1.2.2. LEEC devices characteristics

Entry	Device	Luminance Max (cd/m ²)	Efficiency Max (cd/A)	Power Efficiency max (lm/W)	EL λ_{max} (nm)
1	ITO/PEDOT:PSS/Ir/Ca/Al	2.7 ^a	0.003 ^a	9.1×10 ^{-4b}	686
2	ITO/PEDOT:PSS/Ir/Ag	138 ^c	0.07 ^c	9.2×10 ^{-3c}	660
3	ITO/PEDOT:PSS/Ir:IL, 2:1/Ca/Al	5.5	0.01	5.0×10 ⁻³	650
4	ITO/PEDOT:PSS/Ir:IL=2:1/Ag	162 ^d	0.105 ^d	5.7×10 ^{-2d}	640
5	ITO/PEDOT:PSS/Ir:IL=4:1/Ag	70 ^d	0.027 ^d	5×10 ^{-2d}	680
6	ITO/PEDOT:PSS/Ir:IL=1:2/Ag	27 ^d	0.07 ^e	3.2×10 ^{-3e}	633

^a13 V, ^b9.5V, ^c 23 V, ^d 12 V, ^e 7 V

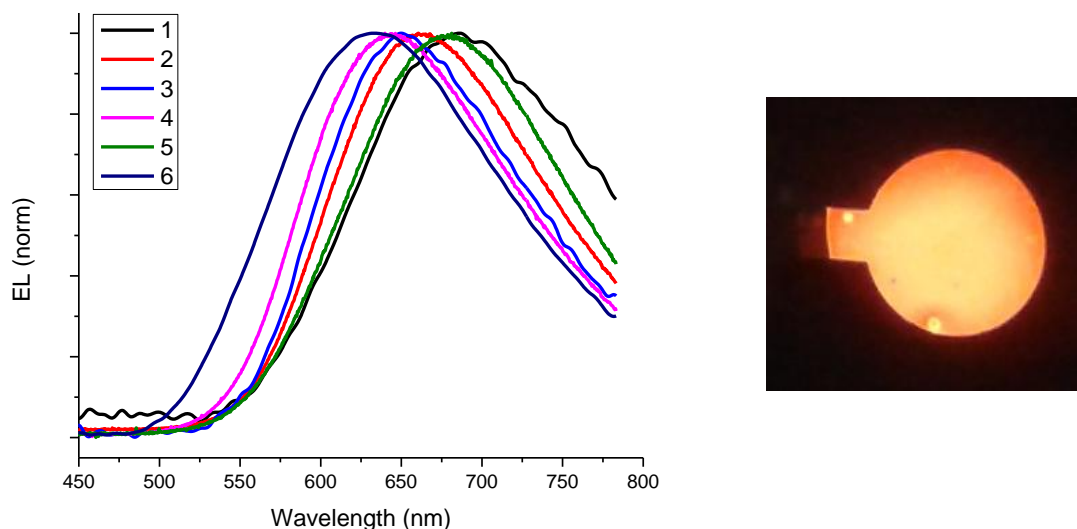
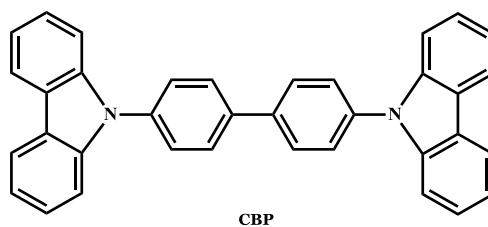


Figure 1.2.19. Electroluminescence spectra of LEEC devices 1-6 (left) and biased LEEC (right).

○ OLED devices with the neutral iridium(III) complexes

In order to test the neutral iridium(III) complexes as emitters, OLED devices were fabricated with the configuration reported in Figure 1.2.20.

As reported in the literature for OLEDs fabricated with similar iridium(III) complexes, the emitting layer was composed of a blend in which the complexes were used as guests at different percentages (2%, 6% and 12% w/w) within the 4,4'-bis(*N*-carbazolyl)-1,1'-biphenyl (CBP), selected as the host.



The choice of using emitting layers doped with organic phosphorescent transition metal complexes affords high efficient OLED devices due to specific mechanisms of energy transfer (see Section 1 - Introduction).

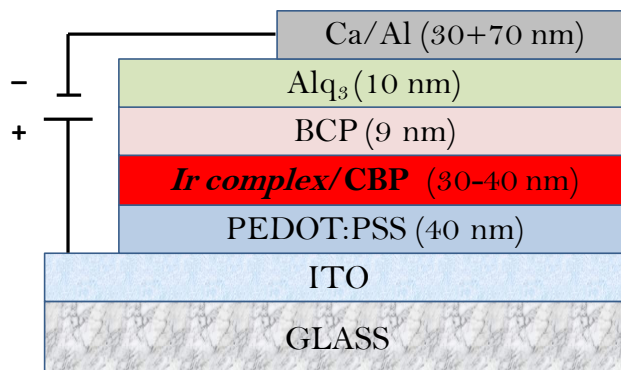


Figure 1.2.20. OLED multilayer structure fabricated with the synthesized neutral complexes.

The steps for the fabrication of the OLED devices are detailed in the experimental section. OLED devices were fabricated on ITO sputtered glass substrates used as anode; subsequently, a hole injection layer (HIL) of PEDOT:PSS was spin coated and baked in a vacuum oven (thickness 40 nm), followed by the spin coating of the blend of the iridium complex in CBP. Finally the substrates were loaded into a glove box system integrated with an evaporation system to allow the evaporation of 2,9-Dimethyl-4,7-diphenyl-1,10-phenanthroline (BCP) as hole blocking layer (HBL), of tris-(8-hydroxyquinoline) aluminium (Alq_3) as electron transport layer (ETL), and of a bilayer of calcium and silver as the cathode.

Before the fabrication of the devices, preliminary deposition tests of the iridium(III) complex-CBP blend onto glass substrates were carried out to assess the optimal conditions that produce homogeneous thin films. In a first stage, tests were carried out by using only CBP solutions and by varying the deposition rate and time, the solvent and the concentration of the CBP solution. The morphological analysis were performed with a Taylor Hobson CCI MP profilometer and the results are reported in Table 1.2.3.

On the basis of the roughness and thickness of the films, the following conditions were selected: Solvent: chlorobenzene (CB); concentration: 10 mg/mL; spin rate program: 3000 rpm for 30 seconds.

Once optimized the deposition conditions, the emitting layers were prepared by using CBP doped with the proper iridium(III) complex at a concentration of 2%, 6% and 12% (w/w). All the thin films proved of good quality for the fabrication of the devices.

Table 1.2.3. Spin coating parameters for CBP thin film deposition.

Test	Concentration and solvent	Deposition Program (speed × acceleration × time (sec))	Thickness (nm)	Sq (nm)
1	10 mg/ml CB	2000×1000×30	45	17
2	10 mg/ml CB	3000×500×30	40	13
3	10 mg/ml CB	4000×500×30	25	20
4	10 mg/ml CB /CHCl ₃ 1/1	3000×500×30	80	40
5	10 mg/ml CB/CHCl ₃ 1/1	4000×500×30	70	10
6	10 mg/ml CB/CH ₃ CN 1/1	3000×500×30	55	10
7	10 mg/ml CB/CH ₃ CN 1/1	4000×500×30	45	8

The general stacked configuration was used:



The devices were named as follows:

Entry	Complex (% in CBP)	Entry	Complex (% in CBP)	Entry	Complex (% in CBP)
1a	Ir_PHQ_1 (2%)	1b	Ir_PHQ_1 (6%)	1c	Ir_PHQ_1 (12%)
2a	Ir_PHQ_2 (2%)	2b	Ir_PHQ_2 (6%)	2c	Ir_PHQ_2 (12%)
3a	Ir_PHQ_3 (2%)	3b	Ir_PHQ_3 (6%)	3c	Ir_PHQ_3 (12%)
4a	Ir_FPHQ_1 (2%)	4b	Ir_FPHQ_1 (6%)	4c	Ir_FPHQ_1 (12%)
5a	Ir_FPHQ_2 (2%)	5b	Ir_FPHQ_2 (6%)	5c	Ir_FPHQ_2 (12%)
6a	Ir_FPHQ_3 (2%)	6b	Ir_FPHQ_3 (6%)	6c	Ir_FPHQ_3 (12%)
7a	Ir_OMePHQ_1 (2%)	7b	Ir_OMePHQ_1 (6%)	7c	Ir_OMePHQ_1 (12%)
8a	Ir_OMePHQ_2 (2%)	8b	Ir_OMePHQ_2 (6%)	8c	Ir_OMePHQ_2 (12%)
9a	Ir_OMePHQ_3 (2%)	9b	Ir_OMePHQ_3 (6%)	9c	Ir_OMePHQ_3 (12%)
10a	Ir_CNPHQ_1 (2%)	10b	Ir_CNPHQ_1 (6%)	10c	Ir_CNPHQ_1 (12%)
11a	Ir_CNPHQ_2 (2%)	11b	Ir_CNPHQ_2 (6%)	11c	Ir_CNPHQ_2 (12%)

Once realized the devices, the electro-optical characterization was carried out.

Table 1.2.4. Performances of OLED devices.

Device	Luminance (cd/m ²) @ 10-11 V	Efficiency (cd/A) @ 10-11 V	Lum. Max (cd/m ²)	Eff. max (cd/A)	Power Efficiency max (lm/W)	λ_{\max} EL (nm)	CIE (1931)
<i>1a</i>	449.5	0.39	527.75@11V	0.49@9V	0.17 @9V	610	0.51 0.40
<i>1b</i>	39.6	0.92	718.9@15V	0.92 @10V	0.30 @10V	610	0.56 0.40
<i>1c</i>	388.5	0.54	709.3@12V	0.54 @10V	0.16 @10V	615	0.56 0.40
<i>2a</i>	628	0.29	682.4 @11V	0.29@10V	0.11@7.5V	620	0.55 0.38
<i>2b</i>	159.2	0.56	495.9@15.5V	0.56 @10V	0.17 @10.3V	620	0.60 0.37
<i>2c</i>	215.5	0.3	483.6@12V	0.32 @9V	0.10 @9V	624	0.60 0.37
<i>3a</i>	509.6	0.24	600.6@10V	0.64@7.8V	0.26 @7.8V	620	0.47 0.39
<i>3b</i>	72	0.5	435@16V	0.55 @11.5V	0.15 @11.5V	625	0.58 0.37
<i>3c</i>	359.4	0.42	518.7@12V	0.44@10.5V	0.13@9.7V	625	0.59 0.38
<i>4a</i>	261	0.18	261@10.5V	0.25 @8.3V	0.09 @8.3V	600	0.46 0.44
<i>4b</i>	764	0.59	764@10V	0.92@8.5V	0.34@8.5V	605	0.54 0.42
<i>4c</i>	450.9	0.13	687@13.5V	0.17 @13.5V	0.04 @13.5V	605	0.55 0.43
<i>5a</i>	1092	0.35	1092@11V	0.35@11V	0.1@11V	585	0.48 0.46
<i>5b</i>	317	0.55	384.9@12.2V	0.55 @10V	0.16 @10V	605	0.54 0.41
<i>5c</i>	149.3	0.35	472.2@13V	0.35@11V	0.1@11V	627	0.59 0.39
<i>6a</i>	559.6	0.39	591.5@10.7V	0.55 @8V	0.22@8V	580	0.43 0.40
<i>6b</i>	343.5	0.2	343@10.7V	0.27 @9.2V	0.1 @8.2V	602	0.48 0.41
<i>6c</i>	175	0.07	175 @10V	0.07 @10V	0.023 @9V	602	0.40 0.38
<i>7a</i>	468.61	1.64	2475.43 @14V	1.78 @13V	0.42 @13V	606	0.57 0.39

<i>7b</i>	319.43	0.064	319.43 @10V	0.064 @10V	0.02 @10V	603	0.56 0.40
<i>7c</i>	466.79	0.18	580.53 @12V	0.18 @12V	0.05 @9V	608	0.57 0.41
<i>8a</i>	606.61	0.81	1008 @13V	0.81 @11V	0.23 @11V	612	0.57 0.39
<i>8b</i>	453.69	0.26	524.11 @13V	0.29 @9V	0.10 @9V	618	0.60 0.37
<i>8c</i>	334.94	0.47	620.56 @13V	0.52 @10V	0.16 @11V	618	0.61 0.38
<i>9a</i>	497.73	0.23	583.71 @12V	0.34 @9V	0.12 @9V	615	0.54 0.36
<i>9b</i>	416.38	0.24	745.68 @13V	0.24 @11V	0.07 @11V	616	0.60 0.37
<i>9c</i>	260.92	0.18	425.57 @13V	0.18 @11V	0.053 @11V	619	0.60 0.38
<i>10a</i>	236	0.33	469.06 @14V	0.33 @10V	0.099 @10V	628	0.47 0.36
<i>10b</i>	177.43	0.062	256.69 @13V	0.065 @12V	0.018 @11V	638	0.53 0.34
<i>10c</i>	35.6	0.05	385.62 @13V	0.17 @12V	0.044 @12V	635	0.57 0.37
<i>11a</i>	323.48	0.15	323.48 @10V	0.15 @10V	0.047 @10V	635	0.39 0.32
<i>11b</i>	131.76	0.051	159.74 @13V	0.051 @11V	0.014 @11V	639	0.56 0.35
<i>11c</i>	67.56	0.047	161.1 @12V	0.056 @12V	0.015 @10V	640	0.57 0.36

Optical characterizations were performed using a Gooch&Housego OL770 spectroradiometer coupled with an integrating sphere and a camera telescope. Electrical measurements were taken by a Keithley 2400 SourceMeter.

The characteristics of all the OLED devices are reported in Table 1.2.4.

By analyzing the data reported in Table 1.2.4, it's possible to deduce that all the fabricated OLED devices exhibit an intense red electroluminescence ascribable to the iridium(III) complexes.

The best devices in terms of luminance and turn-on voltage resulted those prepared by using a 2% wt of the iridium(III) complexes, reaching a maximum luminance of 1092 cd/m² with the device 5a and 2474 cd/m² with the device 7a; only in the case of the *Ir_FPHQ-1* the best results were obtained with the 6% wt blend (device 4b).

In terms of maximum luminance, in the case of the Ir_PHQ and Ir_FPHQ series the best results were obtained in complexes built up with two phenylisoquinoline units, whereas for the Ir_OMePHQ series the best results were given by complex Ir_OMePHQ_1. For the Ir_CNPHQ series there is no appreciable influence of the number of phenylisoquinoline ligands on the maximum luminance.

Analyzing the electroluminescence of the devices it is possible to identify some general trends. When fixing either the structure of the complex and the nature of the substituent, the emission maximum shows a slight red shift when increasing the percentage of the complex. Instead, along each series, the emission maximum remains unaffected. The overall substituent effect on the emission maximum is: F \rightarrow OMe \rightarrow H \rightarrow CN, with the minimum emission λ observed at 580 nm with fluorine and the maximum emission λ observed at 639 nm with the cyano group.

Another interesting aspect concerned the shift of the CIE coordinates as a function of the percentage of the complex used in the device: by increasing the amount of the iridium(III) complex a shift toward the pure red region was observed (devices *2b*, *3b*, *3c*, *8b*, *8c*, *9b* and *9c*) (Figure 1.2.23).

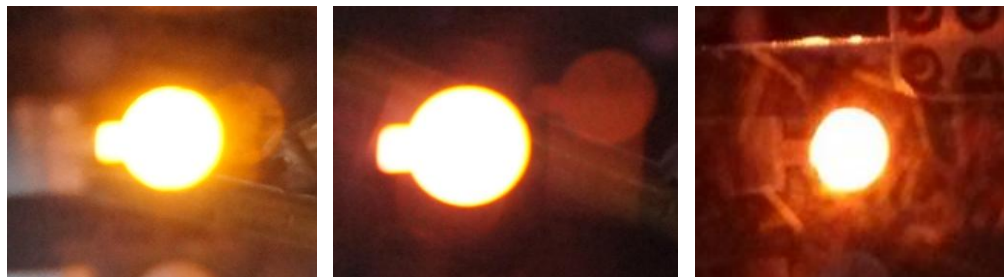
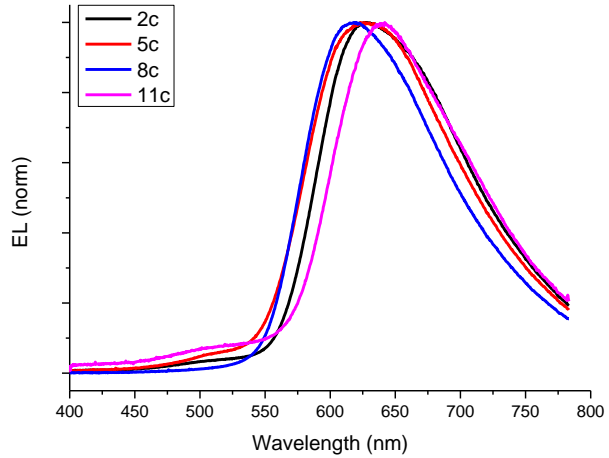
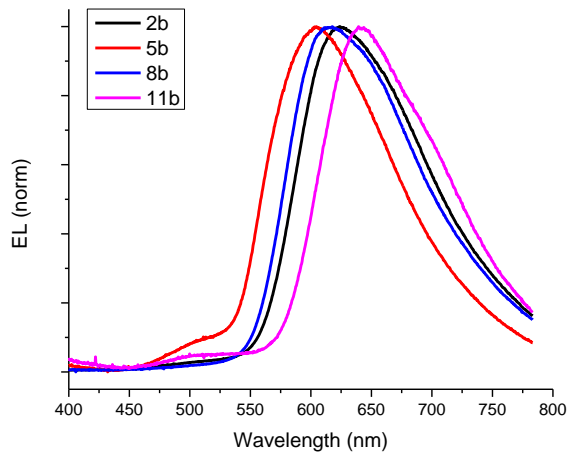
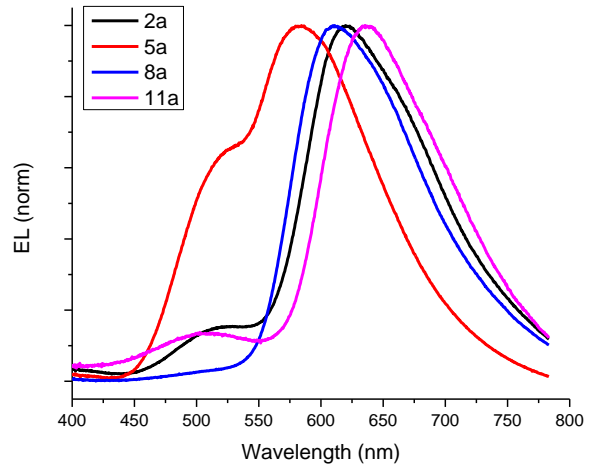
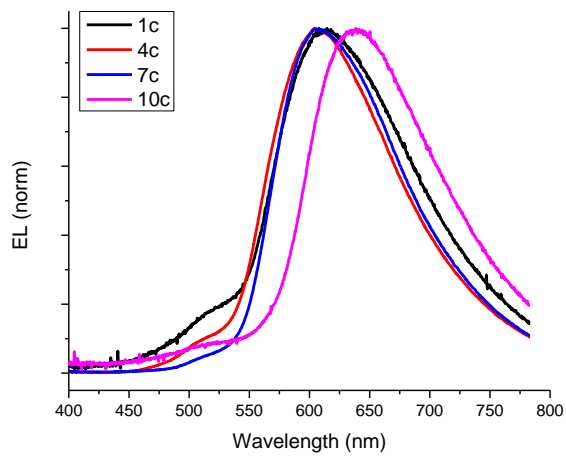
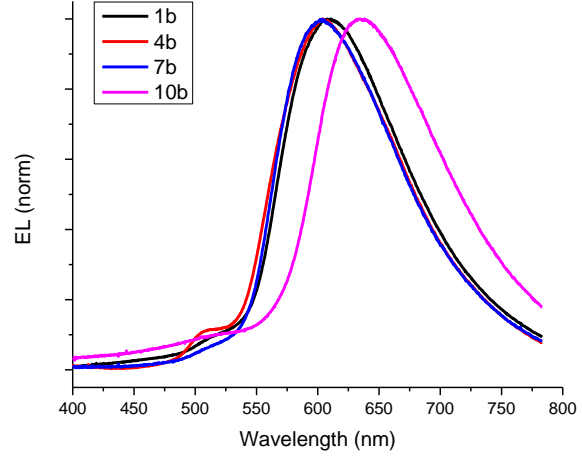
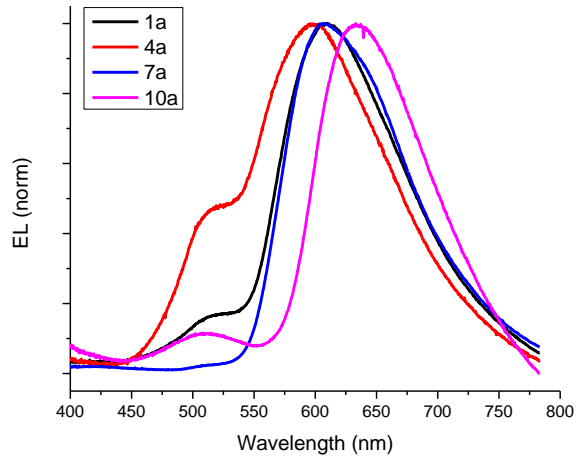


Figure 1.2.21. Biased OLEDs



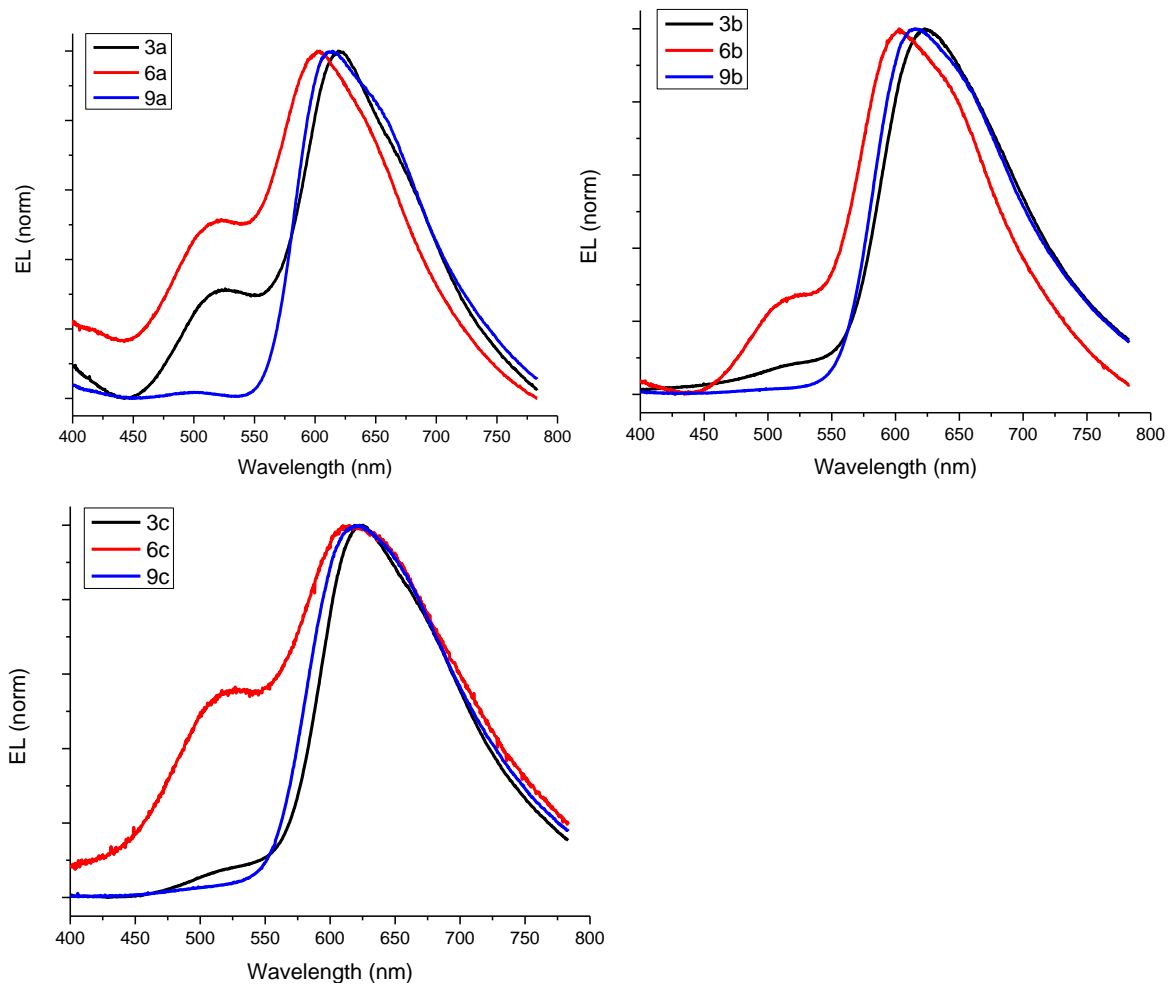


Figure 1.2.22. Normalized electroluminescence of fabricated OLED devices.

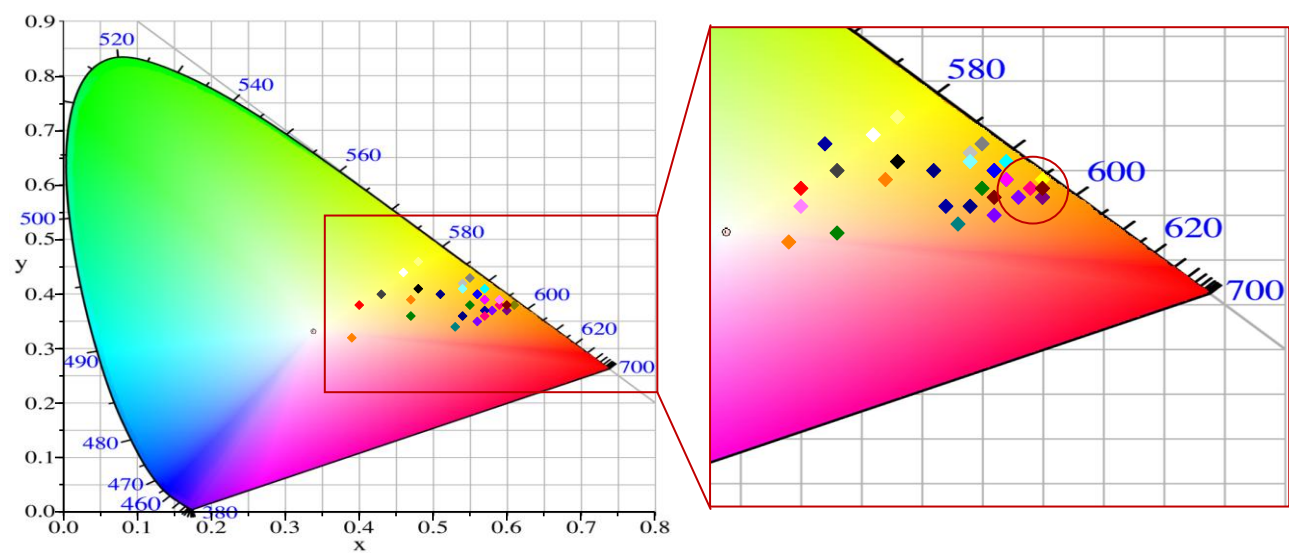


Figure 1.2.23. CIE plot of OLED devices and expansion in the red region.

~CONCLUSIONS~

In conclusion, this chapter reports on the first example of dopamine-inspired iridium complexes for applications in OLED and LEEC devices. In particular, we exploited the reactivity of a dopamine derivative, the *O,O*-dimethyldopamine, in order to synthesize a novel set of bio-inspired ligands for neutral and cationic iridium(III) complexes. The synthesis of the neutral complexes with a set of phenyldihydroisoquinolines (PHQ) as C^N ligands produced surprisingly in a one-pot reaction a set of three different complexes with different ratio between the two cyclometalating selected ligands, ppy and PHQ. The synthesis of the cationic complex with the bis-dihydroisoquinoline as N^N ligand afforded a major product identified as a cis-isomer. All the synthesized complexes showed a red emission in solution with good quantum efficiencies. The encouraging photo-physical properties prompted us to fabricate OLED devices by incorporating the synthesized neutral dopamine-inspired iridium(III) complexes as dopant in the emitter layer, deposited via a solution process unlike common thermal evaporation techniques used for this class of compounds. In particular, we tested the neutral complexes used in blend with CBP (2% or 6% or 12% wt) in the emitting layer. The devices exhibited a red electroluminescence with luminance values up to 2475 cd/m².

The cationic complex was tested as emitting layer in LEEC devices that exhibited a red electroluminescence reaching a maximum luminance value of 162 cd/m² when blended with an ionic liquid.

Therefore these data pointed out the potentiality of these new dopamine-based iridium(III) complexes as organic emitters and represent the first step toward the development of more sustainable OLED devices.

~EXPERIMENTAL SECTION~

○ MATERIALS AND METHODS

O,O-Dimethyldopamine, diethylxalate, potassium carbonate, POCl₃, ethoxyethanol, 2-phenylpyridine, iridium trichloride, benzoic acid, 4-fluorobenzoic acid, 4-methoxybenzoic acid, 4-cyanobenzoic acid, ethyl chloroformate, acetylacetone, triethylamine (TEA), CBP and BCP were purchased from Sigma-Aldrich, PEDOT:PSS was purchased from HeraeusClevios.

¹H, ¹³C and ¹⁹F spectra were acquired on a Bruker DRX (400 MHz) spectrometer. Chemical shifts are given in ppm relative to the internal standard tetramethylsilane (Me₄Si) and *J* values are given in Hz. ¹H,¹H COSY, ¹H,¹³C HSQC, ¹H,¹³C HMBC, ¹H, and NOESY experiments were run at 400.1 MHz using standard pulse programs.

Mass spectra were recorded in positive and negative ion mode using a 1100 VL LC/MSD Agilent instrument.

UV-visible and emission spectra were recorded on a Jasco V-560 and a Jasco FP-750 instruments. Quantum efficiencies (Φ) were calculated using fluorescein ($\Phi = 0.9$ in a 0.1 M solution of NaOH) as reference.

Analytical and preparative TLC were performed on silica gel plates F₂₅₄ (0.25 and 0.5 mm, respectively) and were visualized using a UV lamp ($\lambda = 254$ nm) and a fluorescence lamp ($\lambda = 356$ nm).

Liquid chromatography was performed on silica gel (60-230 mesh).

Thin films of the emitters were deposited with a spin coater Laurell WS-650MZ-23NPP/LITE on quartz from chlorobenzene solutions (10 mg/mL) using the following speed program: 3000 rpm for 30". All the films were annealed at 80 °C for 30' under a stream of nitrogen. Thin film morphology was determined with a Taylor Hobson CCI MP profilometer. The optical characterization of the OLED devices was performed using a Gooch&Housego OL770 spectroradiometer coupled with an integrating sphere and a camera telescope. The electrical measurements of the OLED devices were performed with a Keithley 2400 SourceMeter.

○ SYNTHESIS OF LIGANDS

• *N*-(3,4-dimethoxyphenethyl)benzamide (*Am_1*)

A solution of benzoic acid (500 mg, 3.47 mmol) in 28 mL of dry dimethylformamide (DMF) was cooled with an ice bath, TEA (403 mg, 3.47 mmol) and ethyl chloroformate (394 mg, 3.47

mmol) were added and under stirring and an argon atmosphere. After 1 h, *O,O*-dimethyldopamine (634 mg, 3.47 mmol) was added dropwise. The mixture was stirred at room temperature for 1 h and then heated at 50–60 °C for 1 h. The mixture was evaporated under reduced pressure and the residue extracted with an aqueous solution of NH₄Cl (10% w/w) and chloroform and then with phosphate buffer (0.1 M, pH 7.4) and chloroform. The organic layers were collected, dried over anhydrous sodium sulphate, filtered and evaporated under reduced pressure to afford the pure *N*-(3,4-dimethoxyphenethyl)benzamide (*Am_1*) (969 mg, 98%, *R_f* = 0.8 chloroform/methanol 95:5 (v/v)).

¹H NMR (400 MHz, CDCl₃) δ ppm: 7.83 (dd, *J* = 8.2, 2.3 Hz, 2H), 7.71 (t, *J* = 8.2 Hz, 1H), 7.59 (t, *J* = 8.2 Hz, 2H), 6.56 (bs, 1H), 4.31 (s, 3H, -OCH₃), 4.28 (s, 3H, -OCH₃), 4.12 (dt, *J* = 6.4, 6.0 Hz, 2H), 3.32 (t, *J* = 6.4 Hz, 2H).

- *N*-(3,4-dimethoxyphenethyl)-4-fluorobenzamide (*Am_2*)

A solution of 4-fluorobenzoic acid (140 mg, 1 mmol) in 8 mL of dry DMF was cooled with an ice bath and TEA (116 mg, 1 mmol) and ethyl chloroformate (114 mg, 1 mmol) were added under stirring and an argon atmosphere. After 1 h, *O,O*-dimethyldopamine (182 mg, 1 mmol) was added dropwise. The mixture was stirred at room temperature for 1 h and then heated at 50–60 °C for 1 h. The mixture was evaporated to dryness under reduced pressure and the residue worked-up as described above. The procedure afforded the pure *N*-(3,4-dimethoxyphenethyl)-4-fluorobenzamide (*Am_2*) (275 mg, 91%, *R_f* = 0.81 chloroform/methanol 95:5 (v/v)).

¹H NMR (400 MHz, CDCl₃) δ ppm: 7.70 (dd, *J* = 8.6, 5.3 Hz, 2H), 7.05 (t, *J* = 8.5 Hz, 2H), 6.7–6.85 (m, 3H), 6.28 (bs, 1H), 3.85 (s, 3H, -OCH₃), 3.82 (s, 3H, -OCH₃), 3.6 (dt, *J* = 6.7, 6.0 Hz, 2H), 2.85 (t, *J* = 6.72 Hz, 2H).

- *N*-(3,4-dimethoxyphenethyl)-4-methoxybenzamide (*Am_3*)

A solution of 4-methoxybenzoic acid (152 mg, 1 mmol) in 8 mL of dry DMF and dimethylformamide (DMF) was cooled with an ice bath and TEA (116 mg, 1 mmol) and ethyl chloroformate (114 mg, 1 mmol) were added under stirring and an argon atmosphere. After 1 h, *O,O*-dimethyldopamine (182 mg, 1 mmol) was added dropwise. The mixture was stirred at room temperature for 1 h and then heated at 50–60 °C for 1 h. The mixture was evaporated under reduced pressure and the residue worked-up as described above. The

procedure afforded the pure *N*-(3,4-dimethoxyphenethyl)-4-methoxybenzamide *Am_3* (295 mg, 97%, $R_f = 0.8$ CHCl₃/MeOH 95:5 (v/v)).

¹H NMR (400 MHz, CDCl₃) δ ppm: 7.65 (d, *J* = 8.4 Hz, 2H), 6.87 (d, *J* = 8.4 Hz, 2H), 6.8–6.6 (m, 3H), 6.56 (bs, 1H), 3.85 (s, 6H, -OCH₃), 3.81 (s, 3H, -OCH₃), 3.65 (m, 2H), 2.85 (t, *J* = 6.8 Hz, 2H).

¹³C NMR (100 MHz, CDCl₃) δ ppm: 167.0, 148.9, 147.5, 142.6, 133.3, 131.5, 128.6 (2C), 120.6, 113.7 (2C), 111.9, 111.3, 55.9, 55.8, 55.3, 41.2, 35.2.

- *N*-(3,4-dimethoxyphenethyl)-4-cyanobenzamide (*Am_4*)

A solution of 4-cyanobenzoic acid (147 mg, 1 mmol) in 8 mL of dry DMF was cooled with an ice bath, and under stirring and an argon atmosphere, TEA (116 mg, 1 mmol) and ethyl chloroformate (114 mg, 1 mmol) were added. After 1 h, *O,O*-dimethyldopamine (182 mg, 1 mmol) was added dropwise. The mixture was stirred at room temperature for 1 h and then heated at 50–60 °C for 1 h. The mixture was evaporated to dryness under reduced pressure and the residue worked-up as described above. The procedure afforded the pure *N*-(3,4-dimethoxyphenethyl)-4-cyanobenzamide (**7c**) (275 mg, 92%, $R_f = 0.78$ CHCl₃/MeOH 95:5 (v/v)).

¹H NMR (400 MHz, CDCl₃) δ ppm: 7.79 (d, *J* = 4 Hz, 2H), 7.70 (d, *J* = 8 Hz, 2H), 6.83 (d, *J* = 8 Hz, 1H), 6.76 (d, *J* = 12 Hz, 2H), 6.34 (bs, 1H), 3.87 (s, 3H, -OCH₃), 3.85 (s, 3H, -OCH₃), 3.71 (dt, *J* = 6.4, 6.0 Hz, 2H), 2.89 (t, *J* = 6.4 Hz, 2H).

¹³C NMR (100 MHz, CDCl₃) δ ppm: 132.40, 127.51, 120.63, 111.82 (2C), 111.37 (2C), 55.88 (2C), 41.38, 34.99.

- *N*1,*N*2-bis(3,4-dimethoxyphenethyl)oxalamide (*bis-amide*)

A solution of diethyloxalate (3.66 mL, 27 mmol) in toluene (9 mL) was added to a solution of *O,O*-dimethyldopamine (1 g, 5.9 mmol) in toluene (50 mL). The mixture was heated to reflux under argon for 5 h and then evaporated under reduced pressure. The crude solid was taken in chloroform and purified by liquid chromatography on silica gel using chloroform as the eluent to give the compound **9** (1.17 g, 95%, $R_f = 0.78$ chloroform/methanol 95:5 (v/v)).

^1H NMR (200 MHz, Acetone- d_6) δ ppm: 6.86 (d, $J = 2.0$ Hz, 1H), 6.82 (d, $J = 6.2$ Hz, 1H), 6.76 (dd, $J = 6.2, 2.0$ Hz, 1H), 3.79 (s, 3H), 3.77 (s, 3H), 3.49 (t, $J = 4.0$ Hz, 2H), 2.83 (t, $J = 4.0$ Hz, 2H).

^{13}C NMR (50 MHz, Acetone- d_6) δ ppm: 158.7, 150.2, 148.9, 132.3, 121.3, 113.4, 112.7, 63.2, 62.8, 55.9, 41.6.

- 6,7-dimethoxy-1-phenyl-3,4-dihydroisoquinoline (*PHQ*)

A solution of the amide *Am_1* (989 mg, 3.47 mmol) in 11.7 mL of a mixture 3:11 (v/v) of ethanol/dichloromethane was treated under stirring with POCl_3 (3.28 mL, 34 mmol) and kept under reflux. After 4 h, 8 mL of petroleum ether were added and the mixture was kept under reflux. After 12 h the reaction mixture was filtered and the solid was rinsed with water and treated with an aqueous solution of K_2CO_3 until pH 10 was reached. Then the mixture was extracted with chloroform and the organic layers were dried with anhydrous sodium sulphate, filtered and evaporated under reduced pressure. The crude solid was purified by liquid chromatography on silica gel using dichloromethane/methanol 95:5 (v/v) as eluent to give the pure 6,7-dimethoxy-1-phenyl-3,4-dihydroisoquinoline *PHQ* (885 mg, 95%, $R_f = 0.25$, chloroform/methanol 95:5 (v/v)).

^1H NMR (400 MHz, CDCl_3) δ ppm: 7.61 (m, 2H), 7.43 (m, 3H), 6.78 (m, 2H), 3.93 (s, 3H, - OCH_3), 3.82 (t, $J = 7.28$ Hz, 2H), 3.7 (s, 3H, - OCH_3), 2.75 (t, $J = 7.28$ Hz, 2H).

^{13}C NMR (100 MHz, CDCl_3) δ ppm: 167.0, 151.3, 147.2, 138.5, 132.8, 129.6, 128.9, 128.2, 121.3, 111.9, 110.4, 56.2, 56.1, 47.2, 26.0.

ESI⁺ MS: m/z 268.2.

- 1-(4-fluorophenyl)-6,7-dimethoxy-3,4-dihydroisoquinoline (*FPHQ*)

A solution of the amide *Am_2* (261 mg, 0.86 mmol) in 2.1 mL of a mixture 3:11 (v/v) of ethanol/dichloromethane was treated under stirring with POCl_3 (0.8 mL, 8.6 mmol) and kept under reflux. After 4 h, 8 mL of petroleum ether were added and the mixture was kept under reflux. After 12 h the reaction mixture was filtered and the solid was rinsed with water and worked-up as reported above. The crude solid was purified by liquid chromatography on silica gel using chloroform/methanol 95:5 (v/v) as eluent to give the pure 6,7-dimethoxy-1-phenyl-3,4-dihydroisoquinoline (*FPHQ*) (187 mg, 76%, $R_f = 0.24$, chloroform/methanol 95:5 (v/v)).

^1H NMR (400 MHz, CDCl_3) δ ppm: 7.60 (dd, $J=8.4, 5.6$ Hz, 2H), 7.11 (t, $J = 8.4$, 2H), 6.78 (s, 1H), 6.74 (s, 1H), 3.94 (s, 3H, $-\text{OCH}_3$), 3.79 (t, $J = 7.4$, 2H), 3.73 (s, 3H, $-\text{OCH}_3$), 2.73 (t, $J=7.4$ Hz, 2H).

ESI⁺ MS: m/z 286.1.

- 1-(4-methoxyphenyl)-6,7-dimethoxy-3,4-dihydroisoquinoline (*OMePHQ*)

A solution of the amide *Am_3* (295 mg, 0.97mmol) in 3.1 mL of a mixture 3:11 (v/v) of ethanol/dichloromethane was treated under stirring with POCl_3 (0.86 mL, 9.4 mmol) and kept under reflux. After 4 h, 2 mL of petroleum ether were added and the mixture was kept under reflux. After 12 h the reaction mixture was filtered and the solid was rinsed with water and worked-up as reported above. The crude solid was purified by liquid chromatography on silica gel using ether/ethyl acetate 1:1 (v/v) as eluent to give the pure 1-(4-methoxyphenyl)-6,7-dimethoxy-3,4-dihydroisoquinoline (*OMePHQ*) (200 mg, 70%, $R_f = 0.75$, DCM/MeOH95:5 (v/v)).

^1H NMR (400 MHz, CDCl_3) δ ppm: 7.59 (d, $J = 8.8$ Hz, 2H), 6.95 (d, $J = 8.8$ Hz, 2H), 6.84 (s, 1H), 6.78 (s, 1H), 3.95 (s, 3H, $-\text{OCH}_3$), 3.86 (s, 3H, $-\text{OCH}_3$), 3.82 (t, $J = 7.28$ Hz, 2H), 3.74 (s, 3H, $-\text{OCH}_3$), 2.55 (t, $J = 7.28$ Hz, 2H).

^{13}C NMR (100 MHz, CDCl_3) δ ppm: 166.5, 160.9, 151.3, 147.2 (2C), 133.0, 130.5 (2C), 121.3, 113.6 (2C), 112.0, 110.3 (2C), 56.2, 56.1, 55.4, 46.9, 26.1.

- 1-(4-cyanophenyl)-6,7-dimethoxy-3,4-dihydroisoquinoline (*CNPHQ*)

A solution of the amide *Am_4* (275 mg, 0.92mmol) in 3.1 mL of a mixture 3:11 (v/v) of ethanol/dichloromethane was treated under stirring with POCl_3 (0.86 mL, 9.4 mmol) and kept under reflux. After 4 h, 2 mL of petroleum ether were added and the mixture was kept under reflux. After 12 h the reaction mixture was filtered and the solid was rinsed with water and worked-up as reported above. The crude solid was purified by liquid chromatography on silica gel using ether/ethyl acetate 1:1 (v/v) as eluent to give the pure 1-(4-cyanophenyl)-6,7-dimethoxy-3,4-dihydroisoquinoline (*CNPHQ*) (193 mg, 66%, $R_f = 0.8$, AcOEt/CE 7:3 (v/v)).

^1H NMR (400 MHz, CDCl_3) δ ppm: 7.74 (s, 4H), 6.84 (s, 2H), 6.65 (s, 2H), 3.96 (s, 3H, $-\text{OCH}_3$), 3.85 (t, $J = 8$ Hz, 2H), 3.74 (s, 3H, $-\text{OCH}_3$), 2.76 (t, $J = 8$ Hz).

^{13}C NMR (100 MHz, CDCl_3) δ ppm: 165.39, 151.39, 147.33, 143.60, 132.62, 132.09 (2C), 129.47 (2C), 120.72, 118.63, 112.98, 110.52, 56.21, 56.09, 47.93, 25.84.

- Bis(6,7-dimethoxy-3,4-dihydroisoquinoline) (DHQ)

A solution of the amide **8** (1.17 g, 2.8 mmol) in 11 mL of a mixture 3:11 (v/v) of ethanol/dichloromethane was treated under stirring with POCl_3 (3.7 mL, 39 mmol) and kept under reflux. After 5 h 8.9 mL of petroleum ether were added and the mixture was kept under reflux. After 12 h the reaction mixture was filtered and the solid was rinsed with water and worked-up as reported above. The crude solid was purified by liquid chromatography on silica gel using chloroform as eluent to give the pure bis(6,7-dimethoxy-3,4-dihydroisoquinoline) **2** (650 mg, 61%, Rf = 0.75, chloroform/methanol 95:5 (v/v)).

^1H NMR (400 MHz, CDCl_3) δ ppm: 7.24 (s, 1H), 6.57 (s, 1H), 3.78 (s, 3H), 3.75 (s, 3H), 3.71 (t, J = 7.6 Hz, 2H), 2.56 (t, J = 7.6, 2H).

^{13}C NMR (50 MHz, CDCl_3) δ ppm: 164.4, 151.3, 147.1, 131.2, 118.5, 110.0, 109.8, 55.7, 55.5, 47.2, 24.7.

ESI+ MS: m/z 381

- SYNTHESIS OF COMPLEXES

- Synthesis of $[\text{Ir}(\text{ppy})_2\text{Cl}]_2$ ($\mu\text{-Ir}$)

Iridium trichloride hydrate (500 mg, 1.67 mmol) was dissolved in a mixture of 32 mL of 2-ethoxyethanol and water 3:1 (v/v) and treated with 480 μL (3.6 mmol) of 2-phenylpyridine under reflux and argon atmosphere. After 24 h the reaction mixture was cooled and filtered on a glass filter frit to obtain $\mu\text{-Ir}$ as a yellow precipitate (644 mg, 72%).

^1H NMR (400 MHz, DMSO-d_6) δ ppm: 9.81 (d, J = 5.6 Hz), 9.53 (d, J = 5.6 Hz), 8.26 (d, J = 8.0 Hz), 8.18 (d, J = 8.0 Hz), 8.11 (t, J = 8.0 Hz), 8.02 (t, J = 8.0 Hz), 7.79 (d, J = 8.0 Hz), 7.73 (d, J = 8.0 Hz), 7.56 (t, J = 5.6 Hz), 7.44 (t, J = 5.6 Hz), 6.89 (t, J = 8.0 Hz), 6.83 (t, J = 8.0 Hz), 6.76 (t, J = 8.0 Hz), 6.69 (t, J = 8.0 Hz), 6.25 (d, J = 8.0 Hz), 5.66 (d, J = 8.0 Hz).

- Synthesis of the iridium complexes Ir-PHQ-1-3

A solution of the iridium complex $\mu\text{-Ir}$ (119 mg, 0.11 mmol) in DMF dry (15 mL) was treated under an argon atmosphere with PHQ (276 mg, 0.89 mmol), acetylacetone (22 mg, 0.22 mmol)

and TEA (22 mg, 0.22 mmol) and kept under reflux for 48 h. The solvent was evaporated under reduced pressure and the solid was subjected to liquid chromatography on silica gel (eluent ethyl acetate/cyclohexane 3:7 (v/v)) to afford complexes *Ir_PHQ_1-3* in pure form (*Ir_PHQ_1*: 21.4 mg, 16%, $R_f = 0.67$; *Ir_PHQ_2*: 26.4 mg, 14%, $R_f = 0.6$; *Ir_PHQ_3*: 10.8 mg, 5%, $R_f = 0.48$, ethyl acetate/cyclohexane 7:3 (v/v)).

Ir_PHQ_1: ^1H NMR (400 MHz, CD_2Cl_2) δ ppm: 8.17 (d, $J = 5.2$ Hz, 1H), 7.94 (d, $J = 8.4$ Hz, 1H), 7.89 (d, $J = 8.4$ Hz, 1H), 7.80 (d, $J = 8.4$ Hz, 1H), 7.67-7.72 (m, 4H), 7.61 (t, $J = 8.0$ Hz, 1H), 7.56 (d, $J = 5.2$ Hz, 1H), 7.53 (s, 1H), 7.05 (t, $J = 6.4$ Hz, 1H), 6.6-7.0 (m, 10H), 3.89 (s, 3H, -OCH₃), 3.88 (s, 3H, -OCH₃), 3.42 (m, 1H), 3.00 (m, 1H), 2.67 (m, 1H), 2.41 (m, 1H).

^{13}C NMR (100 MHz, CD_2Cl_2) δ ppm: 175.4, 166.5, 166.2, 165.5, 162.5, 161.1, 151.4, 148.3, 147.7, 144.5, 143.0, 136.8, 136.7, 136.6, 136.1, 135.8, 129.6, 129.5, 129.1, 124.0, 123.6, 122.1, 121.7, 119.8, 119.5, 118.9, 118.8, 118.5, 112.0, 110.5, 56.2, 55.8, 47.7, 27.8.

ESI⁺ MS: $m/z \approx 767.2$.

Ir_PHQ_2: ^1H NMR (400 MHz, CD_2Cl_2) δ ppm: 8.15 (d, $J = 5.2$ Hz, 1H), 7.90 (d, $J = 8.0$ Hz, 1H), 7.6-7.85 (m, 4H), 7.54 (s, 1H), 7.51 (s, 1H), 6.99 (t, $J = 6.4$ Hz, 1H), 6.65-6.95 (m, 11H), 3.93 (s, 9H, -OCH₃), 3.92 (s, 3H, -OCH₃), 3.71 (m, 1H), 3.46 (m, 1H), 3.40 (m, 1H), 2.69 (m, 1H), 2.62 (m, 1H), 2.46 (m, 1H), 2.38 (m, 1H).

^{13}C NMR (100 MHz, CD_2Cl_2) δ ppm: 174.5, 174.2, 167.6, 166.6, 165.0, 162.9, 150.8, 150.7, 148.1, 147.2, 145.4, 145.3, 144.5, 137.3, 137.06, 137.01, 136.2, 132.2, 132.1, 130.1, 129.9, 129.8, 129.7, 126.7, 125.1, 124.1, 122.6, 122.3, 120.0, 119.3, 119.1, 119.0, 114.1, 112.3, 110.9, 56.6, 56.2, 49.1, 48.3, 28.0, 28.2.

ESI⁺ MS: $m/z \approx 879.3$.

Ir_PHQ_3: ^1H NMR (400 MHz, CD_2Cl_2) δ ppm: 7.78 (d, $J = 8.0$ Hz, 1H), 7.51 (s, 1H), 6.7-6.9 (m, 4H), 3.88 (s, 3H, -OCH₃), 3.87 (s, 3H, -OCH₃), 3.68 (m, 1H), 3.38 (m, 1H), 2.68 (m, 1H), 2.43 (m, 1H).

^{13}C NMR (100 MHz, CD_2Cl_2) δ ppm: 174.4, 166.5, 150.9, 147.6, 145.4, 136.8, 131.9, 129.9, 129.7, 122.5, 119.2, 57.8, 54.9, 48.4, 27.9.

ESI⁺ MS: $m/z \approx 991.3$.

- Synthesis of the iridium complexes *Ir_FPHQ_1-3*

A solution of the iridium complex μ _Ir (40 mg, 0.037 mmol) in DMF dry (5 mL) was treated under an argon atmosphere with *FPHQ* (44.4 mg, 0.15 mmol), acetylacetone (7.6 mg, 0.074 mmol) and TEA (7.7 mg, 0.074 mmol) and kept under reflux for 48 h. The solvent was evaporated under reduced pressure and the solid was subjected to liquid chromatography on silica gel (eluent chloroform/ethyl acetate 6:4 (v/v)) to afford complexes *Ir_FPHQ_1-3* in pure form (*Ir_FPHQ_1*: 34 mg, 59%, $R_f = 0.76$; *Ir_FPHQ_2*: 14.2 mg, 21%, $R_f = 0.7$; *Ir_FPHQ_3*: 4.6 mg, 6%, $R_f = 0.65$, chloroform/acetate 6:4 (v/v)).

Ir_FPHQ_1: $^1\text{H NMR}$ (400 MHz, CD_2Cl_2) δ ppm: 8.20 (d, $J = 6.2$ Hz, 1H), 7.99 (d, $J = 8.0$, 1H), 7.93 (d, $J = 8.0$ Hz, 1H), 7.82 (dd, $J = 8.0, 6.2$ Hz, 1H), 7.5-7.7 (m, 4H), 7.65 (t, $J = 8.0$ Hz, 1H), 7.57 (d, $J = 5.5$ Hz, 1H), 7.49 (s, 1H), 7.08 (t, $J = 6.4$ Hz, 1H), 6.85-7.0 (m, 5H), 6.79 (t, $J = 8.0$ Hz, 1H), 6.8 (s, 1H), 6.76-6.72 (m, 2H), 6.60 (t, $J = 8.0$ Hz, 1H), 6.48 (dd, $J = 8.0$ Hz, 1H), 3.92 (s, 3H, -OCH₃), 3.91 (s, 3H, -OCH₃), 3.43 (m, 1H), 3.00 (m, 1H), 2.69 (m, 1H), 2.45 (m, 1H).

$^{13}\text{C NMR}$ (100 MHz, CD_2Cl_2) δ ppm: 176.6, 171.5, 168.47, 168.41, 166.3, 167.1, 164.7, 164.3, 162.3, 153.9, 151.0, 148.3, 145.3, 145.1, 138.5, 138.1, 134.0, 131.9, 126.4, 125.8, 124.3, 123.9, 121.9, 120.9, 56.2, 55.8, 47.6, 27.9.

$^{19}\text{F NMR}$ (376 MHz, CD_2Cl_2) δ ppm: -112.01.

ESI⁺ MS: m/z 785.3.

Ir_FPHQ_2: $^1\text{H NMR}$ (400 MHz, CD_2Cl_2) δ ppm: 8.15 (d, $J = 6.4$ Hz, 1H), 7.95 (d, $J = 8.0$ Hz, 1H), 7.75-8.0 (m, 2H), 7.69 (d, $J = 8.0$, 1H), 7.66 (t, $J = 7.28$ Hz, 1H), 7.47 (s, 1H), 7.43 (s, 1H), 6.93 (t, $J = 7.28$ Hz, 1H), 6.87 (t, $J = 7.28$ Hz, 1H), 6.80 (t, $J = 7.28$ Hz, 1H), 6.73 (s, 1H), 6.71 (s, 1H), 6.74 (d, $J = 7.28$ Hz, 1H), 6.55-6.65 (m, 2H), 6.35-6.45 (m, 2H), 3.93 (s, 3H, -OCH₃), 3.93 (s, 3H, -OCH₃), 3.92 (s, 3H, -OCH₃), 3.89 (s, 3H, -OCH₃), 3.88 (s, 3H, -OCH₃), 3.70 (m, 1H), 3.47 (m, 1H), 3.40 (m, 1H), 2.94 (m, 1H), 2.74 (m, 1H), 2.66 (m, 1H), 2.51 (m, 1H), 2.41 (m, 1H).

$^{13}\text{C NMR}$ (100 MHz, CD_2Cl_2) δ ppm: 174.2, 173.1, 170.6, 168.2, 166.3, 165.2, 162.3, 161.1, 151.1, 150.9, 148.3, 147.3, 147.2, 144.0, 141.4, 136.7, 136.1, 131.9, 131.8, 131.2, 131.1, 129.9, 123.8, 122.0, 121.7, 120.0, 118.8, 111.8, 110.5, 56.2, 55.9, 48.6, 47.7, 28.0, 27.7.

$^{19}\text{F NMR}$ (376 MHz, CD_2Cl_2) δ ppm: -11.75, -112.07.

ESI⁺ MS: m/z 915.5.

Ir_FPHQ_3: ^1H NMR (400 MHz, CD_2Cl_2) δ ppm: 7.83 (dd, $J = 8.0, 6.4$ Hz, 1H), 7.49 (s, 1H), 6.82 (s, 1H), 6.65 (dt, $J = 8.0, 2.7$ Hz, 1H), 6.42 (dd, $J = 8.0, 2.7$ Hz, 1H), 3.93 (s, 3H, $-\text{OCH}_3$), 3.91 (s, 3H, $-\text{OCH}_3$), 3.69 (m, 1H), 3.40 (m, 1H), 2.71 (m, 1H), 2.49 (m, 1H).

^{13}C NMR (100 MHz, CD_2Cl_2) δ ppm: 173.4, 169.3, 165.3, 163.1, 151.0, 147.3, 141.4, 131.8, 130.8, 121.9, 121.6, 111.7, 110.5, 106.2, 56.2, 55.9, 48.8, 27.9.

^{19}F NMR (376 MHz, CD_2Cl_2) δ ppm: -111.77.

ESI⁺ MS: m/z 1045.3.

- Synthesis of the iridium complexes *Ir_OMePHQ_1-3*

A solution of the iridium complex $\mu\text{-Ir}$ (67 mg, 0.064mmol) in DMFdry (4 mL) was treated under an argon atmosphere with *OMePHQ* (150 mg, 0.5mmol), acetylacetone (25 mg, 0.25mmol) and TEA (26 mg, 0.25mmol) and kept under reflux for 48 h. The solvent was evaporated under reduced pressure and the solid was subjected to liquid chromatography on silica gel (eluent cyclohexane/ethyl acetate 4:6 (v/v)) to afford complexes *Ir_OMePHQ_1-3* in pure form (*Ir_OMePHQ_1*: 15.7 mg, 16%, $R_f = 0.76$; *Ir_OMePHQ_2*: 12.1 mg, 11%, $R_f = 0.66$; *Ir_OMePHQ_3*: 12.4 mg, 6%, cyclohexane/acetate 4:6 (v/v)).

Ir_OMePHQ_1: ^1H NMR (400 MHz, CDCl_3) δ ppm: 8.15 (d, $J = 5.2$ Hz, 1H), 7.89 (d, $J = 8.4$ Hz, 1H), 7.84 (d, $J = 8.4$ Hz, 1H), 7.71 (d, $J = 8.4$ Hz, 1H), 7.6-7.7 (m, 4H), 7.53 (m, 1H), 7.51 (s, 1H), 6.6-7.0 (m, 8H), 6.72 (s, 1H), 6.4-6.5 (m, 2H), 3.89 (s, 3H, $-\text{OCH}_3$), 3.88 (s, 3H, $-\text{OCH}_3$), 3.54 (s, 3H, $-\text{OCH}_3$), 3.41 (m, 1H), 3.00 (m, 1H), 2.63 (m, 1H), 2.52 (m, 1H).

^{13}C NMR (100 MHz, CDCl_3) δ ppm: 173.6, 172.9, 170.5, 167.9, 166.8, 162.8, 160.5 (2C), 150.4, 150.2, 148.4, 147.0 (2C), 143.9, 137.9, 137.8, 137.3, 135.5, 131.9, 131.7, 130.4, 129.9, 129.8, 123.5, 122.7, 122.6, 121.7, 120.5, 119.5, 118.5 (2C), 111.7, 110.2, 105.9, 56.4, 56.1, 56.0, 54.5, 47.3, 28.1.

Ir_OMePHQ_2: ^1H NMR (400 MHz, CDCl_3) δ ppm: 8.12 (d, $J = 5.2$ Hz, 1H), 7.85 (d, $J = 8.0$ Hz, 1H), 7.7 (d = 8.0 Hz, 2H), 7.64 (d, $J = 7.6$ Hz, 1H), 7.58 (t, $J = 7.6$ Hz, 1H), 7.52 (s, 1H), 7.50 (s, 1H), 6.8-6.9 (m, 4H), 6.72 (s, 1H), 6.69 (s, 1H), 6.4-6.5 (m, 3H), 6.36 (d, $J = 8.4$ Hz, 1H), 3.89 (s, 9H, $-\text{OCH}_3$), 3.86 (s, 3H, $-\text{OCH}_3$), 3.57 (s, 3H, $-\text{OCH}_3$), 3.5 (m, 1H), 3.3-3.4 (m, 2H), 2.9-3.0 (m, 2H), 2.6 (m, 1H), 2.4-2.5 (m, 2H).

^{13}C NMR (100 MHz, CDCl_3) δ ppm: 173.6, 172.9, 170.5, 167.9, 166.8, 162.8, 160.5 (2C), 150.4, 150.2, 148.4, 147.0 (2C), 143.9, 137.9, 137.8, 137.3, 135.5, 131.9, 131.7, 130.4, 129.9, 129.8,

123.5, 122.7, 122.6, 121.7, 120.5, 120.3, 119.5, 118.5 (2C), 111.7, 110.3, 110.2, 105.9, 105.2, 56.4, 56.3, 56.1, 56.0, 54.6, 54.5, 48.1, 47.3, 28.4, 28.1.

Ir_OMePHQ_3: ^1H NMR (400 MHz, CDCl_3) δ ppm: 7.68 (d, $J = 8.0$ Hz, 1H), 7.50 (s, 1H), 6.74 (s, 1H), 6.43 (dd, $J = 8.0, 1.3$ Hz, 1H), 6.41 (d, $J = 8.0$ Hz, 1H), 3.89 (s, 3H, $-\text{OCH}_3$), 3.86 (s, 3H, $-\text{OCH}_3$), 3.71 (m, 1H), 3.64 (s, 3H, $-\text{OCH}_3$), 3.41 (m, 1H), 2.63 (m, 1H), 2.42 (m, 1H).

^{13}C NMR (100 MHz, CDCl_3) δ ppm: 166.5, 164.4, 150.9, 147.6, 145.4, 136.8, 131.9, 129.9, 125.7, 122.5, 121.3, 112.0, 110.3, 57.8, 57.2, 54.9, 48.4, 27.9.

- Synthesis of the iridium complexes *Ir_CNPHQ_1-2*

A solution of the iridium complex $\mu\text{-Ir}$ (46 mg, 0.043 mmol) in DMF dry (4 mL) was treated under an argon atmosphere with *CNPHQ* (100 mg, 0.34 mmol), acetylacetone (17 mg, 0.17 mmol) and TEA (17.8 mg, 0.17 mmol) and kept under reflux for 48 h. The solvent was evaporated under reduced pressure and the solid was subjected to liquid chromatography on silica gel (eluent cyclohexane/DCM/ethyl acetate 1.5:1.5:7 (v/v)) to afford complexes *Ir_CNPHQ_1-2* in pure form (*Ir_CNPHQ_1*: 14 mg, 22%, $R_f = 0.75$; *Ir_CNPHQ_2*: 12 mg, 15%, $R_f = 0.5$; cyclohexane/DCM/ethyl acetate 1.5:1.5:7 (v/v)).

Ir_CNPHQ_1: ^1H NMR (400 MHz CD_2Cl_2) δ ppm: 8.14 (d, $J = 5.6$ Hz, 1H), 8.00 (d, $J = 7.7$ Hz, 1H), 7.93 (d, $J = 7.4$ Hz, 1H), 7.87 (d, $J = 8$ Hz, 1H), 7.75-7.71 (m, 3H), 7.66 (t, $J = 7.8$ Hz, 1H), 7.56 (d, $J = 5.4$ Hz, 1H), 7.45 (s, 1H), 7.17 (d, $J = 8$ Hz, 1H), 7.13 (s, 1H), 7.07 (t, $J = 6$ Hz, 1H), 6.95-8.85 (m, 6H), 6.81 (s, 1H), 6.70 (d, $J = 8$ Hz, 1H), 6.63 (d, $J = 7.3$, 1H), 3.9 (s, 6H, $-\text{OCH}_3$), 3.52 (m, 1H), 3.41 (m, 1H), 2.79 (m, 1H), 2.47 (m, 1H).

^{13}C NMR (125 MHz CD_2Cl_2) δ ppm: 139.65, 136.84, 136.52, 136.20, 129.95, 128.57, 124.36, 123.75, 122.39, 122.31, 121.95, 120.49, 120.05, 119.21, 118.78, 112.02, 111.59, 110.63, 47.50, 29.67.

Ir_CNPHQ_2: ^1H NMR (400 MHz CD_2Cl_2) δ ppm: 8.11 (d, $J = 4$ Hz, 1H), 7.98 (d, $J = 8$ Hz, 1H), 7.91 (d, $J = 8$ Hz, 1H), 7.88-7.85 (m, 3H), 7.77-7.71 (m, 3H), 7.62 (d, $J = 4$ Hz, 1H), 7.48 (s, 1H), 7.42 (s, 1H), 7.27-7.22 (m, 3H), 7.20 (d, $J = 2$ Hz, 1H), 7.05 (d, $J = 4$ Hz, 1H), 6.96 (d, $J = 2$ Hz, 1H), 6.85 (s, 1H), 6.79 (s, 1H), 3.94 (s, 3H, $-\text{OCH}_3$), 3.93 (s, 3H, $-\text{OCH}_3$), 3.93 (s, 3H, $-\text{OCH}_3$), 3.9 (s, 3H, $-\text{OCH}_3$), 3.48-2.34 (m, 8H)

^{13}C NMR (100 MHz CD_2Cl_2) δ ppm: 173.9, 151.8, 151.4, 147.4, 143.9, 139.5, 136.6, 136.5, 132.2, 131.8, 130.4, 119.1, 112.4, 111.5, 110.6, 66.3, 56.3, 55.9, 33.9, 31.9, 29.7, 29.6, 29.4, 28.9, 27.7, 23.8, 22.7, 13.8.

- Synthesis of the iridium complex *Ir_DHQ*

A suspension of $\mu\text{-Ir}$ (396 mg, 0.37 mmol) in $\text{CH}_2\text{Cl}_2/\text{MeOH}$ (78 mL, 2:1 v/v) was treated under stirring with *DHQ* (280 mg, 0.737 mmol) and heated to reflux. After 45 min the solution was cooled to room temperature and treated with NH_4PF_6 (598.2 mg, 3.07 mmol), dissolved in methanol (9.7 mL). After 30 min the reaction mixture was evaporated under reduced pressure and the red residue was rinsed with CH_2Cl_2 , filtered to remove insoluble inorganic salts and evaporated under reduced pressure. The crude solid was purified by liquid chromatography on silica gel using dichloromethane/methanol 99:1 (v/v) affording the complex *Ir_DHQ* in pure form (564 mg, 75%, $R_f = 0.52$ chloroform/methanol 95:5 (v/v)).

^1H NMR (400 MHz, CDCl_3) δ ppm: 8.72 (d, $J = 5.6$ Hz), 8.65 (s), 8.21 (d, $J = 5.6$ Hz), 7.85 (m), 7.72 (m), 7.56 (m), 7.18 (t, $J = 5.6$ Hz), 7.07 (t, $J = 5.6$ Hz), 6.9-6.6 (m), 6.57 (s), 6.35 (d, $J = 8.0$ Hz), 6.11 (d, $J = 8.0$ Hz), 3.97 (s), 3.87 (s), 3.55 (m), 3.12 (m), 2.62 (m), 2.34 (m).

^{13}C NMR (100 MHz, CDCl_3) δ ppm: 167.2, 155.2, 151.4, 149.6, 147.8, 147.7, 147.3, 146.7, 136.1, 136.0, 131.5, 131.2, 129.7, 128.5, 128.7, 123.3, 123.1, 121.5, 121.2, 121.1, 120.8, 119.8, 118.2, 117.1, 111.8, 116.7, 108.7, 108.0, 107.6, 55.78, 55.59, 47.22, 24.73.

ESI⁺ MS: m/z 879.9; ESI⁻ MS: m/z 144.7.

- DEVICE FABRICATION

Indium tin oxide ITO-coated glass plates ($15 \Omega \text{ sq}^{-1}$) were patterned by conventional photolithography. The substrates were cleaned with deionized water and detergent (deconex) at 80 °C in a ultrasonic bath, then rinsed with water, acetone and isopropyl alcohol and dried in oven at 130 °C for two hours. After drying, the substrates were placed in a UV-ozone cleaner (Jelight 42-220) for 5 min before spin coating a water solution of PEDOT:PSS, previously filtered through a 0.2 μm PVDF filter. To afford a 40 nm thick layer, the following spin-coating parameters were used: 3000 rpm, 500 rpm^{-1} for 30 sec.

The PEDOT:PSS layer was patterned and baked in a vacuum oven at 110 °C for 2 h.

OLED devices were fabricated as follows.

For the deposition of the complexes Ir_PHQ_1-3, Ir_FPHQ_1-3, Ir_OMePHQ_1-3 and Ir_CNPHQ_1-2 as emitting layer, a 10mg/ml solution of CBP in chlorobenzene was added with the proper amount of the dopamine-inspired iridium(III) complex (2%, 6% or 12% wt). Each solution was filtered through a 0.2 μm PTFE filter and spin coated on the glass/ITO/PEDOT:PSS substrate using the following parameters: 3000 rpm, 500 rpm^{-1} for 30 seconds. The samples were placed on a hot plate at 80 $^{\circ}\text{C}$ for 30 minutes in glove box (<0.1 ppm O_2 and H_2O , MBraun). Samples were then loaded in the evaporator process chamber for BCP, Alq₃ and calcium/silver deposition.

LEEC devices were fabricated as follows.

For the deposition of the emitting layer, 90 nm thick films (consisting of the emitter alone or in blend with the dimethylimidazoliumdimethylphosphate [DMIM][DMP] ionic liquid ($>98.5\%$, Sigma-Aldrich) at a molar ratio of 4 to 1) were spin-coated from 20 mg mL^{-1} chlorobenzene solution at 1000 rpm for 20 s. The devices were transferred to an inert atmosphere glovebox (<0.1 ppm O_2 and H_2O , MBraun) and annealed at 100 $^{\circ}\text{C}$ for 1 h. Finally, using a shadow mask, the aluminum electrode (70 nm) was thermally evaporated under vacuum ($<1 \times 10^{-6}$ mbar) with a Lesker evaporator integrated in the glovebox. The area of the device was 6.534 mm^2 . The devices were not encapsulated and were characterized inside the glovebox at room temperature.

Thin films of the emitters and PEDOT:PSS were deposited with a spin coater Laurell WS-650MZ-23NPP/LITE on quartz from chlorobenzene solutions (10 mg/mL) using the following speed program: 3000 rpm for 30". The optical characterization of the LEEC devices was performed using a Gooch&Housego OL770 spectroradiometer coupled with an integrating sphere and a camera telescope. The electrical measurements of the LEEC devices were performed with a Keithley 2400 SourceMeter.

REFERENCES

- [1]. Hui Xu, Wei Huang, Xiaogang Liu et al., *Chem. Soc. Rev.*, **2014**, 43, 3207-3812.
- [2]. C. W. Tang, *Appl. Phys. Lett.*, **1986**, 48, 183-185.
- [3]. C. W. Tang and S. A. Van Slyke, *Appl. Phys. Lett.*, **1987**, 51, 913-915.
- [4]. L. De Cola, et al. *Inorg. Chem.*, **2013**, 52, 1812
- [5]. Y. Cao, et al. *Nature.*, **1999**, 397, 414.
- [6]. S. Sprouse, K. A. King, P. J. Spellane, and R. J. Watts, *J. Am. Chem. Soc.* **1984**, 106, 6647-6653
- [7]. P.J. Hay, *J. Phys. Chem. A*, **2002**, 106, 1634.
- [8]. E. Baranoff, J. H. Yum, M. Graetzel, M.d.K. Nazeeruddin, *Journal of Organometallic Chemistry*, **2009**, 694, 2661-2670
- [9]. P. Manini, L. Panzella, I. Tedesco, F. Petitto, Gian Luigi Russo, A. Napolitano, A. Palumbo and M. d'Ischia, *Chem. Res. Toxicol.* **2004**, 17, 1190-1198
- [10]. K. Chen, C.-H. Yang, Y. Chi, C.-S. Liu, C.-H. Chang, C.-C. Chen, C.-C. Wu, M.-W. Chung, Y.-M. Cheng, G.-H. Lee and Pi-Tai Chou, *Chem. Eur. J.* 2010, 16, 4315 - 4327
- [11]. Sprouse, S.; King, K. A.; Spellane, P. J.; Watts, R. J. *J. Am. Chem. Soc.* **1984**, 106, 6647.
- [12]. F. Neve, M. La Deda, A. Crispini, A. Bellusci, F. Puntoriero and S. Campagna, *Organometallics*, **2004**, 23, 5856-5863
- [13]. J. M. Fernandez-Hernandez, C.-H. Yang, J. I. Beltran, V. Lemaure, F. Polo, R. Frohlich, J. Cornil and L. De Cola, *J. Am. Chem. Soc.* **2011**, 133, 10543-10558
- [14]. Tao Hu, Lei He, Lian Duan* and Yong Qiu, *J. Mater. Chem.*, **2012**, 22, 4206
- [15]. S. T. Parker, J. D. Slinker, M. S. Lowry, M. P. Cox, S. Bernhard and G. G. Malliaras, *Chem. Mater.* **2005**, 17, 3187-3190

SECTION 1

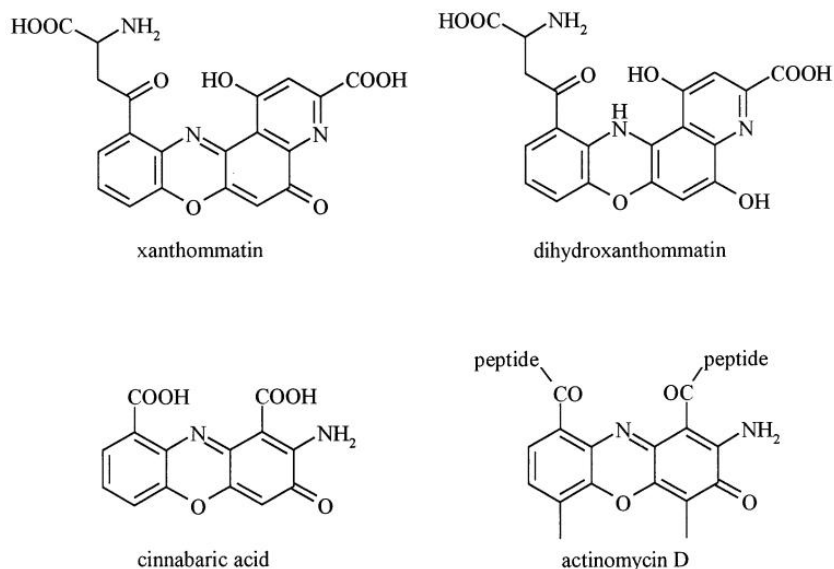
CHAPTER 3

SYNTHESIS AND PHOTOPHYSICAL PROPERTIES OF IRIDIUM(III) COMPLEXES WITH PYRIDOPHENOXAZINONE LIGANDS

~INTRODUCTION~

With the aims of designing other nature-inspired iridium(III) complexes, the potential of the pyridophenoxazinone heterocyclic platform has been explored.

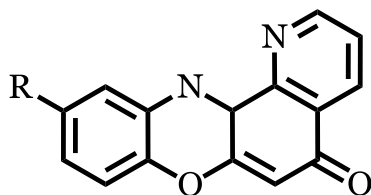
Phenoxazinones, benzo- and pyridophenoxazinones are linear and angular heterocyclic scaffolds containing the iminoquinone moiety responsible for widely reported properties. Natural phenoxazinones are present among the ommochromes (xanthommatin and dihydroxanthommatin) and ommins (pigments responsible for the skin and eye colors of invertebrates), among the cinnabarins (wood-rotting fungi metabolites), and among the actinomycins (powerful antibiotics produced by certain species of *Streptomyces*). Actinomycin D (AMD), obtained from *Streptomyces parvulus*, is known to be the best DNA intercalating agent in nature, but its clinical application is limited because of the side effects associated with myelosuppression and cardiotoxicity. The powerful damaging effect on DNA transcription has been correlated to the formation of a stable DNA/drug complex, where the phenoxazinone moiety is responsible for the intercalation between specific base pairs.¹



The discovery of a novel class of powerful antitumoral intercalating phenoxazinone derivatives has rekindled the interest for this system, which is involved in an array of biochemical roles ranging from the photochemical response of vision pigments to the production of DNA-damaging radicals by anti-proliferative drugs. More in details, particular attention has been paid to a number of natural and synthetic anti-proliferative compounds containing the

phenoxazinone ring system; indeed, it has been shown that the antineoplastic activity is correlated with the ability of the planar heterocyclic moiety to intercalate into double-stranded DNA by forming π - π stacking interactions between the aromatic bases guanine-cytosine and the electron-poor iminoquinone system. In addition, the iminoquinone moiety exploits the well-known ability of the quinones to generate reactive oxygen species (ROS) by reversible oxidation-reduction cycles. These features make these compounds attractive tools that perform their anti-tumoral effect through different and concurrent mechanisms.²

Among phenoxazinone systems we decided to focus the attention on 5H-pyridophenoxazin-5-one (PPH) based molecules in which the iminoquinonic planar system is formed by four conjugate rings exhibiting the suitable configuration of N[^]N-type ligand. So, the research work has been devoted to the synthesis of a series of PPH derivatives differing for the residue on the C-10 position and to the synthesis of the corresponding iridium(III) complexes. Structural and photo-physical characterization will also be discussed.



PPH

This work has been carried out in collaboration with Dr. Silvana Pedatella and Dr. Mauro De Nisco (UniNA).

~RESULTS AND DISCUSSION~

○ SYNTHESIS OF PYRIDOPHENOXAZINONE LIGANDS

The synthesis of compounds PPH, PPH-CH₃, PPH-NO₂ and PPH-F was carried out according to a reported procedure with slight modifications.¹

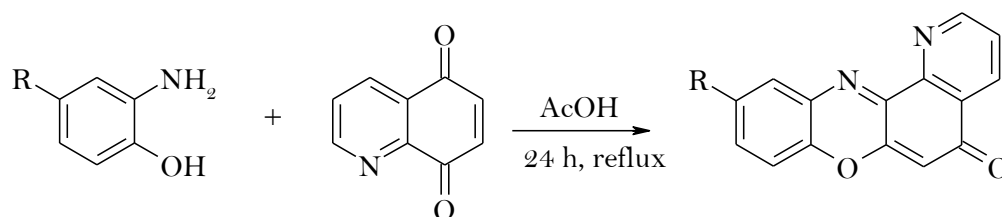


Figure 1.3.1. Reported synthesis of PPH derivatives.

The original synthetic procedure is based on the reaction of 2-aminophenol derivatives with quinoline-5,8-dione in refluxing acetic acid (Figure 1.3.1). Under these conditions, the 5H-pyrido[2,3-a]phenoxazin-5-one derivative is the main product usually isolated in low yields (4-12%) among a series of by-products. The mechanism proposed for this reaction is reported in Figure 1.3.2 and starts with the nucleophilic addition of the amino group of the aminophenol to the C-8 of the quinolinedione system activated by acid catalysis. The following attack of the hydroxyl group of the 2-aminophenol on the C-7 position of the α, β -unsaturated system leads to an unstable 8-hemiaminal that evolves with the formation of the pyridophenoxazinone ring.

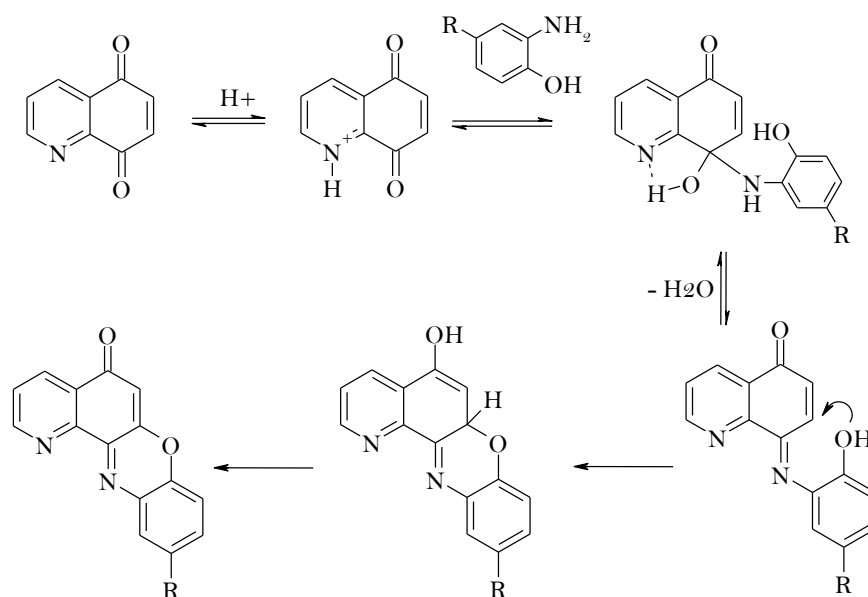


Figure 1.3.2. Proposed mechanism for the formation of the PPH heterocyclic system.

In order to improve the low reaction yields and to explore milder reaction conditions, a novel approach for the synthesis of these derivatives was followed. The first approach consisted in the use of microwaves. The microwave irradiation (μW) promotes a shorter reaction time as well as a reduced formation of by-products, allowing less complex purification conditions of the reaction mixture. With the microwave heating, the reagents are activated by electromagnetic radiation: an instantaneous localized overheating is produced because it is not directly related to the thermal conductivity of the receptacle. In this way, it's possible to achieve a great uniformity of temperature and a selective heating.

Different reaction conditions were explored varying the total volume of solvent, the molar ratio of the reagents, the microwave irradiation time and power. Best results were obtained by using a continuous input power of 50W, a total reaction time of 30 min, a mixture (1:1 molar ratio) of quinolin-5,8-dione and substituted *ortho*-aminophenol in 5 mL of acetic acid (Figure 1.3.3).

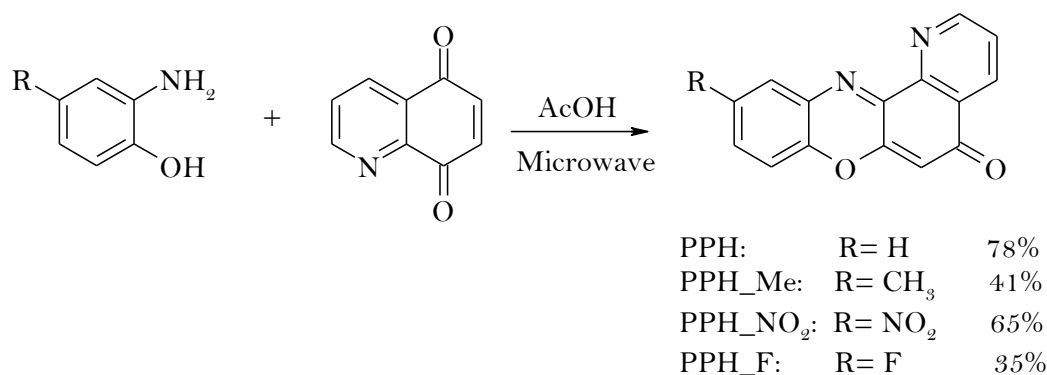
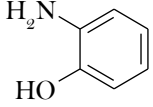
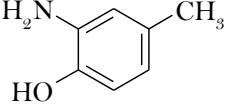
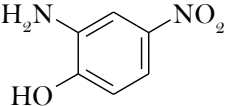
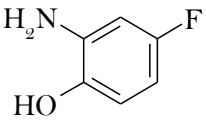


Figure 1.3.3. Synthesis of compounds PPH, PPH_CH₃, PPH_NO₂ and PPH_F.

Under these conditions the PPH derivatives were obtained in higher yields with respect to the reported procedures and in the range of 35-78% as shown in Table 1.3.1. The isolated compounds have been fully characterized by ¹H and ¹³C NMR spectroscopy as well as by mass spectrometry in order to confirm the structures.

Table 1.3.1. Reaction yields of PPH derivatives under classical (AcOH, reflux) and microwave (AcOH, μ W) conditions

2-aminophenol precursor	PPH Yields	
	AcOH, Reflux	AcOH, μ W
	12 %	78 %
	5 %	41 %
	4 %	65 %
	ND	35 %

○ SYNTHESIS AND CHARACTERIZATION OF PYRIDOPHENOXAZINONE-BASED IRIDIUM(III) COMPLEXES

For the synthesis of this set of cationic iridium(III) complexes, the synthetic procedure previously described (see Section 1 – Chapter 2) was followed. In brief, the dinuclear chloro-bridged complex μ -Ir was treated with the proper synthesized PPH derivative to afford the corresponding cationic complexes, namely *Ir_PPH*, *Ir_PPH_Me*, *Ir_PPH_NO₂*, *Ir_PPH_F* (Figure 1.3.4). To allow the isolation of the complex as salt, the reaction mixture was brought to room temperature and then treated with NH_4PF_6 .

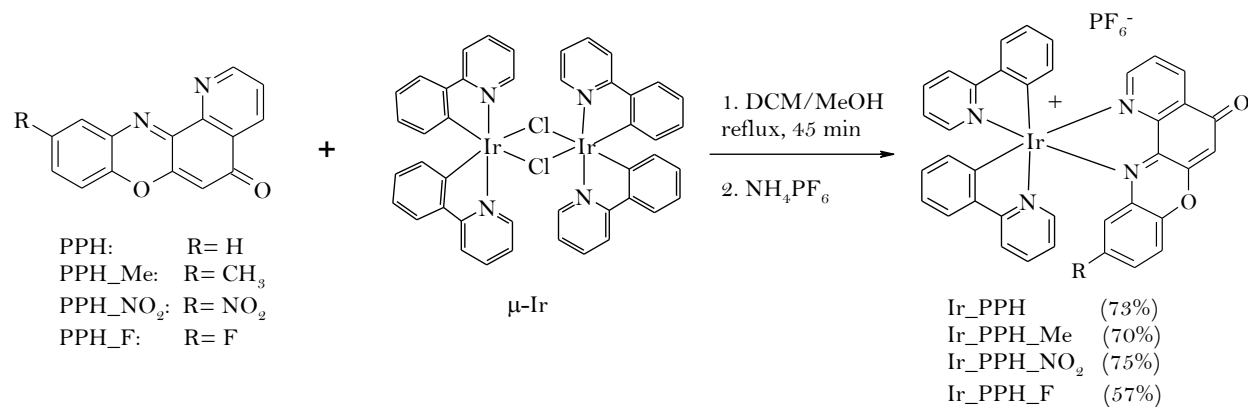


Figure 1.3.4. Synthesis of cationic iridium(III) complexes.

The four complexes have been fully characterized by 1D (¹H and ¹³C) and 2D (COSY, ¹H, ¹³C HSQC, ¹H, ¹³C HMBC and NOESY) NMR.

The identity of the complexes was confirmed also by mass analysis. For our purposes we selected the electrospray ionization both in the positive and negative ion mode. In the spectra registered in the positive ion mode it was possible to identify the ion peak relative to the cationic portion of the complex, whereas in the negative ion mode it was possible to detect the ion peak relative to PF₆⁻.

○ PHOTO-PHYSICAL PROPERTIES OF ANCILLARY LIGANDS AND OF THE CORRESPONDING CATIONIC IRIDIUM(III) COMPLEXES

The photo-physical properties of the synthesized PPH derivatives and of the corresponding iridium(III) complexes were investigated by UV-visible and emission spectroscopy in dilute solution (1·10⁻⁵ M).

The UV-visible spectra recorded in CHCl₃ are reported in Figure 1.3.4. All the compounds exhibit a similar absorption profile characterized by three absorption maxima at around 280, 350 and 450 nm. Worthy of note is the hypsochromic shift observed in the spectrum of Ir_PPH_NO₂ due to the presence of the NO₂ group. For all the four compounds, the absorption maxima are associated with very high ε values (10⁴ M⁻¹cm⁻¹). The emission spectra of PPH derivatives, registered in dilute solutions, denoted the presence of a wide emission band centered at around 550 nm by exciting at around 450 nm. All the photo-physical data for compounds PPH, PPH_Me, PPH_NO₂ and PPH_F are reported in Table 1.3.2.

Table 1.3.2. Photo-physical data of synthesized ligands and corresponding complexes

Compound	Abs λ_{\max} , nm (log ϵ , M ⁻¹ cm ⁻¹)	PL λ_{\max} (nm), λ_{exc}
PPH	244 (4.35), 283 (4.03), 348 (4.08), 433 (4.06)	551, 433
PPH-CH ₃	254 (4.32), 284 (4.02), 351 (3.96), 454 (4.03)	541, 455
PPH-NO ₂	300 (4.26), 415 (3.97)	581, 415 523, 415
PPH-F	290 (4.00), 345 (4.05), 452 (3.99)	510, 452 590, 452
Ir_PPH	253 (3.80), 300 (sh), 375 (3.20), 503 (2.97)	
Ir_PPH-CH ₃	255 (3.92), 367 (sh), 520 (3.57)	
Ir_PPH-NO ₂	251 (4.33), 296 (4.17), 350 (sh), 470 (3.51)	
Ir_PPH-F	253 (4.19), 370 (sh), 515 (3.49)	

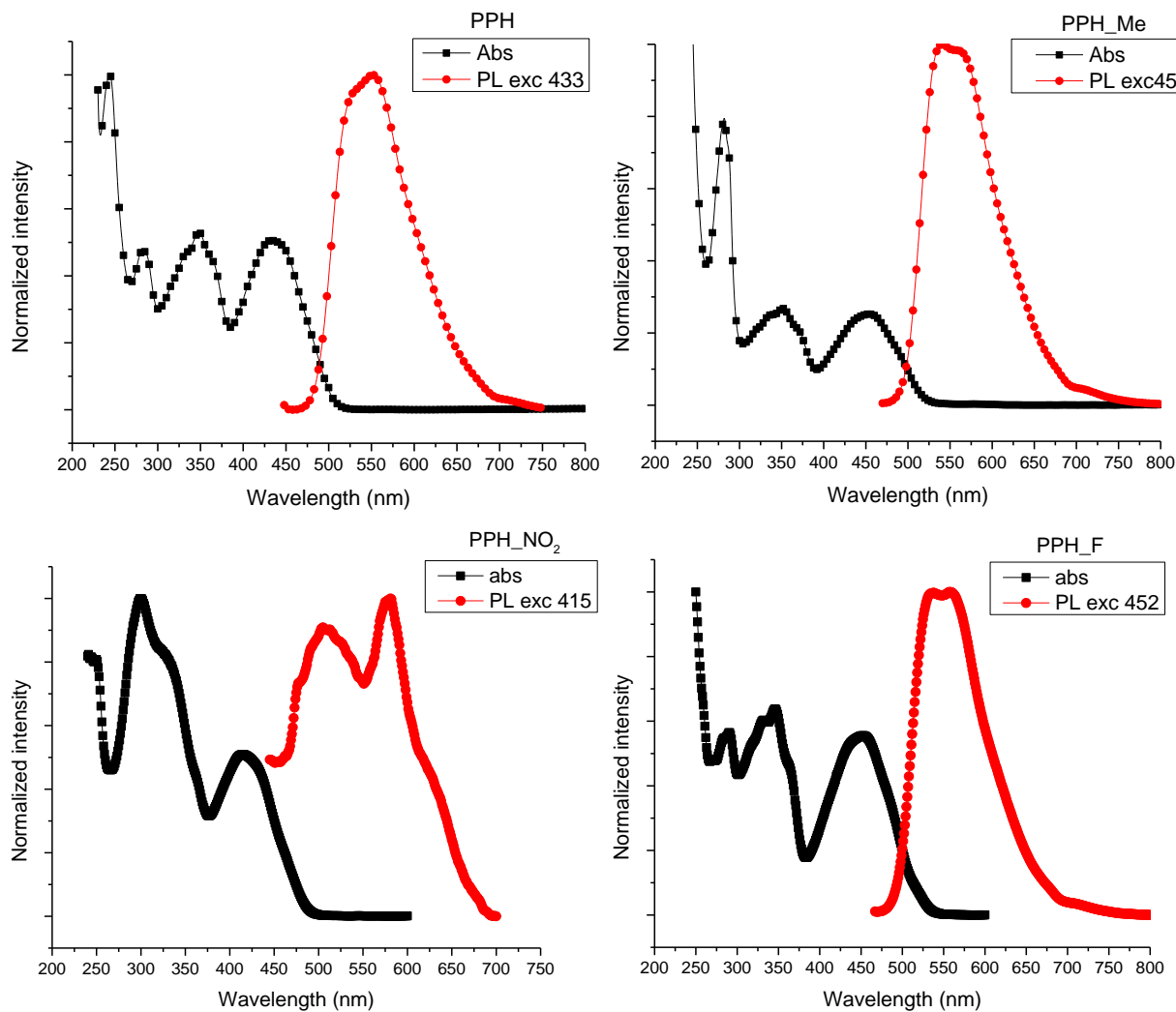


Figure 1.3.4. Absorption and emission spectra of the PPH ligands.

The same spectrophotometric analysis was carried out also for the four iridium(III) complexes. The UV-visible spectra recorded in diluted solutions in CHCl_3 showed a similar absorption profile with maxima centered at around 300, 375 and 500 nm associated with very high ϵ values ($10^4 \text{ M}^{-1}\text{cm}^{-1}$). Also in this case the hypsochromic effect of the nitro-substituent was clearly visible.

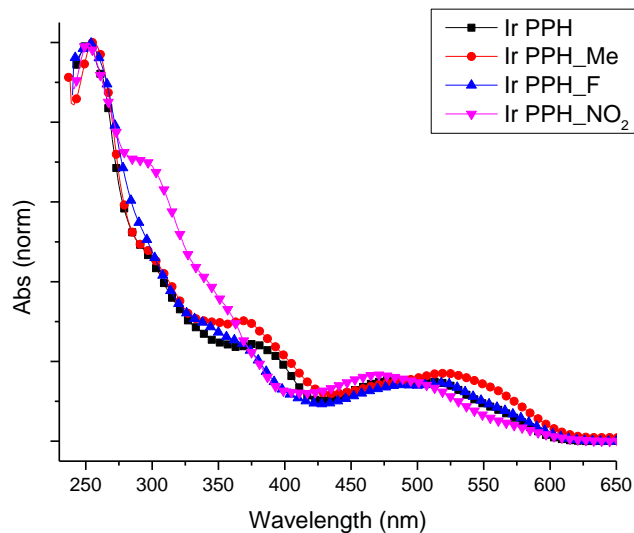


Figure 1.3.5. Absorption spectra of the PPH-based iridium(III) complexes in diluted solutions in CHCl_3

Unfortunately, the synthesized complexes didn't exhibit phosphorescence emission even in oxygen depleted solutions. This effect can be attributed to the presence of the electro-withdrawing carbonyl group on the C-6 position that causes the quenching of the emission. This evidence, together with the low solubility of these complexes in common organic solvents preventing the deposition of good thin films processing, prevented the fabrication of LEEC devices.

~CONCLUSIONS~

In conclusion, this chapter reports on the synthesis of a novel set of cationic iridium(III) complexes obtained by using 5H-pyrido[2,3-a]phenoxazin-5-one derivatives as ancillary ligands.

The first part of the work concerned the synthesis of PPH derivatives differing from the functional group on the C-10 position. Starting from a procedure reported in the literature, the yields of formation of the compounds have been significantly improved (from 10% to 70%) by carrying out the reaction under microwave irradiation. Other advantages offered by the use of microwaves rely on the reduction of the reaction times (from 24 hours to 30 minutes) and on the suppression of secondary pathways leading to undesired by-products. The synthesized heterocyclic platforms were used as ancillary ligands for assembling, together with the primary ligand 2-phenylpyridine, the new iridium(III) complexes, that were obtained in good yields and fully characterized by 1D and 2D NMR and mass analysis.

The second part of the work concerned the preliminary investigation of the photo-physical properties of the complexes. In detail, the UV-visible spectroscopic analysis denoted a quite similar absorption profile for all the four complexes with an evident hypsochromic shift observed in the case of Ir_PPH_NO₂ due to the presence of the NO₂ group on the C-10 position of the 5H-pyrido[2,3-a]phenoxazin-5-onic backbone. Unfortunately, the complexes didn't show any appreciable photoluminescence in solutions probably due to the presence of the carbonyl group on the 6 position.

~EXPERIMENTAL SECTION~

○ MATERIALS AND METHODS

All the reagents were commercially available (Aldrich, Fluka, Sigma). Anhydrous solvents were purchased from commercial sources and withdrawn from the container by syringe, under a slight pressure of Argon. All the solvents were analytical grade quality.

The analytical and preparative thin-layer chromatography was carried out on F254 silica gel plates (0.25 and 0.5mm, respectively). TLC plates were visualized using UV ($\lambda = 254$ nm) and fluorescent ($\lambda = 355$ nm) lamps. Liquid chromatography was carried out on silica gel (70÷230 Mesh). NMR spectra were acquired in CD_2Cl_2 , CD_3COCD_3 and $CDCl_3$ on the following instruments: Bruker DRX (400 MHz) and Varian Inova (500 MHz). The chemical shift are reported in ppm (δ) and referred to TMS as internal standard. J values are given in Hertz. $^1H, ^1H$ COSY, $^1H, ^{13}C$ HSQC, $^1H, ^{13}C$ HMBC and NOESY experiments were run at 400 or 500 MHz using standard pulse programs. UV and fluorescence spectra were recorded with a Jasco V-560 and a Jasco FP-750 instruments. The mass spectra were acquired with a ESI MS spectrometer both in positive and negative ions mode.

○ SYNTHESIS OF LIGANDS

● SYNTHESIS OF QUINOLIN-5,8-DIONE

A solution of 5-amino-8-hydroxyquinoline (3 mol/30 mL of water) was treated with HCl (conc.) and with a solution of $K_2Cr_2O_7$ (2 mol/30 mL of water). Then the reaction mixture was washed with 300 mL of $CHCl_3$ and the organic phase washed with brine until neutrality. The collected organic layers were evaporated under reduced pressure to give quinolone-5,8-quinone (60% yields).

1H (400 MHz, $CDCl_3$): δ 9.07 (dd, $J=4.6, 1.6$ Hz, 1H), 8.43 (dd, $J=7.9, 1.6$ Hz, 1H), 7.73 (dd, $J=7.9, 4.6$ Hz, 1H), 7.17 (d, $J=10.5$ Hz, 1H), 7.07 (d, $J=10.5, 1H$).

● SYNTHESIS OF 5H-PYRIDO[2,3-A]PHENOXAZIN-5-ONE: GENERAL PROCEDURE

A solution of quinolin-5,8-dione (0.1 mmol) in glacial CH_3COOH (5 mL) was poured into a microwave tube and treated with the selected 2-aminophenolic derivatives (0.1 mmol). The solution was shaken until a dark orange solution was obtained, and then it was irradiated for 15

minutes at 50 W. The oxygen was bubbled into the tube for 1 minute, and the mixture irradiated again for 15 minutes. This procedure was repeated ten times, the CH₃COOH was evaporated under reduced pressure. The overall crude was filtered on celite and washed with THF and subjected to silica gel chromatography (CHCl₃/MeOH, 8:2) to afford:

PPH (78% yield): ¹H NMR (400 MHz, CDCl₃): δ 9.17 (dd, J=4.5, 1.7 Hz, 1H), 8.64 (dd, J=8.0, 1.7 Hz, 1H), 8.12 (dd, J=7.9, 1.4 Hz, 1H), 7.72 (dd, J=8.0, 4.5 Hz, 1H), 7.57 (m, 1H), 7.42 (m, 1H), 7.37 (dd, J=8.0, 1.1 Hz, 1H); ¹³C NMR (100 MHz, CDCl₃): δ 182.5, 153.6, 152.3, 147.4, 146.7, 144.2, 134.4, 133.0, 132.8, 131.2, 128.8, 126.2, 125.7, 115.9, 107.0.

PPH-CH₃ (41% yield): ¹H NMR (500 MHz, CDCl₃): δ 9.13 (d, J=4.4, 1H), 8.62 (d, J=7.9 Hz, 1H), 7.89 (bs, 1H), 7.69 (dd, J=7.9, 4.4 Hz, 1H), 7.36 (d, J=8.4 Hz, 1H), 7.24 (d, J=8.4 Hz, 1H), 6.48 (s, 1H), 2.45 (s, 3H); ¹³C NMR (100 MHz, CDCl₃): δ 182.5, 153.5, 152.5, 147.5, 146.5, 142.2, 135.7, 134.4, 133.8, 132.8, 131.1, 128.8, 126.0, 115.5, 106.7, 20.9.

PPH-NO₂ (65% yield): ¹H NMR (400 MHz, CDCl₃): δ 9.21 (dd, J=4.6, 1.7 Hz, 1H), 9.02 (d, J=2.6, 1H), 8.65 (dd, J=7.9, 1.7 Hz, 1H), 8.44 (dd, J=9.0, 2.6 Hz, 1H), 7.80 (m, J=7.9, 4.6, 1H), 7.49 (d, J=9.0 Hz, 1H), 6.60 (s, 1H); ¹³C NMR (125 MHz, CDCl₃): δ 182.3, 154.16, 151.0, 148.9, 148.1, 146.9, 144.9, 134.5, 132.6, 128.9, 127.2, 126.9, 126.5, 116.8, 108.7.

PPH-F (36% yield): ¹H NMR (500 MHz, CDCl₃): δ 9.19 (d, J=3.2 Hz, 1H), 8.66 (dd, J=7.9, 1.4 Hz, 1H), 7.85 (dd, J=8.2, 2.7 Hz, 1H), 8.65 (d, J=7.3 Hz, 1H), 7.76 (m, 1H), 7.37 (dd, J=8.9 Hz, 1H), 7.32 (d, J=9.3 Hz, 1H), 6.61 (s, 1H). ¹³C NMR (125 MHz, CDCl₃): δ 182.4, 160.6, 158.2, 153.7, 152.0, 147.4, 140.5, 134.5, 133.5, 128.9, 126.5, 120.0, 117.0, 116.6, 107.2.

- SYNTHESIS OF CATIONIC IRIDIUM (III) COMPLEXES: GENERAL PROCEDURE

A solution of the complex μ-Ir (40 mg, 0.037 mmol) in a mixture of CH₂Cl₂/MeOH 2:1 (v/v) (8 mL) is treated with the selected 5H-pyridophenoxazin-5-one derivative (0.075 mmol). The solution is refluxed under vigorous stirring for 45 minutes, then is brought to room temperature and NH₄PF₆ (30.6 mg, 0.18 mmol) is added under stirring. After 30 minutes, the mixture was evaporated under reduced pressure, affording a red crude solid. The latter was taken in 10 mL of CH₂Cl₂ and filtered to remove insoluble white inorganic salts. The elute is

subjected to crystallization from CH₂Cl₂/diethyl ether and the solid purified by silica gel chromatography (CH₂Cl₂/MeOH, 8:2) to afford:

Ir_PPH (73% yield): ¹H NMR (400 MHz, acetone-d₆): δ 8.84 (d, J=8.0 Hz, 1H), 8.57 (d, J=5.6 Hz, 1H), 8.38 (d, J=4.2 Hz, 1H), 8.35 (d, J=8.2 Hz, 1H), 8.25 (d, J=8.2 Hz, 1H), 8.15 (dd, J=8.0, 5.4 Hz, 1H), 8.10-7.96 (m, 4H), 7.67 (d, J=8.3 Hz, 1H), 7.71 (d, J=5.7 Hz, 1H), 7.65 (t, J=7.2 Hz, 1H), 7.50 (d, J=8.3 Hz, 1H), 7.20-7.10 (m, 4H), 7.03 (t, J=7.4 Hz, 1H), 6.99 (t, J=7.4 Hz, 1H), 6.92 (t, J=7.4 Hz, 1H), 6.41 (s, 1H), 6.40 (d, J=7.3 Hz, 1H), 6.10 (d, J=7.3 Hz, 1H), 1.84 (s, 3H). ¹³C NMR (100 MHz, acetone-d₆): δ 180.1, 167.5, 166.5, 153.9, 153.3, 153.1, 152.1, 152.0, 150.1, 150.0, 146.6, 146.4, 144.2, 143.3, 139.0, 139.0, 135.6, 135.2, 132.3, 132.1, 131.6, 131.1, 130.7, 130.5, 130.3, 129.7, 125.6, 125.2, 125.2, 124.1, 123.6, 123.6, 123.0, 120.3, 119.9, 116.8, 107.5.

Ir_PPH_Me (70% yield): ¹H NMR (400 MHz, acetone-d₆): δ 8.78 (d, J=8.0 Hz, 1H), 8.19 (d, J=4.2 Hz, 1H), 8.03 (d, J=4.9 Hz, 1H), 8.01 (d, J=8.2 Hz, 1H), 7.98 (d, J=8.2 Hz, 1H), 7.90-7.80 (m, 5H), 7.78 (d, J= Hz, 5H), 7.06 (d, J=5.7 Hz, 1H), 7.36 (dd, J=1.4 Hz, 1H), 7.46 (d, J=5.7 Hz, 1H), 7.28 (d, J=8.4 Hz, 1H), 7.21 (d, J=5.2 Hz, 1H), 7.20-7.01 (m, 4H), 7.04 (t, J=7.4 Hz, 1H), 6.99 (t, J=7.4 Hz, 1H), 6.62 (s, 1H), 6.08 (d, J=7.3 Hz, 1H), 6.35. (d, J=7.3 Hz, 1H). ¹³C NMR (100 MHz, CD₂Cl₂): δ 180.6, 168.3, 166.8, 153.5, 153.4, 151.8, 151.8, 151.3, 149.0, 148.7, 144.8, 144.4, 143.4, 139.5, 137.3, 136.3, 132.4, 132.0, 131.9, 131.5, 131.5, 131.2, 131.1, 131.1, 131.1, 130.8, 130.7, 125.7, 125.7, 124.6, 124.6, 124.2, 124.1, 120.8, 120.8, 116.6, 109.0.

Ir_PPH_NO₂ (75% yield): ¹H NMR (400 MHz, acetone-d₆): δ 8.84-8.81 (m, 2H), 8.60 (d, J=5.6 Hz, 1H), 8.38 (dd, J=8.8, 2.4 Hz, 1H), 8.36 (d, J=4.2 Hz, 1H), 8.28 (d, J=8.2 Hz, 1H), 8.22 (d, J=8.2 Hz, 1H), 8.13 (dd, J=5.4, 8.0 Hz, 1H), 8.0-7.92 (m, 4H), 7.69-7.68 (m, 2H), 7.20-7.05 (m, 5H), 7.03 (t, J=7.4 Hz, 1H), 7.05 (t, J=7.4 Hz, 1H), 6.73 (s, 1H), 6.41 (d, J=7.3 Hz, 1H), 6.10 (d, J=7.3 Hz, 1H). ¹³C NMR (100 MHz, acetone-d₆): δ 180.4, 167.5, 166.2, 155.7, 153.3, 152.5, 152.1, 150.4, 150.2, 147.1, 145.5, 144.6, 143.8, 143.3, 139.1, 139.0, 135.7, 132.1, 132.1, 131.8, 131.6, 131.5, 131.1, 130.8, 130.1, 129.0, 125.3, 125.0, 124.9, 124.2, 123.0, 123.0, 123.0, 120.2, 119.9, 118.0, 108.9.

Ir_PPH_F (57% yield): ¹H NMR (400 MHz, acetone-d₆): δ 8.83 (d, J=8.0 Hz, 1H), 8.58 (d, J=5.6 Hz, 1H), 8.39 (d, J=4.2 Hz, 1H), 8.31 (d, J=8.2 Hz, 1H), 8.26 (d, J=8.2 Hz, 1H), 8.15 (dd, J=5.4, 8.0 Hz, 1H), 7.90-8.0 (m, 2H), 7.97 (d, J=5.2 Hz, 2H), 7.70 (d, J=5.7 Hz, 1H), 7.60-7.40 (m, 3H), 7.16-7.11 (m, 4H), 7.03 (t, J=7.4 Hz, 1H), 6.98 (t, J=7.4 Hz, 1H), 6.63 (s, 1H), 6.40 (d,

J=7.3 Hz, 1H), 6.14 (d, J=7.3 Hz, 1H). ¹³C NMR (100 MHz, acetone-d₆): δ 180.0, 167.3, 166.2, 154.5, 154.3, 153.0, 151.9, 151.8, 150.1, 148.1, 145.3, 145.1, 144.4, 143.3, 139.1, 139.1, 135.2, 134.0, 133.0, 132.7, 131.4, 130.8, 130.5, 130.4, 130.1, 128.1, 125.2, 125.2, 124.2, 123.7, 123.6, 123.3, 121.2, 120.3, 119.9, 115.1, 107.6.

REFERENCES

- [1]. A. Bolognese et. al. *J. Med. Chem.* **2002**, *45*, 5205-5216
- [2]. M. De Nisco, A. Bolognese, M. Sala, S. Pedatella and M, Manfra, *ChemistrySelect* 2016, *6*, 1292 – 1295

SECTION 2

DESIGN, SYNTHESIS AND PROPERTIES OF
EUMELANIN-BASED SEMICONDUCTORS AND
THEIR APPLICATIONS IN ELECTRONIC DEVICES.

~INTRODUCTION~

Among the broad variety of biopolymers found in nature, few have such profound and fascinating interdisciplinary implications at the crossroads of physics, chemistry, biology, and medicine as melanins do. The reasons for this are rooted in the role of these pigments as the key components of the human pigmentary system and their important socio-economic impact and clinical relevance in relation to pigmentary disorders, such as malignant melanoma the most aggressive of the skin cancers, and to their photo-protecting action.¹

Melanins can be classified into two distinct groups, eumelanin (black coloured) and pheomelanin (red coloured). Eumelanin and pheomelanin share a common biosynthetic origin in the amino acid tyrosine. With the formation of the common key-intermediate dopaquinone, which is formed by the action of the enzyme tyrosinase in epidermal melanocytes, two different pathway departs. The first one leads to the formation of 1,4-benzothiazine intermediates, the monomer precursors of pheomelanins, whereas the second one leads to the formation of 5,6-dihydroxyindole (DHI) and its 2-carboxylic acid (DHICA), the monomer precursors of eumelanins (Figure 2.1).²

Working on eumelanins has traditionally been regarded as an intriguing, though sometimes frustrating, experience.³ This is due to their several challenging features, including almost complete insolubility in all solvents, an amorphous particulate character and extreme molecular heterogeneity.⁴

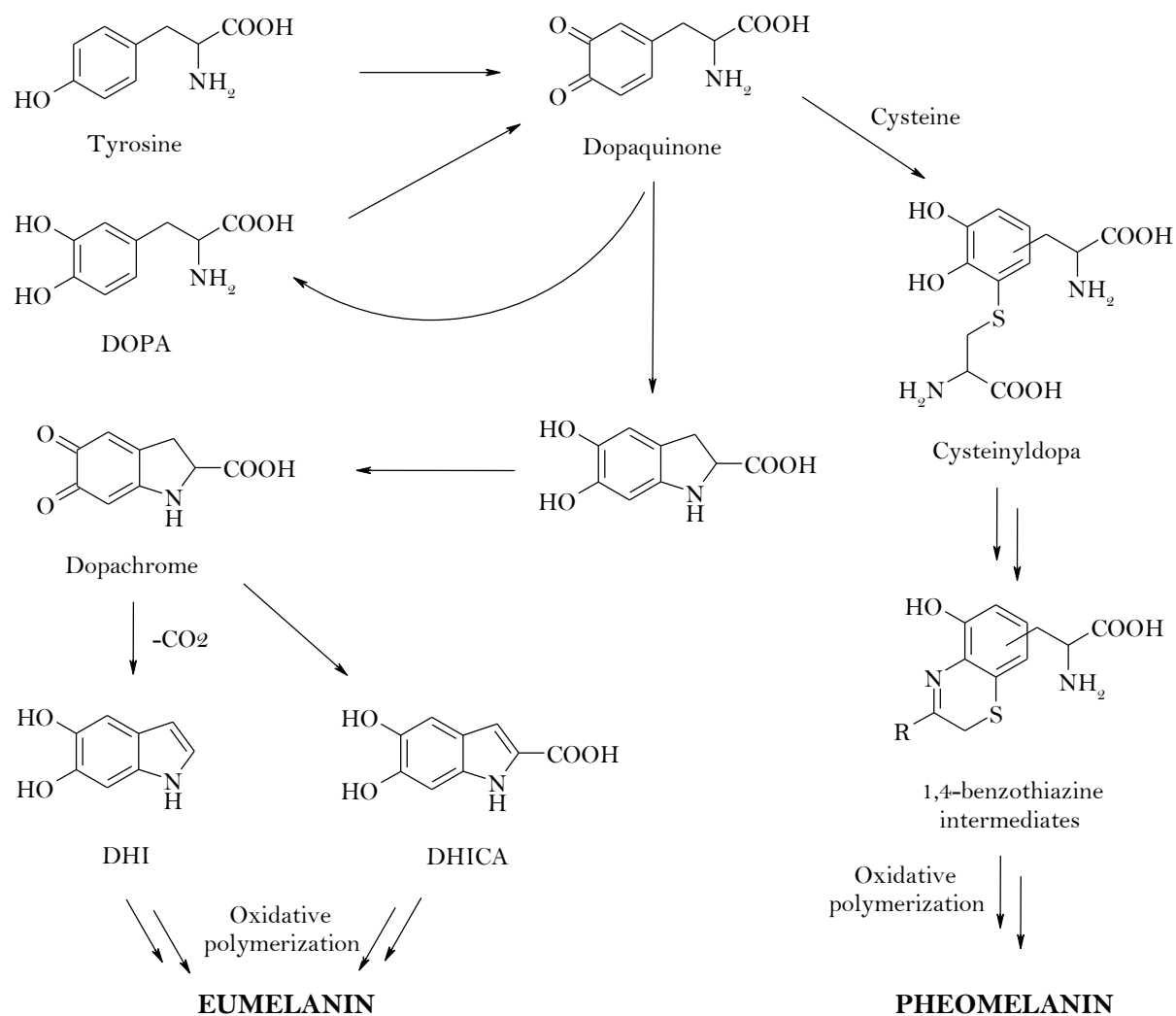


Figure 2.1. Biosynthetic pathways leading to eumelanins and pheomelanins.

In the mid-1990s a different basic supramolecular architecture for eumelanins was proposed.⁵ This model suggested the formation of protomolecular structures, approximately 15 Å in size, made up of four to five planar sheets constituted by four-to-eight 5,6-dihydroxyindole units, each stacked along the z direction with a graphite-like stacking spacing of 3.4 Å. In eumelanin from sepia ink, a sequence of aggregation steps has been suggested to account for the apparent three levels of structural organization (Figure 2.2).⁶

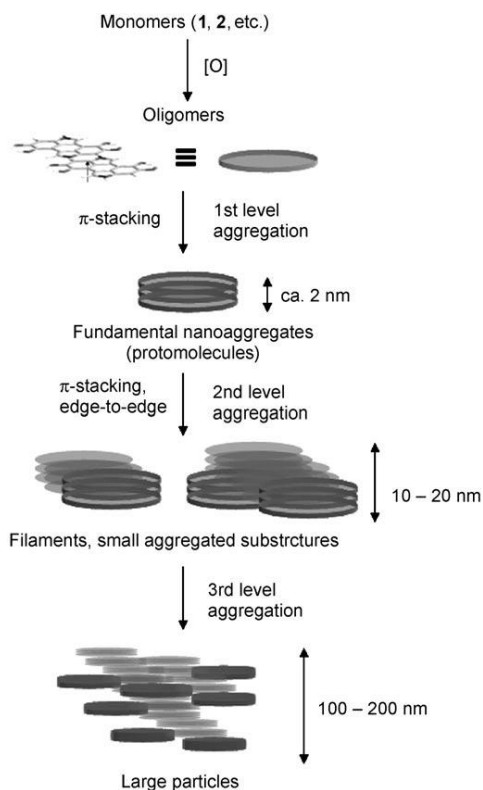


Figure 2.2. The hierarchical aggregate structure proposed for sepiia eumelanin.

Numerous studies carried out by using atomic force microscopy (AFM),⁷ X-ray diffraction,⁸ mass spectrometry,⁹ nuclear magnetic resonance (NMR) spectroscopy¹⁰ and advanced quantum chemical calculations,¹¹ have tried to address the eumelanin structure issue, and though most of them appear to support the stacked-aggregate picture, definitive proof for this model is still missing.

Nonetheless a remarkable bulk of study allowed disclosing a series of physical-chemical properties, such as the persistent electron paramagnetic resonance (EPR) signal, the broadband monotonic optical absorption along the entire UV-visible spectrum, the peculiar excitation and emission properties and the time dependent photo-dynamics. Standard vibrational methods such as infrared absorption and Raman spectroscopy, and more recently inelastic neutron scattering spectroscopy, have also been applied with varying degrees of success to study the vibrational finger-print of eumelanin precursors.¹²

The decisive turn came in 1974, when McGinness and his associates showed that natural and synthetic eumelanins behave like amorphous semiconductors (Figure 2.3).¹³ This result

suggested that eumelanins consist of a very high molecular weight polymer made up of different indolic units set at variable oxidation states and linked with each other randomly, so to fit the band-gap semiconductor model. A critical point to note concerning the observations proposed by McGinness is that switching was only seen when the melanin was hydrated. This observation could be rationalized in terms of the modified dielectric theory, whereby the absorbed water lowers the activation energy for hopping transport.¹⁴

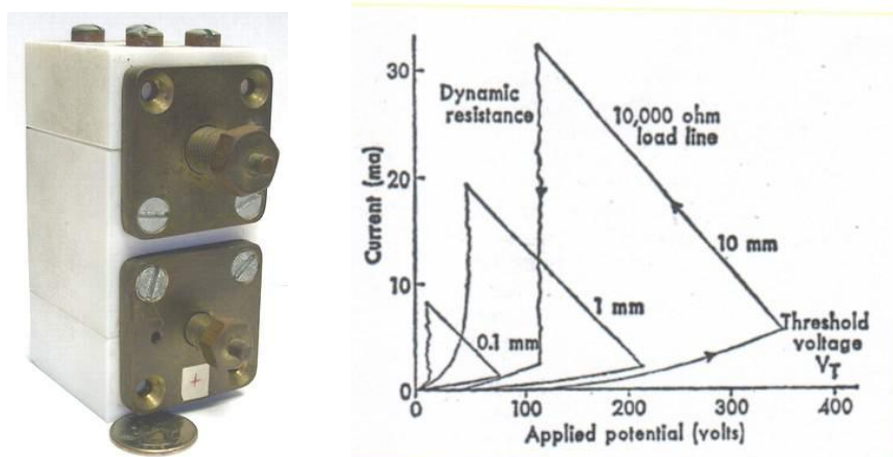
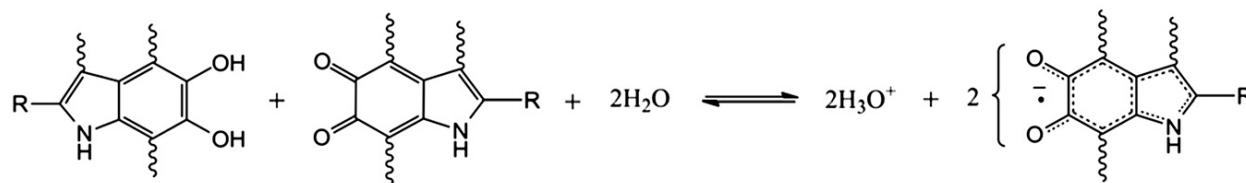
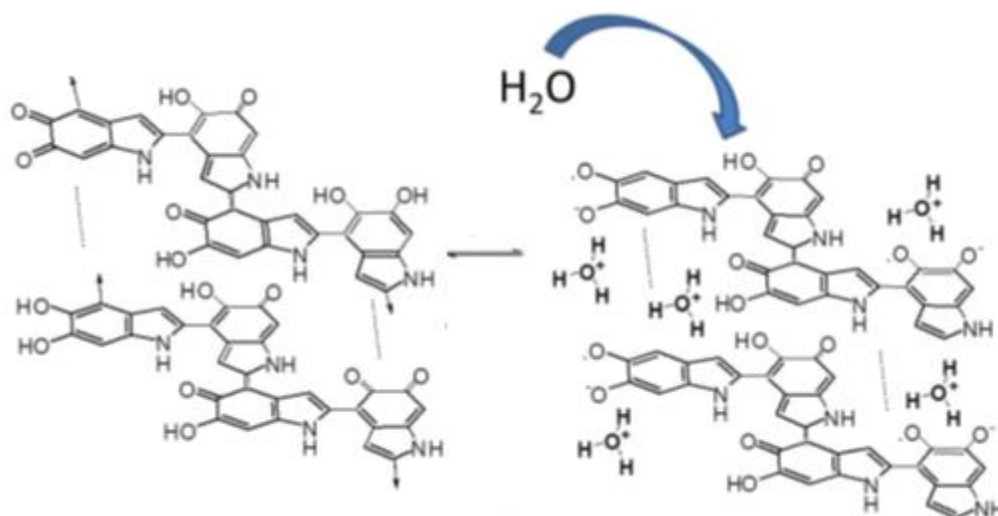


Figure 2.3. McGinness' melanin bistable switch device (left) and current-voltage properties of melanin prepared by autoxidation of L-dopa for various sample thicknesses (right).

Recent works pointed out that the strong humidity dependence of the electrical conductivity in melanin thin films could be attributed to the peculiar electronic-ionic hybrid conductor behavior,¹⁴ in which thermodynamically favorable, water-driven redox equilibrium between catechol and quinone species would generate semiquinone moieties doping electrons and protons into the system (Scheme 2.1).



Scheme 2.1. Comproportionation equilibrium between *o*-diphenol and *o*-quinone units leading to the formation of semiquinone radical anions (electrons) and hydronium ions (protons).



Scheme 2.2. Simplified illustration of the water-dependent self-doping mechanism of DHI melanin based on the suggested water-driven comproportionation equilibrium.

Since the early studies carried out by McGinness, eumelanins have attracted a great deal of interest mainly for their applications in organic electronics.

Synthetic eumelanin thin films have shown a read-only memory effect and the ability to retain accumulated space charge after bias application or light exposure when embedded in an Au/eumelanin/ITO/glass device.¹⁵

Recently, an OEET device was fabricated for the investigation of eumelanin electrical response in a more biomimetic aqueous suspension state in view of the possible development of a biosensor aimed at assessing biopolymer concentration and redox state in its environment. The outstanding finding of this study is the high sensitivity of the device response to eumelanin that can yield new insights into the redox properties of the polymer and guide the rational design and implementation of bio-inspired devices with tailored electrical behavior for bio-electronics.¹⁶

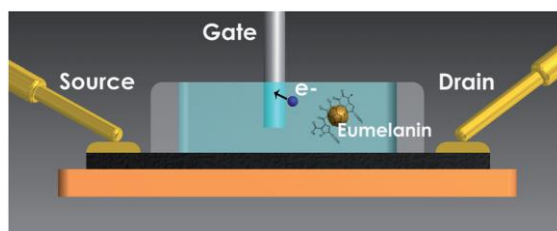


Figure 2.4. Depiction of the OEET device employed for eumelanin particle detection.

In 2011 the first metal-insulator-semiconductor (MIS) device in which eumelanin thin films are deposited on pSi and nSi substrates enabled insight into ambipolar electrical transport mechanisms and represented a significant step toward the integration of melanin-based biopolymers into several kinds of hybrid organic polymer-based devices.¹⁷

In 2012 a new hybrid material for photovoltaic applications composed by *n*-type porous silicon (PSi) filled with eumelanin was proposed and investigated. This work showed that the photovoltaic properties of pSi may be significantly improved by impregnation with eumelanin. In particular, the introduction of the pigment within the porous Si matrix leads to a significantly more efficient photocurrent generation with respect to empty porous Si layers, disclosing the possible role of eumelanins as ‘antenna’ for photo-conversion applications.¹⁸

Another important success has been obtained with the hybrid material constituted by eumelanins integrated within graphene-like (GL) layers, exhibiting conducting properties and high biocompatibility.¹⁹

Despite the great potential of eumelanins as soft biocompatible organic semiconductor, their applications in the organic electronics sector are still very few with the implementation of competitive eumelanin-based technology hindered by the complete insolubility of the polymer in all solvents, preventing the development of standardized and reproducible synthetic procedures, and by the lack of a solid conceptual frame of structure–property relationships. To date all these difficulties have been overcome by preparing thin films from ill-defined commercially available materials (i.e. Melanin purchased by Sigma-Aldrich) or via alkali-induced dissolution of melanin polymers. But these approaches may not reflect the real behavior of the natural pigment, because both the hydrogen peroxide-mediated synthetic process both the severe alkali treatment may induce significant structural changes.

~Aims of the research work~

Starting from this complex background, part of the research activity of this PhD course has been devoted to the design, synthesis, processing and properties of eumelanin-based semiconductors and their applications in electronic devices, with the aim of throwing new light onto this controversial issue.

In details, the following points will be stressed:

- the identification of suitable approaches for a more easy processing of melanin thin films;
- the investigation of the factors influencing the conductivity of melanin thin films;
- the study of the possible role of melanin thin films as innovative bio-interface.

The obtained results along with the rationale of the research will be reported in three main chapters concerning:

- 1) NOVEL APPROACHES TO EUMELANIN THIN FILM DEPOSITION
- 2) ELECTRICAL PROPERTIES OF EUMELANIN THIN FILMS
- 3) NEW MELANIN-BASED BIO-INTERFACES

REFERENCES

- [1]. M. d'Ischia, A. Napolitano, A. Pezzella, P. Meredith and T. Sarna, *Angew. Chem. Int. Ed.* **2009**, *48*, 3914–3921
- [2]. Land, E. J.; Ramsden, C. A.; Riley, P. A. *Acc. Chem. Res.* **2003**, *36*, 300–308
- [3]. Ito, S.; Simon, J. *Pigm. Cell Res.* **2004**, *17*, 422–424
- [4]. Prota, G. *Pigm. Cell Res.* **2000**, *13*, 283–293.
- [5]. Cheng, J.; Moss, S. C.; Eisner, M. *Pigm. Cell Res.* **1994**, *7*, 255–262
- [6]. Liu, Y.; Simon, J. D. *Pigm. Cell Res.* **2005**, *18*, 42–48.
- [7]. Lorite, G. S.; Coluci, V. R.; da Silva, M. I. N.; Deziderio, S. N.; Graeff, C. F. O.; Galvao, D. S.; Cotta, M. A. *J. Appl. Phys.* **2006**, *99*, 113511.
- [8]. Capozzi, V.; Perna, G.; Carmone, P.; Gallone, A.; Lastella, M.; Mezzenga, E.; Quartucci, G.; Ambrico, M.; Augelli, V.; Biagi, P. F.; Ligonzo, T.; Minafra, A.; Schiavulli, L.; Pallara, M.; Cicero, R. *Thin Solid Films* **2006**, *511–512*, 362–366.
- [9]. Pezzella, A.; Napolitano, A.; d'Ischia, M.; Prota, G.; Seraglia, R.; Traldi, P. *Rapid Commun. Mass Spectrom.* **1997**, *11*, 368–372.
- [10]. Ghiani, S.; Baroni, S.; Burgio, D.; Digilio, G.; Fukuhara, M.; Martino, P.; Monda, K.; Nervi, C.; Kiyomine, A.; Aime, S. *Magn. Reson. Chem.* **2008**, *46*, 471–479.
- [11]. Stark, K. B.; Gallas, J. M.; Zajac, G. W.; Golab, J. T.; Gidanian, S.; McIntire, T.; Farmer, P. J. *J. Phys. Chem. B* **2005**, *109*, 1970–1977
- [12]. L. Panzella, G. Gentile, G. D'Errico, N. F. Della Vecchia, M. E. Errico, A. Napolitano, C. Carfagna and M. d'Ischia, *Angew. Chem. Int. Ed.* **2013**, *52*, 12684–12687
- [13]. J. McGinness, P. Corry, P. Proctor, *Science*, **1974**, *183*, 853–855
- [14]. A. B. Mostert, B. J. Powell, F. L. Pratt, G. R. Hanson, T. Sarna, I. R. Gentle and P. Meredith, doi: 10.1073/pnas.1119948109
- [15]. M. Ambrico, A. Cardone, T. Ligonzo, V. Augell, P. F. Ambrico, S. Cicco, G. M. Farinola, M. Filannino, G. Perna and Vito Capozzi, *Organic Electronics*, **2010**, *11*, 1809–1814
- [16]. G. Tarabella, A. Pezzella, A. Romeo, P. D'Angelo, N. Coppede, M. Calicchio, M. d'Ischia, R. Mosca and S. Iannotta, DOI: 10.1039/c3tb20639d
- [17]. M. Ambrico, P. F. Ambrico, A. Cardone, T. Ligonzo, S. R. Cicco, R. Di Mundo, V. Augelli and G. M. Farinola, DOI: 10.1002/adma.201101358
- [18]. G. Mula, L. Manca, S. Setzu and A. Pezzella, *Nanoscale Research Letters*, **2012**, *7*, 377
- [19]. V. Gargiulo, M. Alfe', R. Di Capua, A. R. Togna, V. Cammisotto, S. Fiorito, A. Musto, A. Navarra, S. Parisi and A. Pezzella, *J. Mater. Chem. B*, **2015**, *3*, 5070

SECTION 2

CHAPTER 1

NOVEL APPROACHES TO THE DEPOSITION OF EUMELANIN THIN FILMS

~INTRODUCTION~

Despite the technological potential of eumelanin-based materials and hybrids, it is very hard to obtain homogeneous eumelanin thin films with controllable thickness without compromising the structural integrity of the polymer; this is due mainly to the well-known high insolubility, structural complexity and manifold levels of chemical disorder associated with the eumelanins, hindering a rational property optimization and tailoring for organic electronics applications.

Generally one of the most important pre-requisite for the full realization of high performing organic (opto)electronic devices is the production of high-quality organic thin films.

To this aim, different approaches have been pursued to prepare smooth eumelanin thin films.

One of these consists in the use of DMSO as processing solvent and leads to the formation of homogeneous and smooth films growing in a quasi-layer-by-layer mode, each layer being composed of nanoaggregates (1–2 nm high). By this way, good quality eumelanin films have been obtained only from commercial synthetic eumelanin (SM) by spin-coating a commercial eumelanin sample suspended in DMSO onto ITO or silicon surfaces, exhibiting high conductivity due also to the doping effect exerted by DMSO. A second method consists in the use of ammonia to dissolve the melanin pigment; but, despite of the technological convenience of this method applicable to any kind of melanin, this thin film processing is typically accompanied by significant structural modifications of the polymer.^{1,2,3} A third one consists in the generation of eumelanin thin films by electropolymerization of the monomer precursors. This technique was used in 2006 in order to study the optical properties of eumelanin thin films on ITO coated glass by photopyroelectric spectroscopy. Although the great potentiality of this deposition method, the time required to obtain good thin films was too long.⁴

In parallel, a completely different approach has been pursued based on the design of functionalized melanin monomer precursors for the synthesis of water-soluble melanin polymers. The rationale of this strategy relies on: 1) a more easy thin film processing; 2) an efficient permeation of water molecules through the bulk of the films allowing a more efficient charge transport; 3) the possibility of create melanin-based bioelectronic devices.

Preliminary experiments have been carried out by inserting polyol chains on DHI. In particular, the synthesis of the first water-soluble DHI polymer was reported in 2009, obtained from the polymerization of a glycated-DHI monomer.⁵ A similar approach was reported in 2012, based on the thioglycosidation of 5,6-diacetoxyindole.⁶

Although this approach proved to be useful for the elucidation of the structural and optical properties of eumelanins, its value for electrical property optimization and semiconductor implementation in devices has still to be assessed.

Starting from this background, in this chapter two alternative and efficient methods for the deposition of homogeneous melanin thin films will be discussed.

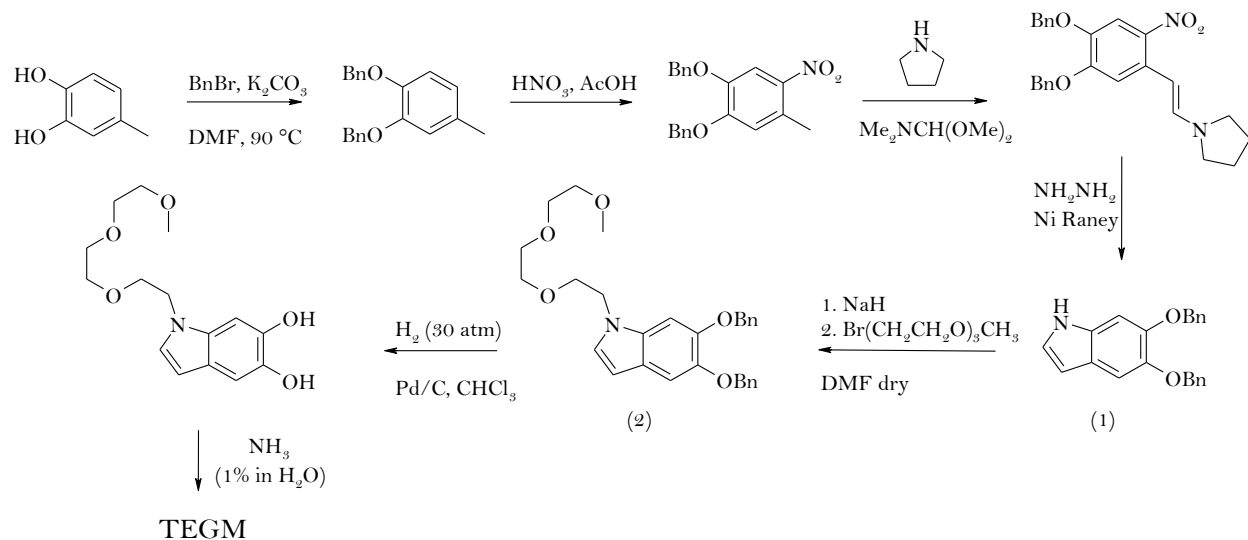
The first one is based on the synthesis of a new water-soluble eumelanin polymer obtained by the oxidative polymerization of *N*-functionalized DHI with a hydrophilic triethylenglycol (TEG) chain. This work has been carried out in collaboration with Prof. Gianluca Maria Farinola of University of Bari.

The second one is based on the innovative ammonia induced solid state polymerization (AISSP) of DHI thin films. This work has been carried out in association with Prof. Antonio Cassinese and Dr. Mario Barra of University of Naples.

~RESULTS AND DISCUSSION~

○ SYNTHESIS OF WATER-SOLUBLE EUMELANIN

One of the possible strategies to overcome the problems concerning the deposition of homogeneous eumelanin thin films has been to design the synthesis of a water soluble eumelanin. To this aim the procedure reported in Scheme 2.1.1 was followed based on these key points: a) synthesis of a DHI derivative with the –OH groups protected with benzyl residues (1); b) insertion of a triethylenglycol chain on the –NH group of the indolic ring (2); c) deprotection of the catechol functionality; d) oxidative polymerization of the 5,6-dihydroxyindolic derivative to afford the corresponding melanin polymer (TEGM). Black TEGM proved to be freely soluble in water, as verified by filtration on nylon membrane (0.45 μm).



Scheme 2.1.1. Synthesis of *N*-functionalized 5,6-dibenzyloxyindole (2) and its conversion to TEGM by aerial polymerization after deprotection from benzyl group.

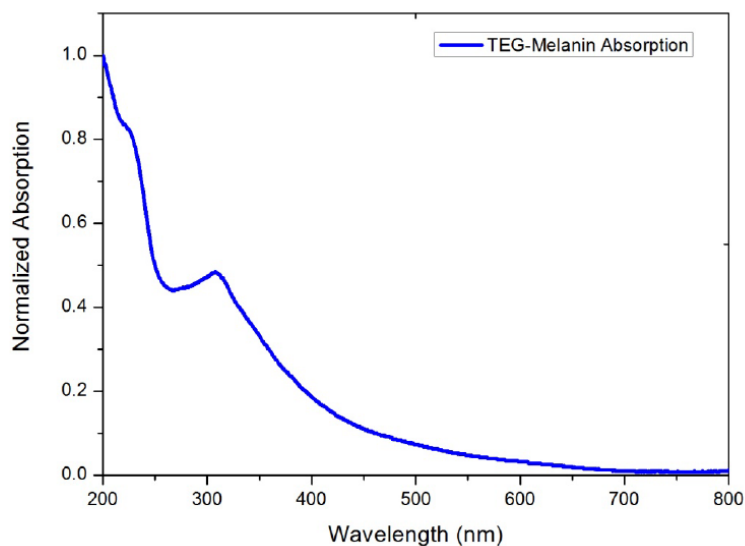


Figure 2.1.1. Normalized absorption spectra of drop casted TEG-Melanin layer on quartz.

Films of TEG-melanin were deposited by drop casting on ITO coated glass substrates in order to investigate the film morphology. The AFM image ($10\ \mu\text{m} \times 10\ \mu\text{m}$) reported in Figure 2.1.2 shows that the surface is fairly smooth except for the presence of micro-scale spaced bumps, not exceeding 90 nm heights. Images acquired at this scan size indicated an average root mean square (RMS) roughness of 7 nm. No other type of structuring could be distinguished at higher resolution scans.

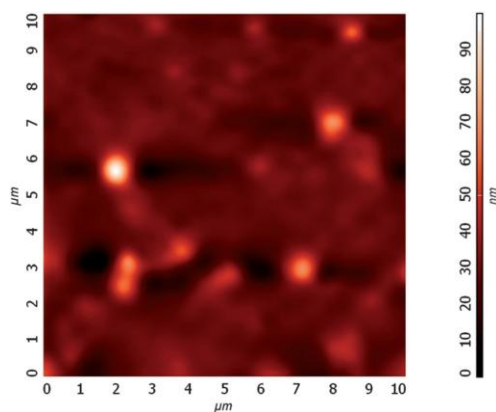


Figure 2.1.2. $10\ \mu\text{m} \times 10\ \mu\text{m}$ AFM image of the surface of the TEGM layer deposited on ITO.

The effect of the TEG chains on eumelanin solid state packing was investigated by X-ray diffraction analysis of TEGM powder and compared with data obtained from commercial synthetic melanin (SM) and DHI melanin (Figure 2.1.3). Typically, melanin-like amorphous

compounds produce broad peaks in the diffraction spectrum.⁷ In the case of TEGM powder, the position of the amorphous peak was found at around $2\theta \sim 21.5^\circ$, suggesting a correlation distance $d = 0.42$ nm, whereas in the case of SM the same peak registered at around $2\theta \sim 25^\circ$ indicated a distance $d = 0.35$ nm (Figure 2.1.3), the former being 20% larger compared to the latter; a correlation distance very similar to that measured for SM was obtained from DHI melanin ($d = 0.35$). These data suggests that the increased distance is likely due to the presence of the TEG chains on the TEGM polymer.

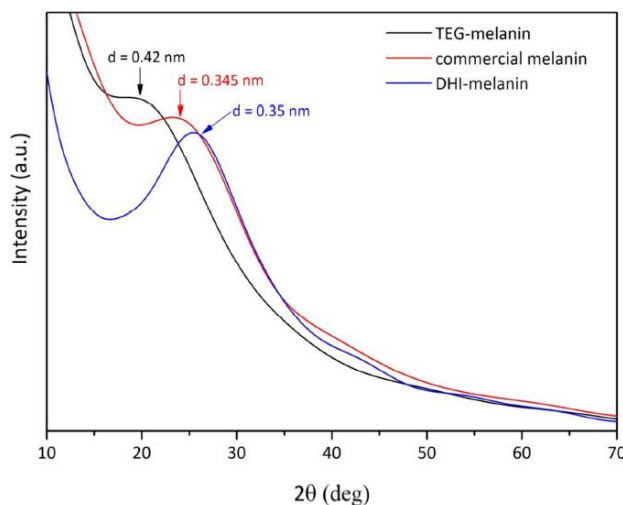


Figure 2.1.3. Powder X-ray diffraction spectra of TEG-melanin (black curve), commercial melanin SM (red curve) and DHI-Mel (blue-curve).

○ EUMELANIN THIN FILM FABRICATION

A second approach for high-quality eumelanin thin film processing has been developed focusing the attention on DHI, the monomer precursor of eumelanins, and on its peculiar oxidative reactivity.

The rationale behind the use of DHI in place of commonly used dopa or dopamine has been summarized as follows: (1) DHI is soluble in organic solvents and is the final monomer precursor in the pathways of natural and synthetic eumelanins, ensuring the generation of homopolymers; (2) the mode of polymerization of DHI and its dimers and oligomers, the mechanisms of aggregation underlying particle growth, and the optical and free radical properties of DHI melanin are known; (3) the electrical properties of DHI melanin suspensions have been characterized using an organic-electrochemical transistor.

Exploiting the high tendency of DHI to undergo oxidative processes even at the solid state, a procedure based on the ammonia induced solid state polymerization (AISSP) of DHI thin films has been developed. These are the key steps of the innovative technique: a) preparation of a DHI solution in methanol (10 mM); b) spin coating of the DHI solution on the selected substrate (glass, quartz, silicon etc.); c) exposure of the DHI thin film to ammonia vapors in an air-equilibrated atmosphere.

Just after few seconds of incubation, the pale yellow DHI thin films rapidly became dark brown suggesting that the polymerization process has occurred, leading to the formation of an eumelanin thin film.

To confirm this, UV spectra of the film before, throughout and after ammonia exposure have been registered. As shown in Figure 2.1.4, the UV spectrum of the DHI thin film exhibited a maximum centered at 300 nm (blue trace). During the 120 minutes exposure to ammonia vapours, the UV profile changed denoting the growth of more than one band in the visible region. At the end of the process, the monotonic profile is clearly visible (red trace).

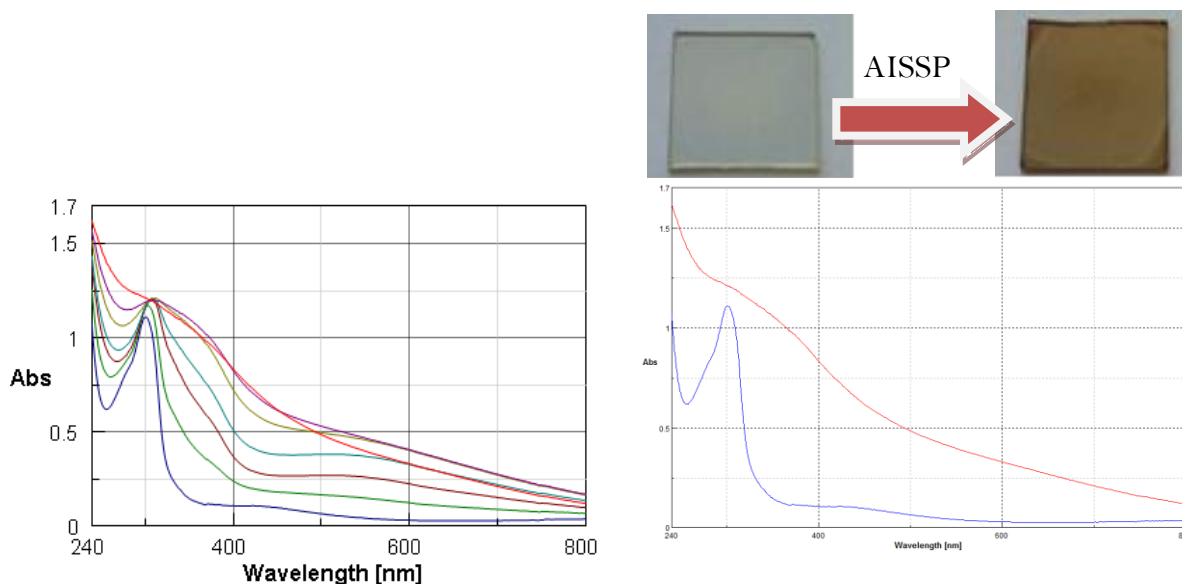


Figure 2.1.4. a) UV-vis profiles of a DHI thin film fabricated by AISSP. Plots are taken at 5, 15, 30, 45, 60 and 180 min after exposition to a polymerization inducing atmosphere; b) UV –vis plots of DHI and DHI melanin (120 min AISSP time) films on quartz substrates are showed with the corresponding substrate picture: DHI, left and eumelanin right.

The formation of DHI melanin films with the AISSP technique was further confirmed by matrix-assisted laser desorption ionization (MALDI) mass spectrometry taking as reference a dopa-melanin sample prepared by auto-oxidation in an alkaline medium according to a reported protocol (Figure 2.1.5). MALDI-MS data allowed us to appreciate several important chemical and technological advances associated with the AISSP technology. From the chemical viewpoint, when compared with representative films obtained by deposition of preformed eumelanins, such as tyrosinase-catalyzed DHI melanin and autoxidative dopa melanin, AISSP DHI films exhibited greater structural integrity, as evidenced by the regular clusters of peaks centered around the expected pseudomolecular ion peak, and a limited degree of polymerization (the highest oligomer detected at the hexamer–eptamer stage, to be compared with the 30-mer identified in the polymerization mixture of DHI).⁸

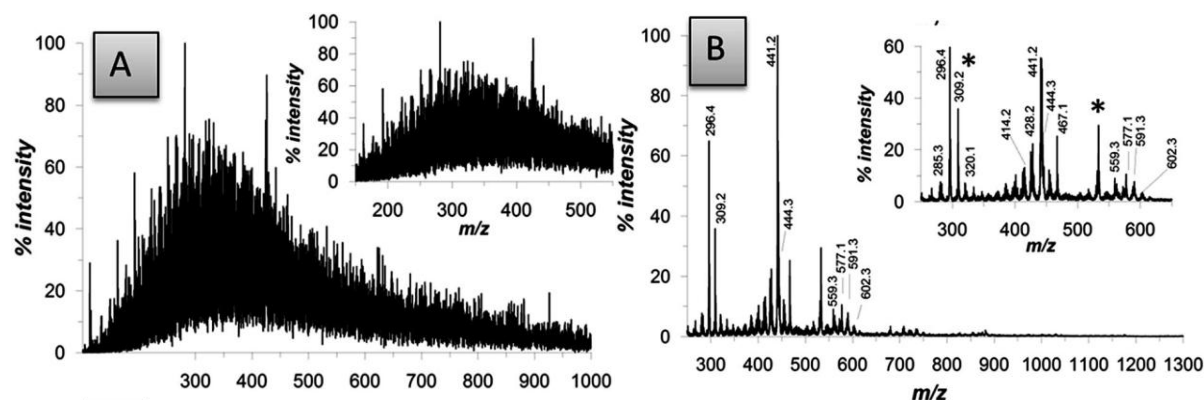


Figure 2.1.5. MALDI-MS spectra of eumelanin thin films on a standard MALDI plate. (A) Dopa melanin prepared by alkaline autoxidation. (B) DHI melanin prepared by the AISSP methodology. Asterisks denote impurities.

Apparently, ammonia is not incorporated into the chemical structure of the DHI polymer. Both structural integrity (i.e. preservation of indole units and avoiding aromatic ring fission) and control of polymerization can be attributed to the specific constraints and the lack of water associated with the solid state conditions, limiting water and/or hydroperoxyl anion induced oxidative cleavage of indole units and uncontrolled oligomer chain growth.

In contrast, preformed eumelanins are shown by mass spectrometry to be highly heterogeneous as a consequence of disordered polymerization of different units, higher molecular weight dispersion and extensive post-synthetic degradation under the solution conditions of the polymerization processes.

To check the morphology of the eumelanin films obtained with the AISSP technique, both SEM and AFM investigations were carried out.

More insights into the morphology of the eumelanin films were gained by acquiring AFM images on different length scales, going from $2\ \mu\text{m} \times 2\ \mu\text{m}$ to $30\ \mu\text{m} \times 30\ \mu\text{m}$ (Figure 2.1.6). From the AFM images, it becomes clear that the film surface is characterized by a very smooth matrix where the only specific morphological feature is the presence of some columnar structures having heights of a few nm. On a $2\ \mu\text{m} \times 2\ \mu\text{m}$ scale, the average roughness is found to be lower than 0.3 nm, while it increases up to about 1 nm, when larger scales are considered.

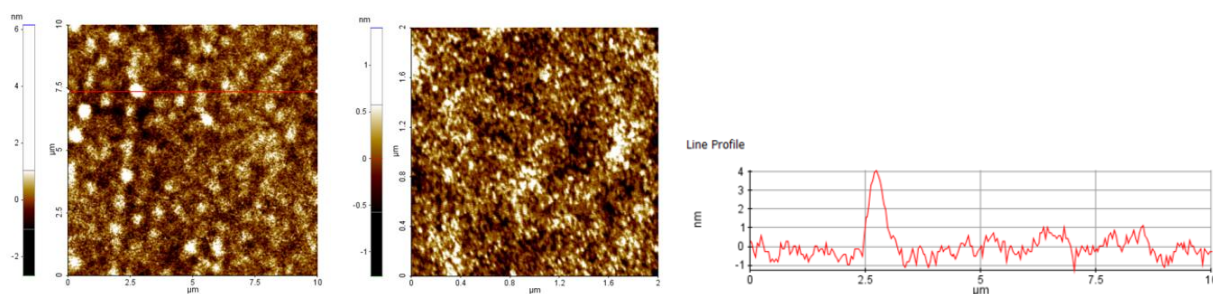


Figure 2.1.6. AFM topographical maps on different scales of a DHI melanin thin film grown by AISSP ($2 \times 2\ \mu\text{m}$, $10 \times 10\ \mu\text{m}$) and height profile caught from the red line on map (red line).

From the technological viewpoint, AISSP thin films proved to be more adhesive (over 3 days in aqueous media without detectable detachment) and smooth. By contrast, films obtained by previously reported techniques exhibited marked surface roughness and, most importantly, could be easily detached from the supporting surface by an aqueous medium (not shown). Such worse features can be attributed to the generation of a range of morphologies and to degradative fission of structural units of preformed eumelanins during the harsh synthetic process, decreasing adhesive functionalities of the biopolymer. Indeed, low adhesion and tendency to detach on water exposition was also observed with a smooth film obtained from dopa fabricated according to a reported procedure that has been known to provide very smooth surfaces. This was expected, again, on the basis of the structural modification induced by aqueous alkaline treatment and the associated backbone fragmentation and carboxyl group generation with consequent loss in adhesion to water resistance.

~CONCLUSIONS~

In conclusion, in this chapter are reported our recent progresses on the fabrication of high-quality eumelanin thin films following two different approaches. A water soluble eumelanin biopolymer TEGM is described, which was obtained by oxidative polymerization of a DHI derivative *N*-substituted with a hydrophilic TEG chain. The AISSP procedure showed important advantages with respect to previously reported protocols including: (1) efficient chemical control of structural disorder and film morphology, due to the facile deposition of the soluble DHI monomer opening the way to more efficient chemical manipulation and tailoring; (2) robustness and strong adhesion of the resulting film to a variety of substrates, from glass to silicon and plastic polymers; (3) the lack of artifacts associated with post-synthetic work-up procedures; (4) synthetic versatility for controlled polymerization and copolymerization with other co-substrates or for engineering wafer architectures; (5) low environmental impact due to the solvent-free, oxygen-based protocol. Very significantly, the AISSP procedure is of general relevance by being applicable to any easily oxidizable and filmable polyphenolic substrate.

Further details about results shown in this chapter can be found in the following articles:

- S. R. Cicco, M. Ambrico, P. F. Ambrico, M. Mastropasqua Talamo, A. Cardonea, T. Ligonzo, R. Di Mundo, C. Giannini, T. Sibillano, G. M. Farinola, P. Manini, A. Napolitano, V. Criscuolo, M. d'Ischia, "A water-soluble eumelanin polymer with typical polyelectrolyte behaviour by triethyleneglycol N-functionalization", *J. Mater. Chem. C*, **2015**, *3*, 2810–2816.
- Pezzella, M. Barra, A. Musto, A. Navarra, M. Alf , P. Manini, S. Parisi, A. Cassinese, V. Criscuolo, M. d'Ischia, "Stem cell-compatible eumelanin biointerface fabricated by chemically controlled solid state polymerization", *Mater. Horiz.*, **2015**, *2*, 212–220.

~EXPERIMENTAL SECTION~

○ MATERIALS AND METHODS

All chemicals were purchased from Aldrich, Alfa Aesar and Acros and used without further purification. DMF was distilled under a reduced pressure over molecular sieves, and stored under nitrogen atmosphere. 5,6-Dihydroxyindole (DHI) was prepared according to a reported procedure. FT-IR spectra were measured on a PerkinElmer 1710 spectrophotometer using dry KBr pellets. ¹H and ¹³C NMR spectra were recorded in CDCl₃ on a Bruker AM 500 spectrometer at 500 MHz and 125 MHz, respectively. Surface topography was characterized by means of an NTEGRA, NT-MDT Atomic Force Microscope in non-contact mode by using high accuracy non-contact (HA-NC) “etalon” probes (high aspect ratio tip, cantilever frequency 140 kHz). Several images at different scan size were acquired on the samples. X-ray diffraction (XRD) analysis of TEGM powders was performed with a Rigaku RINT2500 rotating anode laboratory diffractometer (50 kV, 200 mA) equipped with a silicon strip Rigaku D/teX Ultra detector, using Cu Kα1 monochromatic radiation ($\lambda = 1.5405 \text{ \AA}$). Moreover, a diffraction pattern has been also acquired from a sample of synthetic melanin (SM) in powder (SIGMA-Aldrich) and on DHI–melanin in powder, in order to compare their structures with that of TEGM. The TEGM and SM layer thickness were measured by an Alpha Step profilometer and both found 400 nm thick (D120, Tencor Instruments). Morphological AFM images of films obtained via AISSP technique were taken by means of an XE100 Park instrument operating in non-contact mode (amplitude modulation, silicon nitride cantilever from Nanosensor) at room temperature in ambient conditions. Film thickness was estimated by scratching the film down to the substrate with a needle and measuring by AFM the height of the resulting trench. Film roughness was estimated as Root Mean Square (RMS) from several AFM scans on the same sample.

- Synthesis of 5,6-bis(benzyloxy)-1-(2-(2-(2-methoxyethoxy)ethoxy)-ethyl)-1H-indole
NaH (0.078 g, 60% w/w in mineral oil, 1.95 mmol, 1.2 eq.) was introduced in a three-necked round bottom flask under a nitrogen atmosphere. The mineral oil was washed away with hexane, then dry DMF (10 mL) was added. 5,6-Dibenzyloxyindole (1) (0.536 g, 1.63 mmol, 1 eq.) dissolved in dry DMF (20 mL) was added to the mixture. The resulting mixture was stirred for 30 min, cooled at 0 °C and then 1-bromo-2-(2-(2-methoxyethoxy)-ethoxy)ethane

(1.541 g, 6.79 mmol, 2.5 eq.) dissolved in dry DMF (10 mL) was added dropwise. The reaction mixture was stirred at room temperature for 4 h, then quenched with saturated aqueous NH_4Cl , diluted with ethyl acetate and washed many times with water (5 – 20 mL). The organic layer was dried over anhydrous Na_2SO_4 and the solvent removed under a reduced pressure. The product was purified by silica gel chromatography using a mixture of hexane–ethyl acetate (7 : 3) as the eluent, affording 0.660 g (85% yield) of **2** as a yellowish dense oil.

^1H NMR (500 MHz, CDCl_3): δ = 7.51–7.50 (m, 4H), 7.39–7.36 (m, 4H), 7.33–7.29 (m, 2H), 7.19 (s, 1H), 7.05 (d, 1H, J = 3.1 Hz), 6.96 (s, 1H), 6.35 (d, 1H, J = 3.1 Hz), 5.20 (s, 2H), 5.18 (s, 2H), 4.20 (t, 2H, J = 5.8 Hz), 3.75 (t, 2H, J = 5.8 Hz), 3.54 (m, 8H), 3.37 (s, 3H) ppm; ^{13}C NMR (125 MHz, CDCl_3): δ = 146.57, 144.92, 137.92, 137.65, 131.27, 128.34, 128.31, 127.64, 127.53, 127.46, 127.43, 122.32, 107.16, 100.79, 97.41, 72.46, 72.39, 71.86, 70.70, 70.55, 70.49, 70.10, 58.93, 46.39 ppm; FT-IR: ν = 3062, 3030, 2925, 2872, 1505, 1484, 1453, 1420, 1377, 1350, 1302, 1219, 1197, 1142, 1061, 1026, 1004, 914, 876, 849, 760, 740, 697, 648, 597, 470 cm^{-1} .

- Synthesis of *N*-TEG MELANIN (TEGM)

N-Triethyleneglycol-5,6-dibenzyloxyindole (**2**) (0.250 g, 0.53 mmol) in ethyl acetate (30 mL) was poured into a hydrogenation bomb, added with palladium on charcoal (70 mg) and subjected to a positive pressure of hydrogen gas (30 atm). After 18 h the reaction mixture was filtered to remove the catalyst and the solvent evaporated under a reduced pressure. The residue (0.120 g) was taken into methanol (5 mL) and dissolved into an aqueous ammonia solution (1%). The reaction mixture immediately turned into deep violet and after 24 h was dark brown in color. After 48 h the mixture was acidified to pH 4 with 3 M HCl and evaporated under reduced pressure. The dark residue was taken up in water and freeze-dried overnight to afford TEGM as a dark solid (0.100 g).

- TEGM/SM layers deposition.

A TEGM solution for thin film deposition was prepared by dissolving 70 mg of TEGM in deionized water (3 mL). Synthetic Melanin SM solution for thin film deposition was prepared by dissolving SM powder (70 mg, Sigma-Aldrich) in water (1 mL) and 28% aq ammonia solution (2 mL). The TEGM and SM layers of same thickness were deposited by drop casting on plasma-treated Indium Tin Oxide (ITO)/glass supports. All samples were dried at room temperature under vacuum at a pressure of 2×10^{-3} mbar for 12 h.

- Synthesis of dopa-melanin

A solution of DL-dihydroxyphenylalanine (DL-dopa) (10 g, 0.051 mol) in 2 L of deionized water was adjusted to pH 8 by the addition of concentrated ammonia solution. Air was bubbled through the stirred solution for 3 days. Concentrated hydrochloric acid was then used to bring the pH to 2, and the resulting black precipitate was isolated by centrifugation and washed several times with 0.01 M hydrochloric acid and then with deionized water.

- DHI Thin Film Deposition

DHI thin films were prepared by spin coating with a Laurell WS-650MZ-23NPP/LITE coater; thin films were deposited on quartz. Thin films were obtained from a 30 mg/mL solutions of DHI in methanol after filtering through a 0.2 μm nylon membrane, using the following speed gradients: 2000 rpm for 90"; 800 rpm for 10" and 3000 rpm for 60"; 2000 rpm for 60"; and 3000 rpm for 90". In some cases thin films were annealed at 70 °C for 30' under a nitrogen atmosphere.

- Ammonia-Induced Solid State Polymerization:

The oxidation of DHI thin films (100-200 nm thickness) to give the melanin polymer was achieved by exposure to an oxidizing atmosphere (e.g. oxygen atmosphere and ammonia vapors). In the general procedure, the appropriate film was incubated in the oxygen/ammonia atmosphere at controlled temperature (25 - 40 °C). The ammonia vapors were produced by equilibration of the atmosphere with ammonia solution (28% to 7% NH_3 in H_2O) in a sealed camera at 1 ATM pressure. Exposure times varied in the range 2 to 18 h. When appropriate the whole spin coating procedure was conducted under oxidation promoting atmosphere. Oxidative polymerization was followed by UV-vis spectroscopy. Spectra were reordered in the range 240-800 nm at several reaction times from 1 min to 1 day after AISSP was started. In detail, the film on quartz reported in Figure 2.1.4a was obtained with the following parameters: DHI solution in methanol: 30 mg/mL; speed gradient: 800 rpm for 10" and 3000 rpm for 60"; oxidizing atmosphere: 28% NH_3 in H_2O equilibrated air; oxidation temperature 25 °C; oxidation time: 2 h.

REFERENCES

- [1]. Bothma, J. P.; De Boor, J.; Divakar, U.; Schwenn, P. E.; Meredith, P. *Advanced Materials* **2008**, *20*, 3539-3542.
- [2]. Bettinger, C. J.; Bruggeman, P. P.; Misra, A.; Borenstein, J. T.; Langer, R. *Biomaterials* **2009**, *30*, 3050-3057.
- [3]. Bloisi, F.; Pezzella, A.; Barra, M.; Chiarella, F.; Cassinese, A.; Vicari, L. *Journal of Applied Physics* **2011**, *110*.
- [4]. J. Eduardo de Albuquerque, C. Giacomantonio, A. G. White, P. Meredith, *Eur Biophys J*, **2006**, *35*, 190-195
- [5]. A. Pezzella, A. Iadonisi, S. Valerio, L. Panzella, A. Napolitano, M. Adinolfi and Marco d'Ischia, *J. AM. CHEM. SOC.* **2009**, *131*, 15270-15275
- [6]. M. Adinolfi, M. d'Ischia, A. Iadonisi, L. Leone, A. Pezzella and S. Valerio, *Eur. J. Org. Chem.* **2012**, 4333-433
- [7]. S. N. Deziderio, C. A. Brunello, M. I. N. da Silva, M. A. Cotta and C. F. O. Graeff, *J. Non-Cryst. Solids*, **2004**, 338-340, 634-638.
- [8]. S. Reale, M. Crucianelli, A. Pezzella, M. d'Ischia and F. De Angelis, *J. Mass Spectrom.*, **2012**, *47*, 49-53.

SECTION 2

CHAPTER 2

ELECTRICAL PROPERTIES OF EUMELANIN THIN FILMS

~INTRODUCTION~

Since the first observation from McGinness that eumelanin films can act as amorphous soft organic semiconductors, many studies have been carried out trying to delineate the mechanisms of charge transport. But due to the difficulties to produce homogeneous thin films and due to the undefined structure of the polymer, a mechanism of conduction has not been outlined yet.

Studies of electrical properties of eumelanin thin films reported so far showed the strong dependence of the conductivity from the hydration of the films.

Bothma et al. in 2008 calculated the conductivity of eumelanin thin films by spin coating an ammonia solution of synthetic melanin that reached a maximum of $\sigma = 2.5 \times 10^{-5} \text{ S cm}^{-1}$ at a relative humidity of 100% comparable to amorphous silicon.¹ Bettinger et al. reported in 2009 a conductivity of $7.00 \times 10^{-5} \text{ S cm}^{-1}$ of eumelanin thin films, obtained by spin coating solutions in DMSO or in 1M aqueous sodium hydroxide, in the hydrated state.² All the reported measurements were usually carried out at high hydration states, i.e. at 100% relative humidity (RH), or from very low hydration states to vacuum, with very high applied voltages ($\geq 10\text{V}$).

Investigations on the strong humidity dependence of the electrical conductivity in eumelanin thin films were carried out by Mostert et al. suggesting a peculiar electronic–ionic hybrid conductor behavior, in which thermodynamically favorable, water-driven redox equilibrium between catechol and quinone species would generate semiquinone moieties doping electrons and protons into the system.³

In 2013 the group of Prof. Santato performed a series of conductivity measurement at controlled humidity, ranging from 50% to 90%, using Pt electrodes, upon application of electrical biases $\leq 1 \text{ V}$. The calculated conductivity agrees with the previous works. These measurements suggested a mixed ionic–electronic transport in eumelanin thin films and that the two contributions to the electrical current cannot be considered as independent since the ionic current inevitably affects the electronic current.⁴

The possibility to exploit such hydration dependence in the development of eumelanin-based devices appears quite appealing in technological terms and above all when we deal with bio-electronic devices.

In biological systems, electrical signals are mainly transported by ions, such as small cations and protons; in particular H^+ transport is involved in a variety of processes including adenosine

triphosphate (ATP) oxidative phosphorylation in mitochondria, the HVCN1 voltage gated proton channel in mammals, the light activated proton pumping of bacteriorhodopsin in Archaea, proton activated flagella in bacteria, the antibiotic Gramicidin and proton activated bioluminescence in dinoflagellates. In all of these systems, hydrogen bonded water and hydrophilic residues form hydrogen bonded proton wires along which the protons hop following the Grotthuss mechanism.⁵ In 1804, Theodor von Grotthuss proposed a hopping mechanism involving the exchange of the covalent bond between an H and an O with the hydrogen bond formed by the same H with a neighboring water molecule. In the same fashion as proton-hopping, the absence of a proton, or proton hole (OH^-), will transport along proton wires.⁶

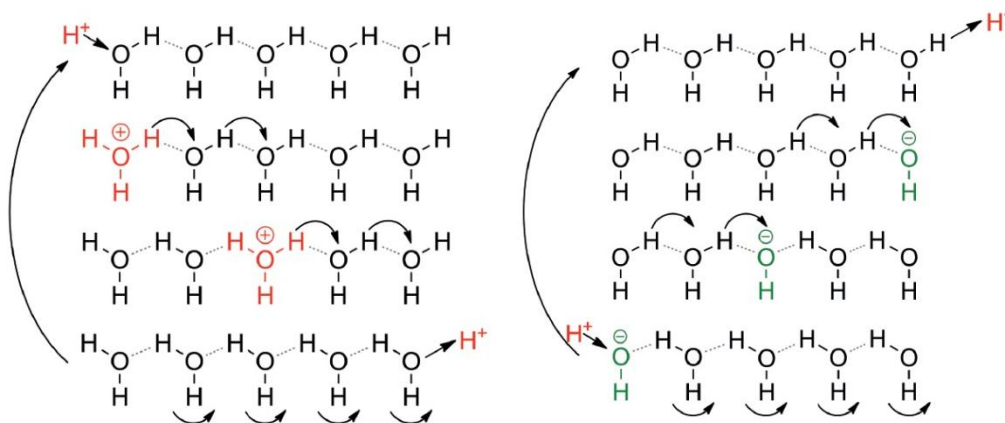


Figure 2.2.1. Grotthuss mechanism for proton (H^+) hopping and proton-hole (OH^-) hopping.

In 2011, for the first time the research group of Professor Rolandi realized a bio-protonic field effect transistor with proton-transparent palladium hydride (PdH_x) contacts using maleic-chitosan nanofibers as protonic channels.⁷

Metal electrodes, such as gold, silver and platinum, are good electron conductors, but palladium is the only one able to form proton-conducting PdH_x electrodes on exposure to gaseous hydrogen. Palladium-black electrodes show the ability to reversibly absorb hydrogen to a considerable extent; when dissolved in the palladium lattice, the hydrogen is almost completely ionized, with its electron going into the palladium d shell, and this provides the basis for hydrogen-saturated palladium-black acting as an efficient source and sink for protons.⁸

In Rolandi's bioprotonic devices, PdH_x contacts (source and drain) inject and drain protons into and from the proton-conducting channel, effectively serving as "protodes". For each proton injected into the material, an electron is collected by the leads, which complete the circuit.

In 2015 this kind of devices has been fabricated by using eumelanin thin films as organic semiconductors with the aim of understanding in which extent protons and electrons contribute to the electrical response of eumelanin films. In this work it has been shown that eumelanin films are proton conductive over micrometric distances and that the contribution of protons to the electrical current strongly increases with hydration. The ionic conductivity reaches about 10^{-4} - 10^{-3} S cm⁻¹ when the device is tested under a 90% of relative humidity (RH) conditions. This effect can be largely ascribed to proton conduction and points out the importance of electrochemical reactions in the electrical response of hydrated eumelanin thin films. Overall, these preliminary results prove to be very interesting even if obtained by using commercial synthetic eumelanin (SM) with poor control over the chemical composition of the polymer.⁹

On these bases, in this chapter the electrical properties of TEGM thin films and of eumelanin thin films obtained with the AISSP technique will be discussed. Moreover, a preliminary investigation on how and in which extent the proton conduction of eumelanin thin films can be influenced by its chemical composition is reported. This latter work has been carried out at the University of Washington (USA) (from 27/07/2014 to 17/08/2014) and at the University of California Santa Cruz (USA) (from 18/06/2016 to 8/09/2016) in collaboration with Prof. Marco Rolandi.

~RESULTS AND DISCUSSION~

○ CURRENT-VOLTAGE AND IMPEDANCE ANALYSIS OF TEGM

The electrical properties of TEGM studied on metal-insulator-metal device (MIM) by thermally evaporating a set of gold (Au) dots ($\text{\O} = 500 \text{ }\mu\text{m}$, 150 nm thick) on top of the structures consisting of casted TEGM layers on plasma-treated ITO/glass supports (Figure 2.2.2).

Current–voltage (IV) and impedance spectroscopy (IS) measurements were performed on TEGM and compared with those collected on SM-based MIM devices. All measurements were performed at room temperature under ambient air at a relative humidity degree of 50%. Figure 2.2.3 displays the results of current–voltage (I–V) hysteresis loops collected in ambient air on TEGM-based MIM devices for different voltage loop amplitudes, V_L ($V_L = 1.0, 2.0$ and 3.0 V), while keeping constant the voltage-sweep speed, s , (a and b) and at different voltage-sweep speeds s by keeping constant the voltage loop amplitude V_L (c).

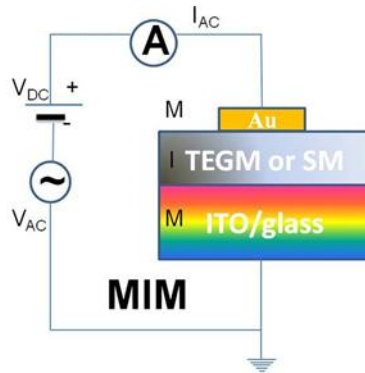


Figure 2.2.2. Scheme of the metal-insulator-metal (MIM) device and of the electrical measurement set up.

An increase in the voltage loop or in the voltage-sweep speed was found to produce larger hystereses (Fig. 2.2.3 a–c). Similar results were previously observed in a SM-based MIM structure, confirming that TEGM melanin shows a typical behavior in space charge storage mechanisms. More specifically, the space charges accumulate at the metal/eumelanin interface, shielding the applied electric field and limiting further carrier injection in the TEGM layer. Based on this hypothesis, the injection occurs during the voltage sweep from 0 V up to V_L followed by the accumulation at one of the electrodes (Au or ITO); afterwards space charges

distribute in the structure. During the reverse sweep and at a certain value of the applied voltage, called open-circuit voltage V_{oc}^+ , a balance is established between the external field and that due to space charge so that no current is flowing any longer. By further decreasing the voltage, the current flows again and at zero bias a non-zero current (negative short circuit current, I_{sc}^-) is observable due to the stored charges flowing back through the external circuit. Moving toward a more negative voltage (from 0 to $-V_L$), charge storage occurs again and in the subsequent forward sweep direction from $(-V_L$ up to $+V_L$) an open circuit voltage (V_{oc}^-) and a positive short circuit current (I_{sc}^+) can be detected. The magnitude of I_{sc}^- and V_{oc}^- in both sweep directions depends on the amount of stored charges at electrode/polymer interface and may differ in the two hysteresis branches due to the different electrode (Au and ITO) work functions.

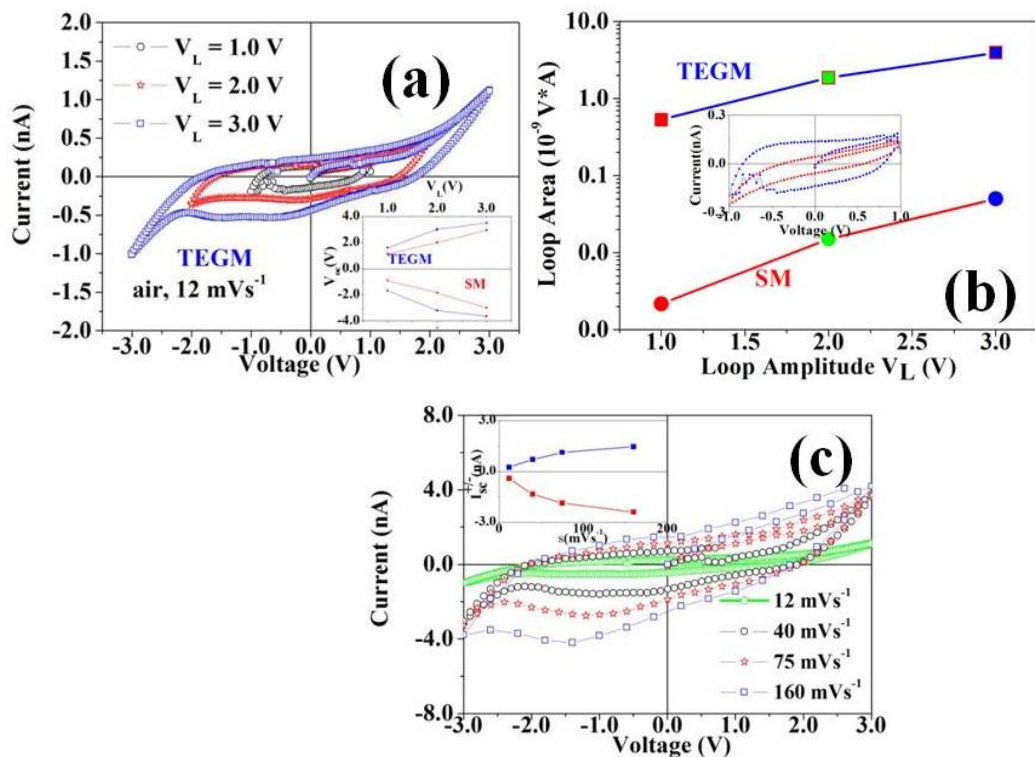


Figure 2.2.3. (a) I–V hysteresis loops collected on TEGM-based MIM structures at different V_L . The inset shows the comparison between V_{oc}^- vs. V_L extracted from TEGM-based and SM-based MIM devices. (b) Loop areas extracted by integrating the I–V hysteresis loops of SM (red curves) and TEGM (blue curves) at different V_L values and fixed voltage sweep speed $s = 12 \text{ mVs}^{-1}$. The inset shows the comparison between representative loops of SM- and TEGM-based MIM devices; (c) I–V hysteresis loops collected on TEGM-based MIM device at different voltage sweep speeds s (see legend). V_{oc}^- and I_{sc}^- meanings are the same as in (a). In the inset the extracted values of I_{sc}^- vs. s .

To detail better on the observed charge storage effect and hysteretic behavior, we start considering the general expression of the displacement current I_d as a function of the voltage flowing across a capacitive medium:

$$I_d = \frac{dQ}{dt} = \frac{d(CV)}{dt} = V \frac{dC}{dt} + C \frac{dV}{dt} = V \frac{dC}{dt} + Cs \quad (1)$$

Such a current adds to conduction current component I_r . It can be deduced that the displacement current can be more or less enhanced depending on the voltage loop amplitudes and on the voltage sweep speeds. The term (dC/dt) represents the increase of capacitance during the voltage sweep.

When fixing the voltage sweep speed s , the variation of the amount of stored charges $vs V_L$, can be obtained by integrating the expression (1) i.e. by calculating the loop area values. The results indicate that the stored charges are almost linearly dependent on the magnitude of the voltage loop amplitude. The comparison between results on TEGM-based and SM-based MIM devices evidences that in the former the stored charge is two orders of magnitude higher than in the latter, thus indicating more effective space charge accumulation mechanisms under a voltage stimulus. This is also evidenced by the comparison between two typical hysteresis loops collected at the same voltage sweep speed s and for $V_L = 1.0$ V on TEGM-based (blue squares) and on SM-based (red squares) MIM devices (see inset in Figure 2.2.3b).

Furthermore, the hysteresis curves showed an increase of the loop area with voltage sweep speed s at a fixed voltage loop. Interestingly, in this case the open circuit voltage values kept approximately the same values, while the short circuit currents increased with speed in both hysteresis branches. Based on the expression (1) the zero bias short circuit current I_{sc} when varying the voltage sweep speed by keeping constant the voltage loop magnitude, could be ascribed to the dependence of the charge-trapping/detrapping mechanisms on the voltage sweep rate. In this case:

$$I_{sc} \sim C \left(\frac{dV}{dt} \right) = Cs \quad (2)$$

i.e. a linear dependence of I_{sc} on s would be expected. The I_{sc}^- vs s data displayed in the inset of Figure 2.2.3c suggested that two linear regimes were present, one at lower voltage sweep speed (up to $s \leq 60$ mV s⁻¹) the other up to $s = 160$ mV s⁻¹. By linearly fitting I_{sc}^+ vs s values the

capacitance varied from 14 nF down to 4 nF as resulting for the low (i.e. $s \leq 60 \text{ mV s}^{-1}$) and high s values range, respectively. A similar capacitance reduction (i.e. from 22 nF to 6 nF going from the low to the high s values range) was observed by linearly fitting I_{sc} vs. s values. This variation was ascribed to the distribution and density of charge trapping sites contributing to the capacitance depending on the specific trapping/detrapping characteristic times. The estimate of the SM capacitance resulting from the data collected on SM-based MIM devices indicated that the layer capacitance was lower than that of the TEGM layer (55 pF for the low s range i.e. $s = 1.0\text{--}12 \text{ mV s}^{-1}$).

The electrical transport properties of both TEGM and SM appeared to depend on the water-ion content, so that they can both be assigned to the class of water-based polyelectrolytes. The analysis of the AC impedance frequency dispersion can provide further insight into the relative extent of the different relaxation mechanisms contributing to the spectra as a result of electrode polarization, ionic motion and possible dipolar contributions.

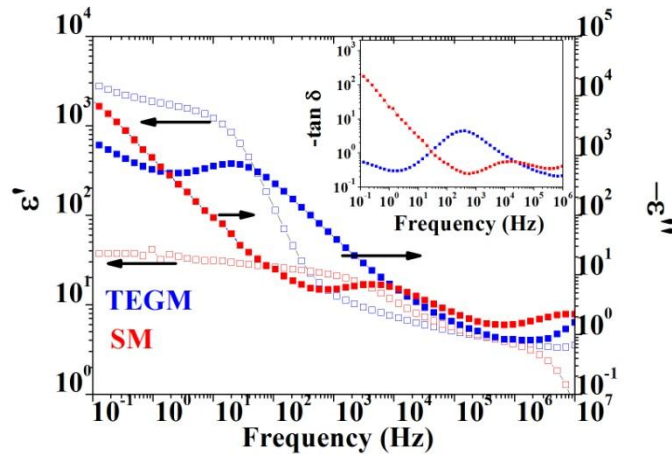


Figure 2.2.4. Dispersion spectra of the real (ϵ' , left axis) and imaginary (ϵ'' , right axis) part of the dielectric permittivity as resulting from impedance spectra collected on TEGM (blue curves) and SM (red curves) MIM devices. The inset shows the calculated $\tan \delta$ loss dispersion spectra.

Figure 2.2.4 illustrates the real (ϵ' , dielectric constant) and imaginary (ϵ'' , dielectric loss) part of dielectric permittivity frequency dispersion, as derived from the impedance data collected in ambient air on TEGM- and SM-based MIM structures. In the inset the loss factor $\tan \delta$ vs f dispersion, i.e. the ratio between the dielectric loss and dielectric constant, is also shown. Interestingly, different behaviors of TEGM and SM permittivity were observed. The real part

of the dielectric permittivity spectra of TEGM revealed the presence of a plateau in the frequency region up to 10 Hz, assigned to the double layer capacitive contribution. Relevant to note, the estimated dielectric constant is two orders of magnitude higher than that of SM, evidencing an increased interfacial polarization effect at the electrode. In the frequency region 10 Hz to 10 kHz the TEGM dielectric constant shows a behavior typically observed in polyelectrolytes and its value was consistently higher than that of SM. This can be attributed to the recognized ability of TEG to increase ionic conductivity and/or dipolar effects, as observed in other polymers. Furthermore, a major water molecules enclosure should be expected due to the TEG major hydrophilicity. The relaxation process then extends up to 1 MHz and the corresponding relaxation time was extracted by the peak frequency in the loss $\tan\delta$ *vs* f spectra and found to be $\tau = 2.56$ ms.

Compared to TEGM, the ϵ' of SM showed a dispersion spectrum whose behavior was similar to those commonly observed in biological items. In particular, the two typical regions generally encountered in biological items ϵ' spectra, were distinguishable. The first one was constituted by a relaxation region generally extending from 1 kHz up to 1 MHz and whose magnitude is strictly related to the embedded water content. Such a region is commonly referred to as the β region. The second one, at a relaxation frequency above 1 MHz, evidenced the presence of the water-molecule dipole reorientation processes and was commonly defined as the γ -region.

Data in Figure 2.2.3 and 2.2.4 clearly showed that the inclusion of the highly hydrophilic TEG chain results in a profound alteration of typical eumelanin electrical properties with a marked increase in the dielectric constant and a distinct polyelectrolyte behavior. It is suggested that the TEG chains allow for the incorporation of water molecules into the bulk of the eumelanin films, with the formation of a hydrogen-bond network enabling efficient charge transport in the solid state. It is tempting to assume, in this context, that the oligoether chains play the dual role of favoring eumelanin aggregation in a relatively regular manner and keeping the water molecules tightly bound between the stacked indolic layers (Figure 2.2.5).

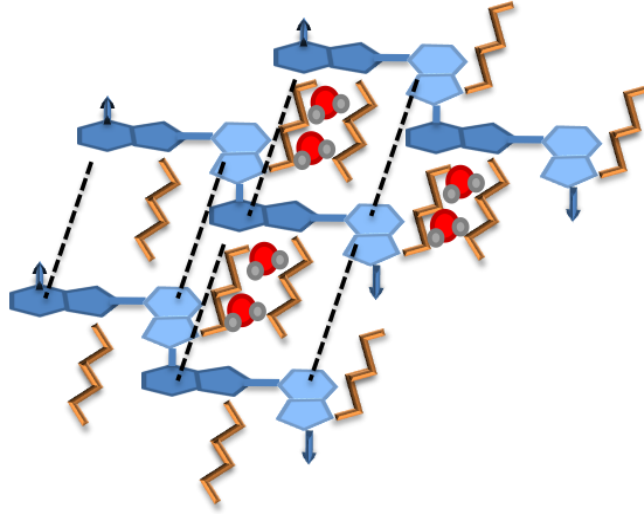


Figure 2.2.5. Pictorial model of possible assembly of TEGM with water incorporation.

○ ELECTRICAL PROPERTIES OF MELANIN THIN FILMS DEPOSED WITH THE AISSP TECHNIQUE.

Exploiting the advantages offered by the AISSP technique, a eumelanin based transistor was fabricated and the electrical properties investigated. The device has been prepared by depositing a thin film of DHI eumelanin on a multilayer structure composed of a thick ($500\ \mu\text{m}$) highly doped (Si^{++}) substrate, a $200\ \text{nm}$ thin SiO_2 insulating barrier and gold pre-patterned electrodes with interdigitated layout (Figure 2.2.6). These $\text{Si}^{++}/\text{SiO}_2/\text{Au}$ structures were considered for investigating the possibility to further modulate the charge transport through eumelanin channels connecting the gold electrodes (source–drain contacts) by applying a gate voltage (V_G) to the Si^{++} substrate, as has been commonly done in basic field-effect transistors (FETs).

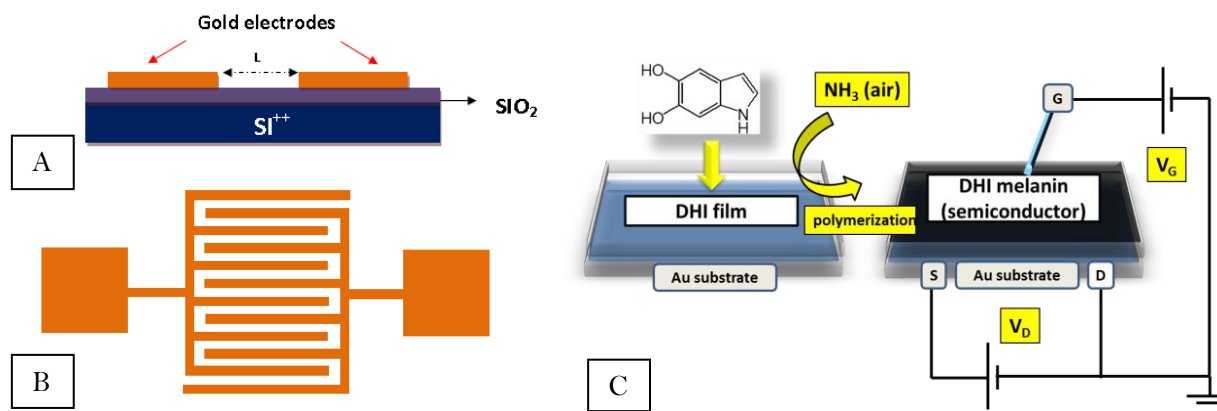


Figure 2.2.6. Schematic illustration of the architecture of the transistor (A and B) and of the procedure for DHI melanin film deposition and of the FET device setup for the determination of electrical properties (C).

The first measurements indicated clearly the lack of any detectable field-effect response and, hence, the current I_{DS} discussed hereafter is referred to the basic condition with $V_G = 0$ V. I_{DS} curves were recorded by sweeping the related V_{DS} voltage first between 0 and 50 V and then in the backward direction (from 50 to 0 V), with the aim to highlight the presence of hysteresis phenomena. The exemplificative measurement reported in Figure 2.2.7 confirms the presence of hysteretic behavior with the I_{DS} values measured in the backward scan being lower than those measured in the forward cycle (clockwise hysteresis).

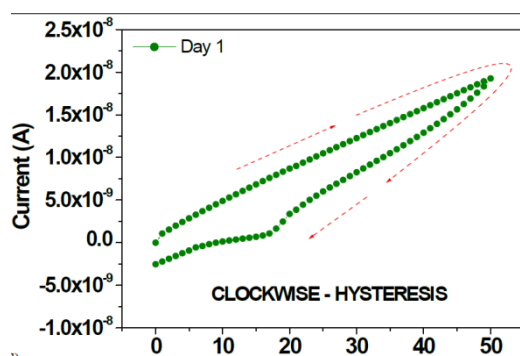


Figure 2.2.7. Current-Voltage (IV) curve with hysteresis loop measured for a DHI melanin thin film during the first day of storage in air.

This phenomenon is quite typical of electrically active materials characterized by poor structural order and gives indications of the occurrence of charge trapping phenomena. For eumelanin layers, in any case, this effect should be associated also with the presence of proton

space charge accumulation effects in the regions close to the electrodes. This specific feature is currently under investigation; here the attention was basically focused on the general capability of AISSP-deposited eumelanin films to carry electrical charges. In this regard, Figure 2.2.8A reports the I_{DS} curves measured only during the forward V_{DS} scan for a sample stored in air within a prolonged period.

From this plot it is possible to appreciate that the measurements carried out on freshly prepared moisture-equilibrated films exhibited well-defined ohmic behavior (i.e. I_{DS} is a linear function of V_{DS}) with a conductivity (σ) value of about 10^{-7} S cm^{-1} .

The conducting properties of a pristine eumelanin film were also assessed by the application of continuously repeated IV measurements. Under this condition, the current flow between the two gold electrodes displayed only a limited (by a few percent) decrease over time. This effect should be basically ascribed to the same charge trapping processes invoked above to justify the hysteretic behavior of these channels. It is worth mentioning, however, that all the repeated IV curves preserve the basic ohmic response.

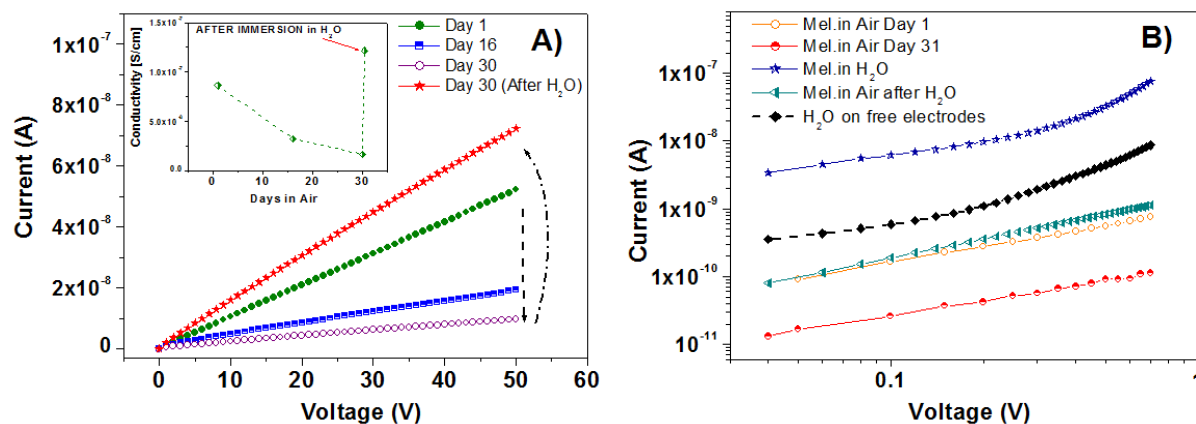


Figure 2.2.8. (A) Current–voltage curves for DHI melanin thin films on $\text{Si}^{++}/\text{SiO}_2/\text{Au}$ substrates recorded after prolonged intervals of storage in air and after the rehydration procedure. In the inset, the related conductivity behavior extracted from IV curves. (B) IV curves measured by sweeping the V_{DS} voltage from 0 to 0.7 V under different environmental conditions.

On the other hand, Figure 2.2.8A shows that, after a prolonged (30 days) standing in air, a gradual drop by about one order of magnitude in conductivity of the same film has occurred.

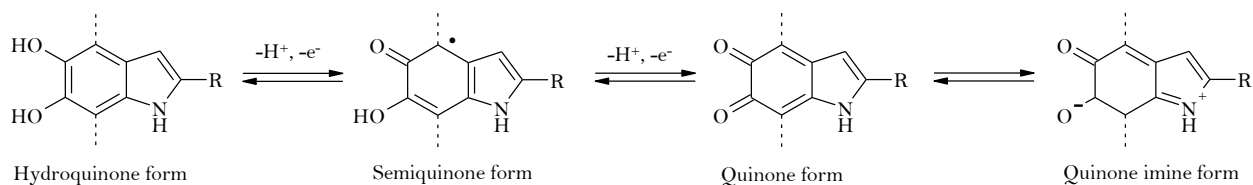
Apparently, the σ lowering was related to the drying process of eumelanin films during the storage in air. In order to confirm this conclusion, eumelanin channels were re-hydrated by

covering them with de-ionized water which was led to evaporate for 30 minutes. A final drying with nitrogen gas was carried out to complete the procedure. As shown, the subsequent IV curve recorded in air confirmed the eumelanin channel capability to recover completely the initial conductivity state. In particular, for these films, several desiccation–hydration cycles could be performed, which states the fully reversible character of the charge doping/dedoping process. After the electrical characterization in air, specific measurements were carried out by keeping the eumelanin channels directly immersed in water. In this case, IV curves were recorded by sweeping V_{DS} voltages between 0 and 0.7 V in order to minimize the occurrence of electrical currents related to the effect of water electrolysis.

As reported in Figure 2.2.8 B, the IV curve measured for the eumelanin film covered with water displayed considerably higher values than those of the corresponding measurements recorded in air at different times (namely, under different hydration conditions). Moreover, the semi-log plot allows us to clarify that the electrical current flowing through the water-covered eumelanin channel exceeds by about one order of magnitude that flowing between two free gold electrodes immersed in the same amount of de-ionized water.

○ PROTON CONDUCTION IN EUMELANIN THIN FILMS

Eumelanin is known to be a heterogeneous polymer arising from the polymerization of L-tyrosine and is composed by oligomeric and/or polymeric species of DHI and DHICA, and their various redox forms, namely the *ortho*-hydroquinone (H₂Q), the semiquinone (SQ), and the (indole)quinone (Q) forms, as well as the tautomer of Q, the quinone imine (QI) (Scheme 2.2.1).



Scheme 2.2.1. Redox forms of DHI and DHICA.⁹

In order to get more insights about the nature of the proton conductivity of eumelanin thin films, it is important to have control over the chemical composition of the film since each species within the polymer can affect the overall electrical and/or protonic conduction.

An important role in the eumelanin proton conduction is believed to be due to the presence and the amount of $-\text{COOH}$ groups of the DHICA unit that can ease and help the proton hopping throughout the melanin scaffold.

To evaluate the contribution of the carboxyl groups on the proton conduction of eumelanins, four eumelanin thin films were prepared by using the AISSP technique, differing for the ratio between the DHI and the DHICA monomers: A) DHI; B) DHI:DHICA = 3:1; C) DHI:DHICA = 1:1; D) DHI:DHICA = 1:3. Proton transport was investigated by transient current measurements with Pd and PdH_x electrodes in a planar two-electrode configuration (Figure 2.2.9).

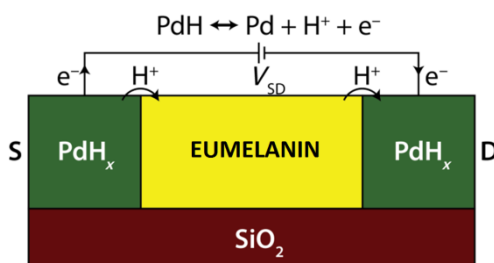


Figure 2.2.9. Scheme of palladium-hydride (PdH_x) protode behavior.

When Pd is exposed to gaseous hydrogen, Pd forms palladium hydride (PdH_x) with a stoichiometric ratio $x \leq 0.6$. With a source-drain potential difference, V_{SD} , the PdH_x source and drain inject and drain protons (H^+) into and from the eumelanin film, effectively serving as protodes. For each H^+ injected into the film, an excess electron is collected by the leads, which complete the circuit and result in a current measured at the drain, I_D . As such, PdH_x contacts are able to measure both the electronic and protonic contribution to the current in eumelanin films.

Measurements were carried out by varying also the relative humidity (RH) parameter, set at 50% and 90%, to assess also the role of water. So, the following four different experimental conditions were used for each type of eumelanin thin film analyzed.

1. 50% RH
2. 50% RH with 5% H_2
3. 90% RH
4. 90% RH with 5% H_2

The proton conductivity was estimated using devices with different lengths between the Pd source and the drain (L_{SD}) in a geometry that is commonly known as a transmission line measurement (TLM). By varying the distance between source and drain (L_{SD}) it's possible to distinguish between the fixed PdH-eumelanin interface resistance and the varying bulk resistance (Figure 2.2.10).

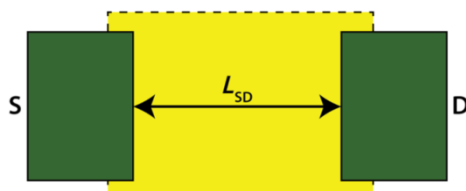


Figure 2.2.10. TLM geometry.

In a first set of experiments a voltage sweep ranging from -1 V to 1 V was applied to each channel for all the films in all the conditions. The IV curves showed a hysteresis profile as already observed in previous works.¹⁰

In a second set of experiments $V_{SD} = 1$ V was applied on devices with L_{SD} ranging from 5 to 200 μm , and the I_D was measured in order to calculate the resistance of each device, R_L .

To extrapolate the resistivity of the films, R_L was plotted as a function of L_{SD} . The slope of this plot is proportional to the resistivity of the film, and the intercept on the R_L axis for $L_{SD} = 0$ is the contact resistance. The calculated conductivities are reported in Table 2.2.1 and depicted in Figure 2.2.11 for comparison.

Table 2.2.1. Measured conductivities σ ($\text{S} \cdot \text{cm}^{-1}$)

	DHI	DHI:DHICA=3:1	DHI:DHICA=1:1	DHI:DHICA=1:3
50 RH,	7.00×10^{-6}	9.98×10^{-6}	1.03×10^{-5}	1.59×10^{-5}
50 RH, H_2	7.17×10^{-6}	1.54×10^{-5}	1.62×10^{-5}	7.61×10^{-6}
90 RH,	2.90×10^{-5}	2.86×10^{-5}	7.23×10^{-5}	2.13×10^{-4}
90 RH, H_2	5.20×10^{-5}	5.77×10^{-5}	9.16×10^{-5}	3.29×10^{-4}

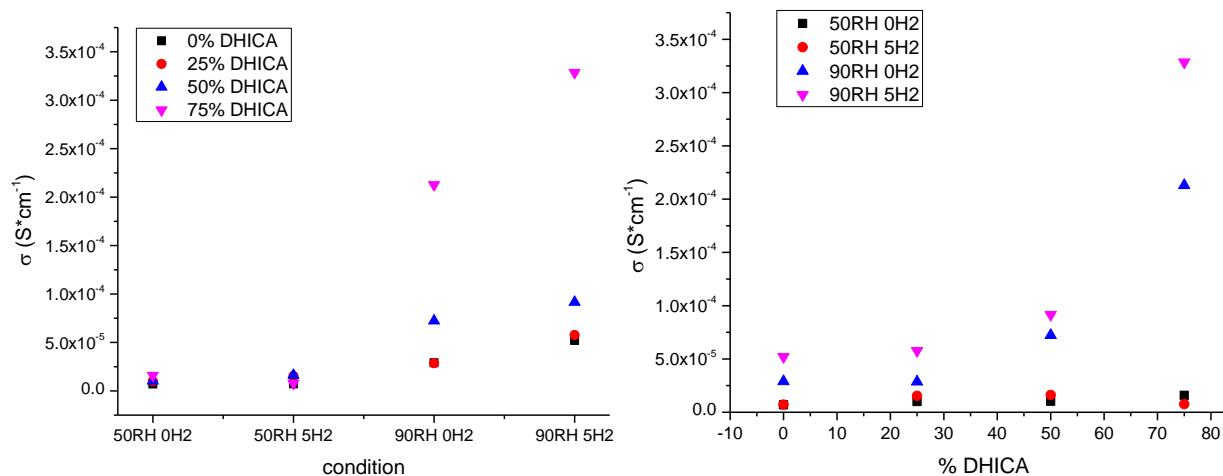


Figure 2.2.11. Comparison of calculated conductivities for the different eumelanin thin films in different ambient conditions.

From these preliminary results it's possible to see that higher degree of hydration can enhance the overall conductivity of the eumelanin as already described.¹⁰

Moreover, the presence of the hydrogen gives a further enhancement of the conductivity in high hydration states suggesting an effective proton conduction mechanism within the films. Interestingly the hydrogen effect is much more prominent with the highest percentage of DHICA reaching a maximum value of $3.29 \times 10^{-4} \text{ Scm}^{-1}$, suggesting that the presence of carboxylic groups can effectively help the proton hopping throughout the eumelanin backbone as hypothesized.

Further experiments and data analysis are in due course in order to get deeper insights about the overall conduction mechanisms and in particular to separate the two contributions, electronic and protonic, to define a theoretical model that fully describes eumelanin conduction.

~CONCLUSIONS~

Current–voltage measurements in MIM devices indicated markedly higher open circuit values and hysteresis loop areas in the case of TEGM compared to the commercial melanin SM, suggesting in the former a more effective space charge mechanism. Impedance data consistently indicated for TEGM a double layer contribution much higher than for the reference SM and a higher dielectric constant. These results point to DHI functionalization with the solubilizing and highly hydrophilic TEG chain as an effective approach to confer polyelectrolyte behavior to eumelanin materials, possibly via the formation of a hydration shell around oligomer molecular components.

The hydration effect was evaluated on DHI-melanin thin films $\text{Si}^{++}/\text{SiO}_2/\text{Au}$ substrates obtained via the AISSP technique on demonstrating how the conductivity is sensitive to desiccation–hydration cycles and in particular how it increases with higher hydration states. The AISSP technique was employed to study the proton conductivity of chemically controlled eumelanin thin films, obtained varying the ratio between DHI and DHICA monomers, with palladium hydride (PdH_x) electrodes. The results showed that the overall conductivity is higher in high hydration states in line with previous works, and that the increasing amount of DHICA increases the conductivity especially in high hydration states in presence of hydrogen.

Further details about results shown in this chapter can be found in the following articles:

- S. R. Cicco, M. Ambrico, P. F. Ambrico, M. Mastropasqua Talamo, A. Cardonea, T. Ligonzo, R. Di Mundo, C. Giannini, T. Sibillano, G. M. Farinola, P. Manini, A. Napolitano, V. Criscuolo, M. d'Ischia, “A water-soluble eumelanin polymer with typical polyelectrolyte behaviour by triethyleneglycol N-functionalization”, *J. Mater. Chem. C*, **2015**, 3, 2810–2816.
- Pezzella, M. Barra, A. Musto, A. Navarra, M. Alfé, P. Manini, S. Parisi, A. Cassinese, V. Criscuolo, M. d'Ischia, “Stem cell-compatible eumelanin biointerface fabricated by chemically controlled solid state polymerization”, *Mater. Horiz.*, **2015**, 2, 212–220.

~EXPERIMENTAL SECTION~

- MIM device fabrication

A series of metal-insulator-metal (MIM) devices were tailored, for statistical purposes, by thermally evaporating a set of gold (Au) dots ($\varnothing = 500$ nm, 150 nm thick) on top of the structures consisting of casted TEGM and SM layers. A simplified sketch of the typical device configuration and measurement set up adopted in MIM structure characterizations is displayed in Figure 2.2.1.

- Electrical characterization of TEGM-based MIM devices

Current–voltage (IV) and impedance spectroscopy (IS) measurements have been performed on TEGM-based MIM devices and compared with those collected on SM-based MIM devices. All measurements were performed at room temperature under ambient air at a relative humidity degree of 50%. Current–voltage hysteresis loops on TEGM-based MIM structures were carried out under dark and by using a Keithley Model 617 electrometer. The loop read outs were performed starting from zero up to a maximum positive value of the continuous bias, defining the hysteresis loop amplitude $+V_L$, and then alternating back and forth between $+V_L$ and $-V_L$. The loop amplitudes V_L were in the range 1.0–3.0 V and the hystereses were acquired at different voltage sweep speeds.

Impedance spectroscopy (IS) measurements were made by using a NOVOCONTROL impedance analyzer in the frequency range 0.1 Hz to 1 MHz of the sine wave voltage signal with a signal amplitude $V_{AC} = 5.0$ mV and at zero DC bias voltage.

- Eumelanin thin film deposition via AISSP

DHI thin films were prepared by spin coating with Laurell WS-650MZ-23NPP/LITE coater on transistor substrates from concentrated methanol solutions (30 mg/mL) after filtering through a 0.2 μ m Whatman membrane. Appropriate volume deposition (10 - 50 μ L) and speed gradients were used. In some cases the films were annealed at 70 °C for 30' under nitrogen atmosphere. AISSP: Melanin thin films were obtained by exposing the DHI films (100-200 nm thickness) for 18 h to air-equilibrated gaseous ammonia from an ammonia solution (28% in water) in a sealed camera at 1 atm pressure at controlled temperature (25 - 40 °C).

- Electrical characterization of eumelanin thin films via AISSP

Electrical measurements were performed both in air and vacuum (10^{-2} Pa) by using a Janis Probe Station connected to a Keithley 2612A Dual-Channel system source-meter instrument. During all electrical measurements, eumelanin films were kept in darkness.

- Electrical and proton conductivity measurements of eumelanin thin films

Two-terminal measurements were performed on Si substrates with a 100-nm SiO₂ layer. Pd contacts were deposited by conventional photolithography and e-beam evaporation. Contacts were 500 μm wide and 100 nm thick with a 5-nm Cr adhesion layer.

Electrical measurements were performed on a Signatone H-100 probe station using a custom atmospheric isolation chamber. Dakota Instruments mass flow controllers were used to set the ratio of wet nitrogen and hydrogen controlled by a LabView DAQ. An Agilent 4155C semiconductor parameter analyzer was used for all electrical measurements.

REFERENCES

- [1]. J. P. Bothma, J. de Boor, U. Divakar, P. E. Schwenn, and P. Meredith, *Adv. Mater.* **2008**, *20*, 3539–3542
- [2]. C. J. Bettinger, J. P. Bruggeman, A. Misra, J. T. Borenstein, R. Langer, *Biomaterials*, **2009**, *30*, 3050–3057
- [3]. A. B. Mosterta, B. J. Powella, F. L. Prattb, G. R. Hansonc, T. Sarnad, I. R. Gentlee and P. Meredith, doi: 10.1073/pnas.1119948109
- [4]. J. Wunsche, F. Cicoira, C. F. O. Graeffc and C. Santato, *J. Mater. Chem. B*, **2013**, *1*, 3836–3842
- [5]. T. Miyake and M. Rolandi, *J. Phys. Condens. Matter*, **2016**, *28*, 023001
- [6]. J. F. Nagle and H. J. Morowitz, *Proc. Natl. Acad. Sci. USA*, **1978**, *75*, 298–302
- [7]. C. Zhong, Y. Deng, A. Fadavi Roudsari, A. Kapetanovic, M.P. Anantram and M. Rolandi, DOI: 10.1038/ncomms1489
- [8]. H. Morgan, R. Pethigt and G T Stevens, *J. Phys. E: Sci. Instrum.*, **1986**, *19*
- [9]. J. Wunsche, Y. Deng, P. Kumar, E. Di Mauro, E. Josberger, J. Sayago, A. Pezzella, F. Soavi, F. Cicoira, M. Rolandi and C. Santato, *Chem. Mater.* **2015**, *27*, 436–442
- [10]. M. Ambrico, A. Cardone, T. Ligonzo, V. Augelli, P. F. Ambrico, S. Cicco, G. M. Farinola, M. Filannino, G. Perna and V. Capozzi, *Organic Electronics*, **2010**, *11*, 1809–1814

SECTION 2

CHAPTER 3

NEW MELANIN-BASED BIO-INTERFACES

~INTRODUCTION~

As previously discussed, the emerging field of bio-electronics aims at integrating electronic devices into living systems in order to sense, record, and monitor different signals and physiological states, as well as to convert relevant parameters into electronic readout for further processing and decision making.

Moreover aim of bio-electronics is to implement multifunctional biocompatible interfaces and devices translating optical and electronic stimuli into bio-signals for engineering functional biological tissues, developing advanced cell culture systems and for single-cell diagnosis, cell sorting and differentiation.^{1,2} More recently increasing attention has been paid to the nature of the surface which the cells adhere to, in particular the topography and mechanical properties, as a means of controlling cell physiology.³⁻⁵ Defined nanopatterns of a surface can control cell adhesion and proliferation making the development of nanostructured and nanopatterned surfaces a most promising approach by which smart interfaces can translate signals to cells and govern their fate.

The majority of bio-interfaces reported so far are made up from classic polymers and copolymers, elastomers (to confer flexibility), or polyelectrolyte multilayer (PEM) films.⁶ Several obstacles and limitations relating to cell-surface interactions, materials strength and durability, biocompatibility, surface property regulation, binding and recognition specificity, need to be urgently overcome for a full maturation of the field. To address these and other issues, the imitation of Nature's structures and principles has emerged as a major competitive strategy^{7,8} for a number of reasons: 1) natural biomaterials usually exhibit superior properties or exemplify successful problem-solving strategies; 2) functional efficiency and diversity are normally related to their complex multi-scale hierarchical organization and supramolecular architecture based on small fundamental components, which confer a variety of properties e.g. self-healing, mechanical stability, high toughness, ability to respond dynamically to stimuli; 3) biological systems are mostly founded on weak yet highly specific non-covalent interactions (e.g. hydrogen bonding, hydrophobic interactions, etc.) that are crucial for structural and functional problems; 4) reproduction of biological systems and principles entails properties such as bioavailability, biocompatibility, robustness, flexibility and adhesion for integration with biological tissues and hosts.

Within this frame, melanins can play an important role thanks to the intrinsic biocompatibility and bioavailability. During the last decade, several key properties of eumelanin-inspired systems prepared by oxidative polymerization of DHI and other precursors have attracted the attention of the materials science community and prompted the realization of device quality thin films.⁹ Despite extensive investigations in the field of organic electronics, surprisingly little work has been devoted to the application of eumelanin for bio-optoelectronic interfaces and nanopatterning studies and, specifically, little attention has so far been directed to exploit DHI-based homopolymers. The only study so far reported demonstrated that solution-processed eumelanin thin films display promising properties as biocompatible and biodegradable semiconducting biomaterial for nerve tissue engineering.¹⁰

Furthermore, DHI-based materials display many appealing properties suitable for the realization of new bio-interfaces:

- 1) DHI-based eumelanin materials have a multifunctional structural and electronic network to respond to chemical stimuli, via acid and basic carboxylic/carboxylate groups, chelating catechol moieties, redox catechol/semiquinone/*o*-quinone systems, H-atom donor groups, and to physical signals by efficient light absorption, non-radiative excited state deactivation, electron photoejection and hydration-dependent hybrid ion-electron conductive behavior.
- 2) DHI-based systems can be chemically manipulated to tailor properties and to prepare high quality films.
- 3) DHI-based systems can self-assemble to mimic the basic architecture of natural eumelanins and can be decorated with bio-molecular side-groups to promote cell viability.

In order to investigate in this sense the potentiality of DHI-based materials, in this chapter is reported the research activity carried out to test the role of DHI eumelanin films as innovative bio-interface for stem cells adhesion, proliferation and differentiation.

This work has been carried out in collaboration with Dr Silvia Parisi, Dr Anna Musto and Dr Angelica Navarra of CEINGE Institute of Naples.

~RESULTS AND DISCUSSION~

For our purposes, murine embryonic stem cells (ESCs) were selected as cell population of particular interest for tissue engineering applications and currently under scrutiny for compatibility with classical electro-active materials.

Starting from the experience reached with the development of the AISSP technique, a set of DHI eumelanin thin films were deposited onto Petri dishes. To improve the film adhesion and proceed with the sterilization of the melanin-coated Petri dishes, an UV exposure step were taken into account.

Preliminary experiments were carried out to assess the ability of eumelanins to support the survival of ESCs; to this aim undifferentiated ESCs were trypsinized into a single-cell suspension and 6×10^4 cells/cm² were plated on 100 μm melanin-coated dish in ESC medium. The medium was changed every day for three days. As reported in Figure 2.3.1, ESCs proliferation, evaluated by counting cells after trypsinization and dissociation at 2 and 4 days in colonies plated on dishes coated with eumelanins, grows with a trend comparable with that observed for the same cells plated on gelatin taken as control.

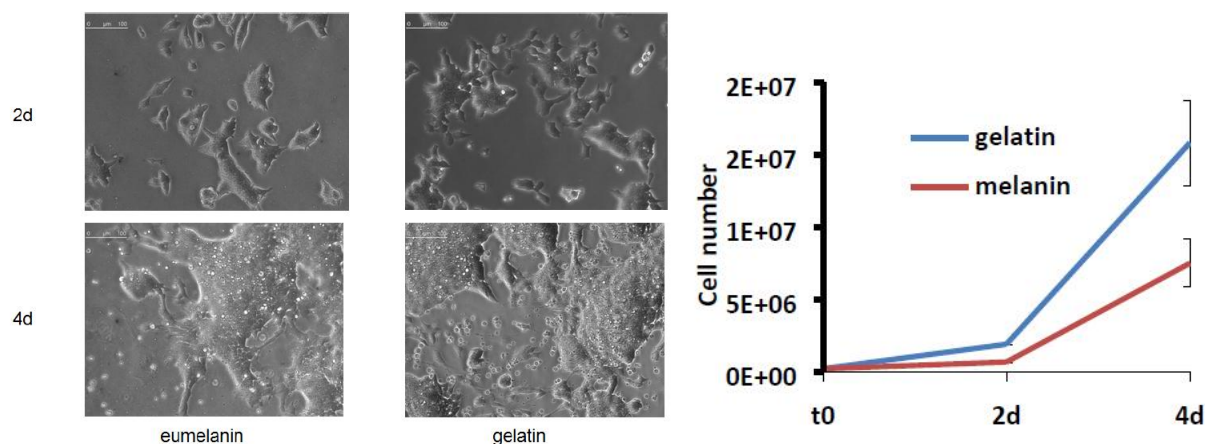


Figure 2.3.1. Phase contrast images of ESC colonies seeded on melanin and gelatin for 2 and 4 days (Scale bars: 100 μm) and the corresponding growth curves of ESCs counted at 2 and 4 days from plating. The data are reported as mean \pm standard error.

We also verified that eumelanins don't impair ESC morphology by staining F-actin. Figure 2.3.2 shows that the structural arrangement of ESCs grown on eumelanin is indistinguishable from those conventionally grown on gelatin. Finally, to confirm that the presence of healthy

colonies highlighted by the morphological analysis corresponds to an absence of abnormal cell death, we have analyzed the level of active caspase-3, an apoptosis hallmark. As shown in Figure 2.3.3, western blot analysis revealed that there is no accumulation of cleaved caspase-3 to the detriment of the uncleaved one that is normally present in healthy cells.

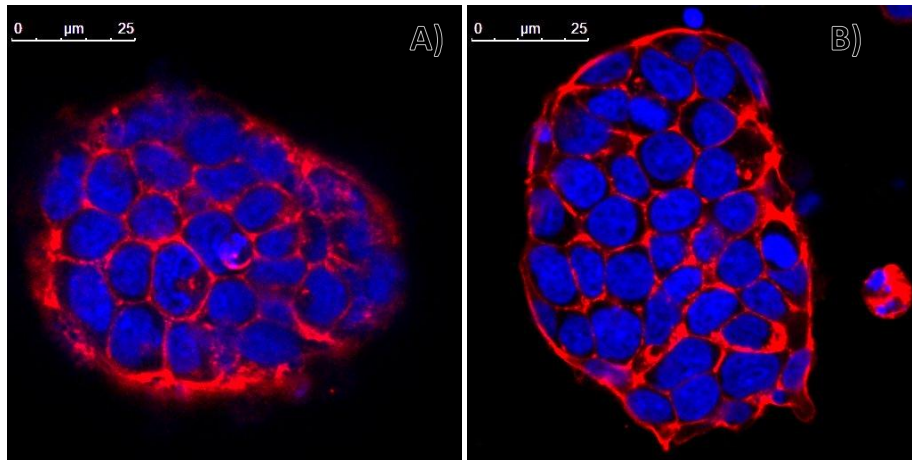


Figure 2.3.2. Confocal analysis of undifferentiated ESCs grown for 2 days on (A) eumelanin- or (B) gelatin-coated plates and stained with TRITC labeled phalloidin that binds to F-actin. Nuclei were counterstained with DRQ5. Scale bars: 25 μ m.

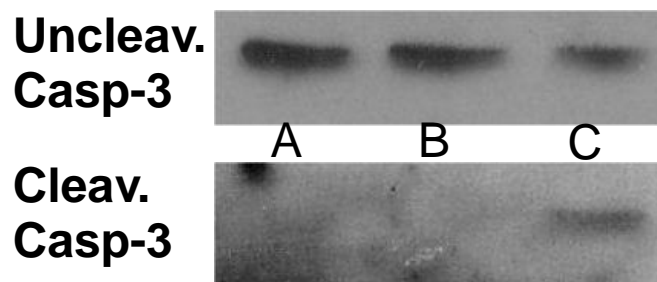


Figure 2.3.3. Western blot analysis of uncleaved and cleaved caspase-3. ESCs were grown on (A) gelatin- or on (B) eumelanin-coated dishes and after 48 hours were collected. The positive control (C) are ESCs exposed to 15Gy of X rays to induce apoptosis.

Given these positive preliminary results, we decided to explore the role of eumelanin coatings in promoting the differentiation of ESCs into neurons.

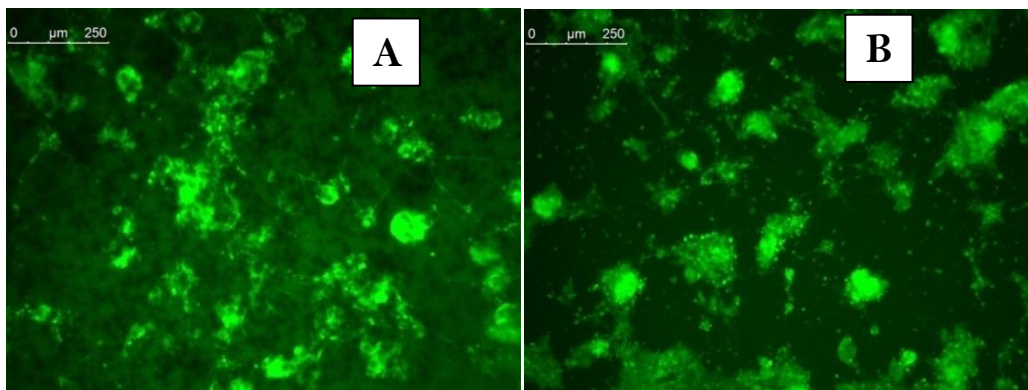


Figure 2.3.4. Fluorescent live inspection of $\alpha 1$ -tubulin-GFP ESCs differentiated for 4 days into neuronal lineage on (A) eumelanin- or (B) gelatin-coated plates. The presence of GFP indicated the formation of neuronal precursors. The presence of mature neurons is indicated by the GFP signal in the neuritis. Scale bars: 250 μ m.

To this aim, a reporter cell line bearing Green Fluorescent Protein (GFP) under the control of $\alpha 1$ -tubulin promoter¹¹ was used. Thus, the GFP is expressed only when the ESCs differentiate into neuronal precursor or mature neurons. We have employed two differentiation protocols to verify the versatility of eumelanin films.

In the first protocol, we allowed neuronal differentiation of ESCs by plating them on gelatin or eumelanin at low density in a chemically defined medium (see Experimental Section and reference¹²). As shown in Figure 2.3.4, after 4 days of differentiation we have found that the differentiation yield reached on eumelanin is comparable to that on gelatin. The presence of both neural precursors and mature neurons with their axonal extensions is visible in both conditions.

In the second differentiation method we induced the formation of serum free embryoid bodies in suspension SFEBs, (see Experimental Section and reference¹³) that allow the formation of neuronal precursors and then, upon adhesion on an appropriate substrate, the formation of mature neurons. Figure 2.3.5 shows that melanin supports the development of mature neurons from neural precursors derived from SFEBs after 11 days of differentiation.

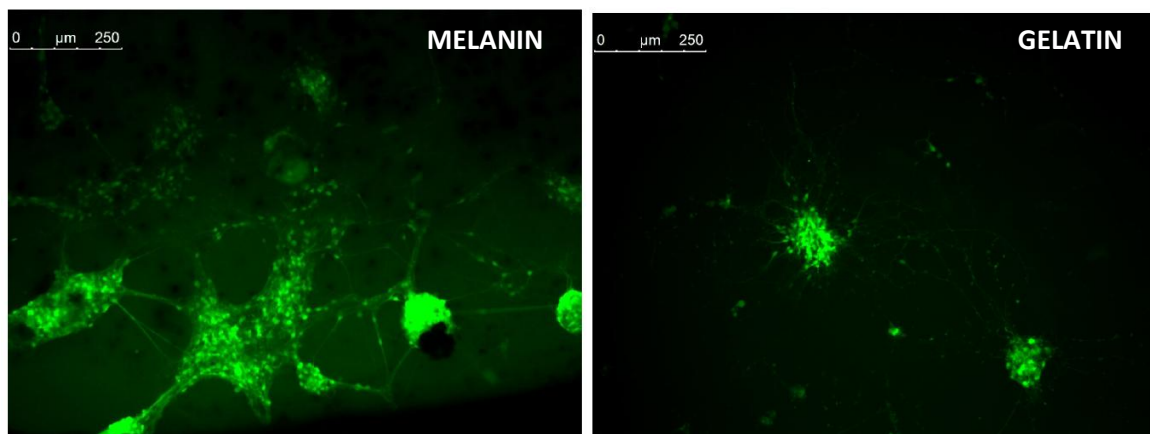


Figure 2.3.5. Fluorescent analysis of neurons after 11 days of differentiation through SFEB formation on eumelanin- or gelatin-coated plates. Scale bars: 250 μ m.

~CONCLUSIONS~

All together these results suggest that eumelanin is able not only to support normal growth of ESCs without impairing proliferation and survival but, importantly, this substrate is able to allow the formation of neuronal precursors and neurons starting from undifferentiated ESCs (first differentiation method) and the development of mature neurons from already established neural precursors (second differentiation method). These evidences open new perspectives toward the future application of eumelanin thin films as bio-interface for the differentiation of pluripotent stem cells into a specific cell fate such as specific neuronal-subpopulations, (i.e. dopaminergic neurons, motor neurons, etc.).

Further details about results shown in this chapter can be found in the following article:

- Pezzella, M. Barra, A. Musto, A. Navarra, M. Alf e, P. Manini, S. Parisi, A. Cassinese, V. Criscuolo, M. d'Ischia, "Stem cell-compatible eumelanin biointerface fabricated by chemically controlled solid state polymerization", *Mater. Horiz.*, **2015**, *2*, 212–220.

~EXPERIMENTAL SECTION~

For the realization of DHI-eumelanin thin films see Experimental Section of Chapter 1 of this section.

Neural differentiation was induced adapting the methods of Ying et al., 2003⁴. Briefly, α -tubulin-EGFP cells⁵ were plated onto gelatine- or melanin-coated dishes at low density (1.5×10^4 cells/cm²) in ESC medium. After 24h the cells were cultured in the following differentiation medium: 1 vol of DMEM/F12 combined with 1 vol of Neurobasal medium, supplemented with 0.5% N2 supplement, 1% B27 supplement, 2 mM glutamine (Invitrogen). Within four days in these conditions the cells undergo neuronal differentiation and start to express GFP.

ESCs differentiation into serum-free embryoid body (SFEB) formation⁶ was induced by placing 1×10^6 ESCs in 100-mm Petri dishes in the following differentiation medium: GMEM supplemented with 2 mM glutamine, 1 mM sodium pyruvate, $1 \times$ nonessential amino acids, 0.1 mM β -mercaptoethanol and 10% Knock-out Serum Replacement (KSR). After 7 days SFEBs are mainly composed of neuronal precursors and they are plated on gelatin or melanin-coated dishes. After further 3 days the presence of neuronal precursors and mature neurons (GFP-positive cells) was analysed with an inverted fluorescent microscope (DMI4000, Leica Microsystems) by using LAS AF software.

For apoptosis induction ESCs were irradiated with 15 Gy of X rays by using RS2000 Biological Irradiator (Rad Source) and incubated for 24h before analysis. Apoptosis was revealed by measuring the levels of cleaved caspase 3.

For western blot analysis ESCs were lysed in a buffer containing 1 mM EDTA, 50 mM Tris-HCl (pH 7.5), 70 mM NaCl, 1% Triton, and protease inhibitor cocktail (Sigma), and analyzed by Western blot. The following primary antibodies were used: rabbit Cleaved Caspase-3 (1:1000 Cell Signaling), rabbit Caspase-3 (1:1000 Millipore). Antibody protein complexes were detected by HRP-conjugated antibodies and ECL (both from Amersham Pharmacia).

For immunostaining, ESCs were plated on gelatin or melanin-coated chamber slides (ThermoScientific) to allow the observation with the confocal microscope. After 48 hours from plating the cells were fixed in 4% paraformaldehyde. The nonspecific block and permeabilization was performed by treatment in 10% FBS, 1% BSA, 0.1% triton and 1X PBS for 10' at room temperature, followed by incubation with The Phalloidin-Tetramethylrhodamine

Bisothiocyanate(1:500 Sigma). After three washes in PBS 1X for 10' at room temperature thenuclei were counterstained with DRQ5 (Cell Signaling, 1:1000).

Confocal microscopy was performed with a Leica TCSSMD FLIM microscope (LeicaMicrosystems) using LAS AF software (Leica Microsystems). When required, the brightness, contrast and color balance of the images were adjusted in Photoshop CS2 (Adobe Systems).

REFERENCES

- [1]. M. R. Antognazza, D. Ghezzi, M. Dal Maschio, E. Lanzarini, F. Benfenati and G. Lanzani, *Nature Commun.*, **2011**, **2**, 166
- [2]. Yang, L. et al. *Adv. Mater.*, **2013**, **25**, 3881-3887
- [3]. Ventre, M. et al. *J. R. Soc. Interface*, **2012**, **9**, 2017–2032
- [4]. Teo, B. K. et al. *Methods Cell. Biol.*, **2010**, **98**, 241-294
- [5]. Drachuk I. et al. *Adv. Funct. Mater.*, **2013**, DOI: 10.1002/adfm.201300038
- [6]. Minev I. R. et al. *Acta Biomaterialia*, **2013**, **9**, 6936–6942
- [7]. Meredith P. et al. *Rep. Prog. Phys.*, **2013**, **76**, 034501
- [8]. Sun T. L. et al. *Chem. Soc. Rev.*, **2011**, **40**, 2909-2921
- [9]. d'Ischia, M. et al. *Angew. Chem. Int. Ed.* **2009**, **48**, 3914-3921
- [10]. Bettinger, C. J. et al. *Biomaterials* **2009**, **30**, 3050-3057
- [11]. S. Parisi, F. Passaro, L. Aloia, I. Manabe, R. Nagai, L. Pastore and T. Russo, *J. Cell Sci.*, **2008**, **121**, 2629–2634.
- [12]. Q. L. Ying, M. Stavridis, D. Griffiths, M. Li and A. Smith, *Nat. Biotechnol.*, **2003**, **21**, 183–186.
- [13]. S. Parisi, M. Battista, A. Musto, A. Navarra, C. Tarantino and T. Russo, *FASEB J.*, **2012**, **26**, 3957–3968

~LIST OF PUBLICATIONS~

- ⊕ S. R. Cicco, M. Ambrico, P. F. Ambrico, M. Mastropasqua Talamo, A. Cardonea, T. Ligonzo, R. Di Mundo, C. Giannini, T. Sibillano, G. M. Farinola, P. Manini, A. Napolitano, **V. Criscuolo**, M. d'Ischia, "A water-soluble eumelanin polymer with typical polyelectrolyte behaviour by triethyleneglycol N-functionalization", *J. Mater. Chem. C*, **2015**, *3*, 2810-2816.
- ⊕ A. Pezzella, M. Barra, A. Musto, A. Navarra, M. Alfé, P. Manini, S. Parisi, A. Cassinese, **V. Criscuolo**, M. d'Ischia, "Stem cell-compatible eumelanin biointerface fabricated by chemically controlled solid state polymerization", *Mater. Horiz.*, **2015**, *2*, 212-220
- ⊕ P. Manini, **V. Criscuolo**, L. Ricciotti, A. Pezzella, M. Barra, A. Cassinese, O. Crescenzi, M. G. Maglione, P. Tassini, C. Minarini, V. Barone, M. d'Ischia, "Melanin-Inspired Organic Electronics: Electroluminescence in Asymmetric Triazatruxenes", *ChemPlusChem*, **2015**, *80*, 919-927
- ⊕ M. Barra, I. Bonadies, C. Carfagna, A. Cassinese, F. Cimino, O. Crescenzi, **V. Criscuolo**, M. d'Ischia, M. G. Maglione, P. Manini, L. Migliaccio, A. Musto, A. Napolitano, A. Navarra, L. Panzella, S. Parisi, A. Pezzella, C. T. Prontera and P. Tassini, "Eumelanin-Based Organic Bioelectronics: Myth or Reality?". *MRS Advances*, **2016**, *57*, 3801-3810.

~COMMUNICATIONS AT MEETINGS~

- ⊕ **V. Criscuolo**, P. Manini, A. Pezzella, O. Crescenzi, M. G. Maglione, P. Tassini, C. Minarini and M. d'Ischia, "Symmetry as an Unexplored Tool for Tailoring Optoelectronic Properties in Melanin-Inspired Triazatruxenes", XXV Congresso della Società Chimica Italiana, Rende (CS), Italy, 07 – 12 September 2014. Poster communication
- ⊕ **V. Criscuolo**, P. Manini, A. Pezzella, O. Crescenzi, E. Picardi, M. G. Maglione, P. Tassini, C. Minarini and M. d'Ischia, "Synthesis and Properties of Melanin-Inspired Triazatruxenes: Diverting the (Di)hydroxyindole Oxidative Pathway Toward new Cyclic Triindoles", IASOC 2014, Ischia, Italy, 21-25 September 2014. Poster communication
- ⊕ **V. Criscuolo**, P. Manini, A. Pezzella, P. Maddalena, S. Aprano, M. G. Maglione, P. Tassini, C. Minarini, M. d'Ischia, "Synthesis and photochemical properties of new melanin-inspired electroluminescent materials for OLED applications", XXXVI CDCO 2015, Bologna, Italy, 13-17 September 2015. Oral communication
- ⊕ **V. Criscuolo**, P. Manini, A. Pezzella, P. Maddalena, S. Aprano, M. G. Maglione, P. Tassini, C. Minarini and M. d'Ischia, "Synthesis and photochemical properties of new melanin-inspired electroluminescent materials for OLED applications", SAYCS, Rimini, Italy, 27-29 October 2015. Poster and Oral communication.
- ⊕ **V. Criscuolo**, P. Manini, A. Pezzella, P. Maddalena, S. Aprano, M. G. Maglione, P. Tassini, C. Minarini and M. d'Ischia, "Synthesis and photochemical properties of new melanin-inspired electroluminescent materials for OLED applications", ENER-CHEM, Firenze, Italy, 18-21 February 2016. Poster communication
- ⊕ **P. Manini**, **V. Criscuolo**, A. Pezzella, O. Crescenzi, M. d'Ischia, S. Aprano, A. Rubino, M. G. Maglione, P. Tassini and C. Minarini, "Melanins and light: when natural pigments inspire the design of biocompatible electroluminescent materials", CM&L 2015, Bologna, Italy, 21-23 September 2015.

- ⊖ P. Manini, **V. Criscuolo**, A. Pezzella, O. Crescenzi, M. d'Ischia, S. Aprano, M. G. Maglione, P. Tassini and C. Minarini, "From Melanins to New Electroluminescent Materials for Bio-Inspired OLED Applications", EOS Topical Meetings at Capri 2015, Capri, Italy 17-19 September 2015.
- ⊖ **V. Criscuolo**, P. Manini, A. Pezzella, M. G. Maglione, P. Tassini, C. Minarini, A. Navarra, S. Parisi and M. d'Ischia, "Eumelanin-based organic electronics", Asilomar Bioelectronics Symposium 2016, Asilomar conference grounds, Pacific Grove, California, USA, 5-8 September 2016. Poster communication.
- ⊖ **V. Criscuolo**, C. T. Prontera, A. Pezzella, M. G. Maglione, P. Tassini, C. Minarini, S. Pedatella, M. De Nisco, M. Manfra and P. Manini, "Bio-Inspired Luminescent Transition Metal Complexes: from Nature to Iridium Based OLED Devices", IASOC 2016, 25-29 September 2016, Ischia, Italy. Poster and selected Oral communication
- ⊖ **V. Criscuolo**, P. Manini, C. T. Prontera, A. Pezzella, M. G. Maglione, P. Tassini, C. Minarini, "From natural systems to lighting electronics: designing melanin-inspired electroluminescent materials", BioEL2017 International Winterschool on Bioelectronics, 11-18 March 2017, Kirchberg in Tirol, Austria. Oral communication.